

# Polymer Analogous Reactions on Redox-Active and Conjugated Polymers for Electronic Applications

Von der Fakultät Chemie der Universität Stuttgart zur Erlangung der Würde eines  
Doktors der Naturwissenschaften (Dr. rer. nat.) genehmigte Abhandlung

vorgelegt von

**Jochen Kuhlmann**

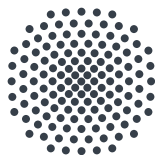
aus Ludwigsburg

Hauptberichterin: Prof. Dr. Sabine Ludwigs

Mitberichterin: Prof. Dr. Sabine Laschat

Prüfungsvorsitzender: Prof. Dr. Elias Klemm

Tag der mündlichen Prüfung: 09.12.2021



**Universität Stuttgart**



Institut für Polymerchemie  
Lehrstuhl für Struktur und Eigenschaften Polymerer Materialien



---

## Erklärung über die Eigenständigkeit der Dissertation

Ich versichere, dass ich die vorliegende Arbeit mit dem Titel

*Polymer Analogous Reactions on Redoxactive and Conjugated Polymers for Electronic Applications*

selbständig verfasst und keine anderen als die angegebenen Quellen und Hilfsmittel benutzt habe; aus fremden Quellen entnommene Passagen und Gedanken sind als solche kenntlich gemacht.

## Declaration of Authorship

I hereby certify that the dissertation entitled

*Polymer Analogous Reactions on Redoxactive and Conjugated Polymers for Electronic Applications*

is entirely my own work except where otherwise indicated. Passages and ideas from other sources have been clearly indicated.

---

Jochen Kuhlmann

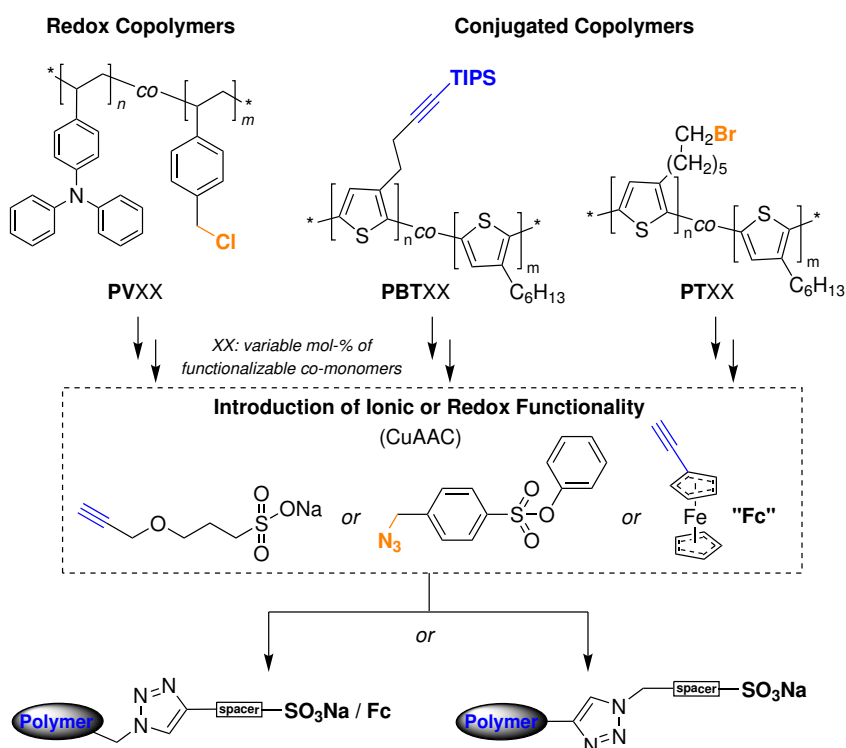
2021



# Summary

In the scope of this dissertation statistic copolymer platforms have been synthesized to serve as variable and tunable base systems for polymer analogous conversions. These conversions were done by copper catalyzed azide-alkyne 1,3-dipolar cycloaddition (CuAAC) and were used to incorporate ferrocene and sodium sulfonate groups into side chains of the polymers. Copolymers were synthesized in different comonomer ratios and are depicted in the figure below.

Copolymers with redox-active and cross-linkable triphenylamine units were created via free-radical polymerization in three different ratios. Furthermore, two conjugated copolymers based on poly(3-hexylthiophene) (P3HT) were polymerized by Grignard metathesis. Those differ in the nature of their side-chain endgroups as is depicted in the figure. CuAAC proceeds between an alkyne and an azide group, forming a covalent linkage in the shape of a triazole. Thus, both polymers offer opposing functionalities with regards to use in CuAAC, broadening the spectrum of applicable reaction partners for the functionalization of a P3HT based system.



The polythiophene platform has been used for the introduction of new functionality in earlier works<sup>[1,2]</sup> while redox properties of TPA based homopolymers and derivatives have been investigated.<sup>[3]</sup> Both platforms have been shown to be able to reach high levels

---

of electronic conductivity under doping.<sup>[1,2,4]</sup> Since they also offer stable redox switching, crosslinking capabilities (in the case of TPA) and adjustable redox properties,<sup>[3]</sup> redox polymers are of great interest for electrocatalytic use and in battery applications.<sup>[5-8]</sup> In this work, copolymers were synthesized to allow for control of the number of functional groups in the polymer and introduction of ferrocene as a defined redox species, as well as ionic sulfonate moieties were probed. This way, conducting redox polymers and mixed ionic/electronic conduction can be achieved. Generally, mixed conducting materials are of particular interest in literature, due to their ability to self- and auto-dope, giving rise to fast redox switching and high achievable conductivity<sup>[9-11]</sup> which can be further improved by careful selection of counterions.<sup>[12,13]</sup>

Corresponding copolymers were functionalized by means of CuAAC click chemistry for which there are different methods to perform. Conversions inside of thin films and in polymer solutions were assessed with infrared spectroscopy and cyclic voltammetry. High degrees of conversion were achieved with both methods and while characterization of in-film functionalizations is limited, their success was confirmed electrochemically by evaluating the relationship between CV peak currents and scan rate of ferrocene-functionalized **PVXX** copolymers in 3 different co-monomer ratios. Analogously functionalized polymer films bearing ionic sulfonate moieties in their side-chains were additionally characterized in AC impedance spectroscopy to decouple ionic and electronic conductivity and determine humidity dependence of these values. Hereby, in-film functionalized samples did not consistently result in ionic conduction during experiments, a finding that was attributed to the fact that these films were electrochemically crosslinked prior to CuAAC for stability reasons, which likely reduced accessibility of azide groups within the polymer films. However, films prepared from pre-clicked polymers, where sulfonate groups were covalently introduced in solution prior to spin-coating, resulted in ionic conductivities of up to  $9.5 \text{ mS cm}^{-1}$  at a relative water uptake of the polymer films of 67 wt-%, as determined by quartz crystal micro balance (QCM). These values were reached with 73 % of ionic co-monomers, which was the highest ratio employed. Pre-clicking of polymer **PV26-A**, where only 26 % of monomers can be functionalized, lead to solubility issues, thus no impedance characterization was possible with this co-monomer ratio.

Thiophene based conjugated copolymer systems were assessed in one co-monomer ratio, each. System **PT71** was attempted to be solution-clicked with the alkyne sulfonate displayed in the image above but yielded only partial conversion which in turn lead to solubility issues. This was attributed to an unfavourable steric situation in this polymer, due to long side chains and the relatively long sulfonate moiety. System **PBT24** on the other hand was clicked with a protected azide sulfonate as shown, which circumvented solubility

---

issues and allowed for film preparation. Deprotection of the ionic groups was performed in-film and subsequent impedance and QCM characterization gave mixed ionic/electronic conduction with maximum conductivities in the undoped state of  $0.1 \text{ mS cm}^{-1}$  ( $\sigma_{el}$  at 0 mbar  $p_{H_2O}$ ) and  $1.4 \text{ mS cm}^{-1}$  ( $\sigma_{ion}$  at 30 mbar  $p_{H_2O}$ ). The highest relative water uptake achieved by this polymer was 44 wt-%.

## Publications

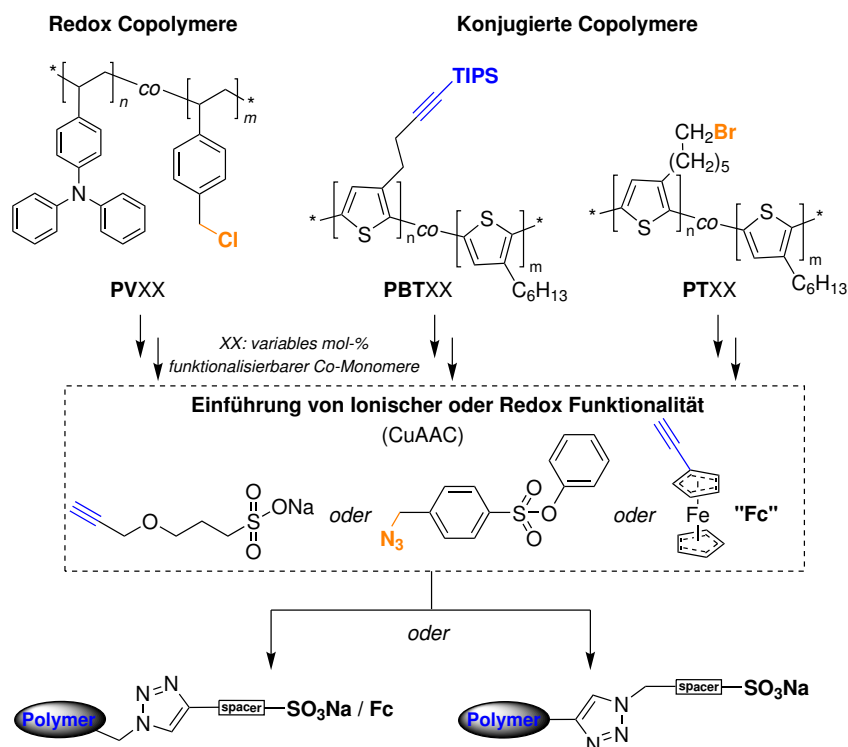
Parts of this work have been published in:

J. E. Kuhlmann, S. S. Y. Liu, K. Dirnberger, M. Zharnikov, S. Ludwigs, *Electrochemical Characterization of Redox Probes Confined in 3D Conducting Polymer Networks*, *Chem. Eur. J.* **2021**, *27*, 17255, doi: 10.1002/chem.202103257.

# Zusammenfassung

Im Rahmen dieser Dissertation wurden statistische Copolymere synthetisiert, um als vielseitige und einstellbare Basissysteme für polymeranaloge Umsetzungen zu fungieren. Diese Umsetzungen fanden mittels kupfer-katalysierter Azid-Alkin 1,3-Cycloaddition (CuAAC) statt und wurden verwendet, um Ferrocen- und Natriumsulfonat-Einheiten in die Seitenketten der Polymere einzubringen. Die Polymere wurden in verschiedenen Co-Monomer Verhältnissen synthetisiert und sind in der unten stehenden Abbildung dargestellt.

Copolymere mit redox-aktiven und quervernetzbaaren Triphenylamineinheiten wurden über freie radikalische Polymerisationen in drei unterschiedlichen Verhältnissen hergestellt. Desweiteren wurden zwei konjugierte Copolymere, basierend auf Poly(3-hexylthiophen) (P3HT), mittels Grignard-Metathese polymerisiert. Diese beiden unterscheiden sich in der Art der Seitenketten und deren Endgruppen, wie in der Abbildung zu sehen ist. CuAAC verläuft über die kovalente Verknüpfung eines Azids mit einem Alkin, wobei ein Triazol gebildet wird. Dementsprechend bieten die beiden Polymere entgegengesetzte Funktionalitäten im Hinblick auf die CuAAC, was eine große Bandbreite an möglichen Reaktionspartnern für die Funktionalisierung eines P3HT basierten Systems eröffnet.



Die gezeigten Polythiophen-Plattformen wurden für die Einführung neuer Funktionalitäten in früheren Arbeiten verwendet<sup>[1,2]</sup> und auch TPA basierte Homopolymere und

---

Derivate wurden bereits untersucht.<sup>[3]</sup> Für beide Plattformen wurde gezeigt, dass sie im dotierten Zustand hohe elektrische Leitfähigkeiten erreichen können.<sup>[1,2,4]</sup> Da sie außerdem stabiles *redox switching*, Quervernetzbarkeit (im Falle von TPA) und einstellbare Redox Eigenschaften aufweisen,<sup>[3]</sup> sind Redoxpolymere von großem Interesse für elektrokatalytische Einsatzbereiche und Batterieanwendungen.<sup>[5-8]</sup> In dieser Arbeit wurden Copolymere synthetisiert, um Kontrolle über die Anzahl der funktionalen Gruppen im Polymer zu erhalten. Die Einführung von Ferrocen als definierte Modell-Redoxspezies und die Einführung von ionischen Natriumsulfonat-Einheiten wurden untersucht. Auf diese Weise können leitfähige Redoxpolymere und gemischte Leitfähigkeit (ionisch/elektrisch) erreicht werden. Gemischt leitfähige Materialien sind von besonderem Interesse aufgrund ihrer Fähigkeit zur Selbst- und Autodotierung, welche schnelles *redox switching* und hohe erreichbare Leitfähigkeiten ermöglichen<sup>[9-11]</sup>, welche durch sorgfältige Auswahl der Gegenionen noch weiter verbessert werden können.<sup>[12,13]</sup>

Die entsprechenden Polymere wurden durch CuAAC Click-Chemie funktionalisiert, welche auf verschiedene Weisen durchgeführt werden kann. Umsetzungen in dünnen Polymerfilmen und in Polymerlösungen wurden durch Infrarotspektroskopie und Cyclovoltammetrie evaluiert. Hohe Umsätze konnten durch beide Methoden erzielt werden und auch wenn die Möglichkeiten zur Charakterisierung der Umsetzung innerhalb von Filmen limitiert sind, konnte der Erfolg elektrochemisch bestätigt werden, durch die Untersuchung des Zusammenhangs von CV Stromstärkemaxima und Scanrate in ferrocen-funktionalisierten **PVXX-Fc** Copolymeren. Dies geschah mit Polymeren in drei unterschiedlichen Co-Monomer Verhältnissen. Auf die gleiche Weise funktionalisierte Polymerfilme mit Natriumsulfonateinheiten in den Seitenketten wurden zusätzlich durch AC Impedanzspektroskopie charakterisiert, um ionische und elektrische Leitfähigkeit zu entkoppeln und die Feuchtigkeitsabhängigkeit der erhaltenen Werte in kontrollierter Atmosphäre zu überprüfen. Die im Film funktionalisierten Proben zeigten in den Experimenten jedoch keine zuverlässige ionische Leitfähigkeit, ein Resultat, welches damit erklärt wurde, dass besagte Filme vor der Click-Umsetzung elektrochemisch quervernetzt wurden, um stabil genug für die mehrtägige CuAAC Reaktion zu sein. Dies wiederum führte vermutlich dazu, dass Azidgruppen im Inneren der Polymerfilme weniger zugänglich sind.

Filme, welche aus bereits geclickten Polymeren hergestellt wurden, also bei welchen Sulfonatgruppen in Lösung kovalent eingeführt wurden, bevor die schließlich aufgereinigten Polymere im *spin-coating* verwendet wurden, zeigten ionische Leitfähigkeiten von bis zu  $9.5 \text{ mS cm}^{-1}$  bei einer relativen Wasseraufnahme des Polymerfilms von 67 wt-%, wie aus Schwingungsfrequenzmessungen mittels einer Quartzkristall Mikrowaage (QCM) hervor ging. Diese Werte wurden mit einem Anteil ionischer Co-Monomere von 73 % erreicht, was der höchste eingesetzte Anteil war. Die gleiche Vorgehensweise bei Polymer **PV26-A**,

---

welches nur 26 % funktionalisierbare (Azid-)Monomereinheiten enthält, führte zu Löslichkeitsproblemen, sodass keine Filme erzeugt und damit keine Impedanzmessungen mit dieser Monomerzusammensetzung möglich war.

Die beiden thiophenbasierten konjugierten Copolymere wurden in jeweils einer Zusammensetzung untersucht. System **PT71** wurde versucht in Lösung und mit dem oben dargestellten Alkylsulfonat zu clicken, was allerdings nur zu einer partiellen Umsetzung führte. Dies wurde der sterisch anspruchsvollen Situation im Polymer zugesprochen, welche durch die langen Seitenketten und die ebenfalls langen Sulfonateinheiten entsteht. System **PBT24** andererseits wurde, wie abgebildet, mit einem geschützten Azidsulfonat geclickt, welches Löslichkeitsprobleme umging und die Präparation von Filmen ermöglichte. Die polymeranaloge Entschützung der ionischen Gruppen wurde schließlich im Film durchgeführt. Anschließende Impedanz- und QCM-Charakterisierung ergab eine gemischt ionisch/elektrische Leitfähigkeit mit Höchstwerten im undotierten Zustand von  $0.1 \text{ mS cm}^{-1}$  ( $\sigma_{el}$  bei 0 mbar  $p_{H_2O}$ ) und  $1.4 \text{ mS cm}^{-1}$  ( $\sigma_{ion}$  bei 30 mbar  $p_{H_2O}$ ). Die maximal erreichte relative Wasseraufnahme dieses Polymers betrug 44 wt-%.

## Publikationen

Teile dieser Arbeit wurden publiziert in:

J. E. Kuhlmann, S. S. Y. Liu, K. Dirnberger, M. Zharnikov, S. Ludwigs, *Electrochemical Characterization of Redox Probes Confined in 3D Conducting Polymer Networks*, *Chem. Eur. J.* **2021**, *27*, 17255, doi: 10.1002/chem.202103257.

# Danksagung

Diese Arbeit wurde im Zeitraum von Juli 2017 bis Oktober 2021 am Institut für Polymerchemie, am Lehrstuhl für Struktur und Eigenschaften Polymerer Materialien angefertigt. In dieser Zeit hatte eine Reihe von Menschen einen entscheidenden Einfluss auf den Erfolg dieser Dissertation, welche ich hier anerkennen möchte.

Als Erstes möchte ich mich bei *Prof. Dr. Sabine Ludwigs* dafür bedanken, mir die Dissertation in ihrem Arbeitskreis zu ermöglichen. Mit einer Zielsetzung und einer Thematik, die viele verschiedene Teilbereiche der Chemie verknüpfte, wurde die Forschung nie langweilig und die großartige Laborausstattung eröffnete viele Möglichkeiten. Prof. Ludwigs' stete Bereitschaft für fachliche Diskussionen und die Freiheit, auch eigene Ideen zu verfolgen, schätzte ich sehr.

Prof. Dr. Sabine Laschat danke ich vielmals für die freundliche Übernahme des Mitberichts und Prof. Dr. Elias Klemm für die Übernahme des Prüfungsvorsitzes.

Ich danke aktiven und ehemaligen Doktoranden und Studenten des Arbeitskreises für eine immer grandiose Arbeitsatmosphäre, großen Zusammenhalt und lustige, sowie wertvolle fachliche Diskussionen innerhalb und außerhalb des Labors. Dies umfasst in keiner besonderen Reihenfolge *Sherri Liu, Claudia Malacrida, Yannic Gross, Peter Reinold, Lukas Stein, Matthias Wieland, David Geppert, David Neußer, Kirsten Bruchlos, Daniel Bauer, Carsten Dingler, Marc Schnierle* und *Lea Hornberger*.

Hervorheben möchte ich hierbei *Matthias Wieland* für die Unterstützung und fachliche Einweisung in Impedanzspektroskopie und QCM Messungen, sowie *Claudia Malacrida* für ihren kompetenten Rat bei Fragen zur Elektrochemie.

Meinen Forschungspraktikanten *Nils Hübener, Nils von Seggern* und *Boshra Kachmar* bin ich sehr für ihren wertvollen Beitrag zu meiner Dissertation dankbar.

*Dr. Klaus Dirnberger* danke ich von Herzen für sein stets offenes Ohr, seine große Bereitschaft mich an seiner langjährigen Erfahrung teilhaben zu lassen und mir mit seiner wertvollen fachlichen Einschätzung immer helfend zur Seite zu stehen, was speziell in schwierigen Phasen von unschätzbarem Wert war.

*Beatrice Omiecienski* danke ich ebenso herzlich für ihre stete Hilfsbereitschaft und ihren unermüdlichen Einsatz, um bei Problemen jeglicher Art mit Rat und Tat zur Stelle zu sein.

*Corinne Rost-Schmidt* und *Philipp Sliskovic* danke ich für den immer freundlichen Umgang und ihren bereitwilligen Beitrag zu Synthesen in dieser Arbeit.

*Dr. Rotraut Merkle* vom *Max Planck Institut für Festkörperforschung* in Stuttgart danke ich für ihren wertvollen fachlichen Rat bei meinen Fragen zur Impedanzspektroskopie.

Besonderer Dank gebührt außerdem *Prof. Dr. Frank Gießelmann* vom *Institut für Physikalische Chemie* dafür, mir die Nutzung seines PM-IRRAS zu gestatten und *Dr. Stefan Jagiella* für eine Einführung in die Nutzung des Gerätes und die Auswertung der Daten. Diese Charakterisierungsmethode wurde zu einem zentralen Aspekt dieser Dissertation.

Für den immerwährenden Rückhalt und die bedingungslose Unterstützung in allen Phasen danke ich meiner Familie und Mary-Ann Chua.

# Contents

<b>Abkürzungsverzeichnis</b>	<b>xiv</b>
<b>1 Introduction</b>	<b>1</b>
1.1 Conjugated Polymers . . . . .	2
1.2 Polythiophenes . . . . .	5
1.2.1 Synthetic Methods . . . . .	6
1.2.2 Polymer Analogous Functionalisation . . . . .	10
1.3 Redox Systems derived from Triphenylamine . . . . .	12
1.4 Conjugated Polyelectrolytes - combining ionic and electronic conductivity .	16
1.5 Method of Copper-Catalyzed Azide-Alkyne Cycloaddition (CuAAC) . . . .	21
<b>2 Objectives</b>	<b>27</b>
<b>3 TPA-based Polyelectrolytes</b>	<b>31</b>
3.1 Synthesis of Azide-bearing Copolymers . . . . .	31
3.1.1 Monomer Synthesis . . . . .	32
3.1.2 Copolymerization . . . . .	33
3.1.3 Polymer analogous Halide/Azide Exchange . . . . .	36
3.2 Thin Film Characterisation of Ferrocene-Functionalized Copolymers . . . .	44
3.2.1 Electrochemical Crosslinking of Polymer Films . . . . .	45
3.2.2 Introduction of Ferrocene Units in Thin Films <i>via</i> Click Chemistry	52
3.3 Sulfonate-functionalized Copolymers . . . . .	66
3.3.1 Polymer Analogous Conversion of Copolymer Films . . . . .	68
3.3.2 Polymer Analogous Conversion of Dissolved Copolymers (BC) . . .	77
3.4 Summary . . . . .	87
<b>4 Thiophene-based Conjugated Polyelectrolytes</b>	<b>90</b>
4.1 Preparation of Polymers . . . . .	91
4.1.1 Synthesis of 3HT-based monomers . . . . .	91
4.1.2 Synthesis of Butynyl-substituted thiophene monomer (3TBT) . . .	97
4.1.3 Polymer Synthesis . . . . .	99
4.2 Polymer Functionalization with sodium sulfonate moieties . . . . .	107
4.2.1 Synthesis of Protected and Azide-Bearing Sulfonate (-SO <sub>3</sub> -Prot) .	108
4.2.2 Polymer Analogous Reactions of Alkyne-bearing PBT24 . . . . .	112
4.2.3 Polymer Analogous Reactions of Bromine-bearing PT71 . . . . .	118

---

4.3	Characterization . . . . .	121
4.3.1	Impedance Spectroscopy of PBT24-SO <sub>3</sub> . . . . .	122
4.3.2	Water Uptake of PBT24-SO <sub>3</sub> by QCM . . . . .	128
4.4	Summary . . . . .	129
<b>5</b>	<b>Conclusion and Outlook</b>	<b>131</b>
<b>6</b>	<b>Experimental Part</b>	<b>140</b>
6.1	Analytical Methods and Devices . . . . .	140
6.2	Drying of organic solvents . . . . .	149
6.3	Polymer film preparation . . . . .	149
6.4	Click Chemistry . . . . .	150
6.5	Synthesis of Monomers and Reactants . . . . .	151
6.5.1	1-Step synthesis of 3-(6-Bromohexyl)thiophene . . . . .	151
6.5.2	3-Step synthesis of 3-(6-Bromohexyl)thiophene . . . . .	152
6.5.3	2,5-Dibromo-3-(6-bromohexyl)thiophene . . . . .	153
6.5.4	3-Chloromethylthiophene . . . . .	154
6.5.5	Triisopropyl-(4-thiophenyl-1-butynyl) silane . . . . .	155
6.5.6	4-(2,5-dibromothiophenyl)-1-butynyl triisopropylsilane . . . . .	155
6.5.7	3-(Prop-2-ynyloxy)propane-1-sulfonate . . . . .	156
6.5.8	Phenyl 4-(bromomethyl)benzene sulfonate . . . . .	157
6.5.9	Phenyl 4-(azidomethyl)benzene sulfonate . . . . .	157
6.5.10	N,N-Diphenyl-2-vinylaniline (VTPA) . . . . .	158
6.6	Model Reactions . . . . .	159
6.6.1	4-(Azidomethyl)styrene . . . . .	159
6.6.2	CuAAC Model Reaction . . . . .	159
6.6.3	Sulfonate Deprotection . . . . .	160
6.7	Polythiophenes . . . . .	160
6.7.1	Poly[3-hexylthiophene- <i>co</i> -3-(6-bromohexyl)thiophene] (PT71) . . . . .	161
6.7.2	Poly[3-hexylthiophene- <i>co</i> -3-(6-azidoethyl)thiophene] (PT71-A) . . . . .	162
6.7.3	Poly[3-hexylthiophene- <i>co</i> -3-(4-triisopropylsilylbutyne)thiophene] (PBT24) . . . . .	163
6.7.4	Poly[3-hexylthiophene- <i>co</i> -3-(2-(3-(phenyl-benzyl-4-sulfonate)triazole)-ethyl)thiophene] (PBT24-SO <sub>3</sub> -Prot) . . . . .	164
6.7.5	Poly[3-hexylthiophene- <i>co</i> -3-(2-(3-(sodium-benzyl-4-sulfonate)triazole)-ethyl)thiophene] (Deprotection, PBT24-SO <sub>3</sub> Na) . . . . .	165
6.8	Redox Polymers . . . . .	166
6.8.1	Poly[vinyl(triphenylamine)- <i>co</i> -(chloromethyl)styrene] . . . . .	166
6.8.2	Poly[vinyl(triphenylamine)- <i>co</i> -(azidomethyl)styrene] . . . . .	168

---

6.8.3 Solution Clicking of Poly[vinyl(triphenylamine)-*co*-(azidomethyl)styrene] 169

**Bibliography** **171**

# Abkürzungsverzeichnis

<b>3HT</b> .....	3-Hexylthiophene
<b>3TBT</b> .....	(4-(thiophen-3-yl)-but-1-ynyl)-triisopropylsilane
<b>AFM</b> .....	Atomic Force Microscopy
<b>AIBN</b> .....	Azobisisobutyronitrile
<b>AMS</b> .....	4-(Azidomethyl)styrene
<b>ATR</b> .....	Attenuated Total Reflectance
<b>BC</b> .....	chemical CuAAC-reaction of dissolved bulk materials (no thin films)
<b>BHJ</b> .....	Bulk Heterojunction
<b>CA</b> .....	Water Contact Angle
<b>CC</b> .....	chemical CuAAC-reaction in thin films
<b>CMS</b> .....	4-(Chloromethyl)styrene
<b>CP</b> .....	Conjugated Polymer
<b>CPE</b> .....	Conjugated Polyelectrolyte
<b>CuAAC</b> ...	copper(I)-catalyzed alkyne-azide cycloaddition click chemistry
<b>CV</b> .....	Cyclic Voltammetry
<b>DCM</b> .....	Dichloromethane
<b>DFT</b> .....	Density Functional Theory
<b>DMF</b> .....	Dimethylformamide
<b>DMF</b> .....	Dimethylformamide
<b>DSC</b> .....	Differential Scanning Calorimetry
<b>DTGS</b> ....	Deuterated Triglycine Sulfate
<b>E-Fc</b> .....	Ethynyl Ferrocene
<b>EC</b> .....	electrochemical CuAAC-reaction in thin films
<b>ECD</b> .....	Electrochromic Display
<b>F4TCNQ</b> .	7,7,8,8-tetracyano-2,3,5,6-tetrafluoroquinodimethane

<b>FRP</b> . . . . .	Free-Radical Polymerization
<b>GRIM</b> . . . .	Grignard Metathesis Polymerization
<b>HOMO</b> . . .	Highest Occupied Molecular Orbital
<b>IRRAS</b> . . .	Infrared Reflection Absorption Spectroscopy
<b>KCTP</b> . . . .	Kumada Catalyst Transfer Polymerization
<b>LUMO</b> . . . .	Lowest Unoccupied Molecular Orbital
<b>MCT</b> . . . . .	Mercury Cadmium Telluride
<b>MS</b> . . . . .	Mass Spectrometry
<b>NBS</b> . . . . .	N-Bromosuccinimide
<b>NMR</b> . . . . .	Nuclear Magnetic Resonance
<b>OECT</b> . . . .	organic electrochemical transistor
<b>OPV</b> . . . . .	Organic Photovoltaic
<b>P3HT</b> . . . . .	Poly(3-hexyl)thiophene
<b>PCE</b> . . . . .	Power Conversion Efficiency
<b>PEDOT:PSS</b>	polymer blend of poly-(3,4-ethylenedioxythiophene) and poly(styrenesulfonate)
<b>PPV</b> . . . . .	Polymer Photovoltaic
<b>QCM</b> . . . . .	Quartz Crystal Microbalance
<b>RH</b> . . . . .	relative Humidity
<b>SEC</b> . . . . .	Size-Exclusion-Chromatography
<b>SPS</b> . . . . .	solvent purification system
<b>TBAF</b> . . . .	Tetra- <i>n</i> -butylammonium fluoride
<b>TGA</b> . . . . .	Thermogravimetric Analysis
<b>THF</b> . . . . .	Tetrahydrofuran
<b>TIPS</b> . . . . .	Triisopropylsilane
<b>TPA</b> . . . . .	Triphenylamine
<b>TPB</b> . . . . .	Tetra-N-phenylbenzidine
<b>VTPA</b> . . . .	4-Vinyl-triphenylamine



# 1 Introduction

Organic and polymer electronics have been on the rise in recent years. Although silicon based processes have been optimized and advanced for decades, the development of organic electronics offers meaningful advantages over this conventional technology, namely their cheap production, light-weight materials, easy processability into printed electronics and the ability to produce flexible circuits. Furthermore, biocompatible electronic devices open up a whole new range of applications for in-vivo systems.<sup>[14–16]</sup> Tunable properties allow for tailoring of materials for specific purposes and smart compounds have been developed for applications in sensors or redox switchable films like electrochromic windows or polymer actuators.<sup>[17–20]</sup>

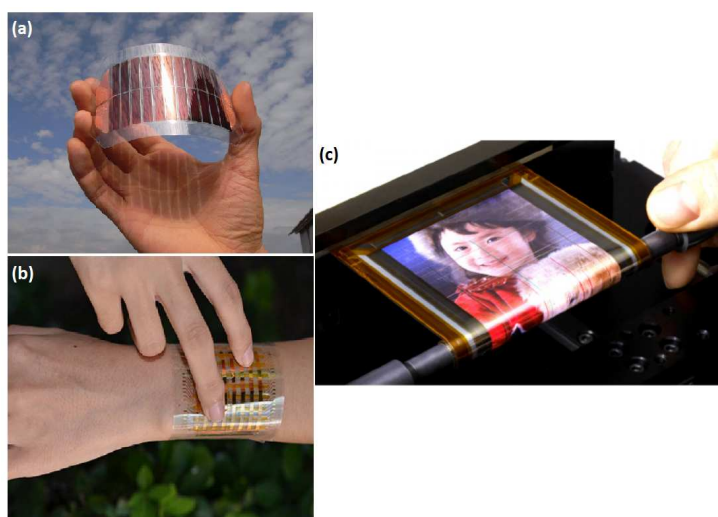
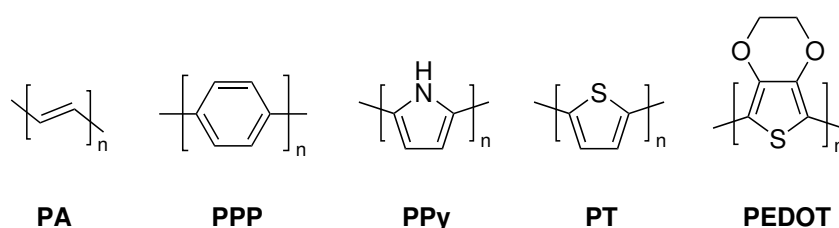


**Figure 1.1:** Examples of flexible organic electronic devices. (a) Organic solar cell.<sup>[21]</sup> © Fraunhofer ISE (b) Organic pressure sensor. Image taken from reference.<sup>[22]</sup> © 2015 Springer Nature (c) Rolled-up organic light emitting diode display. Reproduced with permission from reference.<sup>[23]</sup> © Copyright 2011 Society for Information Display

Oftentimes these properties are accomplished by employment of conducting polymers, providing either electronic conduction, ionic one, or both. An introduction into these classes of polymers and fundamental principles of their working shall be given in the following chapters.

## 1.1 Conjugated Polymers

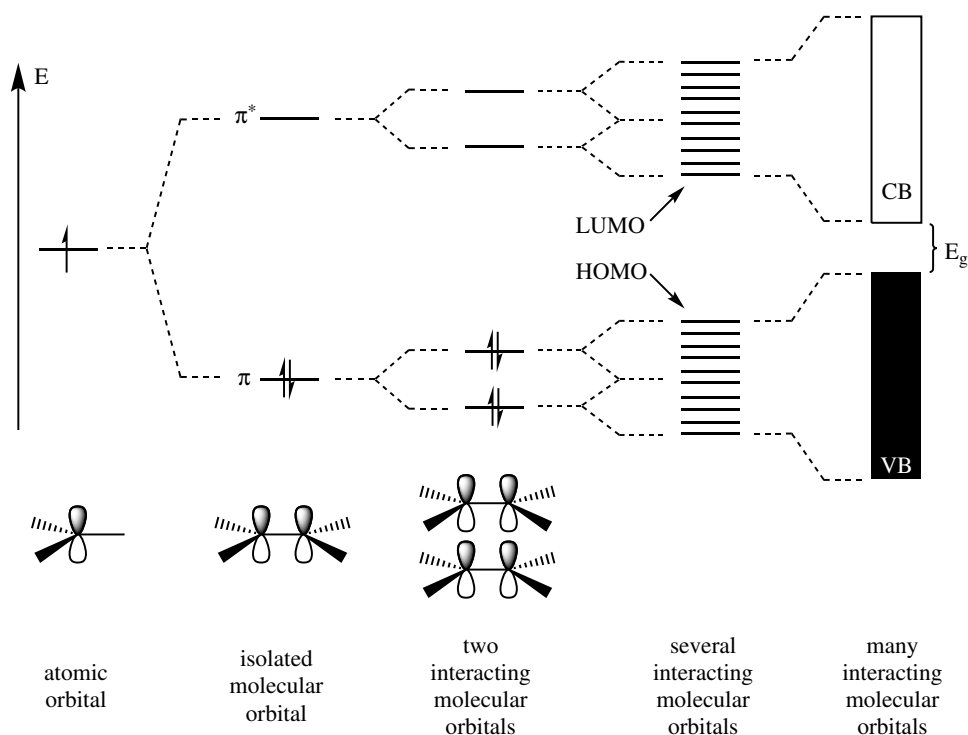
First conjugated polymers (CP) were reported by *Heeger*, *MacDiarmid* and *Shirakawa* in 1977 in the form of polyacetylene.<sup>[24-26]</sup> Even though the reported conductivities were extremely low, a new class of compound was born and advances in polymer design and doping procedures have been made in the decades to come. Focus quickly switched to aromatic based polymers like polythiophenes, polyphenylenes or polypyrroles, among others, which are highly relevant to this day due to versatile chemical modifications and relative stability in ambient conditions.<sup>[27-30]</sup> Since these aromatic polymers show poor solubility in their pristine form, alkyl side chains are often incorporated into their backbone to induce solubility in many common solvents.



**Scheme 1.1:** Basic chemical structures of common conjugated polymers. **PA** polyacetylene, **PPP** poly(*p*-phenylene), **PPy** polypyrrole, **PT** polythiophene, **PEDOT** poly-(3,4-ethylenedioxythiophene).

Scheme 1.1 gives the basic structures of a selection of these polymers. What all of these have in common is their fully conjugated backbone which is responsible for their ability to conduct charges. The principles of this will be explained with the help of Scheme 1.2 where the energy level situation is depicted for different numbers of interacting conjugated carbon atoms. In a conjugated system, a single carbon atom is  $sp^2$ -hybridized and offers three  $sp^2$  orbitals and one  $p_z$  orbital. In Scheme 1.2,  $p_z$  orbitals are pictured. Double bonds are then formed by interaction of two  $sp^2$  and two  $p_z$  orbitals to form molecular orbitals - a binding molecular orbital  $\pi$  and an anti-binding molecular orbital  $\pi^*$  as shown according to the theory of Linear Combination of Atomic Orbitals (LCAO).<sup>[31]</sup> Adding more conjugated carbons to the molecule adds more  $p_z$  orbitals that can be interacted with. Each new interaction between carbon atoms adds a new set of  $\pi$  and  $\pi^*$  molecular orbitals. With increasing chain length, more and more energy levels are created with ever smaller energy differences between them until a differentiation between different energy levels becomes unfeasible. This is the case in long conjugated polymer chains. Instead of binding  $\pi$  and anti-binding  $\pi^*$  orbitals there then exist bands of energy levels within which electrons can move freely, the valence band (VB), occupied by electrons and the conduction band (CB), consisting of unoccupied orbitals. A perfect conjugation with

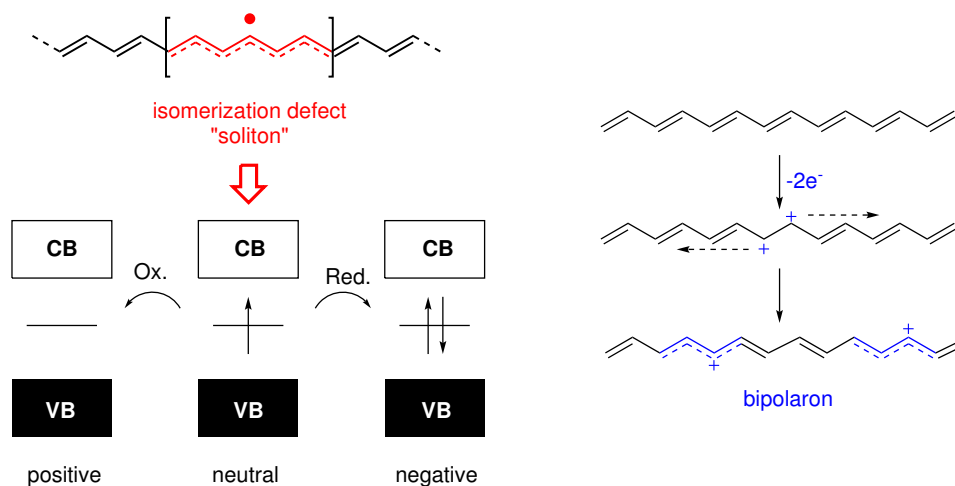
equidistant carbon atoms would result in the two bands building an energy continuum, providing the polymer with metal-like conductivity. However, due to an effect described by Rudolf Peierls in 1955 and termed as *peierls distortion*, fully equal bond lengths don't exist here and some degree of bond length alternation between the carbon atoms still remains, leading to an energy gap between the two bands called bandgap  $E_g$ .<sup>[30]</sup> This energy gap causes conjugated polymers to behave like semi-conductors and amounts to e.g. 1.5 eV in polyacetylene. For conduction to be achieved, electrons have to be excited across this energy gap.<sup>[25,32]</sup>



**Scheme 1.2:** Build-up of energy bands in conjugated carbon chains of increasing length. CB: conduction band. VB: valence band.  $E_g$ : energy bandgap. HOMO: highest occupied molecular orbital. LUMO: lowest unoccupied molecular orbital. Depiction reproduced and modified from reference.<sup>[33]</sup> © 2003 WILEY-VCH Verlag GmbH & Co. KGaA, Weinheim

This can be facilitated by doping. It has to be noted here that *doping* in organic and polymer electronics differs from inorganic doping in so far that no atoms are replaced in a crystal lattice to produce freely moving electrons or vacancies ('holes'). Instead, the existing polymer structure is oxidized (p-type) or reduced (n-type) electrochemically or *via* strong oxidizing (reducing) agents.<sup>[30]</sup> This shall be illustrated with two examples. In the case of polyacetylene (depicted in Scheme 1.3) isomerization defects can introduce

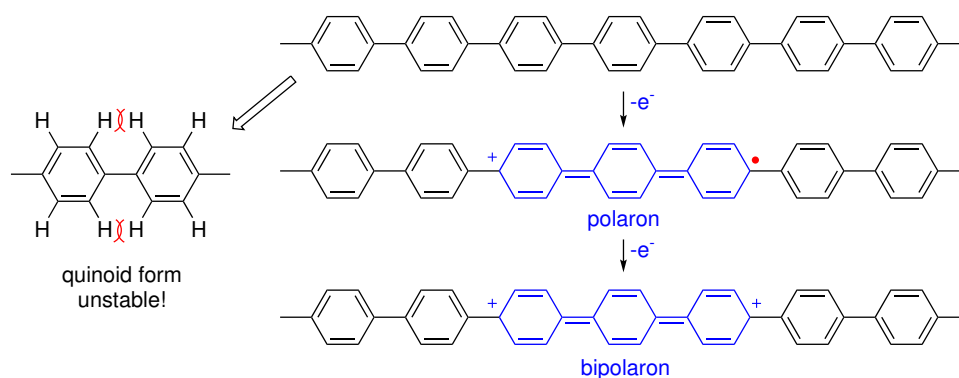
local radicals delocalized over a couple of carbon atoms. This causes PA to show higher undoped conductivity compared to poly(*p*-phenylene) (PPP). Oxidation of the polymer stabilizes the conducting stage and introduces positive charges that can move relatively freely along the polymer chains, due to PA's degenerated mesomeric structures, drastically increasing its conductivity.<sup>[26,34]</sup> The same can be accomplished by reduction, yielding negative charges.



**Scheme 1.3:** Spontaneous creation of radicals (solitons) in polyacetylene. Oxidation or reduction ("doping") stabilizes this conducting species. Strong oxidation can lead to formation of bipolarons (dications).<sup>[33]</sup>

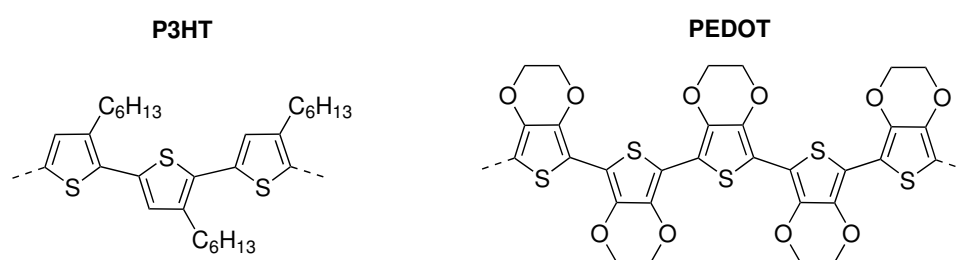
Moving on to aromatic systems, in the example of poly(*p*-phenylene) (Scheme 1.4) the quinoid form, which would afford solitons in the polymer chain analogous to PA, is unstable, due to steric interactions between aromatic protons on the polymer backbone and the energetic favourability of the aromatic form over the quinoid one. However, charged species can be introduced by doping as well. The resulting radical cations (polarons) are usually delocalized over 3-5 repeating units. Interestingly, strong doping does not result in charges repelling each other and moving to opposite directions in the polymer chain. Instead, dications (bipolarons) form because they are energetically favoured, due to a lower number of energetically unfavourable quinoid structures to be built.

Energetically, doping results in the creation of new energy levels between valence band and conduction band as is visualized in Scheme 1.3, reducing the energy gap required to be crossed by electrons. As such, CPs can be tuned from insulators to metal-like behaviour by control of bandgap size and degree of doping, opening up new interesting areas for application.



**Scheme 1.4:** Introduction of charged polaron species by *p*-type doping (oxidation) in poly(*p*-phenylene). Spontaneous formation of (neutral) solitons like in polyacetylene doesn't occur in PPP because of steric hindrance and aromatic stability.

## 1.2 Polythiophenes



**Scheme 1.5:** Molecular structures of poly(3-hexylthiophene) (P3HT) and poly(3,4-ethylenedioxythiophene) (PEDOT).

One of the most thoroughly investigated conjugated polymers that found its way into numerous applications is the class of polythiophene derivatives. Among the most famous examples is poly(3-hexylthiophene) (P3HT), where the hexyl side chain provides the otherwise insoluble polymer with solubility in common solvents like chloroform or THF. P3HT and other alkyl derivatives (P3AT) find use in many areas of organic electronics like organic photovoltaic (OPV), organic field-effect transistors (OFETs), organic light-emitting diodes (OLEDs) and more.<sup>[35–37]</sup> Poly(3,4-ethylenedioxythiophene) (PEDOT) may be the most well-known polythiophene derivative and is right up there with P3HT, reaching remarkable electronic conductivities of up to  $4380 \text{ S cm}^{-1}$  when post-treated with  $\text{H}_2\text{SO}_4$ .<sup>[38]</sup> This is ultimately made possible by its high lying HOMO, a result (mostly) of non-covalent intramolecular S–O interactions in its repeating units, giving way to a highly planar trans-configuration in the polymer. Combined with the electron-donating effects

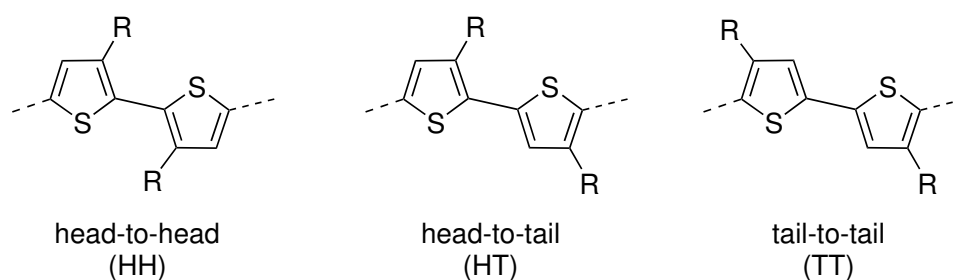
of the oxygen atoms, aromaticity in the conjugated system is stabilized and the electron density of the overall system increased, causing the HOMO to be at higher energy levels. This in turn provides PEDOT with a notable stability against oxidation in environmental conditions, making it possible to be stabilized in its (p-type) doped state by corresponding counterions, most noteworthy by poly(styrene sulfonate) (PSS).<sup>[39]</sup>

Both, P3HT (or P3ATs) and PEDOT:PSS polymer blends are intriguing materials, due to countless possibilities for straight-forward molecular modifications, easy processability, great thermal and chemical stability and highly promising electronic properties that can be altered for the desired application with the aforementioned derivatization, justifying the huge scientific interest put in them over the last decades.

Given their central aspect in this thesis, focus in the following chapter shall be put on P3HT derivatives. Polymerization methods and polymer analogous functionalisation of these polythiophenes will be discussed.

### 1.2.1 Synthetic Methods

Early procedures for the polymerisation of 3-alkyl thiophenes consisted of random oxidative coupling, either chemically induced by oxidating agents (e.g.  $\text{FeCl}_3$ ) or electrochemically by application of suited electronic potentials.<sup>[27,40,41]</sup> However, due to the asymmetric structure of alkylated thiophene monomers, the resulting polymers differed in the respective orientation of monomer units in the polymer chain with regards to their neighbouring molecules. This orientation can be described in three ways which are depicted in Scheme 1.6.



**Scheme 1.6:** Possible respective orientations of thiophene units in P3AT polymer chains.

Generally, chain building occurs by coupling between the 2- and 5-positions of the thiophene rings. Since the 2-position is closer to the 3-substituent it is referred to as the *head* position while 5 is considered the *tail* of the molecule. If *head-to-head* (HH) coupling occurs during polymerisation, steric complications occur between side-chains, causing the thiophene units to twist out of plane and as such weakening or breaking

the  $\pi$ -conjugation. This results in a relative increase in the bandgap and thus a lower conductivity performance. In the opposite case, the *tail-to-tail* (TT) coupling this steric problematic might not exist in the respective thiophene pair, however, subsequent TT coupling is impossible and often followed by, again, HH coupling. Both those cases afford what is referred to as *regioirregular* P3AT, because neither HH, nor TT can exist alone, conceptionally. Ultimately, only *head-to-tail* (HT) polymerisations afford polymer chains where no steric hindrance inhibits the planarity and as such the  $\pi$ -conjugation of the polymer. HT coupled P3AT is referred to as *regioregular* polythiophene and is able to adopt a coplanar conformation, increasing average conjugation length in the polymer and allowing for a smaller bandgap and better electronic performance.

McCullough *et al.* were the first to report on synthesis of regioregular P3AT in 1992, reaching average conductivities of  $600 \text{ S cm}^{-1}$ .<sup>[42]</sup> This was achieved by preliminary creation of mono-brominated 3-alkyl thiophene (**3AT-Br**) with  $\text{Br}_2$ , followed by regioselective lithiation with lithium diisopropyl amide (LDA). Transmetalation into the respective organomagnesium intermediate and *in-situ* conversion with catalytic  $\text{Ni}(\text{dppp})\text{Cl}_2$  gave defined HT coupled P3ATs with regioregularities of about 90%.<sup>[43]</sup> Around the same time Rieke *et al.* succeeded with 90% to 98% regioselective oxidative addition of *Rieke Zinc* into 2,5-dibromo-3-alkylthiophene (**3AT-Br<sub>2</sub>**), depending on reaction temperature. Subsequent polymerization with  $\text{Ni}(\text{dppe})\text{Cl}_2$  catalyst gave highly regioregular P3AT.<sup>[44]</sup>

The drawback of both methods was their requirement for sub-zero temperatures for the production of the active monomer species (McCullough  $-40^\circ\text{C}$  to  $-60^\circ\text{C}$ , Rieke  $-78^\circ\text{C}$ ). McCullough's procedure additionally requires thorough purification of the starting materials and long reaction times. Rieke's monomer is easier to prepare, however production of *Rieke Zinc* isn't trivial and reaction times are long as well.

Other cross-coupling methods found wide-spread use at the time as well, most notably *Suzuki* and *Stille* cross coupling reactions, where Suzuki type polymerisations are more suitable for benzene-based monomers and Stille type reactions are better suited for thiophene-based monomers, due to stannyl substitution of benzene derivatives, which is necessary in Stille couplings, giving poor reactivity with aryl halides.<sup>[36]</sup> However, toxicity of stannyl organyl compounds is an additional drawback of Stille type couplings, compared to the methods of McCullough and Rieke.

In 1999 McCullough reported on an improved and facilitated synthetic approach (see Figure 1.2).<sup>[45]</sup> This new route, termed *Grignard Metathesis* (GRIM) reaction, started from di-brominated **3HT-Br<sub>2</sub>**, like in Rieke's method. The monomer is converted by a *Grignard* transfer reaction with aliphatic organomagnesium halides into the active monomer species at room temperatures in 1 h. The group reported a regioselectivity of this transfer of about

85:15 with preferential conversion in the 5-position. Even though the selectivity of this first step was lower than that of Rieke's method, interestingly it turned out to be independent of the employed Grignard compound, with *t*-BuMgCl and *i*PrMgCl as popular choices. This can likely be explained by steric reasons from unfavourable interactions between the Grignard reagent and the side-chains of the thiophene monomer in the 2-position, favouring the less hindered 5-position. Remarkably, polymerization of this isomeric mixture with catalytic Ni(dppp)Cl<sub>2</sub> afforded highly regioregular P3AT with HT-HT couplings of over 95% and typically 98%.<sup>[46]</sup> From kinetic and competition experiments they concluded that the 5-position shows faster reaction rates in polymerization with Ni(dppp)Cl<sub>2</sub> as a bulky catalyst, making it the kinetically preferred active species. Furthermore, despite 15% 2-functionalized monomer with sterically hindered Grignard groups, HT-HT coupling is kinetically and thermodynamically preferred for both monomer species and all main reaction pathways favour HT-HT coupling, ultimately leading to the reported 95–98% HT. Additionally, P3ATs with less than 95% HT could be expected to be less crystalline than polymers with less defects, making it potentially possible to be removed during *Soxhlet* extraction.

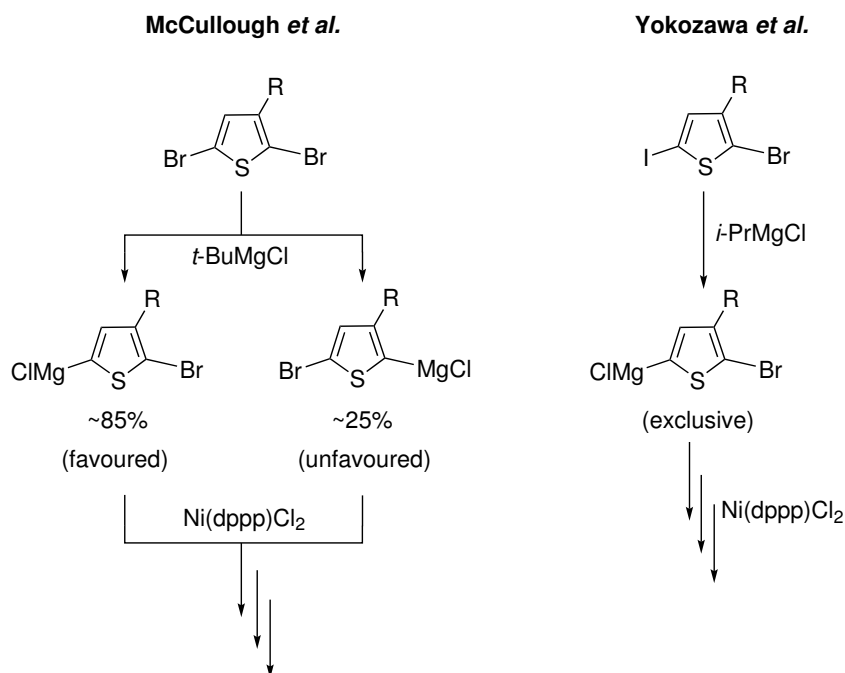


**Figure 1.2:** Synthetic approaches to highly regioregular polythiophenes from the research groups of McCullough and Yokozawa.

Further examination of reaction conditions has been performed by Thelakkat *et al.* and Yokozawa *et al.* over the years.<sup>[47,48]</sup> The latter group also offered an alternative approach to the GRIM polymerization with an asymmetrically substituted 2-bromo-5-

chloromagnesio-3-hexylthiophene leading to the exclusive formation of the desired species, however, the kinetic and thermodynamic preference for HT couplings with McCullough's simpler approach often makes it the method of choice, still.<sup>[49]</sup>

The mechanism of GRIM polymerisations, often also referred to as *Kumada Catalyst Transfer Polymerization* (KCTP) has been demonstrated to proceed *via* living chain growth instead of a step-growth pathway that would have been expected at the time. This allows GRIM polymerisations to afford narrow molecular weight distributions with dispersities  $D$  of typically 1.2 to 1.3.<sup>[36,49,50]</sup> Yokozawa and McCullough investigated and reported on the mechanism independently and the generally accepted pathway is depicted in Figure 1.3.<sup>[36,47,51,52]</sup>

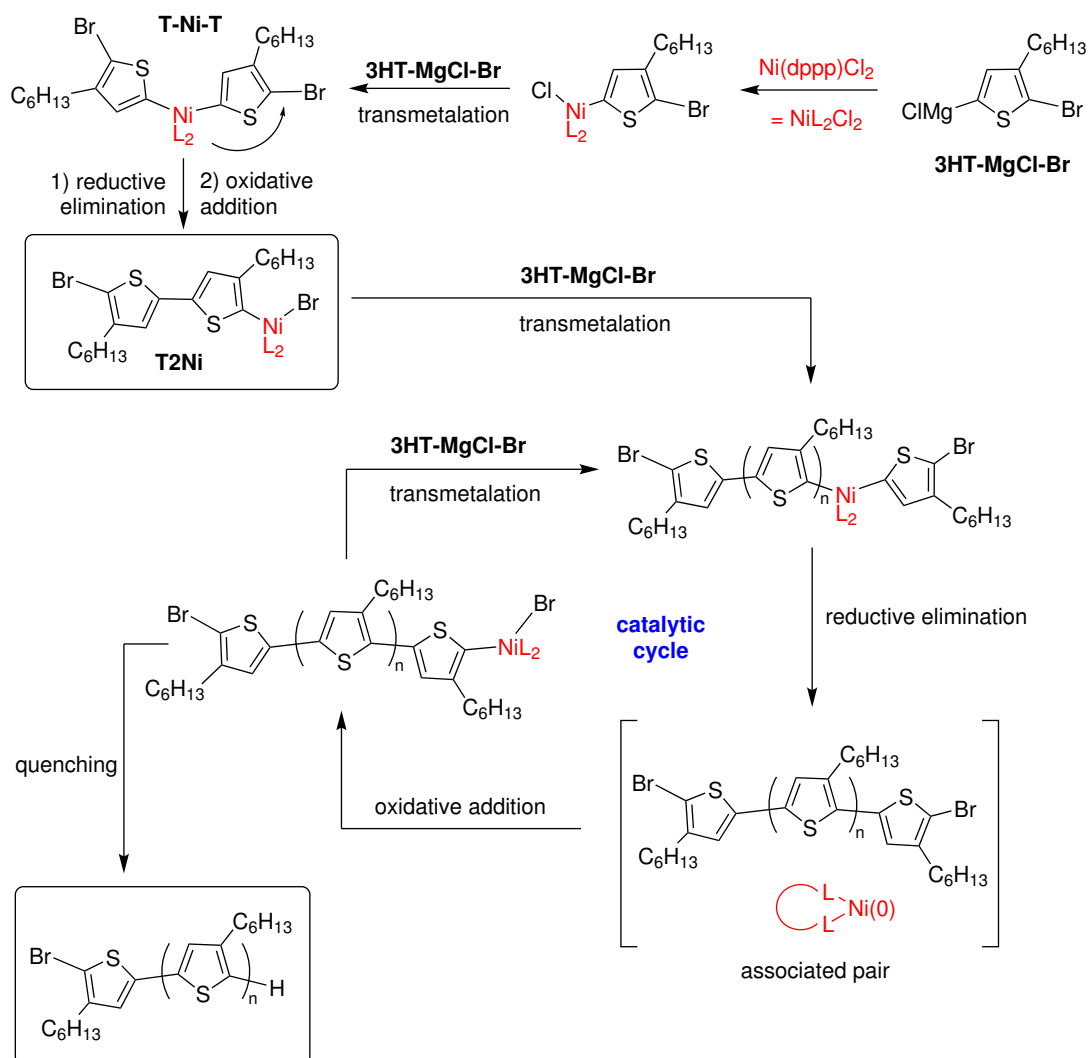


**Figure 1.3:** Proposed mechanism of GRIM chain-growth polymerisations, starting from the favoured monomer isomer.

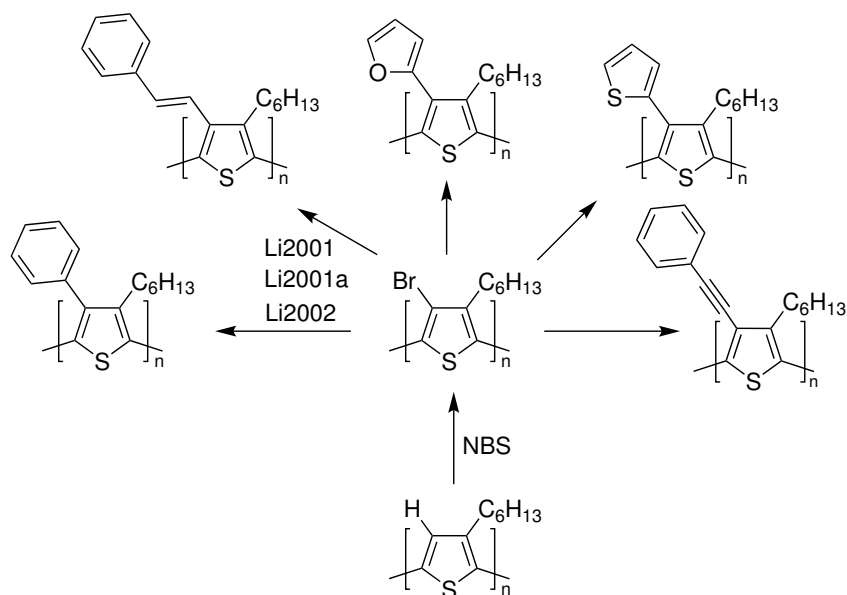
Prior to the catalytic cycle, initiating species **T2Ni** is formed. This happens by consecutive transmetalations of two Grignard monomer molecules **3HT-MgCl-Br** with the Nickel catalyst, affording the Ni-dimer **T-Ni-T**. Following that is a step that can either be viewed as an intramolecular catalyst transfer, or succession of reductive elimination and oxidative reinsertion of the catalyst into one of the C–Br bonds of the dimer. The initiating species obtained this way is TT-coupled as a result of the lower steric hindrance in the 5-position, so independent of which side the catalyst is inserted into afterwards, polymerisation starts from a *head* (2-) position. The catalytic cycle now starts with transmetalation of another **3HT-MgCl-Br** monomer, followed by reductive elimination of a Ni(0) catalytic species. The state between reductive elimination and subsequent oxidative addition into the terminal C–Br bond can be described as an associated pair in which the catalyst "moves" to the end of the polymer chain, which gives GRIM (KCTP) polymerizations a *quasi*-living chain growth character.<sup>[50]</sup> After oxidative addition, the first HT-coupling is accomplished. Further cycles of transmetalation of new monomer molecules, reductive elimination and oxidative addition advance the polymer chains until the reaction is stopped by quenching or end-group functionalization.

Because GRIM polymerizations afford highly regioregular polythiophenes, and polymers with narrow molecular weight distributions of controlled length can be achieved due to its living character, the method has been established as a reliable synthetic approach not only for thiophene-based polymers but for other CPs as well. Polymer brushes, conjugated block copolymers, side-chain functionalized derivatives and more have been synthesized this way.<sup>[47,53,54]</sup>

### 1.2.2 Polymer Analogous Functionalisation

Tailor-made conjugated polymers can be accomplished either by modification of monomer structures before polymerisation or afterwards by polymer analogous conversion. For example, by selection of appropriate di-functional monomers, interchain crosslinked polymers can be polymerised directly, giving them improved ageing and solvent stability and potentially improving charge transport properties. However, effects vary with degree of crosslinking and can even show opposite results.<sup>[36,55]</sup> On the other hand, post-polymerisation influences on the electronic structure are made possible by side-groups impacting the electronic properties of the backbone by either influencing electron-density and -distribution directly or indirectly by affecting chain twisting,  $\pi$ -stacking or other morphological properties. Also, new functions and behaviour can be introduced this way, like water solubility, light emittance, stable redox switching or the ability for interchain

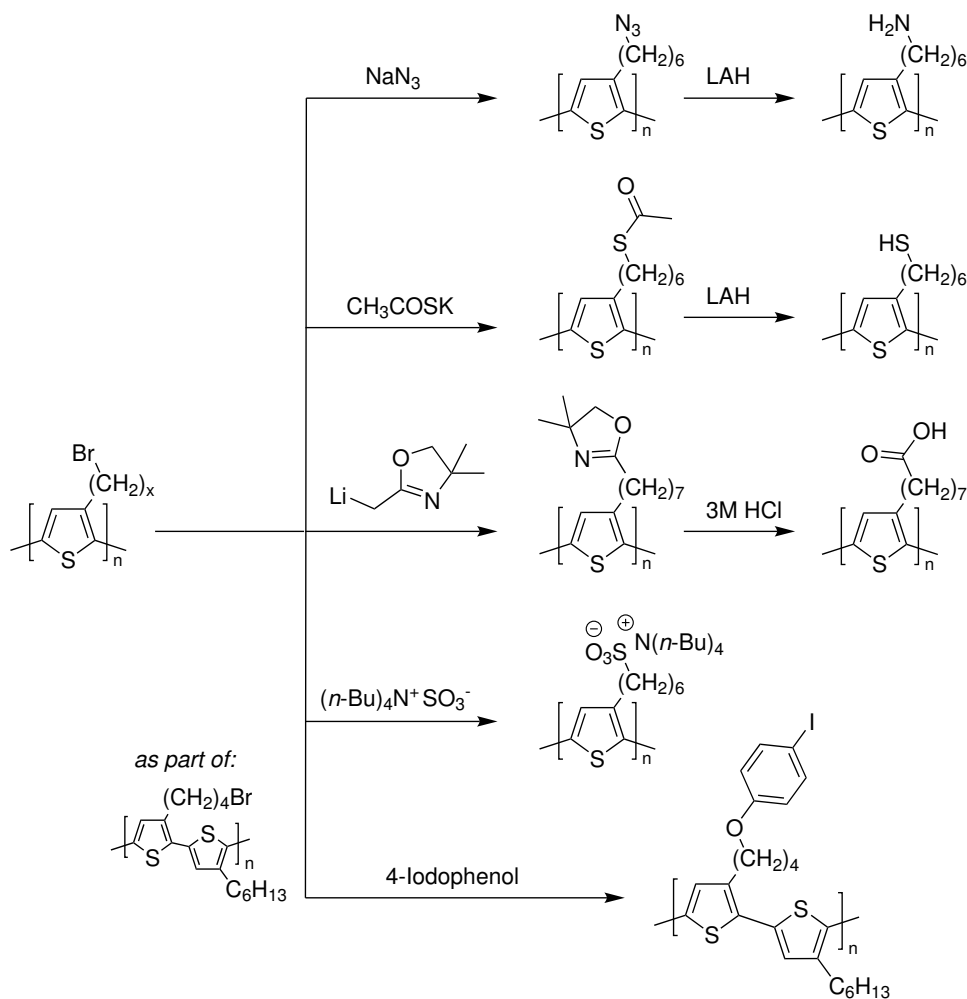
crosslinking of polymer chains.<sup>[2,56–58]</sup>



**Scheme 1.7:** Examples for polymer analogous conversions of polythiophenes by initial electrophilic substitution and subsequent Suzuki, Stille or Heck style cross coupling with corresponding reagents.<sup>[59–61]</sup>

In polythiophenes, in most cases the 3-position will be occupied by a solubility-inducing side-chain already, leaving two possible pathways for functionalisation – a second side-group at the 4-position or modification of the existing side-chain in position 3. The 4-position can be converted by electrophilic substitution into halide or nitro derivatives, opening up a large range of subsequent functionalisation possibilities. Scheme 1.7 gives a number of examples starting from the initial replacement of hydrogen by bromine *via* NBS treatment. All conversions can then be performed by classic cross-coupling reactions, namely Suzuki, Stille or Heck style couplings. Most of these proceed in a quantitative manner as well.<sup>[59–61]</sup>

Another approach is to include monomers with functionalizable side-chains in the polymerisation and subsequently modify these groups polymer-analogously. Commonly, bromine is chosen as part of an alkyl side-chain which can then be replaced in numerous ways. In Scheme 1.8 a number of examples is given for this approach, showcasing the versatility of this route, as even multi-step polymer analogous conversions are, of course, possible.<sup>[62–64]</sup> In one example it could be shown this way that side-chain functionalized polymers can result in notably higher power conversion efficiencies (PCE) when incorporated into bulk heterojunction (BHJ) solar cells.<sup>[64]</sup>

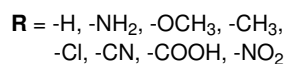
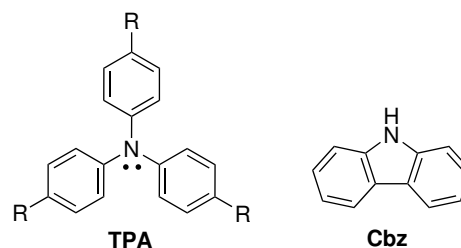


**Scheme 1.8:** Examples for polymer analogous reactions of functionalizable polymer side-chains in P3ATs.<sup>[62–64]</sup>

### 1.3 Redox Systems derived from Triphenylamine

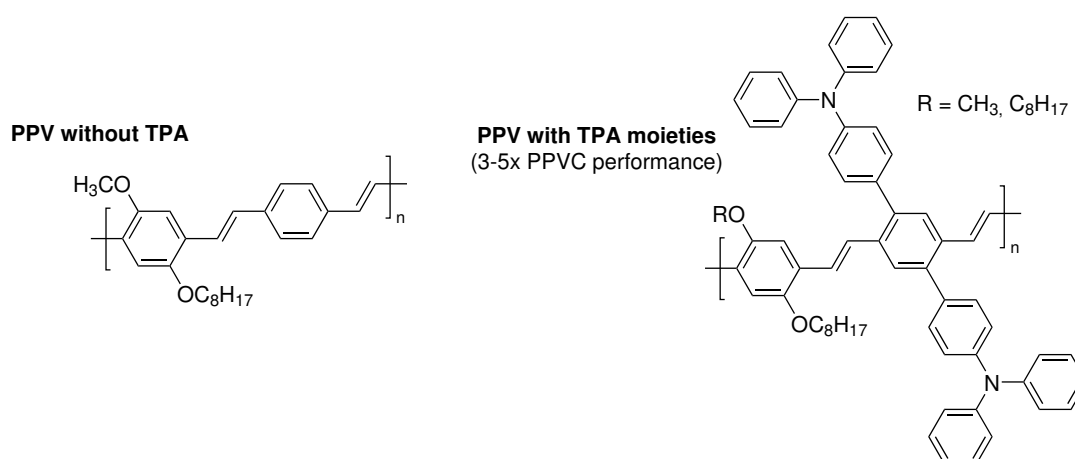
Triphenylamine (TPA) is a tertiary aromatic amine building block which has invoked interest for similar applications as conjugated polymers, namely in OLEDs, ECDs and photovoltaic cells (dye sensitized and perovskite type) due to its hole transport capabilities.<sup>[65–70]</sup> The lone electron pair at the nitrogen makes it an electron-rich compound with the electron pair delocalized over all three benzene rings, making it an interesting option for energy storage applications.<sup>[3,71–74]</sup> It can be synthesized by copper catalyzed nucleophilic substitution of aryl halides, while derivatives are accessible by palladium catalyzed cross coupling of aryl halides with amines or iron catalyzed aromatic amination.<sup>[75–77]</sup>

TPA and derivatives have been incorporated into polymers to introduce redox activity and cross linking capabilities. Redox properties can be fine-tuned by incorporation of



**Scheme 1.9:** Examples of triphenylamine (TPA) derivatives. Cbz: carbazole.

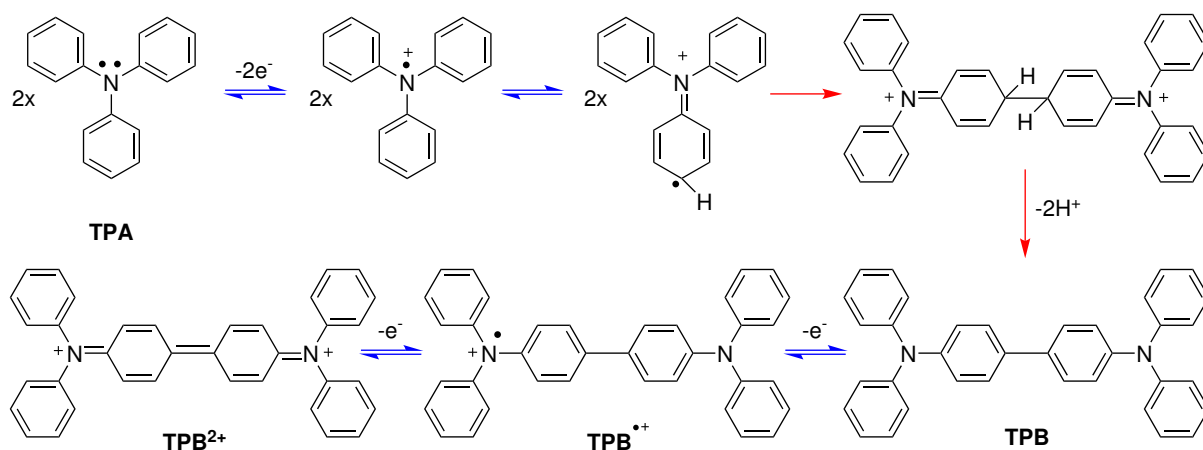
suitable substituents (usually in *para* position) which can either increase its HOMO energy level (electron-donating groups) or reduce its LUMO (electron-withdrawing groups).<sup>[3]</sup> For example, poly(*para*-phenylenevinylene) (PPV) derivatives carrying TPA moieties can be synthesized by Wittig-Horner reactions, providing 3D  $\pi$ - $\pi$  stacking in the polymer and resulting in extended conjugation lengths and improved hole transporting properties.<sup>[78]</sup> This has been shown to improve bulk heterojunction, polymer photovoltaic cells' (PPVC) power conversion efficiency 3-5 fold compared to the non-TPA polymer. Both were separately synthesized and incorporated into photovoltaic cells for characterization. The corresponding structures are shown in Scheme 1.10.



**Scheme 1.10:** Structures of poly(*para*-phenylenevinylene) (PPV) derivatives. The TPA containing derivative shows notably better power conversion efficiency in bulk heterojunction polymer photovoltaic cells.<sup>[78]</sup>

Synthesis of side-chain functionalized polymers is possible, e.g. by controlled radical (co)polymerisation of the corresponding monomers<sup>[79]</sup> or by *Click* chemistry of applicable pre-functionalized polymers.<sup>[2]</sup> Here, although non-conducting in its pristine form, TPA

groups can provide electronic conduction when doped either chemically or electrochemically. Since in the form of isolated side-chain groups there is no conjugation through the polymer, conduction occurs *via* a hopping mechanism between redox pairs. Different redox species can be induced in TPA derivatives and inspection of corresponding conductivities at different doping levels revealed that highest conductivity can be expected when a mixture of different redox states is present.<sup>[4,80]</sup> These different redox species are another feature of TPA functionalisation, as shall be explained with help of Scheme 1.11.



**Scheme 1.11:** Cross-linking mechanism of two TPA units upon oxidation.

Herein it is depicted what happens upon chemical or electrochemical oxidation of TPA units. Removal of one electron from the electron-rich group results in a radical cation which can be reversibly reduced again. However, because the radical cation is unstable due to high spin-density at the *para* position, two such groups quickly recombine to a dimeric dication species which rearomatizes by loss of two protons to the neutral dimeric tetra-N-phenylbenzidine (**TPB**). This step is irreversible and can serve to cross-link between polymer chains as is depicted in Figure 1.4. Once **TPB** is formed it can be reversibly oxidized to the radical cation **TPB**<sup>•+</sup> and the dication **TPB**<sup>2+</sup>. Both processes can be observed in cyclic voltammetry as shown in Figure 1.4, as well as spectroscopically.<sup>[81]</sup> In cyclic voltammetry, cross-linking occurs during the first cycle and typically presents a strong maximum at  $E_p \approx 0.65$  V (vs. Fc/Fc<sup>+</sup>). This peak can be attributed to the initial formation of charged TPB species as a result of crosslinking, as is depicted in Figure 1.4. In all future cycles, only the redox processes TPB/TPB<sup>•+</sup> (at  $E_{1/2} \sim 0.53$  V) and TPB<sup>•+</sup>/TPB<sup>2+</sup> (at  $E_{1/2} \sim 0.62$  V) can be observed.<sup>[2]</sup> Cross coupling strongly increases a polymer's stability against organic solvents which can be beneficial in applications where the material comes in contact with such solvents or solvent vapour. On the other hand, if desired, this cross coupling process can be prevented by blocking off the *para* position.

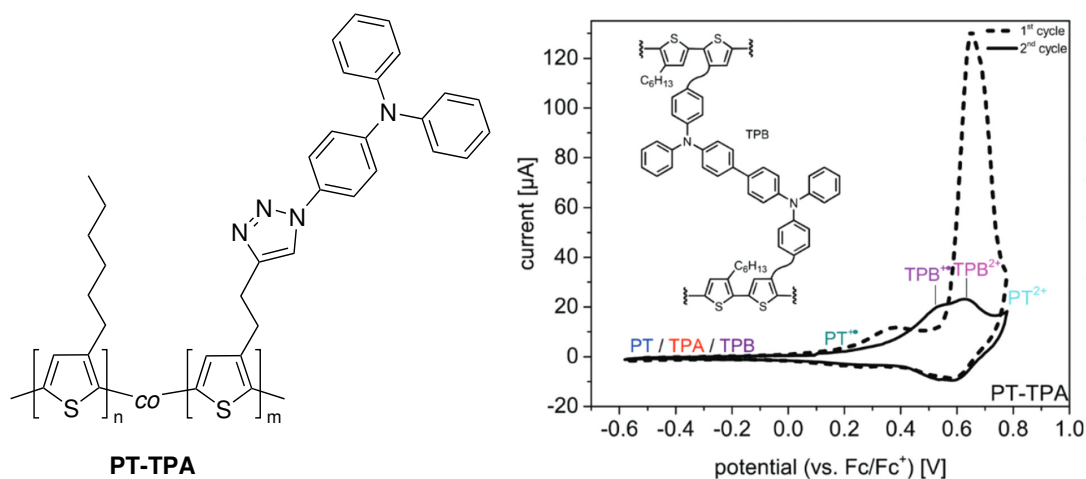


**Figure 1.4:** Cross linkable TPA bearing polymer with respective cyclic voltammetry and schematic representation of cross-linked polymer.<sup>[2]</sup> CV spectrum reproduced from Ref.<sup>[2]</sup> with permission from the Royal Society of Chemistry.

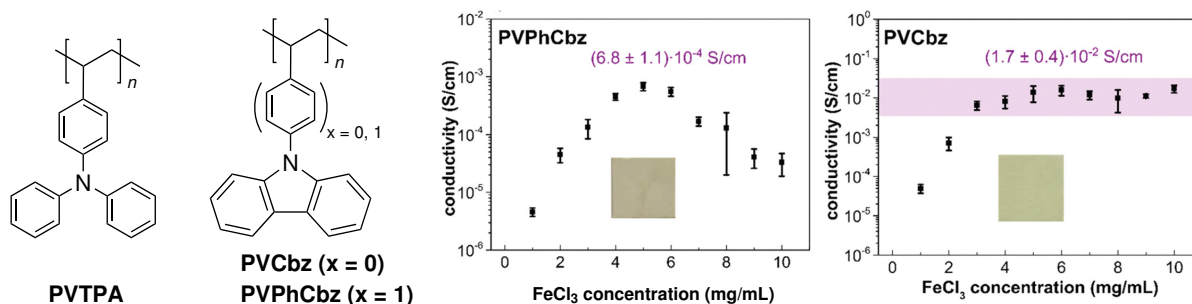


**Figure 1.5:** TPA derivative polymers and respective depictions of doped conductivities.<sup>[4]</sup> Graphs reproduced from Ref.<sup>[4]</sup> with permission from the Royal Society of Chemistry.

When looking at the depicted doped conductivities, polymers PVTTPA and PVPPhCbz show a bell-shape behaviour with increasing level of doping, which is typical for such redox polymers. Interestingly though, in the case of PVCbz it could be shown that, despite being a redox polymer, it exhibits conductivity behaviour similar to P3HT in that it reaches a plateau value with increasing level of doping, a characteristic typical of conjugated polymers (see Figure 1.5).<sup>[4]</sup> As a possible explanation it was concluded that the higher tendency of PVCbz to undergo  $\pi$ -stacking is responsible, due to its more planar structure compared to triphenylamines, where the phenyl groups are rotated with respect to each other.<sup>[71,72]</sup> This can improve interaction between different redox sites, thus improving charge transport. A combination of a conjugated backbone with pending TPA units like

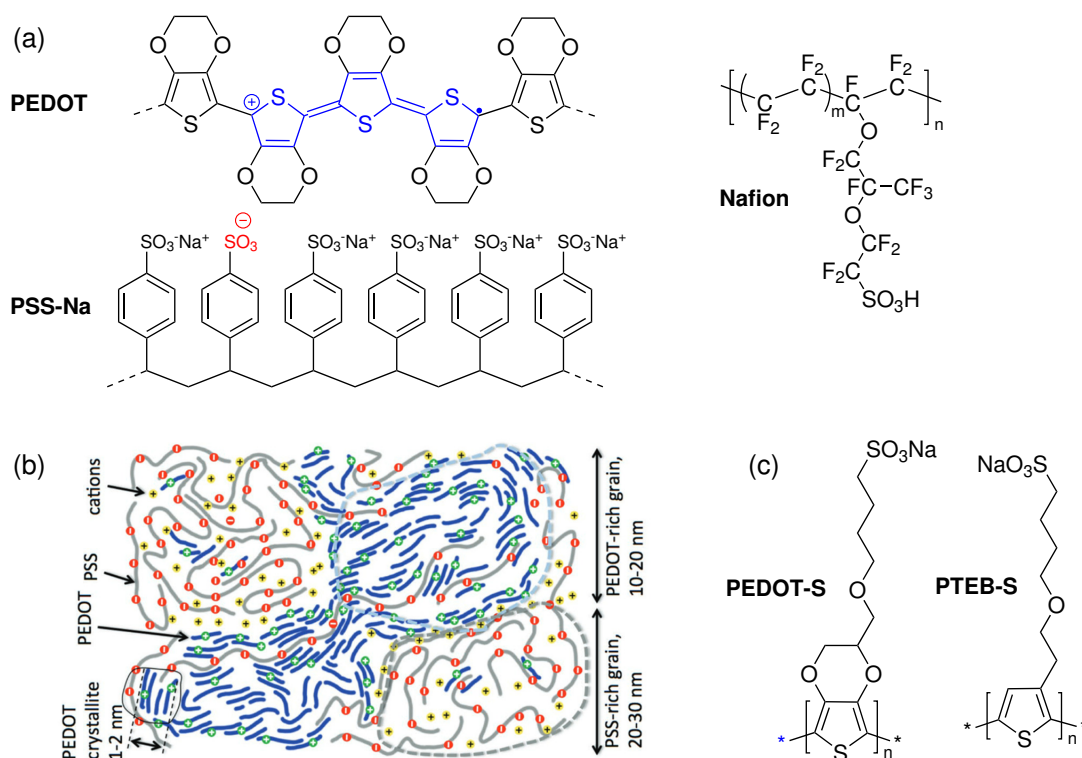
in **PT-TPA** can serve to make use of both, the generally higher electronic conductivity of conjugated polymers (in absence of conductive additives) and the stable redox switching of TPA.<sup>[2]</sup> Furthermore, as described, it presents a way to stabilize thin polymer films against dissolution in organic solvents or solvent vapour by crosslinking.

## 1.4 Conjugated Polyelectrolytes - combining ionic and electronic conductivity

Among many advantages of conducting polymers over silicon based electronics is their potential ability to not only conduct electrons but to transport ions as well, giving way to materials exhibiting electronic and ionic conduction simultaneously.<sup>[82]</sup> Mixed conductivity systems like this are of great interest for both, a number of applications and scientific inquiries. This includes, but isn't limited to, organic electrochemical transistors<sup>[83,84]</sup> (OECT), battery technology<sup>[85]</sup>, polymer actuators<sup>[20]</sup>, electrochromic windows or displays<sup>[19]</sup> and light emitting electrochemical cells<sup>[86]</sup>, as well as answers regarding the role of ionic contributions to the overall conductivity of a system and influences of humidity in both, the material's environment and within the system itself.<sup>[13,82,83,85]</sup> Especially in the form of thin and solution processable films these aforementioned aspects are highly relevant in a time when printed electronics are becoming more and more prevalent.

A famous and intensively studied example of such a system is poly(3,4-ethylenedioxythiophene) in a blend with poly(styrenesulfonate) (PEDOT:PSS). Here, doped PEDOT chains provide electronic conduction while being stabilized in aqueous media by PSS, a polyelectrolyte acting as ion conductor and counter charges in PEDOT, rendering the whole system electroneutral overall (see Scheme 1.12). Ultimately this is widely reported to lead to formation of small crystallites consisting of electron conducting,  $\pi$ - $\pi$  stacking PEDOT chains and granular structures of PEDOT-rich and PSS-rich domains with the latter providing ion conduction (Scheme 1.12 (b)).<sup>[87,88]</sup> A similar phase separation behaviour can be observed in Nafion, a perfluorinated aliphatic sulfonic acid polymer membrane commonly used in fuel cells.<sup>[89]</sup> However, in Nafion there is no electron conduction and ion mobility is provided by the polymer's hydrophilic side-chain end-groups. These groups usually make up a low percentage of the polymer, categorizing Nafion as an ionomer. PSS on the other hand consists of a large amount of sulfonate groups, thus having high local concentrations of ionic moieties, putting it in the category of polyelectrolytes.<sup>[89,90]</sup> The chemical structures of PEDOT:PSS and Nafion are depicted in Scheme 1.12.

Because of its electron conduction capabilities of  $4000 \text{ S cm}^{-1}$  and higher,<sup>[13,85]</sup> PE-

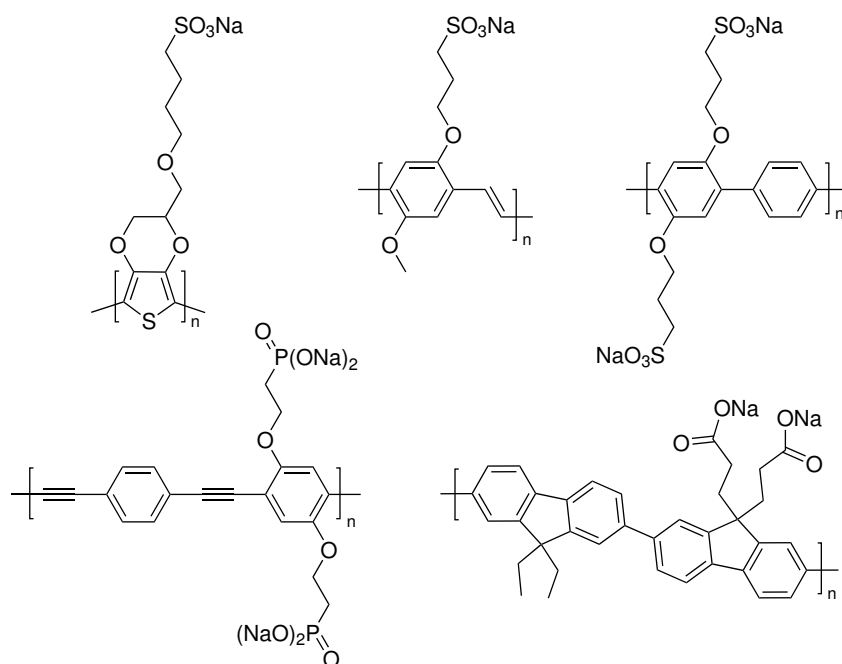


**Scheme 1.12:** (a) Structures of PEDOT:PSS-Na and Nafion. In PEDOT:PSS the charge balancing of a polaron is visualized. (b) Exemplary schematic depiction of PEDOT:PSS morphology, reproduced from reference<sup>[87]</sup> © 2017 WILEY-VCH Verlag GmbH & Co. KGaA, Weinheim. (c) Derivatives used for fast redox switching by Inganäs *et al.*<sup>[91]</sup>

DOT:PSS is well suited to be employed as a transparent and flexible electrode in organic electronics. However, in applications like electrochromic displays (ECD) its polymer blend nature leaves room for improvement. As color change is induced *via* redox switching, counterions from either the second polymer (PSS) or the electrolyte have to enter (or leave) the polymer by diffusion to balance out charges that were either introduced or removed during switching and ensure electroneutrality.<sup>[19]</sup> This process can be optimized by choosing PEDOT derivatives and different partner polymers in the construction of the ECD but will ultimately still be limited by diffusion processes outside of the PEDOT chains. A promising alternative approach to this mechanism is to have the equilibrating counterions inside the polymer's side-chains themselves. This enables shorter diffusion pathways and as such faster color switching of the ECD. Inganäs *et al.* reported redox switching times as low as 30 ms in 2015, employing PEDOT- and polythiophene-based derivatives with ion containing side chains (see Scheme 1.12 (c)).<sup>[91]</sup>

Due to their high ion content and conjugated, electron-conducting polymer backbones

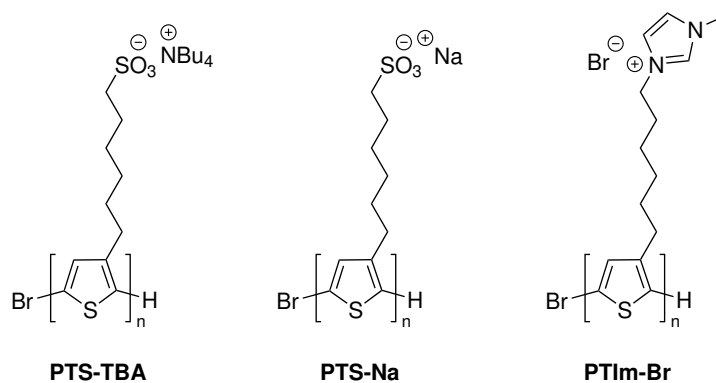
these materials fall into the category of *conjugated polyelectrolytes* (CPE). Commonly, sulfonate end groups are used in the side chains to accomplish ion transport but carboxylic acids have been used as well.<sup>[92–94]</sup> Their negative charges render the polymer able to stabilize positive charges introduced in the backbone upon oxidation by fast expulsion of their positive counter ions, a process that is referred to in literature as *self-doping*.<sup>[95]</sup> Early examples of CPEs based on poly(*p*-phenylene) were introduced by Reynolds *et al.* and Wegner *et al.*<sup>[96,97]</sup> and many new structures have been developed over the years.<sup>[98]</sup> Scheme 1.13 gives a selection of example structures.



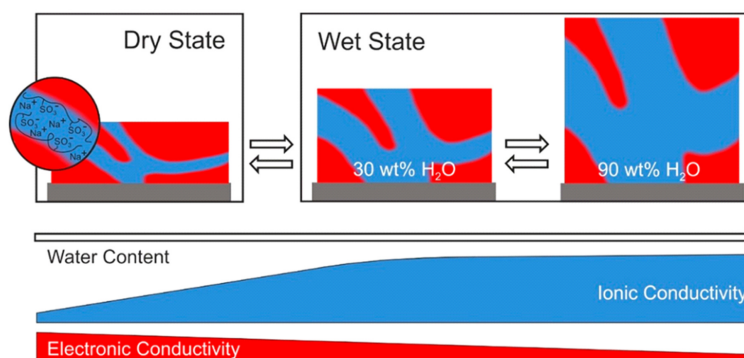
**Scheme 1.13:** Examples of CPE structures.<sup>[98]</sup>

Typically, ionic contributions to the overall electric conduction of mixed conductivity systems is comparably small and rarely determined independently of the electronic part. Ion mobility can be quantified by either moving front experiments or Kelvin probe force microscopy, although only external ionic contributions (e.g. ion diffusion into a PEDOT:PSS layer) are accessible this way.<sup>[82,99,100]</sup> The intrinsic ionic and electronic contributions can, however, be extracted by impedance spectroscopy when applying appropriate equivalent circuit fitting and has been done by Crispin *et al.* on a selection of different PEDOT-based systems.<sup>[101]</sup> In their PEDOT:PSS batch they measured an overall conductivity of up to  $0.15 \text{ S cm}^{-1}$  that was largely independent of relative humidity (RH) in its surrounding, thus dominated by electronic contributions. Introducing additional PSS-Na into such a system then yielded lower overall conductivity at  $0.04 \text{ S cm}^{-1}$ , but variation of relative humidity gave a strong dependency which in turn pointed to ionic

dominance in this system. Separation into the respective partial conductivities  $\sigma_{el}$  and  $\sigma_{ion}$  confirmed this. Another look into PEDOT:PSS conductivity in humid settings was done by Muckley *et al.* by investigating water mass uptake of PEDOT:PSS in the range of 0–80% RH and its correlation to electronic and optical conductivity.<sup>[102]</sup> However, they did not assess ionic conductivities.



**Scheme 1.14:** Some polythiophene based CPEs.



**Scheme 1.15:** Schematic depiction of dry and wet states of a CPE structure like **PTS-Na** during increasing water uptake. Blue: hydrophilic ionically conducting phase. Red: hydrophobic electronically conducting phase. Reprinted with permission from reference<sup>[13]</sup>. Copyright © 2020 American Chemical Society.

In our group in cooperation with Prof. Joachim Maier we have been focusing on polythiophene derivatives with either positively or negatively charged side-chains<sup>[1]</sup> as well as comparative experiments with PEDOT:PSS based blends.<sup>[13]</sup> Three structures recently reported on are given in Scheme 1.14. Impedance spectroscopy supported by DC polarisation experiments allowed for separation of electronic ( $\sigma_{el}$ ) and ionic ( $\sigma_{ion}$ ) conductivity in varying relative humidity environments. A schematic representation of the

polymer **PTS-Na**'s behaviour is given in Scheme 1.15. In AC impedance spectroscopy, the polymer system is subjected to alternating current of varying frequency and the system's resulting answer is measured. Figure 1.6 (b) gives exemplary spectra where each semi-circle is representative of a conducting process in the polymer. Going to higher values on the x-axis is equivalent to lower frequencies and vice versa. In this figure, the blue curve shows two semi-circles, reminiscent of an ionic and an electronic conduction mechanism at this medium humidity setting. At higher humidity, the red data, the lower frequency semi-circle is notably larger, indicating bigger resistance for this process. For systems like this it is often assumed that the low-frequency semi-circle gives  $R_{el}$  directly as obtained from galvanostatic DC experiments and the high-frequency region is comprised of both resistances.  $R_{ion}$  can be calculated from  $R_{hf}$ , the diameter of the high-frequency semi-circle and  $R_{el}$ , the diameter of both, *via* the equation  $R_{hf} = R_{el} \cdot R_{ion} / (R_{el} + R_{ion})$ <sup>[103]</sup> or be determined by fitting the experimental data with equivalent circuit models. For more information and experimental details, the reader is referred to the Experimental Part of this thesis, as the same experiments will be discussed in the chapters to come.

In Figure 1.6, water partial pressure ( $p_{H_2O}$ ) dependent measurements of the ionic conductivity of the sodium sulfonate polythiophene derivative **PTS-Na** showed similar behaviour to that of Nafion membranes, in particular a steep increase at low  $p_{H_2O}$  values when starting from the dry state as hydration of the ionic side-groups increases and water molecules and counterions gain mobility. At high  $p_{H_2O}$  a saturation effect can be observed and increases in  $\sigma_{ion}$  slow down (see Figure 1.6 (d)). Seeing the similarity in behaviour and considering that ion conduction in Nafion is described to happen within water channels created by hydrophobic/hydrophilic domain separation, a similar mechanism was assumed to be responsible for ion conduction in this system (see Scheme 1.15). Strong humidity dependence gave ionic conductivity of up to  $10^{-2} \text{ S cm}^{-1}$  and ion mobilities in the range of  $10^{-7} \text{ cm}^2 \text{ V}^{-1} \text{ s}^{-1}$ .<sup>[13,90]</sup> Values for  $\sigma_{ion}$  in the range of  $10^{-3} \text{ S cm}^{-1}$  can also be reached with PSS derivatives.<sup>[104]</sup>

Another important aspect of CPEs is their ability to take up water. In the given example this has been determined by quartz crystal micro balance experiments, where the polymer film's weight is measured with ultra high precision *via* its vibrational frequency. With increasing water uptake and thus mass of the polymer film, this frequency changes which can in turn be calculated into relative water uptake as depicted in Figure 1.6(c), where it reached a maximum of about 92 wt-%.

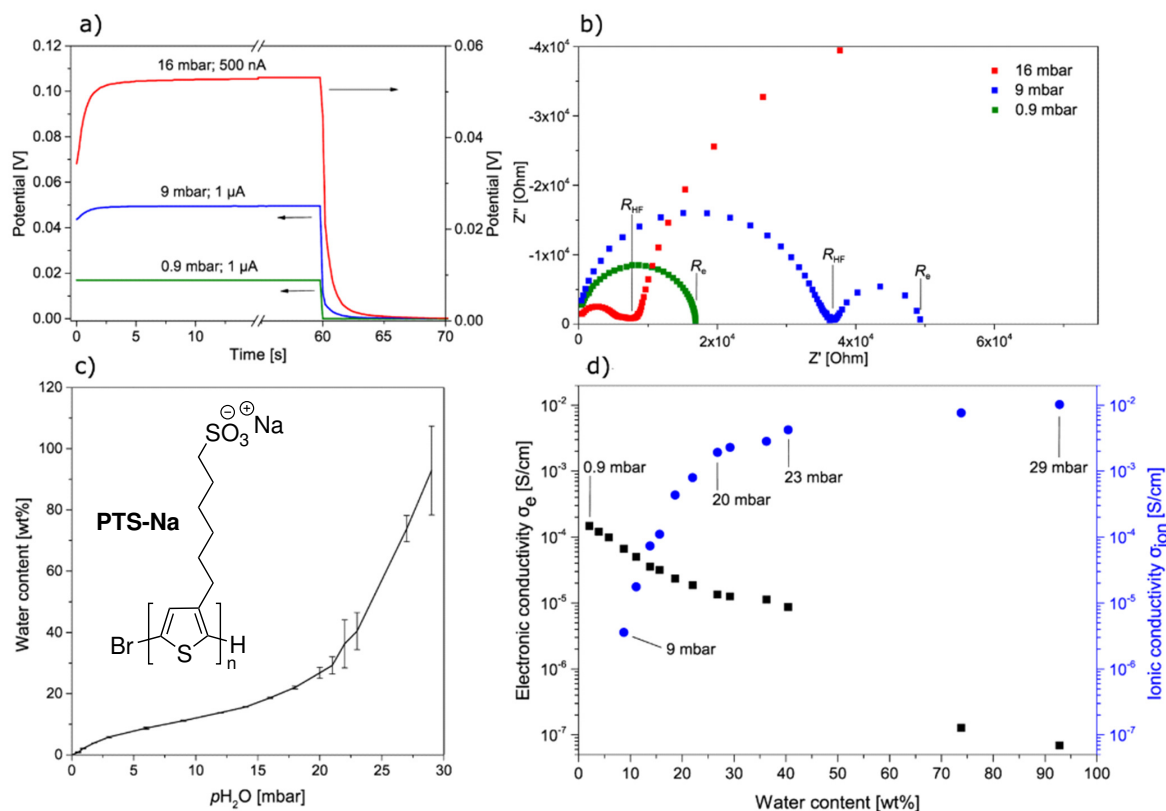


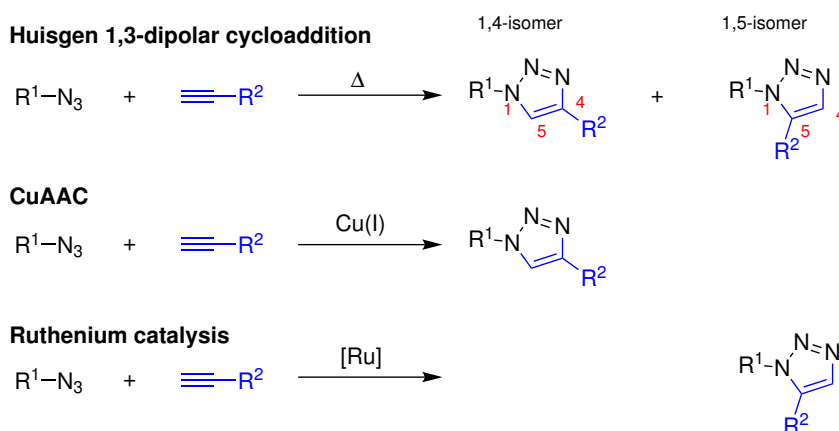
**Figure 1.6:** Humidity dependent characterization of a polythiophene based CPE, structure depicted in (c). (a) Galvanostatic DC experiments at different water partial pressures  $p_{H_2O}$ . (b) AC impedance spectra at different  $p_{H_2O}$  with indicated  $R_{el}$  as obtained from DC experiments. (c) Humidity dependent water uptake as obtained from quartz crystal micro balance. (d) Electronic and ionic conductivities at different  $p_{H_2O}$ . Graphs adapted with permission from reference<sup>[13]</sup>. Copyright © 2020 American Chemical Society.

## 1.5 Method of Copper-Catalyzed Azide-Alkyne Cycloaddition (CuAAC)

As was discussed within the last chapters, versatility of polymer functionalisations has improved greatly in the last decades and this was not in small part due to the emergence of a new concept of reactions to build carbon-carbon and carbon-heteroatom bonds with a set of pre-determined criteria, pioneered by Sharpless *et al.* in 2001.<sup>[105]</sup> These reactions, termed by Sharpless, Finn and Kolb as *Click Chemistry* are to exhibit, among other criteria, a modular characteristic, be wide in scope, high-yielding, include only easily removable side-products if any and provide simple reaction conditions and product isolation. This is accomplished by reactions with a high thermodynamic driving force. Examples

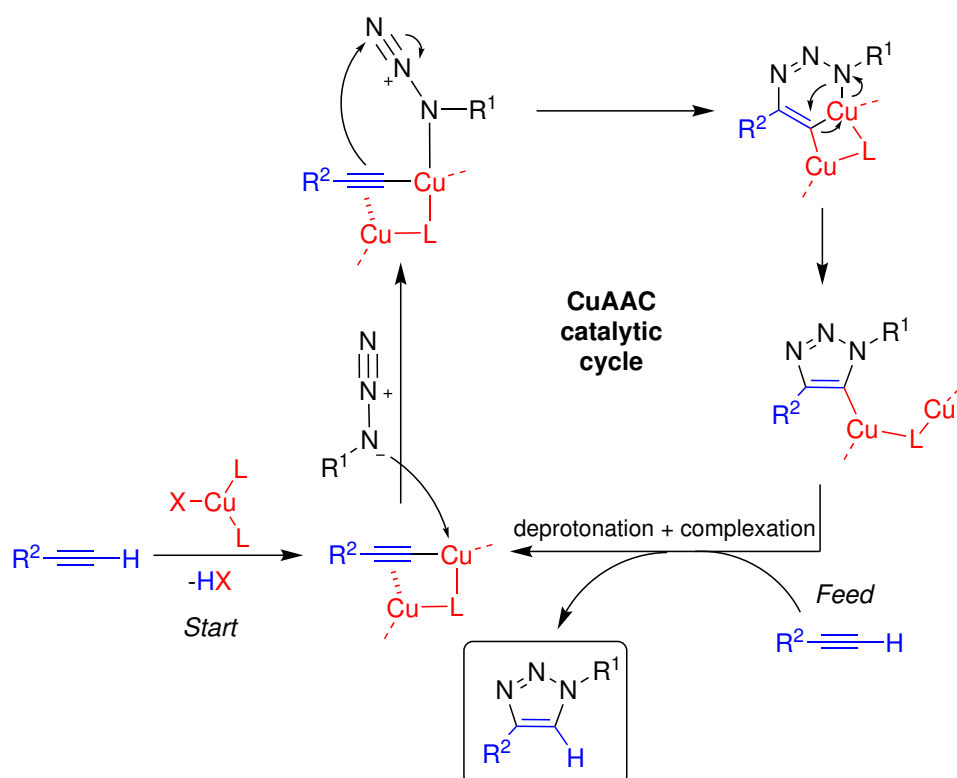
include cycloadditions like 1,3-dipolar cycloadditions or Diels-Alder reactions, nucleophilic ring-opening reactions or additions to carbon-carbon multi bonds.

Combining the latter with the first, one type of reaction that fits these criteria and has found wide-spread application is the class of copper-catalyzed azide-alkyne cycloadditions (CuAAC). As a variation of the Huisgen 1,3-dipolar cycloaddition it can be performed by thermal activation (equating to standard Huisgen cycloaddition, though the use of organic azides warrants special care to minimize danger of violent decomposition) or Cu(I)-catalyzed. In the presence of Cu(I), the reaction is versatile in terms of applicable reaction conditions and reaction environment (aqueous, organic, solution, on solid phase).<sup>[106,107]</sup> In the course of the reaction an azide and an alkyne form a triazole, which is largely inert in environmental conditions. This formation can result in two triazole isomers, 1,4- or 1,5-coupled. Classic Huisgen 1,3-dipolar cycloaddition gives a mixture of both isomers, while CuAAC selectively affords the 1,4-isomer, though it can be modified to provide the 1,5-isomer instead by use of ruthenium catalysis (see Scheme 1.16).<sup>[108–110]</sup> These factors, combined with the ease at which CuAAC reactions can be carried out, made them the most widely used *Click* reactions in organic and polymer chemistry, but also biosciences, with extensive research and continuous expansion of its scope over the years.<sup>[56,111–114]</sup>



**Scheme 1.16:** Regioselectivity in Huisgen 1,3-dipolar cycloaddition and in *Click* chemistry with different catalysis.

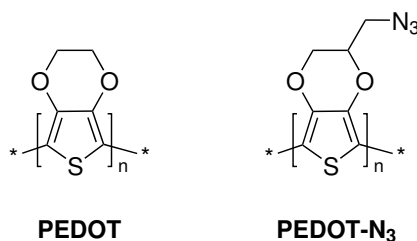
Scheme 1.17 displays the current model of the accepted mechanism of CuAAC reactions.<sup>[107,115]</sup> After it was originally postulated to proceed with one Cu(I) species,<sup>[111]</sup> consensus exists today on the involvement of two Cu(I) ions in the catalytic cycle, albeit not fully understood at this point. Cycle initiation occurs by formation of a  $\sigma, \pi$ -dicopper acetylide with the alkyne species and concurrent loss of the terminal proton. In the catalytic complex formed by addition of the azide species, both copper centres are considered equivalent



**Scheme 1.17:** Currently generally accepted mechanism of CuAAC *Click* reactions.<sup>[107,115]</sup>

and have been demonstrated by Fokin *et al.* to present a rapidly rearranging equilibrium with scrambling of both copper centres.<sup>[116]</sup> In the six-membered metallacycle following some rearrangements, the second Cu(I) ion is thought to alleviate ring strain, based on kinetic experiments and density functional theory (DFT) calculations. Reductive ring closure is then followed by deprotonation of another alkyne molecule, affording the final coupling product and starting a new catalytic cycle. In aprotic conditions, this last step of deprotonation has been shown to be rate determining.<sup>[115,117]</sup> Generally, steps facilitating either alkyne deprotonation or azide binding to the copper centre can accelerate the reaction. The Cu(I) species needed can be generated *in-situ* by oxidation or reduction or be provided by preformed catalysts and the reaction can be performed in aqueous or organic solution. As solubility of ionic copper species can be problematic in many organic solvents, catalysts like  $(\text{MeCN})_4\text{Cu(I)PF}_6$  are used, where the ligands stabilize the ions in polar solvents and avoid pitfalls of oxidative coupling by-products or formation of unreactive polynuclear copper acetylide complexes that can occur when using copper halide catalysts. Elemental copper in form of a powder or wire can be added to reduce any oxidized Cu(II) back to Cu(I) in the course of the reaction, preventing the catalytic system from becoming inactive or less reactive.<sup>[118,119]</sup> In addition to preformed Cu(I) catalysts, reactions can be

done starting from Cu(II) compounds as well. One popular such system uses the *in-situ* generation of Cu(I) from CuSO<sub>4</sub> by reduction with sodium ascorbate and is typically performed in a water/alcohol mixture.<sup>[114,115]</sup> Another one has been shown to be effective in electrochemical CuAAC conversions of PEDOT-N<sub>3</sub> films by potentiostatic *in-situ* generation of Cu(I) from Cu(II)SO<sub>4</sub> in DMSO.<sup>[120,121]</sup> This last example is particularly of interest, as the base polymer, PEDOT (Scheme 1.18) is a well-known and heavily studied conducting polymer, which has found use in flexible, organic electronics as an electrode material and other applications in optoelectronic devices.<sup>[122]</sup> As described in the previous chapter, PEDOT is commonly used in a polymer blend with poly(styrenesulfonate) to form the PEDOT:PSS polyelectrolyte system. Introduction of azide groups into the polymer allows for versatile functionalizations which can be beneficial in many ways, like removing the necessity of separate PSS counterions or improving PEDOT's solubility properties.<sup>[119]</sup>



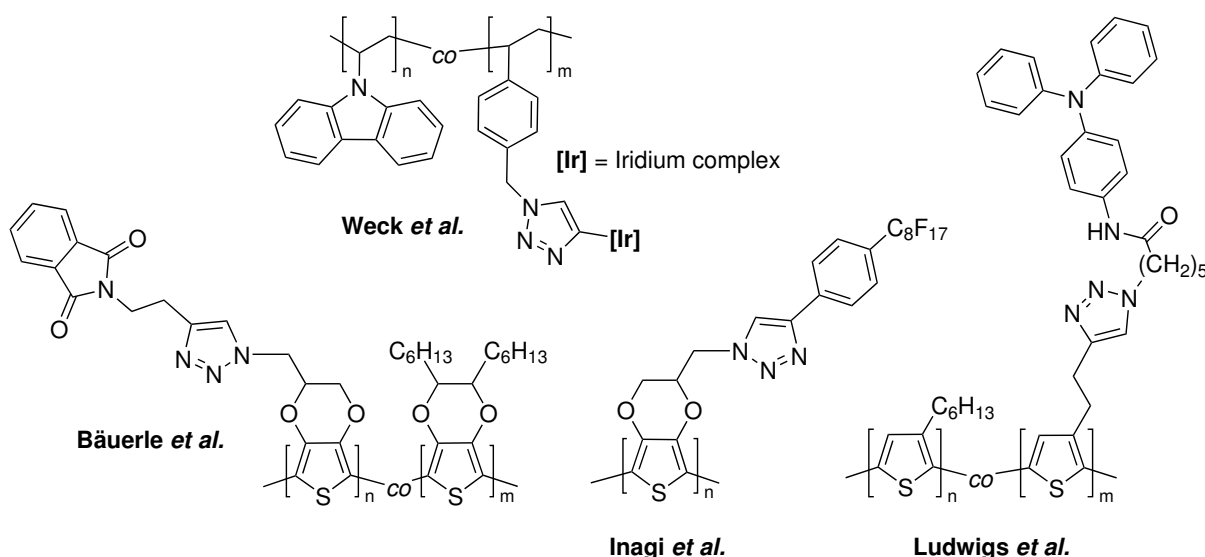
**Scheme 1.18:** Chemical structures of PEDOT and PEDOT-N<sub>3</sub>.

Further examples of polymer functionalizations *via* CuAAC exist. One other popular base material is azidomethylstyrene (AMS) which is readily incorporated as a comonomer into copolymer systems. Weck *et al.* used it to produce styrene/AMS and N-vinylcarbazole/AMS copolymers to which they successfully attached phosphorescent iridium complexes by means of CuAAC (see Scheme 1.19).<sup>[123]</sup> Graft polymers have also been created with this method.<sup>[124]</sup>

For such CuAAC conversions of polymers, different reaction environments are feasible. Polymers can be either reacted in their dissolved form in a stirred solution or in the shape of thin films. Larsen *et al.* showed that conversion of PEDOT-N<sub>3</sub> polymer films strongly depends on the degree of swelling in the respective solvent, with a low degree of swelling only affording surface modification of the films as the necessary reagents don't enter far enough into the polymer.<sup>[125]</sup> Using the CuSO<sub>4</sub>/sodium ascorbate catalytic system they noted the importance of DMSO as a solvent or cosolvent, as it is capable of dissolving the catalytic Cu(I) ions and serves to accelerate the *Click* reaction, generally independent of the type of alkyne used. While they investigated the influence of different DMSO contents on the reaction in this system with reaction times up to 22 h, Bäuerle *et al.* converted

PEDOT-N<sub>3</sub> polymer and copolymer films employing Acetonitrile (MeCN) as the sole solvent using another catalytic system based on the aforementioned preformed catalyst [Cu(I)(MeCN)<sub>4</sub>]<sup>+</sup>PF<sub>6</sub><sup>-</sup>. With elemental copper for oxidation protection they successfully functionalized their polymers at room temperature over the course of 72 h.<sup>[119,126]</sup>

The same catalytic system has been used successfully in our group for the functionalization of P3AT derivative copolymers dissolved in THF<sup>[2]</sup> and with DMSO for the polymer-analogue functionalization of PEDOT-N<sub>3</sub> repeating units.<sup>[127]</sup> Examples of both structures (PEDOT-based and P3AT-based copolymers) are included in Scheme 1.19. Contrary to conversion of PEDOT-N<sub>3</sub>, the given P3AT copolymer was built from an alkyne-bearing thiophene derivative, which is apparent when looking at the orientation of triazole in the resulting polymer. Here, CuAAC enabled the introduction of additional redox functionality and the ability to crosslink the polymer due to incorporation of triphenylamine groups into the side-chains.



**Scheme 1.19:** Selected literature examples of structures achieved *via* CuAAC.<sup>[2,58,119,120,123,128]</sup>

Examples for the electrochemical application of CuAAC were published by Larsen *et al.* as well.<sup>[121,129]</sup> They used 1-bromo-4-ethynylbenzene and 5-iodopentyne to achieve micro-patterned substrates by applying  $-0.5$  V for 5 min to targeted azide-functionalized electrodes in presence of the respective alkyne and Cu(II)SO<sub>4</sub> in a DMSO/H<sub>2</sub>O mixture. In unpublished work from our group, within the scope of his master thesis *Jonglack Kim* replicated the electrochemical conversion of PEDOT-N<sub>3</sub> on coated gold substrates at different potentials and found  $-0.5$  V (vs. Ag/AgCl) to work best in electrolyte-free DMF

solutions of the employed alkyne.<sup>[130]</sup> However, 30 min of constant potential was applied here.

Another example by Inagi *et al.* used bipolar electrodes. By passing a constant current through the electrode a potential gradient was achieved which allowed for partial and space-selective functionalization *via* this "electro-click" method.<sup>[120]</sup>

*Click* chemistry and CuAAC in particular open up a wide variety of polymer and surface modifications with relative ease and allow for tweaking of properties and introduction of new functionalities like fluorescence, cross-linkable and redox active units, receptor ligands, Michael acceptors, bio-compatibility and more.<sup>[2,56,106,119,120,123,128]</sup>

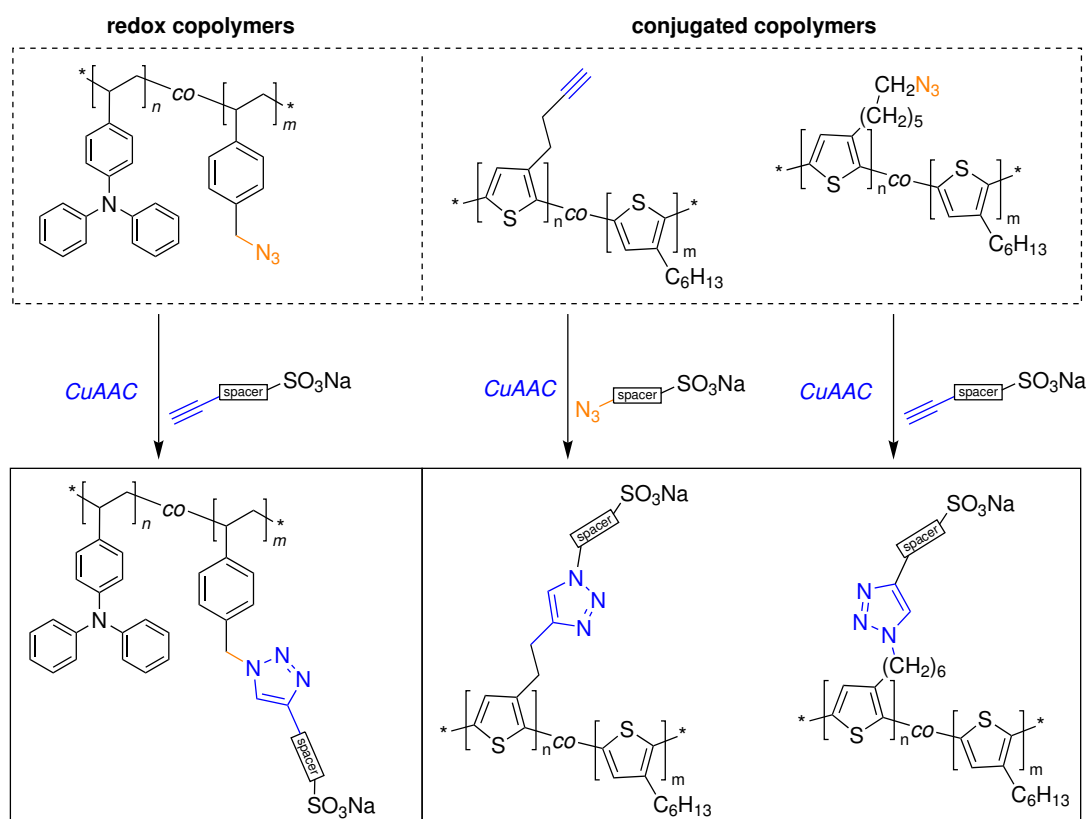
## 2 Objectives

Earlier work in this group has involved the decoupling of electronic and ionic conductivity in conjugated polyelectrolytic systems based on poly(3-hexylthiophene), where electronic conductivity occurs within the conjugated backbone and ionic conductivity is realized by ionic side-chains.<sup>[1]</sup> Decoupling of both pathways allows for distinguished evaluation of factors influencing the respective degree of conductivity. On the other hand, presence of ionic moieties within a conducting polymer influences its properties beyond the introduction of ionic charge carriers as they can also influence the electronic behaviour of the material, its solubility and its morphological make-up, effects, that depend both on the nature of these ionic moieties and on their share in the polymer. A prime example of these effects being in place and giving way to electrochemical applications as described in the introduction chapters is the widely known PEDOT:PSS, albeit being a polymer blend and not a copolymer. Its mixed conductivity and water uptake behaviour has been compared with a thiophene-based polyelectrolyte as well.<sup>[13]</sup>

In other work, statistical polythiophene copolymers bearing TIPS-protected alkyne side-chains have been synthesized in different ratios *via* GRIM polymerization and successfully functionalized with redox-active triphenylamine groups by means of CuAAC.<sup>[2]</sup> This approach allows for tailoring of the amount of cross-linkable redox units to be introduced into the copolymer.

### **Task 1 - Preparation of versatile copolymer systems for polymer analogous functionalization**

The present work shall pick up on both topics by establishing a set of versatile, functionalizable copolymer systems. From those, new polyelectrolytic copolymers are to be created and probed for their electrochemical properties, which includes the aforementioned decoupling of electronic and ionic conductivity by impedance spectroscopy, where applicable. Particularly important for polyelectrolyte systems is their ability to take up water, as this can heavily influence the ionic charge carrier mobility. Thus, water-uptake shall be evaluated by means of Quartz Crystal Microbalance (QCM) and compared between systems. The structures of the systems to be created and converted are shown in Scheme 2.1. These are two conjugated polyelectrolytes based on regioregular polythiophenes with inverted CuAAC functionality to each other ( $N_3$  vs. alkyne) and a TPA-based polyelectrolyte system, which thus provides inherent crosslinking and redox functionality.



**Scheme 2.1:** Copolymer systems targeted in this work, providing different side-chain lengths, inverted CuAAC-functionality with respect to each other and adjustable content of *clickable* units.

## Task 2 - Introduction of ionic moieties *via* Click Chemistry

Introduction of ionic functionalities will be performed by CuAAC reactions with the polythiophene-based systems being accessible by opposing CuAAC reaction partners (alkynes *vs.* azides). This means that the corresponding precursors of the systems shown would provide a highly versatile basis for future polymer functionalization which is not at all limited to ionic moieties of various nature, due to CuAAC giving way to countless possible modifications which can be of interest for a range of applications. The depicted copolymers are to offer great flexibility in terms of functionalities to be introduced and the degree of functionalization by tailoring the co-monomer ratios. More precise investigations into effects of side-chain functionalizations will be possible this way.

Here, functionalizations will introduce terminal sulfonate groups. Polyelectrolytes like this are of great interest. For example, with counterions being positioned right inside the polymer, neutralization times after external introduction of charges are short, which can reduce switching times of electrochromic displays. Introduction of cross-linkable

units (like triphenylamine (TPA)) can allow for greater solvent and ageing stability which can be beneficial in future applications (e.g. energy storage) as well. Further potential applications include sensors and interlayers in organic photovoltaic (OPV) or polymer photovoltaic (PPV) devices.

As many such applications require the production of functional layers from the corresponding polymers and both, impedance spectroscopy and QCM measurements are done in film, the ultimate goal of this thesis is to obtain thin functionalized polymer films with mixed ionic/electronic conduction capabilities. There are two principal ways to achieve this, visualized in Figure 2.1. The first is to produce films from the bulk polymer or solutions thereof, which contains groups that can be converted later. In a second step these films are reacted polymer analogously to introduce the desired functionality into them. Another way is to reverse the approach and functionalize the polymer first and then creating films from the already converted material.

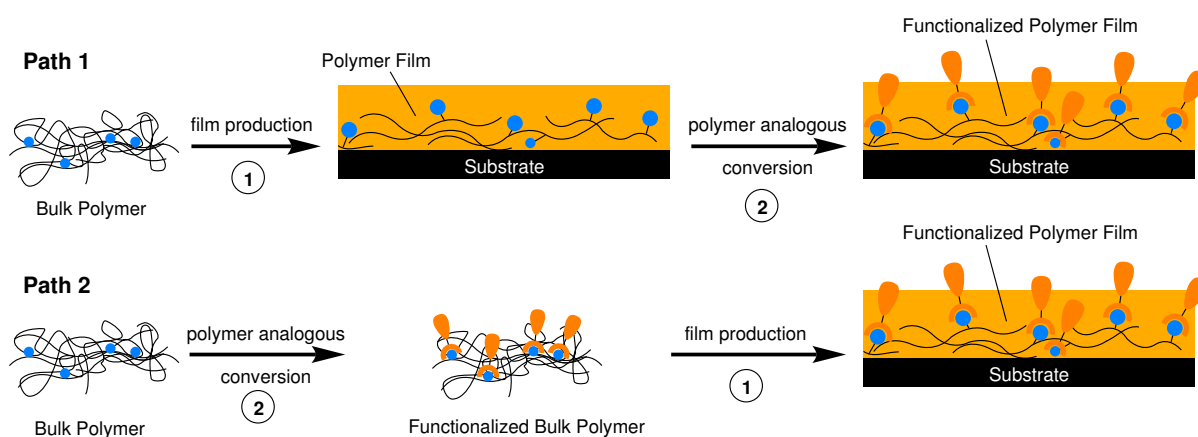


**Figure 2.1:** General paths to functionalized polymer films. Blue dots: convertible groups. Orange shapes: Desired functionality.

Both paths include a step of polymer analogous conversion which can be done by CuAAC in this work. Three *click*-functionalization procedures have previously been applied in our group on polymer systems different to the ones used in this work, covering both paths described in Figure 2.1. Those three methods shall be discussed briefly. For more background information the reader is referred to the introduction chapter of this thesis. The three methods are electrochemical CuAAC-reaction in thin films (here termed "Electroclick" or **EC**), chemical CuAAC-reaction in thin films (here termed "Chemical Click" or **CC**) and chemical CuAAC-reaction in solution (here termed "Bulk Click" or **BC**). Figure 2.2 visualizes them.

Those three approaches have different advantages and disadvantages. EC can be done within 30 min as was demonstrated in the master thesis of *Jonglack Kim* on a PEDOT

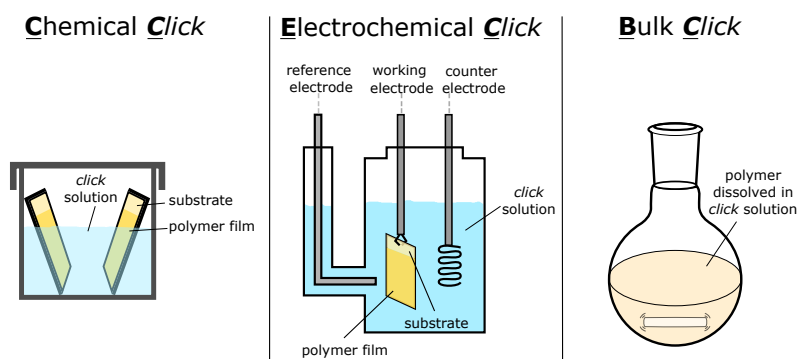


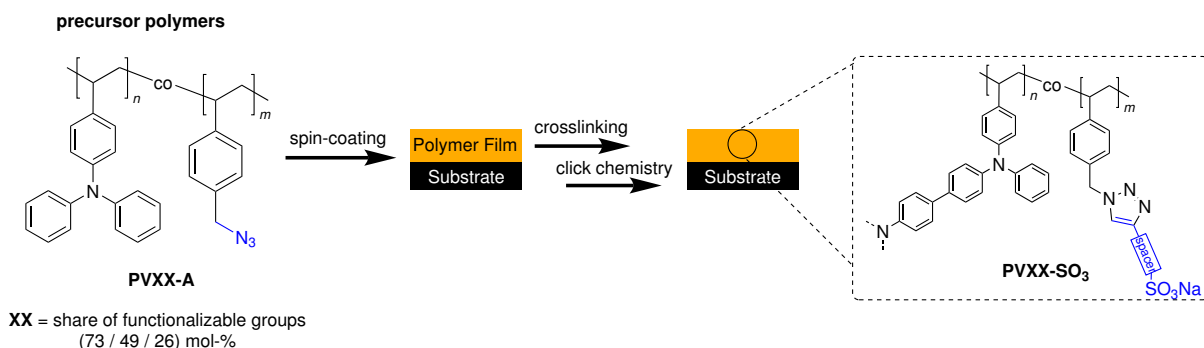
**Figure 2.2:** Different procedures for CuAAC reactions in thin films or dissolved bulk material.

system with seemingly reliable conversions. Drawback of this method is that only one film can be converted at a time. Furthermore, since the reaction is done in thin films on conducting templates, subsequent analysis and interpretation of the conversion is difficult and severely limited.

This same drawback applies as well for the CC reaction, but in this case, many thin films can be reacted at the same time if necessary. On the other hand, since the catalytic system and mechanism of this reaction are different, the conversion takes place over the course of three days instead of 30 min.

Lastly, the BC reaction uses the same catalytic system as CC which needs three days for full conversion. Here, only one compound can be clicked at a time but since the reaction isn't done in thin films but with dissolved bulk materials or liquids, characterization of the obtained material can be done more easily and with a wider variety of methods. Also, greater amounts of material can be functionalized in one batch. This method can be complicated by changes in physical properties induced by the *click*-functionalization, for example when clicking ionic groups. Here, drastic changes in the solubility of a clicked polymer can hinder conversion and even render the obtained polymer non-processable.

# 3 TPA-based Polyelectrolytes

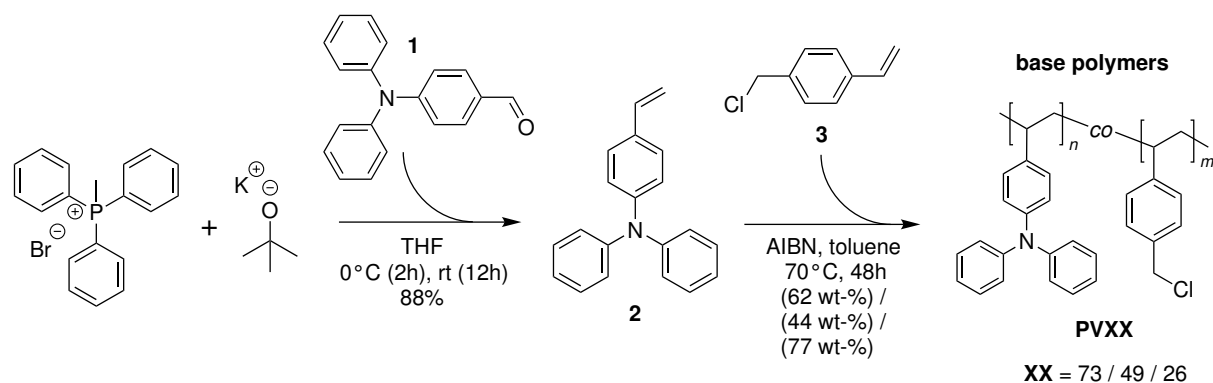


**Scheme 3.1:** Schematic representation of *click*-functionalizations of VTPA-based precursor polymers to obtain mixed conducting polymer films.

For the preparation of VTPA-based polyelectrolyte systems, copper-catalyzed alkyne-azide cycloaddition *Click* chemistry (CuAAC) was used. The azide-bearing copolymer systems **PVXX-A** prepared for this approach (here often referred to as "precursor polymers") allow for great versatility regarding the functionalization of said copolymers by *Click* chemistry. This copolymer system was chosen due to TPA groups providing inherent crosslinking and redox capabilities while the azide bearing styrene derivative is easily available from respective halide derivatives. Scheme 3.2 shows the synthetic route leading to the preparation of said precursor polymers. Further functionalization was then carried out by different approaches involving copper-catalyzed click chemistry as has been described in chapter 2, referred to by their abbreviations EC, CC and BC. Monomer and copolymer synthesis will be discussed in the following chapter.

## 3.1 Synthesis of Azide-bearing Copolymers

Copolymers were synthesized by free radical polymerization involving initiation of monomers by Azobisisobutyronitrile (AIBN). The monomers used were 4-Vinyl-triphenylamine (VTPA) **2** and 4-(chloromethyl)styrene (CMS) **3**. The latter is commercially available, although stabilized by *tert*-Butylcatechol which was removed by filtration over activated alumina prior to polymerization. Synthesis of VTPA was done by *Philipp Sliskovic* employing WITTIG-olefination of 4-(Diphenylamino)benzaldehyde **1** in THF and in good yield, as is shown in Scheme 3.2. Subsequent copolymerization was carried out by both, *P.S.* and me, in toluene with VTPA/CMS co-monomer feed ratios of 25:75, 50:50 and 75:25, yielding copolymers **PV73**, **PV49** and **PV26**, respectively. Hereby, choosing the



**Scheme 3.2:** Schematic synthesis route to VTPA-based precursor copolymers.

appropriate amount of solvent for each monomer feed ratio proved essential to prevent the occurrence of gelation during polymerization. Polymer names were given based on the in-polymer share of (functionalizable) styrene derivatives as determined by  $^1\text{H-NMR}$  spectroscopy of the subsequent azide-bearing polymer templates (**PVXX-A**).

### 3.1.1 Monomer Synthesis

#### VTPA Synthesis

First, monomer VTPA **2** had to be synthesized, which was performed in THF under inert atmosphere in an overnight reaction. After slow addition of the base to a solution of Methyltriphenylphosphonium bromide in THF at  $0^\circ\text{C}$  the mixture was combined with 4-(Diphenylamino)benzaldehyde **1**. Stirring overnight at room temperature was followed by quenching with methanol to stop the reaction. Column chromatography with Cyclohexane and Dichloromethane in a 10-to-1 ratio then afforded the clean monomer in an isolated yield of 88%.

#### CMS Preparation

As mentioned before, (4-Chloromethyl)styrene was used as bought except for removal of the included stabilizer by filtration over activated alumina prior to polymerization. The non-stabilized monomer was then stored in the cold.

NMR spectra for both, VTPA and CMS are given in Figure 3.1 and show a clean compound in both cases. The vinyl group of both monomers result in three signals each, because of the terminal  $\text{CH}_2$ -protons **a**, which split into two signals due to different  $^3J$ -coupling with proton **b**. Benzylic protons of CMS show as a singlet **g** at 4.58 ppm which will be important for evaluation of the coming halide-azide-exchange reaction. Overall

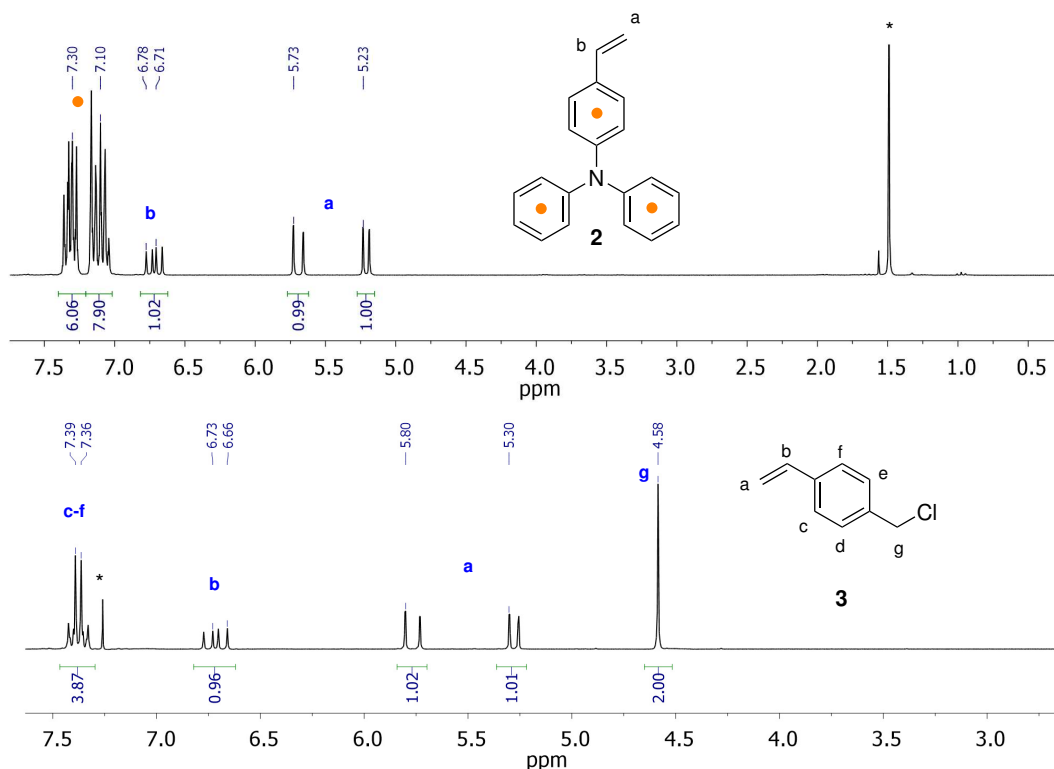


**Figure 3.1:**  $^1\text{H-NMR}$  spectra in  $\text{CDCl}_3$  of monomers **2** and **3**. Integration fits well with the targeted molecular structures.

integral values fit well with the expected values for the corresponding molecular structures, although the aromatic region of VTPA is overlapping with the residual chloroform peak of the deuterated solvent.

### 3.1.2 Copolymerization

Polymerization test runs by *Philipp Sliskovic* and prior polymerizations by me revealed that with increasing amounts of VTPA in the reaction mixture, gelation became a bigger issue when sticking to the reaction conditions used before. Those conditions, based on literature procedure,<sup>[131,132]</sup> had been used for the synthesis of VTPA-*co*-Styrene copolymers, characterized in detail in the Ludwigs group within the scope of the PhD thesis of *Kirsten Bruchlos*. They worked well for lower shares of VTPA, namely 25%. But at the same overall monomer concentration of 1.5 M simply changing the co-monomer ratio of VTPA to higher amounts introduced a high increase in viscosity during polymerization. Figure 3.2 gives the chromatogram of an early approach with 80% VTPA monomer feed. The high number average molecular weight is quite notable here. Even though dispersity  $D$  still remained within reasonable dimensions it was higher than was expected from previous

polymerizations in earlier works and more importantly, the bell curve of the size exclusion chromatography (SEC) given here shows a high- as well as a low-molecular shoulder of notable scale. Depending on the intended purpose of the polymer this could be acceptable but the increased viscosity during polymerization calls in question the reproducibility of the procedure.

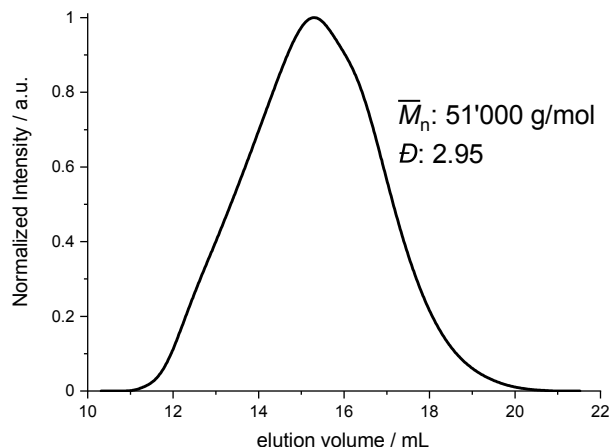


**Figure 3.2:** SEC of copolymerization with 80 % VTPA and 20 % CMS following conditions applied in earlier works.  $\bar{D}$  was higher than expected from these previous polymerizations, albeit still in an acceptable region. Bell curve of the chromatogram is disturbed by a shoulder on each side. Eluent: THF. Calibration: PS standards.

Accordingly, for future polymerizations solvent volume was increased, going from an overall monomer concentration in the reaction mixture of about 1.5 M down to 1.0 M and prolonging the polymerization time from an overnight reaction to 48 h. Both monomers were then reacted with their aforementioned relative amounts aiming for copolymers with CMS contents of 75 %, 50 % and 25 %. The free-radical polymerizations (FRP) proceeded with yields of 62 % (**PV73**), 44 % (**PV49**) and 77 % (**PV26**). SEC chromatograms are given in Figure 3.3. Number average molecular weights are given as well as dispersity values. Highest molecular weight could be achieved with a 1:1 ratio of **2** and **3**, leading to a  $\bar{M}_n$  of 11 500 g mol<sup>-1</sup> and  $\bar{D}$  of 2.15 for **PV49**. Cutting the share of either of the two lead to a similar decrease in overall molecular weight in each case by 40–50 %, affording **PV26** and **PV73** with  $\bar{M}_n$  values of 6900 g mol<sup>-1</sup> ( $\bar{D}$  2.01) and 6000 g mol<sup>-1</sup> ( $\bar{D}$  2.41), respectively. All three chromatograms show good bell curve shapes with dispersities in the range of 2.00 to 2.50, typical for the SCHULZ-ZIMM-distributions of free-radical polymerizations, although the bell curves found here seem more resembling of a GAUSS-distribution. In the case of free-radical polymerizations like these, typical dispersities in ideal scenarios lie between 1.5 and 2.0, depending on the main cause of termination.<sup>[133]</sup> Deviations from this

are not uncommon in real-life polymerizations, though. The fact that all of the prepared polymers have values of  $D$  greater than 2 is an indicator that chain transfer reactions are taking place, which leads to both lower overall molecular weight and broader molecular weight distributions.<sup>[134]</sup> The deviations are small, however, as the comparably wider distribution of **PV73** is certainly caused at least partially by the slight low-molecular peaks that can be seen in its chromatogram (most notably). Those peaks are situated closely to the lower limit of the SEC's calibration range and could generally, at least in part, be due to residual toluene or methanol, from the polymerization procedure, being stuck inside the polymer. Especially for **PV73**, though, there is also a sign of a small degree of low molecular coupling products, oligomers or short polymer chains, which were created during polymerization, the origin of which is thought to likely be a small flaw in the reaction execution. For the intended use of the polymer they were not deemed problematic, so subsequent functionalization was performed without further purification.

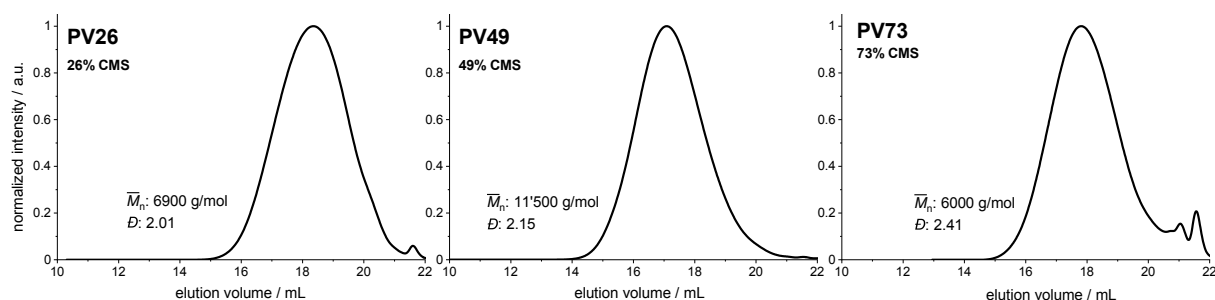


**Figure 3.3:** Normalized SEC chromatograms of copolymers **PV26**, **PV49** and **PV73**. Eluent: THF. Calibration: PS standards.

The  $^1\text{H-NMR}$  spectrums of all three copolymers are given in Figure 3.4. Aromatic protons of the triphenylamine groups and the styrene unit can be found as well as the aliphatic signals belonging to the polymer backbone. Residual water is overlapping the aliphatic region, making the evaluation of this area less precise. The chloroform signal on the other hand occurs right next to the aromatic region and doesn't superimpose on those peaks. Conveniently, the benzylic protons ( $\text{H}_{benz}$ ) neighbouring the chlorine group of the CMS units are situated right between them and so can be used to track the halide-azide-exchange reaction as the chemical shift of these protons is expected to change as a result of the substitution (see chapter 3.1.3 for evaluation). Furthermore, this benzylic signal can be used to evaluate the co-monomer ratio in the polymer. Co-monomer ratios can be calculated from these spectra and give CMS contents of 27 %, 49 % and 74 % accordingly. As these polymers are in essence only precursors for their azide analogues which will be employed in the experiments to come, calculation of the co-monomer ratios shall be described on the example of those instead as they were used as the basis for

naming the polymers. The corresponding section can be found on page 39 in chapter 3.1.3.

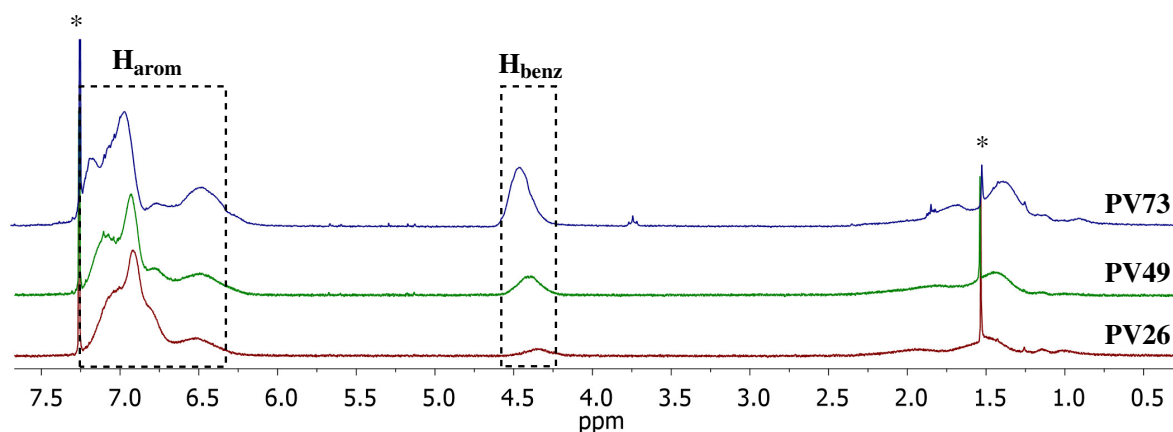
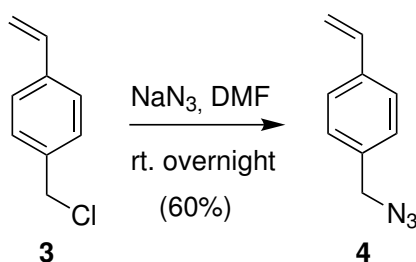


**Figure 3.4:**  $^1\text{H-NMR}$  in  $\text{CDCl}_3$  of the 3 copolymers. Benzylic and aromatic protons are marked

### 3.1.3 Polymer analogous Halide/Azide Exchange



**Scheme 3.3:** Model reaction for the nucleophilic substitution of chlorine in 4-(chloromethyl)styrene **3** with sodium azide to afford 4-(azidomethyl)styrene **4**.

Prior to the polymer analogous conversions of the prepared polymers, a model reaction was employed as depicted in Scheme 3.3 to ensure the conversions are working well and can ideally be examined both qualitatively and quantitatively when done in the actual polymers. Reaction of **3** to the respective azide **4** is a straight forward nucleophilic substitution of the better leaving group chlorine with an excess of sodium azide. The reaction is performed in an overnight reaction in dimethylformamide (DMF) at room temperature. The relatively low yield of 60% in this case can be explained with losses due to repeated liquid-liquid extractions which are necessary to completely remove DMF, used as the reaction solvent. As solubility doesn't change when converting compound **3**

to compound **4**, unreacted starting material would remain in the organic phase as well. Thus, by measuring  $^1\text{H-NMR}$  spectroscopy of the extracted product, statements about the conversion can be made. Figure 3.5 (bottom) shows the spectrum of the obtained product in comparison with the starting material (top). The complete disappearance of signal **g** at 4.58 ppm, which corresponds to the benzylic  $\text{CH}_2$ -group next to the chlorine, is a clear indicator of a quantitative reaction. In turn, a new signal **g'** at 4.33 ppm appears and corresponds to the same  $\text{CH}_2$ -group but neighbored by the  $\text{N}_3$ -group. Vinylic proton signals remain unaffected as is to be expected and integral values fit very well overall. However, the structure of the aromatic signals changed and is overlapping the residual chloroform peak in the spectrum of **4**, which causes a deviation in the integral value. The change in structure is merely a change in coupling constants between the aromatic protons, signalling that despite the methylene unit in between, the  $\text{N}_3$  group has some influence on the aromatic character of the molecule.

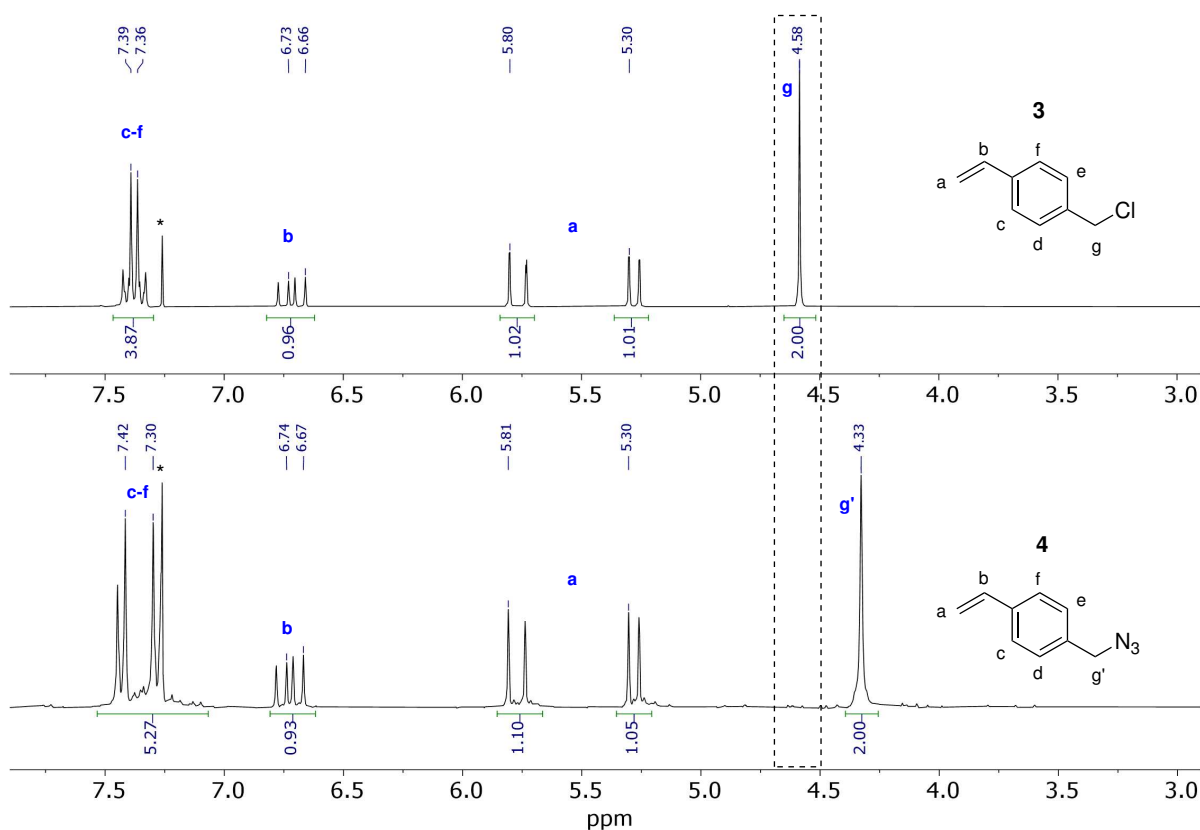
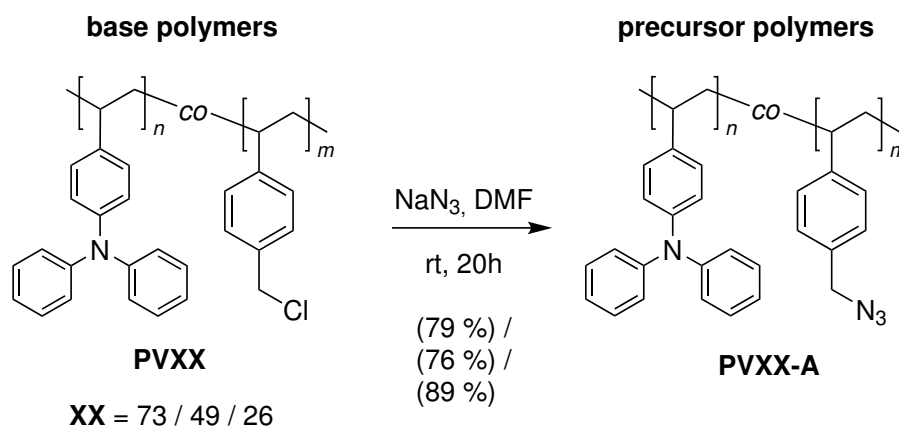


**Figure 3.5:**  $^1\text{H-NMR}$  ( $\text{CDCl}_3$ ) spectra of compounds **3** and **4**. Substitution of chlorine with azide is clearly indicated by the shift of signal **g** from 4.33 ppm to **g'** at 4.58 ppm

Since the reaction proceeded reliably without traces of unreacted starting material it

was possible to move on to the polymer analogous azide exchange reaction. Here, a similar change in the chemical shift of the benzylic protons can be observed, although the precise ppm values deviate from the monomeric model reaction. Figure 3.6 shows this exemplarily for the case of **PV49** and **PV49-A**, where the signal in question shifted from originally 4.40 ppm to 4.12 ppm. Here as well, no remains of the original benzylic protons can be found. Complete substitution of chlorine by azide can thus be assumed. NMR spectra of all three polymers converted this way can be found in Figure 3.7 (top) in comparison with the chlorine derivatives (bottom). These spectra have been used to calculate co-monomer ratios in the polymers which shall be demonstrated briefly on the example of **PV73-A**. The corresponding integral values for this polymer are depicted additionally. Respective numbers of the other polymers can be found in the appendix of this work.



**Scheme 3.4:** Polymer analogous conversion of chlorine bearing base copolymers into their azide analogues.

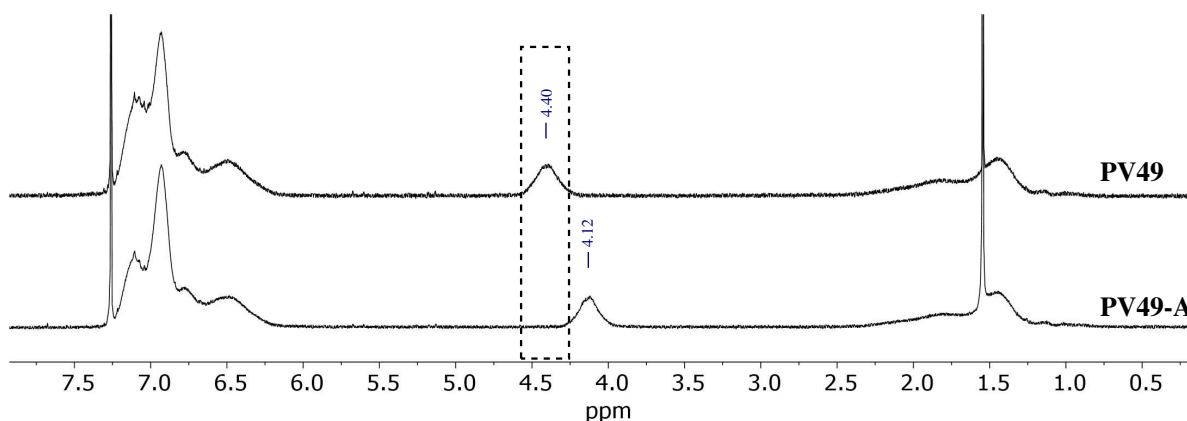


**Figure 3.6:** <sup>1</sup>H-NMR spectra of **PV49** and **PV49-A**. Change in the chemical shift of the benzylic protons after Cl/N<sub>3</sub>-exchange is apparent.

Using the integral ratios of benzylic signals  $H_{benz}$  to the aromatic regions  $H_{arom}$ , the amount of  $H_{ar,vtpa}$  relative to  $H_{ar,ams}$  can be calculated. Here and in future descriptions, AMS stands for 4-(Azidomethyl)styrene (in analogy to CMS), the converted styrene derivatives in the polymer. Having the integral of  $H_{benz}$  set to 2, representing one full unit of AMS,  $H_{arom}$  has a total integral of 9.17 in the case of **PV73-A**, out of which 4 correspond to the 1 eq of AMS groups in the polymer.

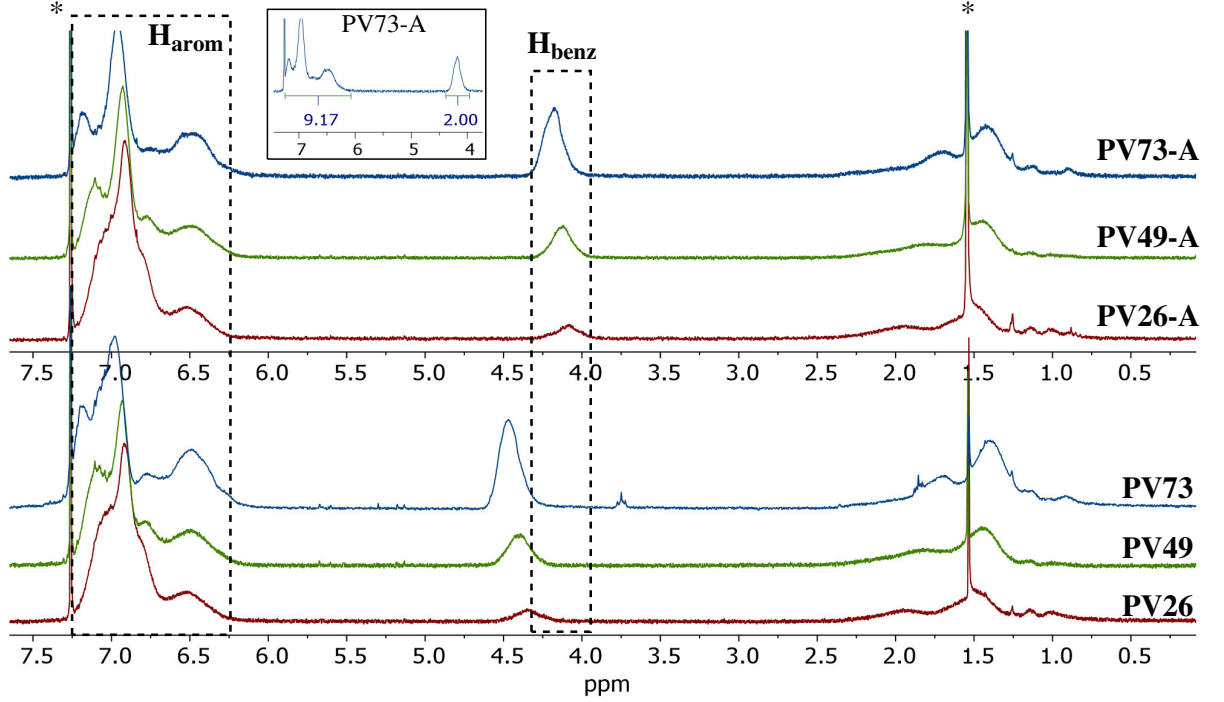


**Figure 3.7:**  $^1\text{H}$ -NMR spectra of azide-copolymers with various  $\text{N}_3$ -contents (top) and their respective precursors (bottom).

$$1 \text{ eq AMS} \hat{=} 4 H_{arom} \quad 1 \text{ eq VTPA} \hat{=} 14 H_{arom} \quad (3.1)$$

$$(9.17 - 4) H_{arom} = 5.17 H_{ar,vtpa} \hat{=} 0.37 \text{ eq VTPA} \quad (3.2)$$

$$\frac{0.37 \text{ eq VTPA}}{(0.37 \text{ eq VTPA} + 1 \text{ eq AMS})} \approx 0.27 \quad (3.3)$$

Thus, the aromatic region includes 0.37 eq of VTPA when AMS integrals are normalized to 1 eq. This corresponds to 27% of the polymer and in turn a content of 73% AMS. It is to be noted that the exact co-monomer ratio derived from these calculations can vary within 1%, depending on the exact positioning of the integral boundaries and complicated by the slightly overlapping solvent peak, which is inherent of the deuterated solvent. In

any case, the numbers obtained for all polymers show a good correlation of monomer feed ratio to the resulting co-monomer ratio, as has already been the case for their chlorine analogues.

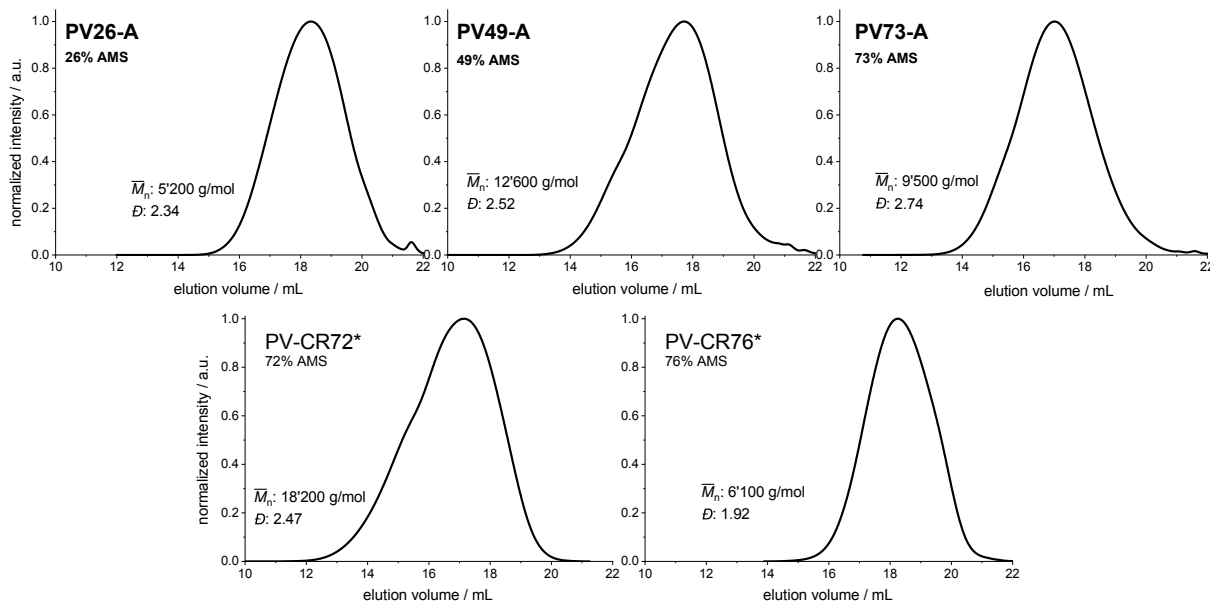


**Figure 3.8:** Normalized SEC chromatograms of copolymers **PV26-A**, **PV49-A** and **PV73-A**. \*polymers converted from early smaller batches which were provided by *Corinne Rost-Schmidt*. Eluent: THF.

SEC chromatograms of the converted polymers are shown in Figure 3.8. Polymers PV-CR72 and PV-CR76 displayed here are early batches of the same copolymer system synthesized by *Corinne Rost-Schmidt* (C.R.) prior to this work, which were then converted to their azide analogues in the same manner. Those were used for early experiments in this work before being replaced by the **PVXX-A** main polymer batches. Their molecular weight details are given in Table 3.2.

Looking at the chromatograms of the converted main polymers, both, the measured number average molecular weight and the polymer dispersity increased noticeably in all polymers, except for the  $\bar{M}_n$  of **PV26-A** which actually decreased in value. With the margins being too big to be entirely accounted for by variations between measurements, one assumption to be made is that the simple exchange of chlorine atoms by azide groups causes the polymer to take up a different conformation. Also, azide groups likely interact differently with the eluent THF, leading to a change in the hydrodynamic volume of the polymer chains and in turn different interactions with the mobile phase of the SEC. This would lead to changes in retention times and as such to changes in calculated values. **PV73-A**, again, is a special case, as it was subjected to Soxhlet extraction with cyclohexane after the conversion reaction, in order to remove or reduce the low-molecular

signals. This worked reasonably well and can explain the strong increase in the average molecular weight for this polymer. Another minor curiosity is the appearance of a slight high-molecular weight shoulder in **PV49-A**. It seems as if small amounts of longer polymer chains potentially remained in the DMF phase during liquid-liquid-extraction and thus got removed from the remaining polymer in the process. Of course it is non-intuitive that only a specific part of the longer chains should disappear like this. However, all of this shouldn't influence the width of molecular weight distributions, let alone increase the dispersity values  $\bar{D}$ . Accordingly, a change in polymer conformation as discussed is the most likely explanation for the observed changes and shapes of the chromatograms and obtained values still represent good quality polymers that are well suitable for their intended purpose. Key values of all polymers are given in Table 3.1.

**Table 3.1:** Molecular weight distribution characteristics of VTPA-based copolymers as obtained from SEC.

	PV26	PV49	PV73	PV26-A	PV49-A	PV73-A
$\bar{M}_n / \text{g mol}^{-1}$	6900	11500	6000	5200	12600	9500
$\bar{D}$	2.01	2.15	2.41	2.34	2.52	2.74

**Table 3.2:** SEC data of early small batches of azide-bearing copolymers analogous to PVXX-A polymers. Detector: UV-VIS.

	PV-CR72	PV-CR76
$\bar{M}_n / \text{g mol}^{-1}$	18000	6100
$\bar{D}$	2.47	1.92

Further characterization was performed on the obtained polymer powders by use of attenuated total reflectance (ATR) infrared spectroscopy. Transmission spectra are given in Figure 3.9. The azide bands at  $2093 \text{ cm}^{-1}$  stand out with their strong and sharp character. Backbone and aromatic bands can be seen as well in the region of  $2850 \text{ cm}^{-1}$  to  $3050 \text{ cm}^{-1}$ , albeit with lower (typical) intensity in comparison. The signal at  $2923 \text{ cm}^{-1}$  in **PV73-A**, corresponding to C–H-stretching in  $\text{CH}_2$ -groups, has a higher intensity compared to the other spectra in relation to the other signals which might be due to minor amounts of residual solvent. Traces of isopropanol, used to clean the instrument in between measurements, can still be found at around  $1440 \text{ cm}^{-1}$  so it is likely that increased aliphatic band intensity in the upper wavenumber region originates here. The band at  $1589 \text{ cm}^{-1}$  has been used as an optical reference point due to its intermediate intensity, allowing weaker and stronger signals in all spectra to still fit into the plot well. Together with the other two bands around  $1500 \text{ cm}^{-1}$  it likely corresponds to aromatic C=C bond stretching.

In agreement to that, azide band intensity at  $2093\text{ cm}^{-1}$  relatively increases with greater AMS share. Since with higher AMS content the number of benzene rings in the polymer decreases this observation fits the band assignment. Also with regards to other signals this change in signal intensity nicely depicts the different shares of AMS groups in the polymers. But because the  $\text{CH}_2$  bands around  $3000\text{ cm}^{-1}$  are possibly altered by residual solvent as was just mentioned,  $\text{C}=\text{C}$  bond stretching at  $1589\text{ cm}^{-1}$  is used for reference. Care must be taken to not over-interpret band intensities, as different characteristic groups and features of a compound produce bands of different intensity and quality in general so that no direct statements about absolute amounts can be made from the comparison of two different signals. But comparisons can be drawn between the same two bands across different compounds. In this case we can look at the reference band and compare its intensity with the azide bands. Fittingly, for **PV49-A** both bands have the virtually identical intensity, although this is merely a coincident. In accordance with co-monomer ratios these relative intensities change by the same amount of about 17% in opposite directions when looking at **PV26-A** or **PV73-A**.

At lower wave numbers, below  $1400\text{ cm}^{-1}$ , band assignment is non-trivial due to partially overlapping general band regions but one major signal might belong to  $\text{C}-\text{N}$  bond stretching which can be found in the polymer in multiple places.

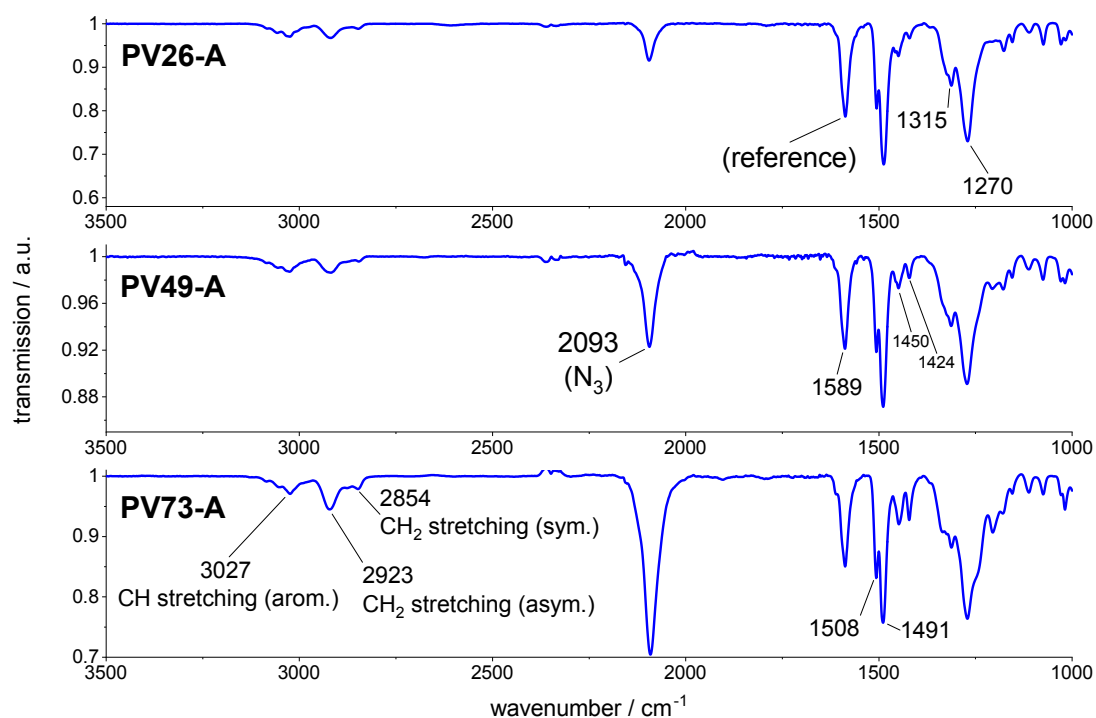


**Figure 3.9:** Infrared spectroscopy spectra measured in attenuated total reflectance (ATR). The signal named "reference" has been adjusted to the same intermediate size in all spectra to provide a fix point for visual comparison.

Thermogravimetric analysis (TGA) of the polymers gave two degradation steps in all cases, from which onset temperatures have been determined. Furthermore, polymers have been characterized with differential scanning calorimetry (DSC) from which glass transition temperatures were determined, if found. TGA and DSC spectra are given in Figure 3.10.

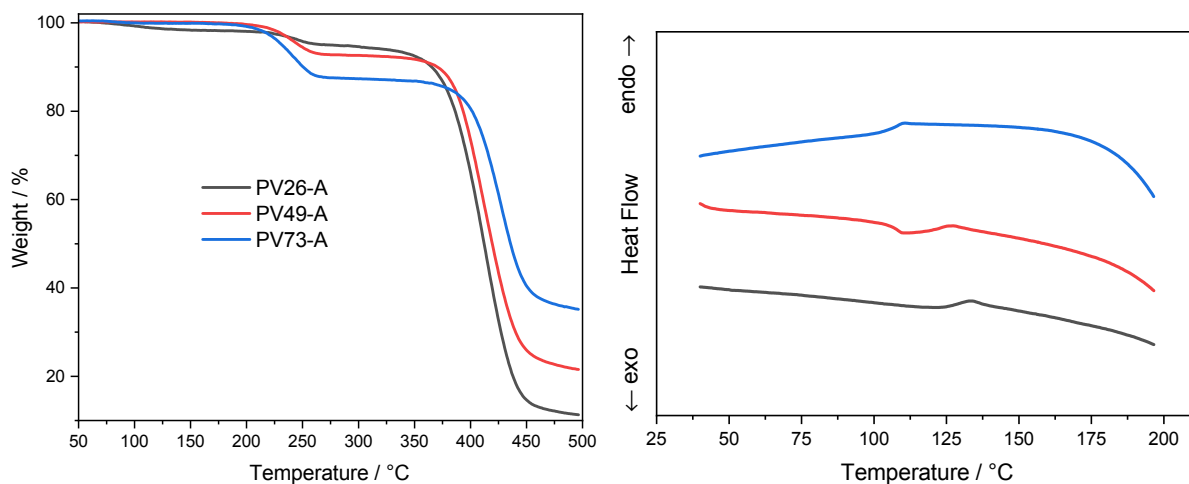


**Figure 3.10:** TGA (left) and DSC (right) spectra of **PVXX-A** copolymers. TGA: 30 °C to 500 °C at 5 °C/min. DSC: 2nd heat curve at 10 °C/min, sorted by name.

In TGA, a first step can be seen around 220 °C in all spectra. This was attributed to azide groups decomposing, due to the step size increasing with azide content in the polymer. This assignment fits close to the range found in literature, as well.<sup>[135]</sup> Exact determination of step sizes is difficult because of slanted baselines but they roughly fit with calculated weight shares of N<sub>3</sub> units in the corresponding polymers. Thermal stability of polymers increased with increasing azidomethylstyrene content with the second steps in a close range of 380 °C to 400 °C and **PV73-A** as the most stable polymer. This second step likely corresponds to backbone decomposition. Apart from the azide groups, no side-chain decomposition (TPA) separate from the backbone could be observed.

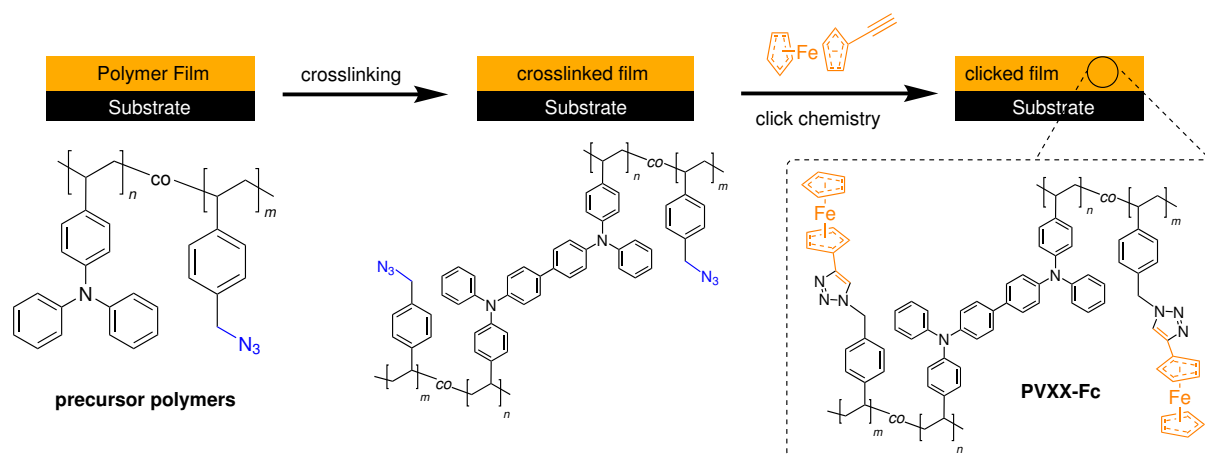
**Table 3.3:** Onset temperatures found in corresponding TGA spectra.  $T_g$  taken from DSC spectra.

Polymer	$T_{Ons,1}$ / °C	$T_{Ons,2}$ / °C	$T_g$ / °C
PV26-A	223	380	128
PV49-A	218	385	110
PV73-A	213	400	107

In DSC, one endothermic step was found in each polymer, corresponding to glass

transition temperatures. Figure 3.10 gives the second heating cycles at 10 °C/min. With increasing AMS content  $T_g$  approaches that of polystyrene (about 107 °C in practice<sup>[136]</sup>). Higher VTPA content resulted in a higher  $T_g$  with **PV26-A** giving a value of 128 °C.

## 3.2 Thin Film Characterisation of Ferrocene-Functionalized Copolymers



**Scheme 3.5:** Schematic representation of *click*-functionalizations of VTPA-based precursor polymers with ethynyl ferrocene probe molecules.

The next experiments involved characterization and functionalization of the polymers in thin films, for which they were prepared on gold-coated or ITO-coated glass substrates. ITO substrates were used in early experiments and for optical measurements due to their transparency. In all other cases gold was used. The gold coating consisted of a 50 nm gold layer on top of a 5 nm chromium adhesive layer. Spin-coating was done from 5 g L<sup>-1</sup> solutions in chloroform or toluene, which afforded films with a thickness of (30.0 ± 1.5) nm and (18.6 ± 0.7) nm, respectively, as determined by AFM. The coated films were first crosslinked electrochemically as part of cyclic voltammetric measurements before being subjected to CuAAC with ethynyl ferrocene (E-Fc) *via* in the next step. Using E-Fc as the reaction partner was done to introduce a functional group into the polymer with its own defined redox potential which can act as a probe molecule in electrochemistry and a new functional group capable of storing electronic charge in principal. This allows for additional possibilities of making assessments about the efficiency of the chosen *clicking* method. This is possible because the ferrocene group shows a distinct half-wave potential and as such offers a clear indicator of a successful reaction in the film. Crosslinking on the other hand was intentionally performed beforehand to strengthen the film's resilience

towards solvents, as they have to withstand being immersed in DMSO for 3 days during CC. Simultaneously, this crosslinking process provides a first cyclic voltammogram characterisation of the samples before being further functionalized and so can be used to track any changes in electrochemical behaviour of the samples caused by the *clicking* reaction.

### 3.2.1 Electrochemical Crosslinking of Polymer Films

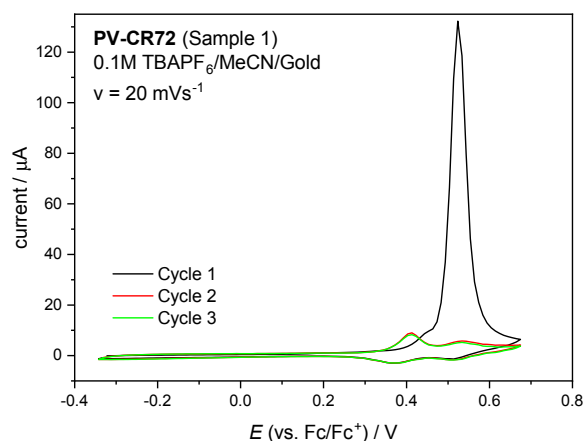


**Figure 3.11:** Cyclic voltammogram of **PV-CR72** sample on gold being crosslinked. The large characteristic peak in current corresponding to the crosslinking process can be seen in the first cycle.

Figure 3.11 shows the cyclic voltammograms of two films prepared from a small early batch of copolymer analogously to PV73-A. This early batch was synthesized by *Corinne Rost-Schmidt*, containing 72% CMS. Azide groups were introduced as described above. To avoid confusion with PV73-A, this earlier batch will be called **PV-CR72**, with  $\bar{M}_n$  of  $18\,000\text{ g mol}^{-1}$  and  $D$  of 2.47. The first cycle of each voltammogram shows a big peak in the current of the first forward cycle which then proves to be irreversible in the backward cycle. This current corresponds to TPA groups in the polymer being electrochemically crosslinked with each other, creating Tetraphenylbenzidine (TPB) units in the process. It is a literature-known process<sup>[3]</sup> but shall be explained briefly.

Figure 3.12 (top) shows a separated view of a first and second cycle of this crosslinking process, measured on a different sample which was prepared analogously. The first, irreversible oxidation is marked red and occurs at a peak potential of 0.52 V, when referenced against ferrocene. Figure 3.12 (bottom) elaborates the mechanism behind it, as it includes three distinct steps. The first is a single oxidation step creating a radical cation in the TPA units. This radical cation then equilibrates into a more stable state, by delocalizing across the aromatic system. Both steps are technically still reversible, but a

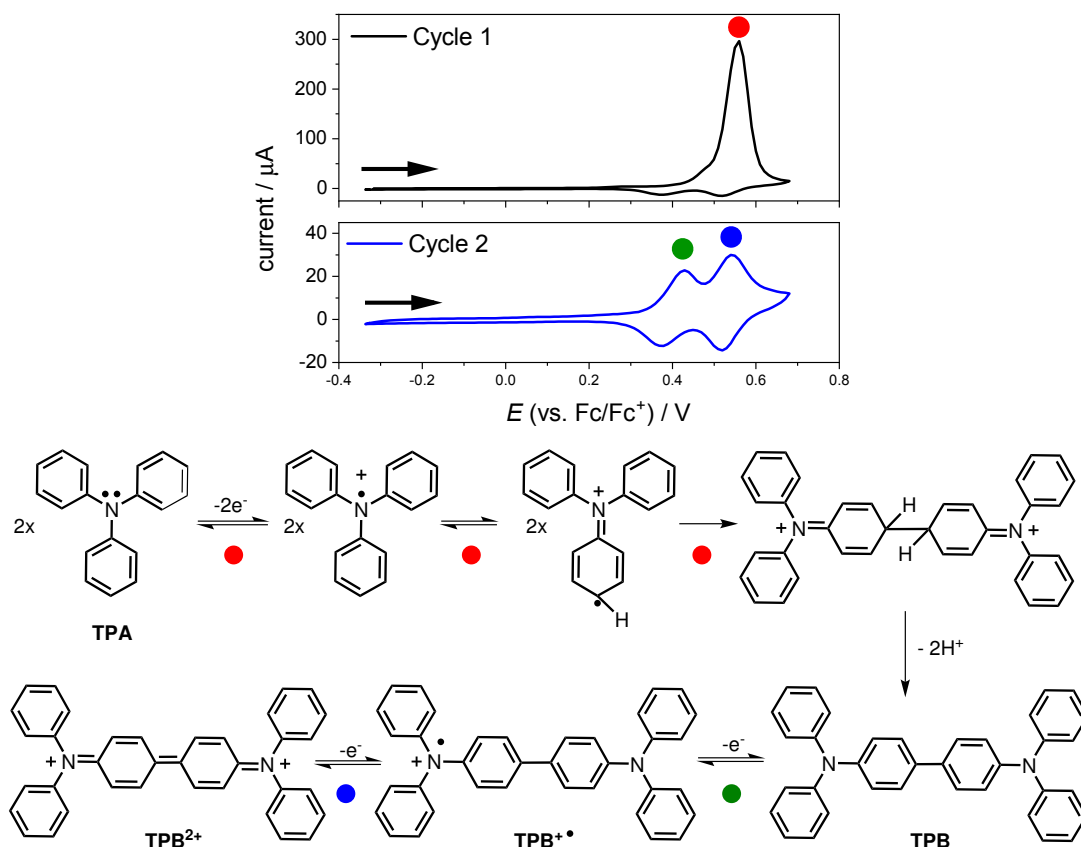


**Figure 3.12:** Representation of the crosslinking process in TPA-bearing polymer films (here: on gold) and their respective peaks found in a CV. First two oxidation steps are reversible but quickly lead to recombination of two radicals into a dication, which renders the whole "red" process irreversible. The green and blue step on the other hand remain reversible, as can be seen from the second CV cycle shown.

recombination of two of these "stabilized" radicals happens quickly which renders the red process irreversible as a whole. Deprotonation occurs to re-establish the aromatic system and TPB is formed, which at the given potential is quickly oxidized itself to form  $\text{TPB}^{2+}$  as is depicted by the green and blue dots and can be seen in the second cycle as well. Hereby, again, first a radical cation is formed which can then be further oxidized into a dication, with both processes being fully reversible and, accordingly, the backward cycle during CV leading back to neutral TPB units. As the corresponding half-wave potentials are overlapping, with green at  $E_{1/2} \approx 0.39 \text{ V}$  and blue at  $E_{1/2} \approx 0.53 \text{ V}$ , all three processes (red, green, blue) actually occur in the first forward cycle already, as can be seen from the first backward cycle where reduction peaks of green and blue can be found.

From **PV-CR76**, more samples on ITO-coated glass slides were prepared for measurements with *in-situ* spectroelectrochemistry, during which the materials' absorption is

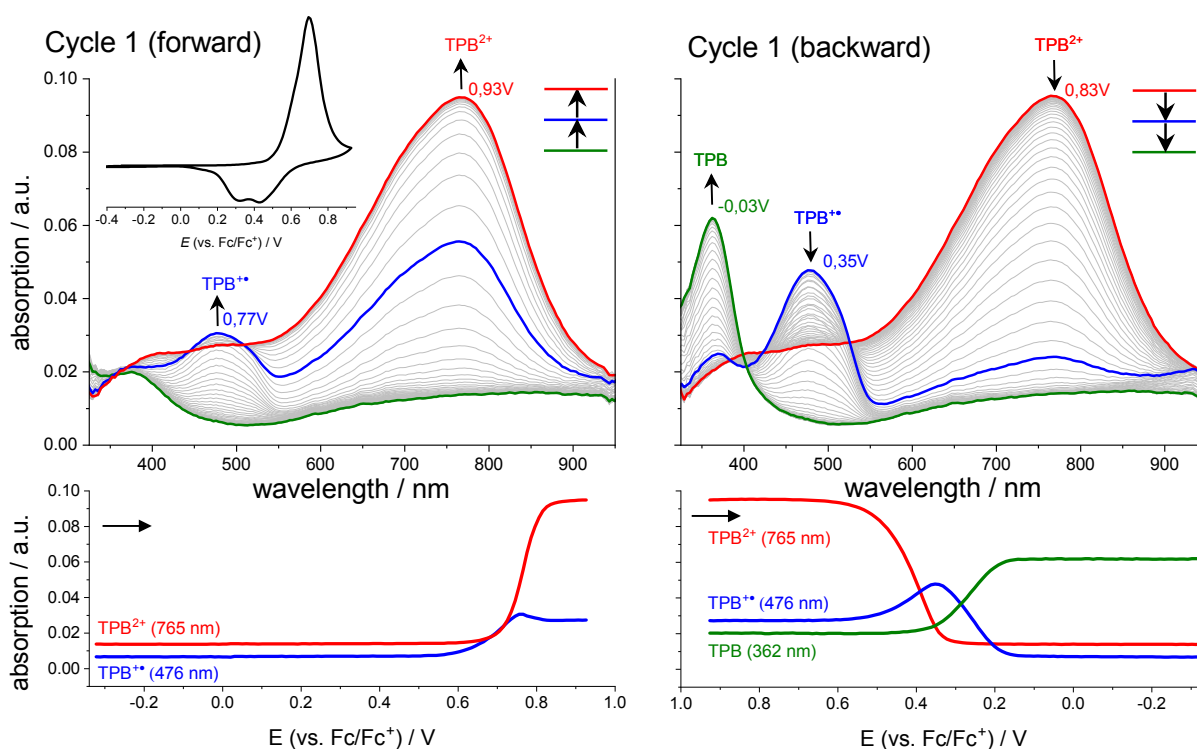


**Figure 3.13:** *In-situ* spectroelectrochemical characterisation of **PV-CR76** on ITO electrode with corresponding CV cycle as insert, measured at  $20 \text{ mV s}^{-1}$  in  $0.1 \text{ M NBu}_4\text{PF}_6$  in MeCN.

recorded for every step in potential during cyclic voltammetry. Increase and decrease in absorption bands corresponding to the different electronic states of the polymer can be tracked here and are shown in Figure 3.13 alongside the corresponding cyclic voltammogram. Top spectra depict UV absorption of the first forward and backward half-cycle, respectively, where one spectrum was recorded at each potential step of the CV. Bottom spectra show the evolution of absorption at selected wavelengths with applied potential. The general process of what is happening in this measurement is the same as depicted in Figure 3.14 on page 48.

In the forward scan, UV absorption develops from the green spectrum to blue and then red with increasing potential applied. In agreement with TPA crosslinking mechanics and wavelength assignments in our earlier work<sup>[80,81]</sup> formation of the TPB radical cation starts first and is soon overlapped by further oxidation into TPB dication. At higher potentials absorption of  $\text{TPB}^{\bullet+}$  decreases again while  $\text{TPB}^{2+}$  absorption sees a continuous sharp increase, pointing towards all available TPA pairs being crosslinked, so that supply of radical cations dwindles. Ultimately, both bands reach a plateau before the end of the forward scan.

On the backward cycle, evolution moves from red to blue and then green, opposite to the forward cycle. With decreasing amount of  $\text{TPB}^{2+}$  units the number of  $\text{TPB}^{\bullet+}$  groups increases. At around 0.4 V a new absorption band starts to evolve at 362 nm belonging to neutral TPB which wasn't present yet in the forward cycle before crosslinking. Reduction of  $\text{TPB}^{2+}$  groups is completed at  $\sim 0.30$  V, shortly after  $\text{TPB}^{\bullet+}$  concentration reached its maximum at 0.35 V. With  $\text{TPB}^{2+}$  supply depleting,  $\text{TPB}^{\bullet+}$  absorption intensity then also decreases while absorption of the fully neutralized TPB units keeps increasing up until around 0.15 V where a plateau is reached. Intensities of the  $\text{TPB}^{\bullet+}$  and  $\text{TPB}^{2+}$  bands before the forward and after the backwards cycle are identical, indicating the reversibility of the oxidation process.

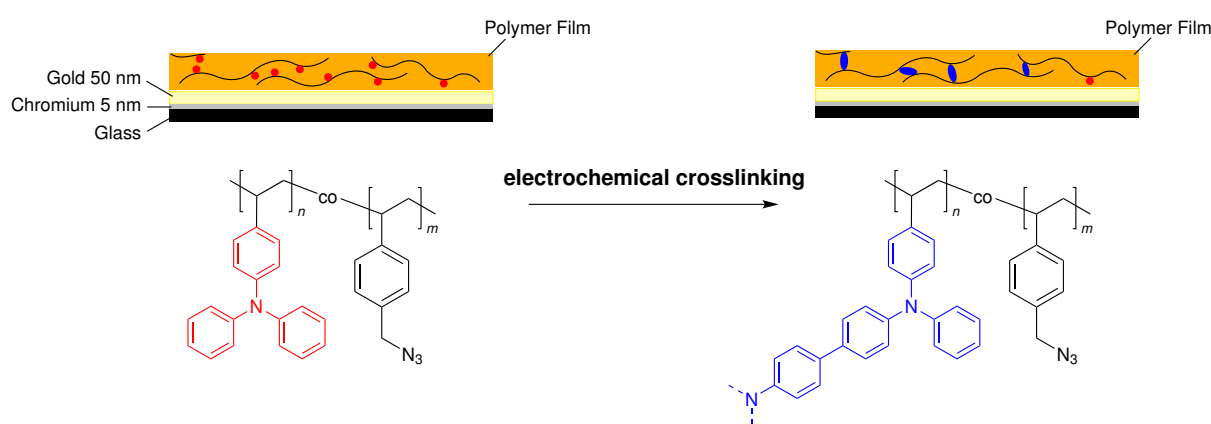


**Figure 3.14:** Schematic depiction of samples produced for electrochemical crosslinking and characterisation and visualization of the crosslinking step.

Later, samples of new and bigger polymer batches **PV26-A**, **PV49-A** and **PV73-A** have been prepared for further characterisation and subsequent conversions. Again, electrodes with 50 nm gold coatings were used with 5 nm chromium adhesive layers between gold and the underlying glass substrates. Thin films were created by spin-coating from 5 M solutions in toluene, affording film thicknesses of  $(18.6 \pm 0.7)$  nm as determined by atomic force microscopy before.

Figure 3.14 schematically shows the make-up of the prepared samples as well as the change in polymer structure due to the crosslinking process. TPA groups are depicted as red circles and TPB units linking the polymer chains as blue shapes. It is worth considering that not all TPA units within the polymer chains can undergo the crosslinking process in films because of the statistical nature of the copolymers. This means that not all TPA groups will be guaranteed to have a second TPA unit nearby to form TPB with and will remain within the "red phase" of the electrochemical process (see Figure 3.12). This situation is visualized in Figure 3.14 as well by the remaining red circle after crosslinking.

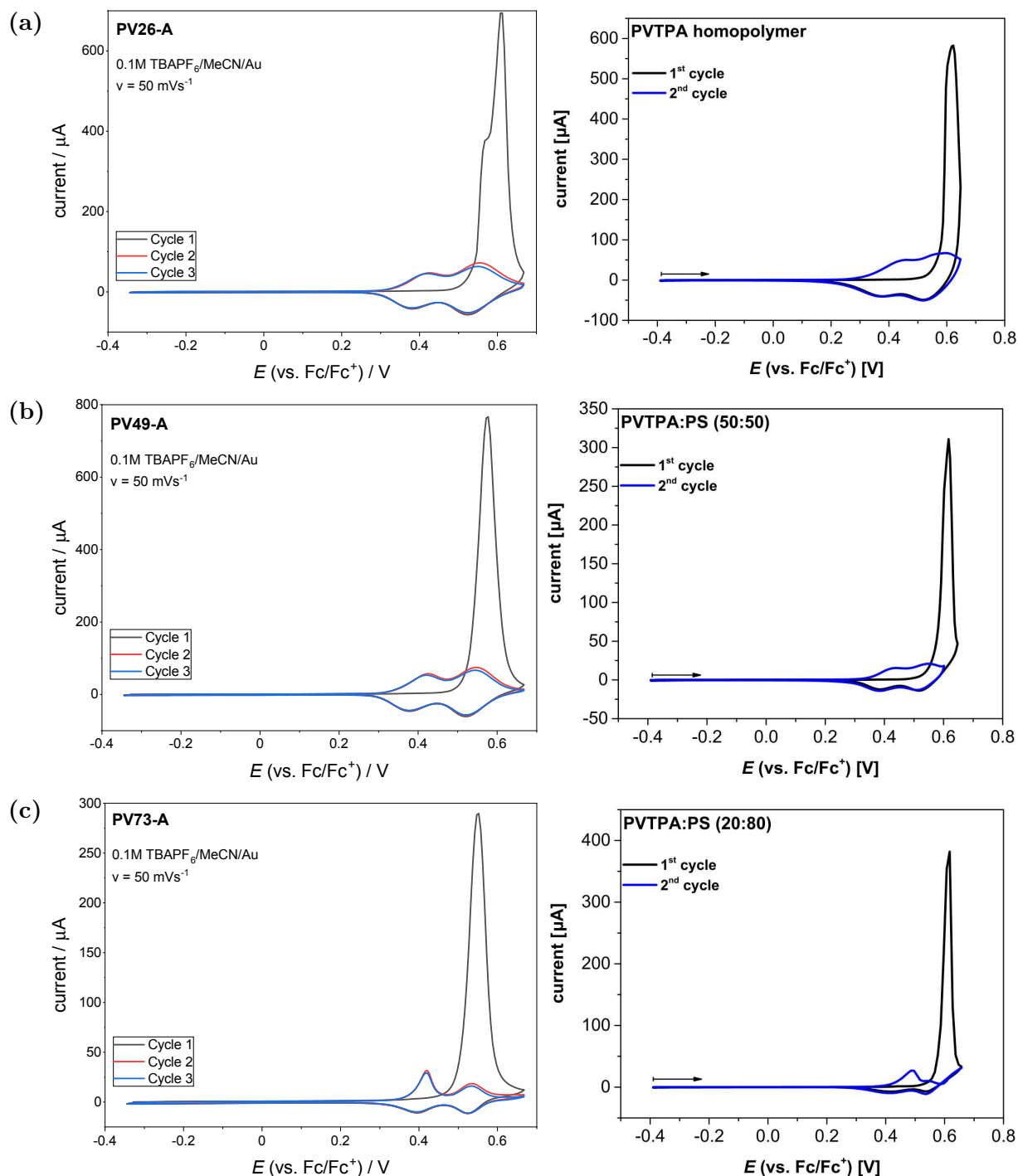
**Table 3.4:** Redox potentials of VTPA-based copolymers as determined by cyclic voltammetry. *Italic* polymers are taken from PhD thesis of *Kirsten Bruchlos*.<sup>[137]</sup>

Polymer	Redox Process	Parameter	Potential (vs Fc/Fc <sup>+</sup> ) / V
PV26-A	TPA $\longrightarrow$ TPA <sup>•+</sup>	E <sub>Peak</sub>	0.61
	TPB $\rightleftharpoons$ TPB <sup>•+</sup>	E <sub>1/2</sub>	0.40 - 0.41
	TPB <sup>•+</sup> $\rightleftharpoons$ TPB <sup>2+</sup>	E <sub>1/2</sub>	0.53
		E <sub>Peak</sub>	0.55
PV49-A	TPA $\longrightarrow$ TPA <sup>•+</sup>	E <sub>Peak</sub>	0.57
	TPB $\rightleftharpoons$ TPB <sup>•+</sup>	E <sub>1/2</sub>	0.40 - 0.41
	TPB <sup>•+</sup> $\rightleftharpoons$ TPB <sup>2+</sup>	E <sub>1/2</sub>	0.53
		E <sub>Peak</sub>	0.55
PV73-A	TPA $\longrightarrow$ TPA <sup>•+</sup>	E <sub>Peak</sub>	0.55
	TPB $\rightleftharpoons$ TPB <sup>•+</sup>	E <sub>1/2</sub>	0.40 - 0.41
	TPB <sup>•+</sup> $\rightleftharpoons$ TPB <sup>2+</sup>	E <sub>1/2</sub>	0.53
		E <sub>Peak</sub>	0.53
<i>PVTPA</i>	TPA $\longrightarrow$ TPA <sup>•+</sup>	E <sub>Peak</sub>	0.62
	TPB $\rightleftharpoons$ TPB <sup>•+</sup>	E <sub>1/2</sub>	0.41
	TPB <sup>•+</sup> $\rightleftharpoons$ TPB <sup>2+</sup>	E <sub>1/2</sub>	0.55
<i>PVTPA:PS (50:50)</i>	TPA $\longrightarrow$ TPA <sup>•+</sup>	E <sub>Peak</sub>	0.62
	TPB $\rightleftharpoons$ TPB <sup>•+</sup>	E <sub>1/2</sub>	0.41
	TPB <sup>•+</sup> $\rightleftharpoons$ TPB <sup>2+</sup>	E <sub>1/2</sub>	0.54
<i>PVTPA:PS (20:80)</i>	TPA $\longrightarrow$ TPA <sup>•+</sup>	E <sub>Peak</sub>	0.62
	TPB $\rightleftharpoons$ TPB <sup>•+</sup>	E <sub>1/2</sub>	0.45
	TPB <sup>•+</sup> $\rightleftharpoons$ TPB <sup>2+</sup>	E <sub>1/2</sub>	0.54

Cyclic voltammograms of the prepared copolymer samples are given in Figure 3.15. Voltammograms from the PhD thesis of *Kirsten Bruchlos*<sup>[137]</sup> have been included as a comparison, which were measured on statistical PVTPA:Polystyrene copolymer films on gold electrodes, albeit on a lower scan rate of 20 mV s<sup>-1</sup>. Similarities in the CVs are apparent and confirm that the introduction of azide groups into the polymers does not have any major influence on its electrochemical behaviour. TPB half-wave potentials of the PVTPA:PS copolymers are given as 0.41 V to 0.42 V and 0.54 V to 0.55 V for the radical cation and the dication, respectively. In the PVXX-A copolymers used here, similar values are obtained with 0.40 V to 0.41 V and 0.53 V, respectively. Interestingly, in the case of the 80 % PS copolymer a notable shift in half-wave potential of the radical cation to 0.45 V was observed while in **PV73-A** no such change is visible and the potentials remain practically identical to the other two **PVXX-A** polymers. On the other hand, peak potentials of the anodic crosslinking peak were given as 0.62 V for all three PVTPA:PS copolymers

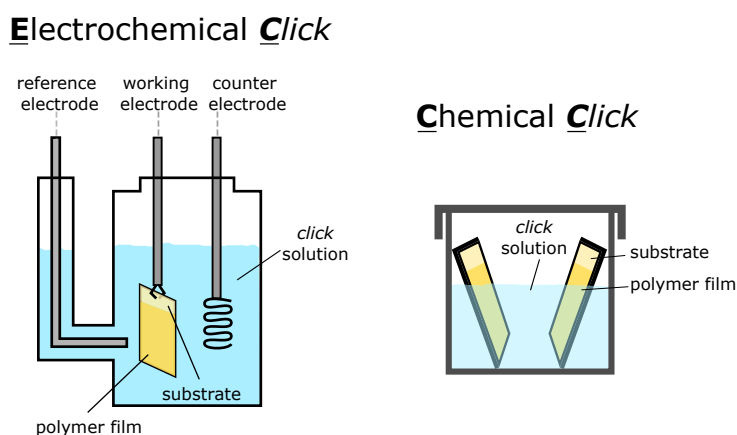
included here while they show slight variation from 0.61 V in **PV26-A** down to 0.57 V in **PV49-A** and 0.55 V in **PV73-A**.

For both polymer systems, those with lowest amounts of TPB units show a higher intensity of the  $\text{TPB}^{\bullet+}$  oxidation peak in relation to that of  $\text{TPB}^{2+}$ . For the PVTPA:PS systems this behaviour is described as superimposing of one anodic wave over the other, attributed to hindered ion diffusion and is quite apparent when looking at the subsequent voltammograms in that work.<sup>[137]</sup> Here, this circumstance is not as clearly visible also due to the fact that no copolymer with even lower TPA content was prepared which could pronounce this effect more. Looking at the peak potential of the anodic half-waves, though, reveals a slight shift of the  $\text{TPB}^{2+}$  peak from 0.55 V in **PV26-A** and **PV49-A** to 0.53 V in **PV73-A**, suggesting the start of the aforementioned superimposition.



**Figure 3.15:** Cyclic voltammograms of electrochemical crosslinking of thin copolymer films on gold electrodes. Crosslinking peak can be seen in each first cycle.  $\text{TPB}^{\bullet+}$  and  $\text{TPB}^{2+}$  oxidation and reduction peaks are then present in every consecutive cycle. **Left** This work. **Right** Comparable CVs taken from the PhD thesis of *Kirsten Bruchlos*<sup>[137]</sup>, measured at  $20 \text{ mV s}^{-1}$ .

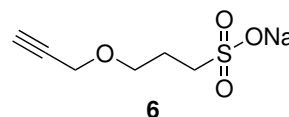
### 3.2.2 Introduction of Ferrocene Units in Thin Films *via* Click Chemistry



**Figure 3.16:** Experimental setups for electro-click and chemical click procedures.

Both, "Electroclick" (EC) and "Chemical Click" (CC) seemed suitable for functionalization inside of these polymer films (see chapter 2). As mentioned in an earlier chapter, *Jonglack Kim* investigated the EC method on PEDOT-N<sub>3</sub> films, based on conditions found in literature.<sup>[121,129,130]</sup> In his results, potentiostatic treatment for 30 min at  $-0.5$  V (vs. Ag/AgCl) inside an electrochemical cell, using the same 3-electrode setup used for cyclic voltammetry (see Figure 3.16) gave good results in electrolyte-free DMF solutions of the employed alkyne. Hereby, CuSO<sub>4</sub> is added to the solution and provides Cu(I) ions for CuAAC conversion, which is created *in-situ* at the working electrode due to the applied potential. However, the copolymers used here share no similarities with PEDOT. As such there is no guarantee that those conditions work the same. Accordingly, test reactions were done with alkyne sulfonate **6** (see also chapter 3.3) in thin films on gold and ITO substrates for comparison. Films were prepared from the early batches **PV-CR72** and **PV-CR76**.

Comparisons of infrared spectra of EC and CC experiments are shown in Figure 3.17. Blue spectra are before (top) and after (bottom) *Chemical Click*, orange spectra underwent *Electroclick*. On the left **PV-CR76** films on ITO were converted and analysed with grazing incidence IR spectroscopy. Lower wavenumber regions show artefact signals from the instrument but the azide bands before conversion are clearly visible. In these experiments a second (reference) signal of the film was not yet included but intensities of all unreacted N<sub>3</sub>-bands are very consistent, thus a reasonable comparability was assumed. The grazing incidence setup hit its resolution limits on these



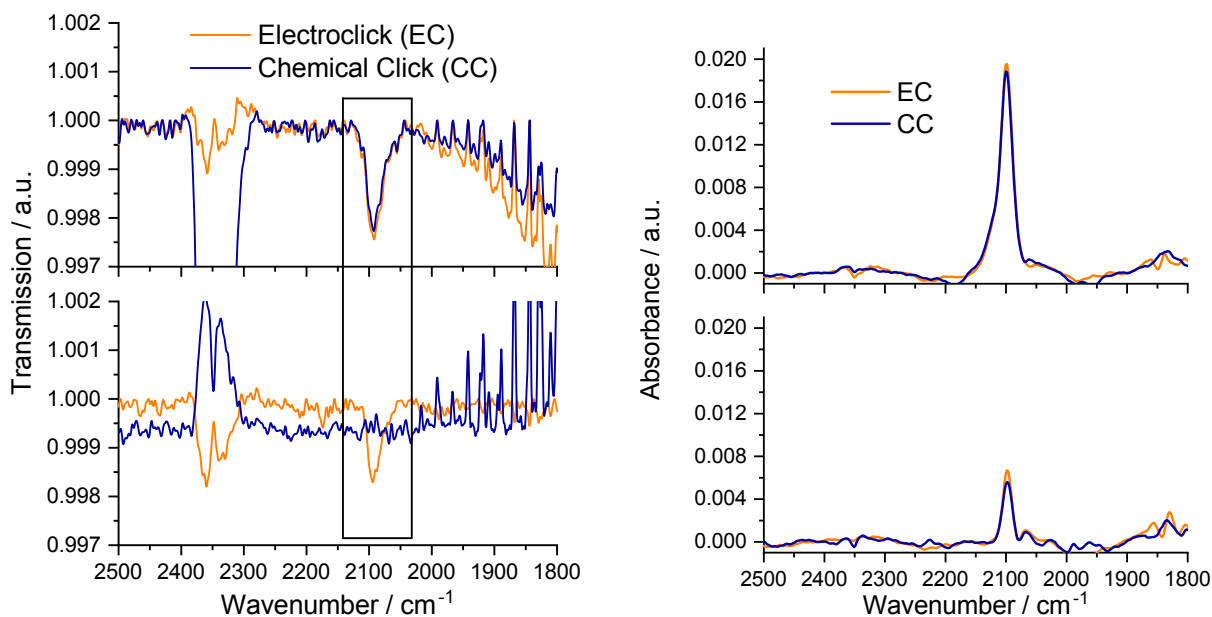


**Figure 3.17:** **Left** Grazing incidence IR spectroscopy of PV-CR76 films on ITO substrates. Top is before *Click* and bottom is afterwards. **Right** PM-IRRAS spectroscopy of PV-CR72 films on gold substrates.

thin films but it is obvious that on these ITO substrates CC performed notably better than EC, with the latter still showing a considerable amount of residual azide.

On the right, the difference isn't as clear. Both methods afforded residual azide bands after film conversion on these gold substrates with a slight edge for CC, as well. With future conversions being intended to be done on interdigitated platinum electrodes, results on gold electrodes could be considered more relevant compared to ITO. However, experiments didn't show a clear winner in terms of conversion. Ultimately, other factors were included to decide between the two techniques. While CC reaction time is longer, conversions seemed to proceed slightly better and simultaneous clicking of multiple samples is straightforward. Furthermore, reaction conditions are essentially the same as for clicking of dissolved compounds with the BC method, providing a better comparability between the two and allowing for evaluation *via* model reactions. Lastly, while performing EC experiments, software issues arose repeatedly, calling in question its reliability under these conditions.

Ultimately, while EC provides advantages of its own it was decided to proceed with CC for conversions of thin films. Accordingly, these conditions were applied to thin film samples of **PV-CR72** and **PV-CR76**. Figure 3.18 illustrates this process inside the polymer film, with the samples being placed in small reaction flasks.

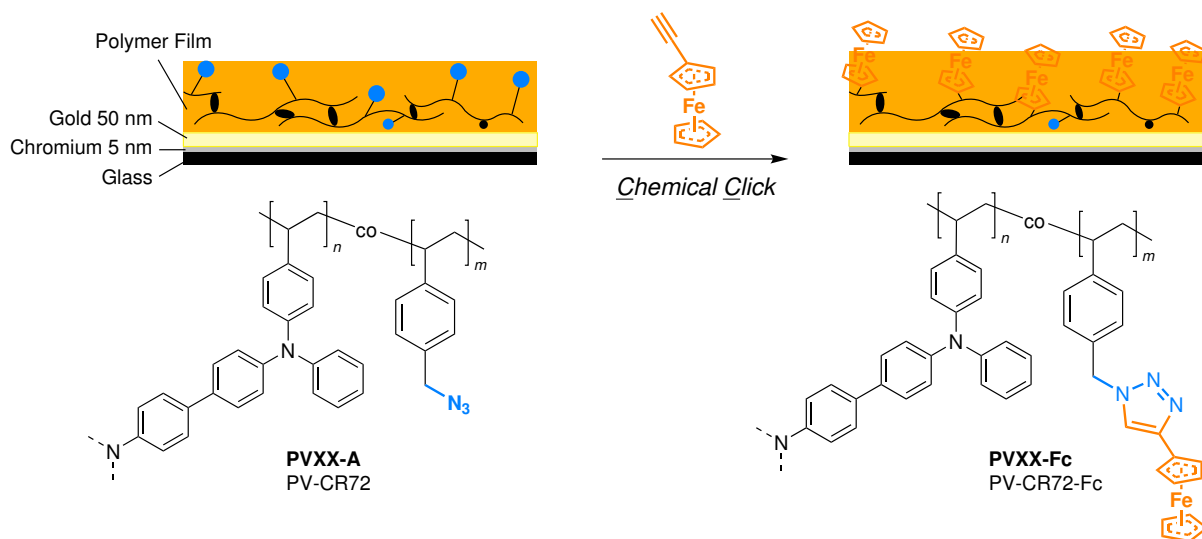


**Figure 3.18:** Schematic depiction of the chemical *click* of E-Fc into thin polymer films.

Infrared spectroscopy was performed on the samples in grazing incidence prior to the reaction as well as afterwards. With azide groups giving a strong and characteristic band in the infrared spectrum at about  $2100\text{ cm}^{-1}$ , conversion can in principle be evaluated on a semi-quantitative level. Unfortunately, due to the thin nature of the produced films, IR bands are not particularly strong with the instrument used at this point, which is using a room-temperature-operated DTGS (deuterated triglycine sulfate) detector. Still, some qualitative statements could be made about the success of the respective reactions. Figure 3.19 (left) shows the corresponding IR spectra. Although weak, azide bands are clearly visible before CC (top), as is a reduction in their intensity following click chemistry. Closer inspection reveals a minor residual signal, but overall CC seems to proceed well, as far as can be told from the obtained spectra.

The sample shown on the right side of Figure 3.19 was measured with a noticeably more sensitive Infrared Reflection Absorption Spectroscopy (IRRAS) system, using a nitrogen-cooled MCT (mercury cadmium telluride) detector. This method shows an almost quantitative conversion in the measured sample, albeit having a small residual azide band, owing to the higher sensitivity of the employed detector. Signals at around  $2900\text{ cm}^{-1}$  were first thought to be bands of the aliphatic backbone but later turned out to be outside impurities measured on the sample holder. An issue, that arose from the comparably small size of the used substrates of  $1 \times 1.5\text{ cm}$  but was resolved for future measurements by optimized positioning in the sample holder.

Consequently, future IR characterisation of thin films was done exclusively using PM-IRRAS. From the main polymer batches **PV26-A**, **PV49-A** and **PV73-A**, films were

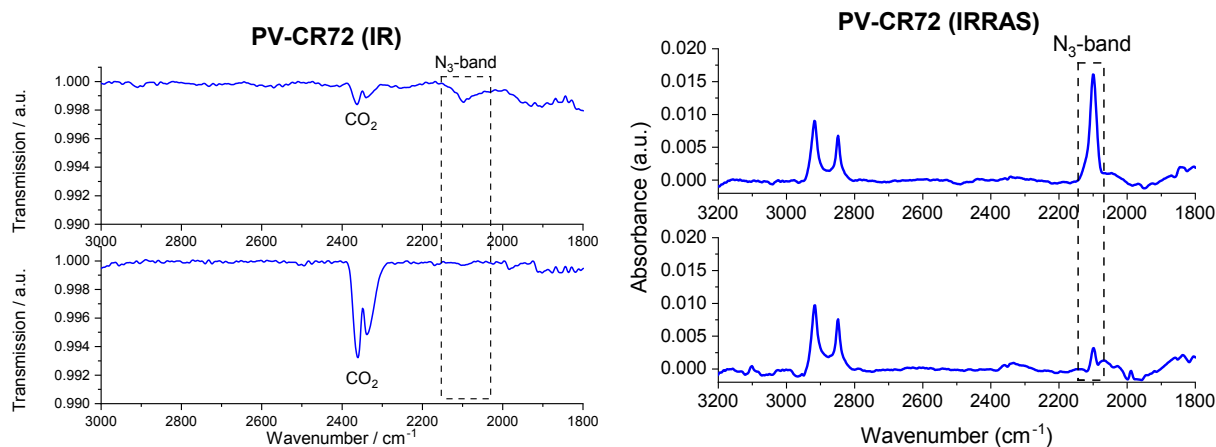


**Figure 3.19:** IR spectra before (top) and after CC (bottom). **Left** Grazing incident IR spectra of first sample, DTGS detector. **Right** PM-IRRAS spectra of second sample, MCT detector.

functionalized with ethynyl ferrocene. Figure 3.20 shows the spectra before and after click chemistry. The suffix "Fc" indicates the functionalization with the ferrocene group. Here again, the relation between bands at  $1589\text{ cm}^{-1}$  and  $2100\text{ cm}^{-1}$  in the "before" spectra correlates nicely with the amounts of AMS in the respective polymers. Comparative measurements after CC cannot show a quantitative conversion in any of the samples but a stark reduction in intensity of the azide band for the two more azide-rich polymers. In difference to that, **PV26-A** only shows a relatively low conversion of what appears to be not more than 50%, although estimations are difficult for this polymer. Analysis of the *clicked* spectrum is further complicated here by an ill-defined baseline and appearance of new and unexpected signals. Most of the spectra show the correct C–H stretching bands in the upper wavenumber region but changes can be seen after *clicking* of **PV26-A**. Both, those wrong  $\text{CH}_2$  bands and the new band at  $1980\text{ cm}^{-1}$  in the spectrum of **PV26-Fc** possibly stem from precipitation onto the polymer films which happened during the CC procedure. Later experiments revealed that this precipitate seems to only occur when clicking ethynyl ferrocene and not when clicking the alkyne sulfonate **6**. Removing these precipitations proved difficult and questions still stand as to what the nature of this precipitate is. However, its influence in spectrum structure has been observed in other experiments as well, most notably in first cycles of cyclic voltammetry. Samples often show visibly less precipitate residue after a few CV cycles. It's reasonable to assume it is a form of iron salt resulting from the oxidative reaction conditions during CC which then goes into solution when being charged by cyclic voltammetry. In most cases, though, it does not pose a problem in characterisation of the produced films as is evident from the presented IRRAS spectra. Even in problematic cases, general statements can still be

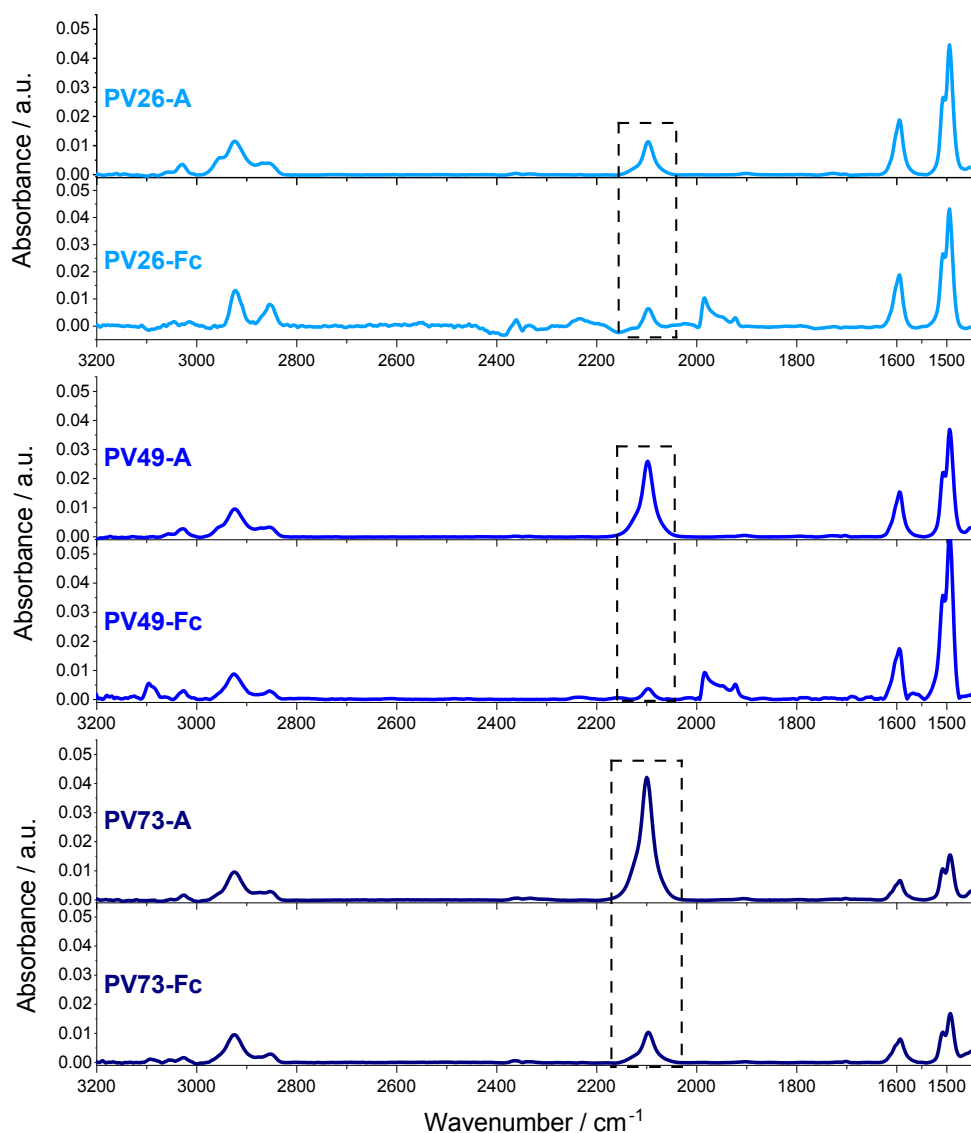


**Figure 3.20:** IRRAS spectra of the prepared polymer films before and after being *clicked* with ethynyl ferrocene *via* the CC procedure. Azide bands are marked with dashed boxes.

made from these spectra, albeit not all bands can be safely assigned.

In terms of conversion, IRRAS measurements suggest more complete reactions when higher amounts of functionalizable units are present in the polymer which in this series means about 50 % or more (**PV49-A**, **PV73-A**). Here the azide band intensity decreased notably, even though some N<sub>3</sub> groups still remain untouched. The reason for this is likely that units on the surface of the polymer films are more easily accessible for the reaction partners. This should become more pronounced with larger *click* partners. Access to azide groups within the polymer film is probably more difficult, especially since the films here were crosslinked before further conversion as has been described in chapter 3.2.1.

Mobility of the polymer chains is thus reduced. As such, the more azide groups exist in the polymer in total, the more are accessible for reaction, possibly explaining why conversion in **PV26-A** is rather low. This explanation also suggests there is an upper limit to how many groups can be reacted, as some might always be situated in the polymer in a way that simply makes them inaccessible during reaction. As the more azide-rich polymers contain more units in total, the relative degree of conversion is then higher.

Following IRRAS characterisation, cyclic voltammetry was measured on the *clicked* samples to not only confirm the disappearance of azide groups (which was just shown) but the actual presence of ferrocene as well. First, CVs of the preliminary **PV-CR72** sample which was measured with PM-IRRAS before are shown in Figure 3.21.

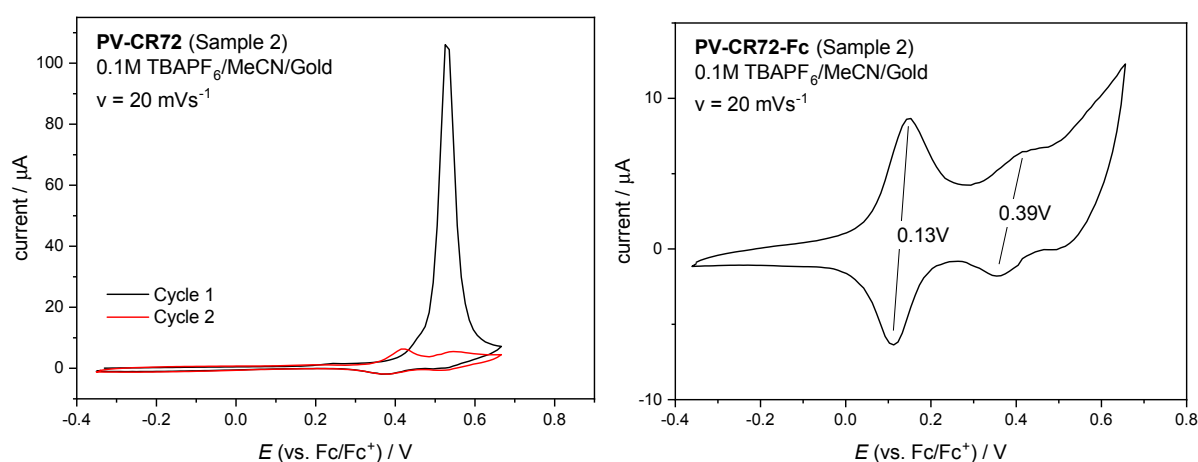


**Figure 3.21:** CV of sample on gold before and after CC conversion.  $E_{1/2}$  values are given for the respective redox processes. A new reversible signal can be found with a half-wave potential of about 0.13 V.

CV shows a new, reversible process with a half-wave potential of about 0.13 V in which can at a first glance be assumed to belong to the ferrocene units. The polymer's TPB signals can still be found as well, with the TPB radical cation being more well-defined than the TPB dication. Overall though, a change in structure is apparent compared to the unreacted films, with the polymer's electronic processes becoming less defined. First, it is necessary to actually confirm the new electron process observed in the CV is in fact proof of a successful attachment of ferrocene to the polymer, so comparative CV measurements were performed. Figure 3.22 (left) shows additional scans of the sample while the right side of the figure provides a measurement of a *non-clicked* sample to which loose ethynyl ferrocene was simply added as part of the CV's electrolyte solution. In the latter case, the CV's structure basically resembles that of pristine ethynyl ferrocene with the polymers TPB-peaks added "on-top", meaning that both don't share a common baseline but rather

the polymer's signals seem to be added on top of ethynyl ferrocene's. Comparing that to the *clicked* sample on the left, both do share a common baseline and build a shared system. Furthermore, as with the CVs shown before, the shape of the polymer signals differs from the *non-clicked* one. As is shown on the left side, the *clicked* polymer is also stable over a number of cycles and remains fully reversible.

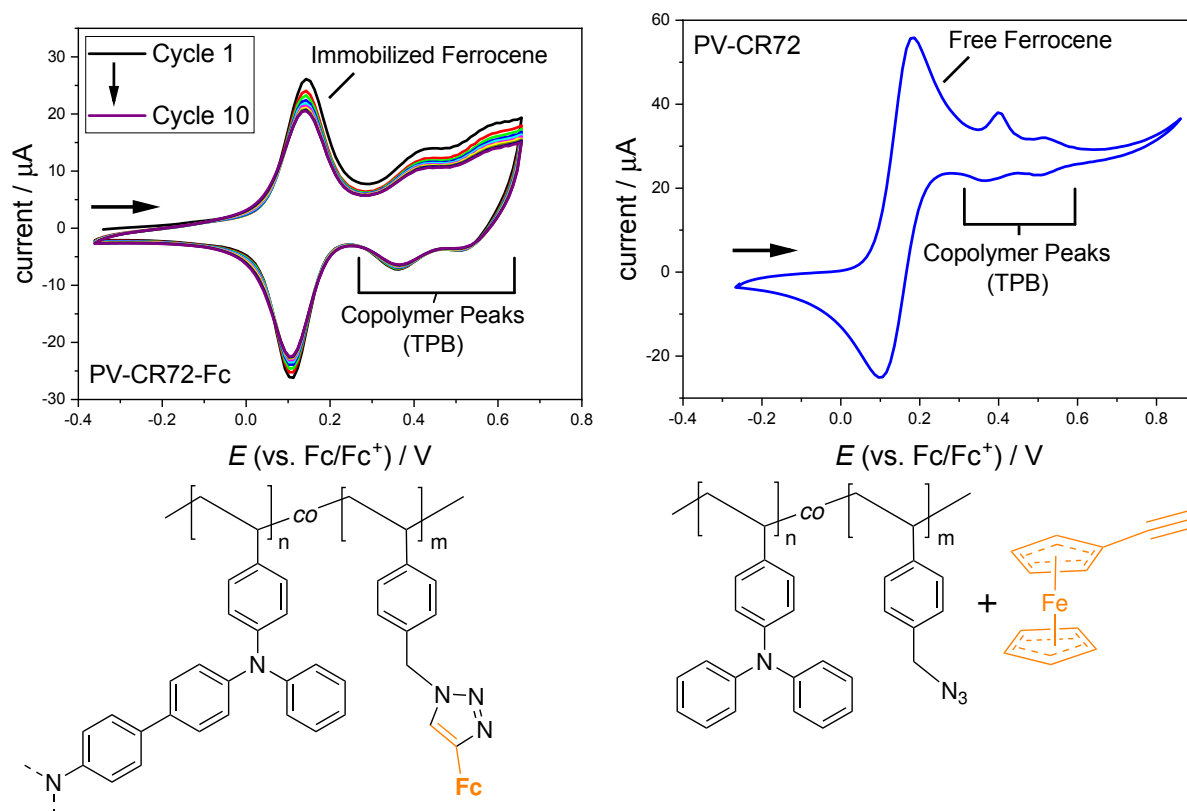


**Figure 3.22:** Comparative CV of covalently bound ferrocene (left) and loose ferrocene in the electrolyte solution (right). Measured at  $50 \text{ mV s}^{-1}$  (left) and  $20 \text{ mV s}^{-1}$  (right) in  $0.1 \text{ M NBu}_4\text{PF}_6$  in MeCN.

This fact is important in that it opens up the possibility of another method of characterisation and evaluation of the covalent character of the ferrocene attachment, namely scan rate sweeps. With changing scan rates in cyclic voltammetry, peak currents change accordingly. The *Randles-Sevcik* equation gathers this dependency in its description of peak currents for reversible one-electron processes<sup>[138,139]</sup>:

$$i_p = 0.4463nFA \left[ \frac{nF}{RT} \right]^{1/2} CD^{1/2}\nu^{1/2} \quad (3.4)$$

with  $i_p$ : peak current,  $n$ : number of electrons transferred,  $F$ : Faraday Constant,  $A$ : electrode area,  $R$ : gas constant,  $T$ : temperature,  $C$ : concentration,  $D$ : diffusion coefficient

and  $\nu$ : scan rate.

This relationship holds true for reversible one-electron processes which are diffusion-controlled. Since all other variables can be considered constant, one can write in simplified terms  $i_p \sim \nu^{1/2}$ . In a case where the mentioned conditions are met, a plot of  $\log(i_p)$  versus  $\log(\nu)$  will yield a linear relationship which can be fitted with a line of slope 0.5. This is not true, however, for cases where the species of interest is adsorbed to the electrode surface, as is assumed here. In this case, the relationship is directly linear with  $i_p \sim \nu$  and as such should allow for a linear fit with a slope of 1 in the aforementioned plot. This is depicted graphically in Figure 3.23. Running CV measurements at varying scan rates and noting down the initial forward sweep peak currents of the electron process of interest can thus be used to confirm or refute a covalent attachment of a certain redox-active species.

On this basis, the aforementioned measurements were taken with **PV-CR72-Fc** sample 2, employing scan rates of  $10 \text{ mV s}^{-1}$ ,  $20 \text{ mV s}^{-1}$ ,  $50 \text{ mV s}^{-1}$ ,  $100 \text{ mV s}^{-1}$  and  $200 \text{ mV s}^{-1}$ . Peak current values of each first forward scan were noted and plotted accordingly. With the previous characterisation techniques pointing to a successful covalent attachment of ethynyl ferrocene, the resulting linear fit of the obtained data here is expected to show a slope of 1, and indeed, Figure 3.23 (right side) shows good agreement of the experimental data with theoretical expectations for peak current values of  $\text{TPB}^{\bullet+}$ . The same evaluation of ferrocene peak currents gave a slope above 1, although this is mostly caused by a comparably big step in peak current between the  $20 \text{ mV s}^{-1}$  and  $50 \text{ mV s}^{-1}$  voltammograms. Linear fits of either data points 1 and 2 or 3 to 5 gave slope values of 1.06–1.10, which puts them close to the expected 1 when considering standard deviation (up to 0.06).

Subsequently, CV and scan rate characterisation was repeated on samples of **PV26-Fc**, **PV49-Fc** and **PV73-Fc**. Figure 3.24 (a) to (c) show the respective spectra, each depicting the crosslinking procedure on the top spectrum and characterisation after CC on the bottom one. All experiments were performed with the same scan rate of  $50 \text{ mV s}^{-1}$ , so intensities of signals (respectively currents) can be compared across experiments. Of course, it is already clearly noticeable that signal intensity of ferrocene peaks change in relation to TPB peaks according to the change in polymer composition. In this regard, CV results follow what had been observed in IRRAS measurements and the disappearance of azide bands do correlate with an increase in ferrocene content. Numerical comparisons can be drawn as well, for which the peak intensities of the oxidation peaks of ferrocene and  $\text{TPB}^{\bullet+}$  in the third cycles were used. E-Fc/ $\text{TPB}^{\bullet+}$  ratios amount to 0.46 in **PV26-Fc**, 1.17 in **PV49-Fc** and 4.30 in **PV73-Fc**. Ratio of the latter clearly exceeds the expected value of roughly 1.5 when referencing the other two samples. From the CVs it can be seen

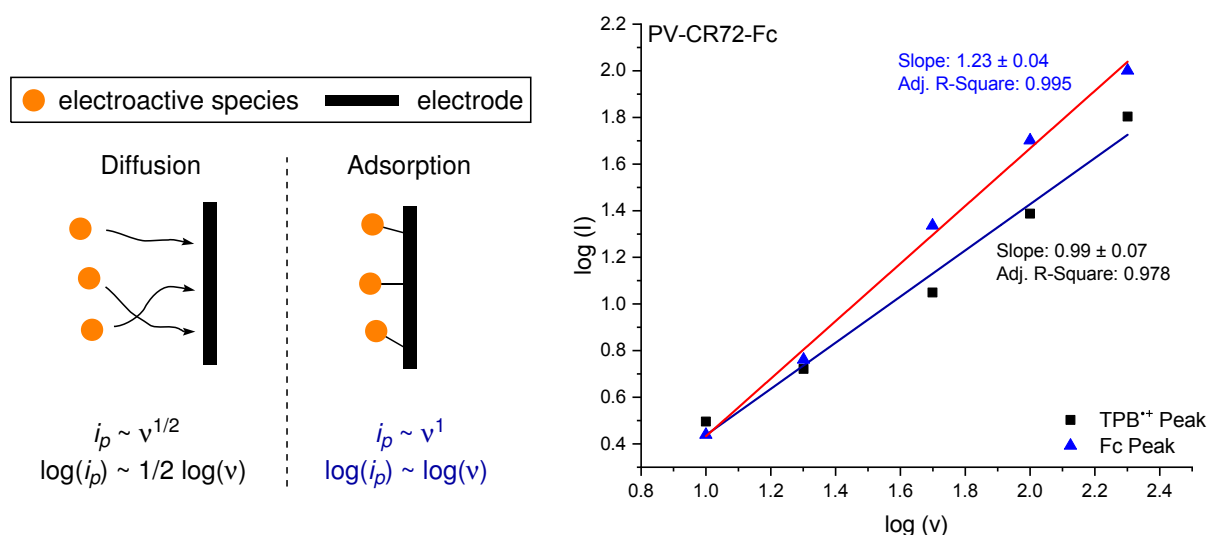


**Figure 3.23:** **Left** Visual representation of applicable dependencies between peak currents  $i_p$  and scan rates  $\nu$  in cyclic voltammetry for reversible one-electron processes. **Right** Results of a scan rate sweep test for the CC attachment of ethynyl ferrocene to **PV-CR72**.

that in **PV73-Fc** equilibration had not yet finished in the 3rd cycle, so a slight reduction in the ratio could be expected after hysteresis stopped with more cycles.

Looking at half-wave potentials during crosslinking, all three polymers show the same, as would be expected, with  $E_{1/2}$  of  $\text{TPB}^{\bullet+}$  at 0.4 V and  $\text{TPB}^{2+}$  at 0.53 V. Interestingly though, these divert more the more the content of TPA groups decreases. In **PV26-Fc**,  $\text{TPB}^{\bullet+}$  and  $\text{TPB}^{2+}$  half-wave potentials are still very similar after *clicking* with 0.37 V and 0.53 V, but in **PV49-Fc** the difference is already more notable with 0.33 V and 0.50 V, respectively. Even more pronounced is the difference in the **PV73-Fc** sample with only 0.31 V for  $\text{TPB}^{\bullet+}$  and 0.48 V for  $\text{TPB}^{2+}$ . Some variation of course can be assigned to the placement of the data reader as the true peak of the curves is not always obvious, which holds more true the more the TPB curves flatten due to reduced TPA/TPB content. However, shifts in half-wave potentials are also visible by the naked eye in the provided stacked plots. Further evaluation reveals that this shift can also be found in the respective ethynyl ferrocene signals, with  $E_{1/2}$  of 0.11 V in **PV26-Fc**, down to 0.08 V in **PV49-Fc** and 0.06 V in **PV73-Fc**. All measurements have been referenced against the regular ferrocene/ferrocenium redox couple, the half-wave potential of which only varied within 0.015 V across experiments (with actually identical values in the **PV49-Fc** and **PV73-Fc** experiments), so these shifts cannot be assigned to coincidental fluctuations in the reference potential as might be assumed at first glance.

Scan rate sweeps have been performed on these samples as well and improved with a

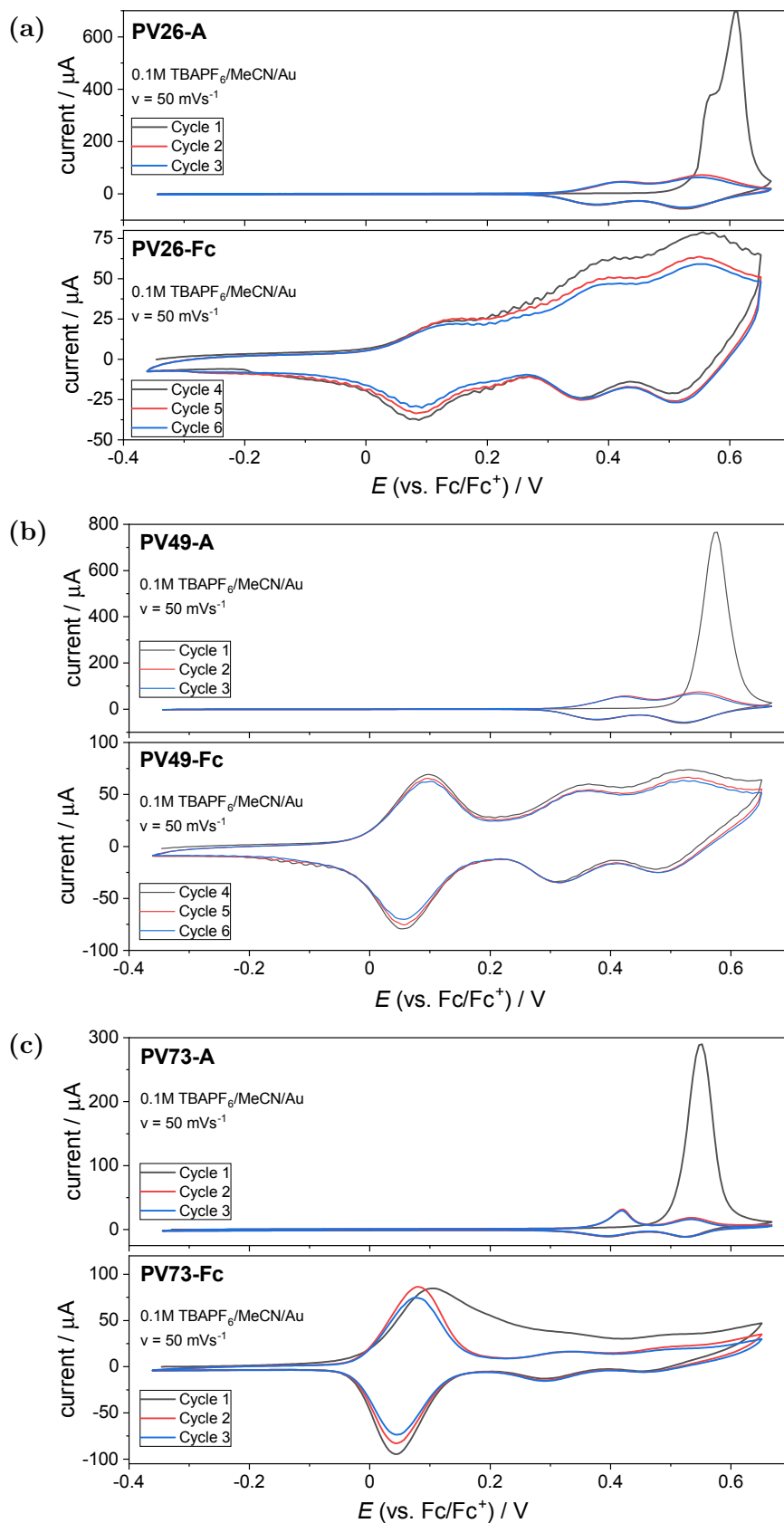


**Figure 3.24:** CVs of copolymer films on gold electrode substrates. Top voltammogram in each case shows the crosslinking process, bottom one characterisation after CC conversion.

greater number of different scan rates to improve the quality of the obtained data sets. Cycles and data analysis is given in Figure 3.25 on page 64. Cycles were run with scan rates between 5 and 408 mV s<sup>-1</sup>. The resulting voltammograms are depicted on the left side of the figure. From these CVs, peak currents of each initial forward cycle were determined for both, the ferrocene half-waves and the TPB<sup>•+</sup> signals as a reference. Logarithmic values of the obtained numbers were plotted against the logarithmic scan rates and fitted with linear functions to obtain the respective slopes, following the relationship of these values as described in equation 3.4. For species adsorbed to the electrode, respectively the polymer film, a slope of 1 is expected. When evaluating the ferrocene values one can see that all 3 slopes are close to 1, more so when considering the uncertainty of those values as given in the graphs. The biggest deviation from 1 can be seen in the case of **PV73-Fc** with a slope of about 0.87. However, it is worth noting that even the polymer reference signals don't all give ideal values. Plotting and fitting of the TPB<sup>•+</sup> peaks afford slopes of 1.02 in **PV49-Fc** and 1.04 in **PV73-Fc**, but deviate to 1.17 in **PV26-Fc**. One reason for this is the imprecise determination of the peak values in cases where half-waves are not sharply separated from each other. Another reason is likely the fact that these systems don't entirely conform to the ideal theoretical prerequisites of the *Randles-Sevcik* equation because not all parts of the polymers are directly attached to the electrode surface, due to them being films (as opposed to mono-layers). Of course, it's also possible the ferrocene content in the polymer plays a role in this behaviour. As we have seen in the preceding CVs, half-wave potentials slightly change with varying ferrocene contents and so an influence on this characteristic is not out of the question, although the exact processes leading to these variations are not obvious.

Further characterisation was done by water contact angle (CA) measurements to probe the ferrocene's influence on surface properties. To get the most-pronounced results the polymer with the highest content of functionalizable groups was used. In light of future functionalisations with ionic groups this will also provide another point of comparison, which is why not only samples on gold were prepared but on IDE as well. Reaction evaluation on IDE samples is severely limited even when compared to thin film gold samples, due to the structure of interdigitated electrodes which disturbs any optical method. As functionalisations with ionic groups will later require the use of IDEs for impedance characterisation, these samples now can aid later by providing a side-by-side comparison of plain gold and interdigitated platinum electrodes.

Films were prepared from toluene solutions as before and crosslinked as usual. Contact angles were determined on the films before and after CC conversion. 3 spots or more were measured on the gold substrate and 2 (due to the smaller size) on the IDE. Representative images are given in Figure 3.26 together with the calculated average contact angles.

CA of both, gold and IDE sample is the same within margin of error before conversion with  $79^\circ$  on average. Introduction of ferrocene units into the films yields an increase in contact angle and thus a higher hydrophobicity in both cases as well. Again, obtained values are similar on both substrates and amount to about  $90^\circ$  on average, although standard deviation is relatively high for the IDE sample. This is due to the fact only two spots could be reliably measured on it, so local differences on the film (partially because of the precipitate that has been discussed earlier) are not averaged out as well as on the gold sample.

Overall from this set of sample conversion and surface modification seem to be comparable on both kind of electrodes.

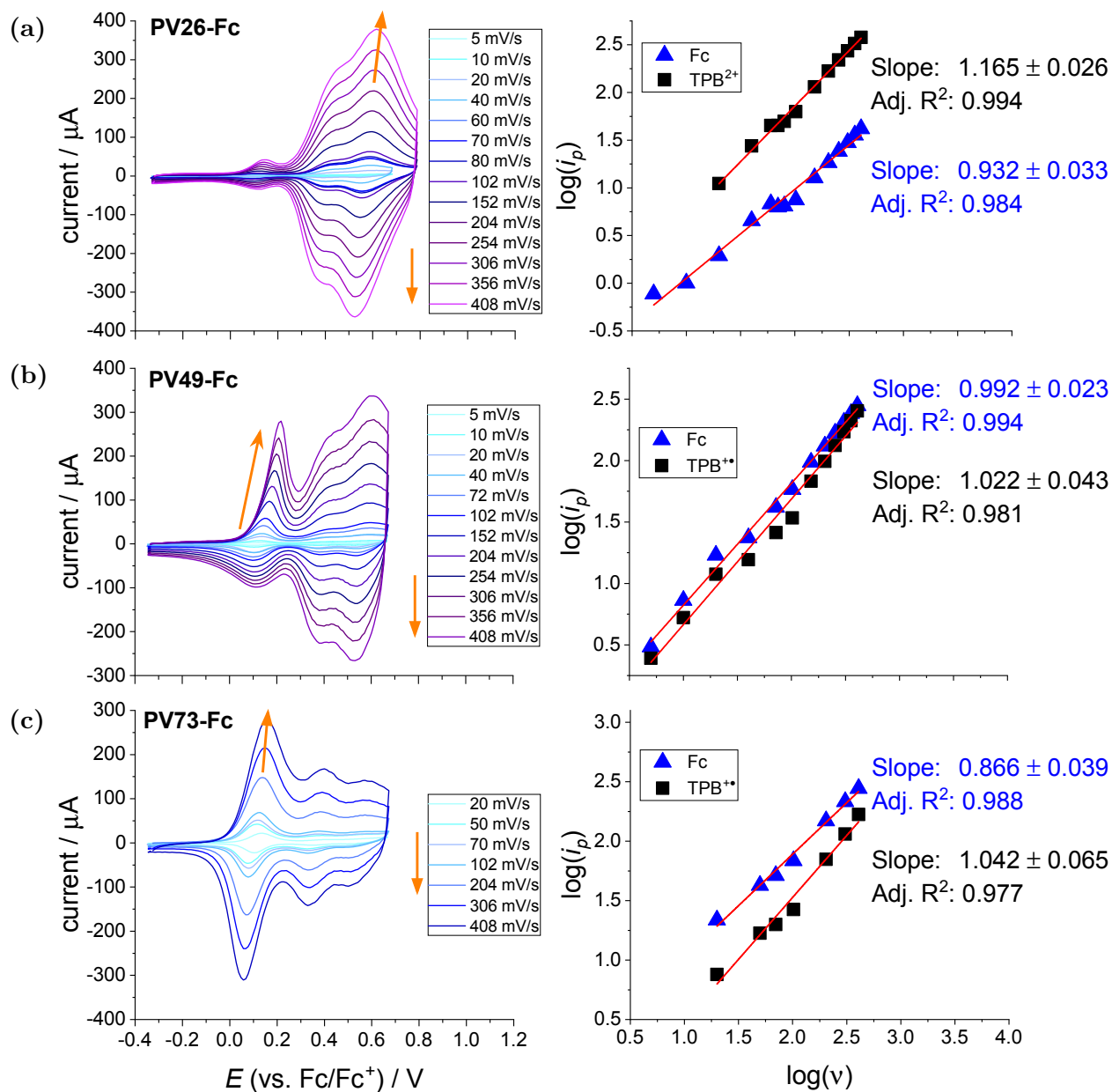


**Figure 3.25:** CVs of polymer films at different scan rates and their respective linear plots of scan rate against the peak currents. Measured in 0.1 M  $\text{NBu}_4\text{PF}_6$  in MeCN.

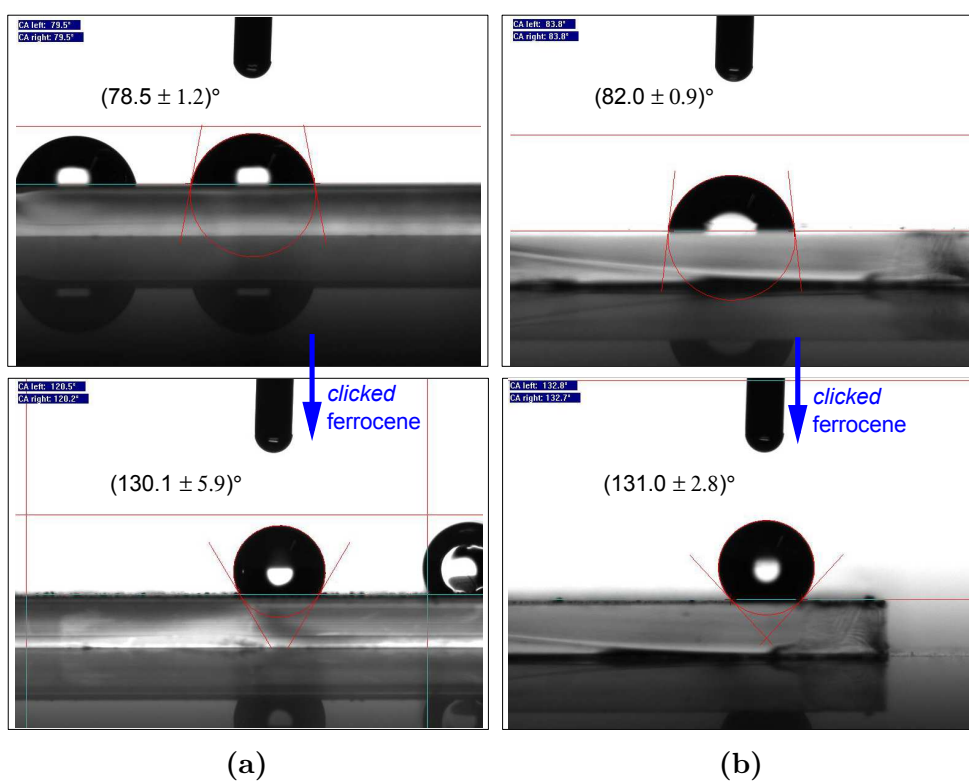
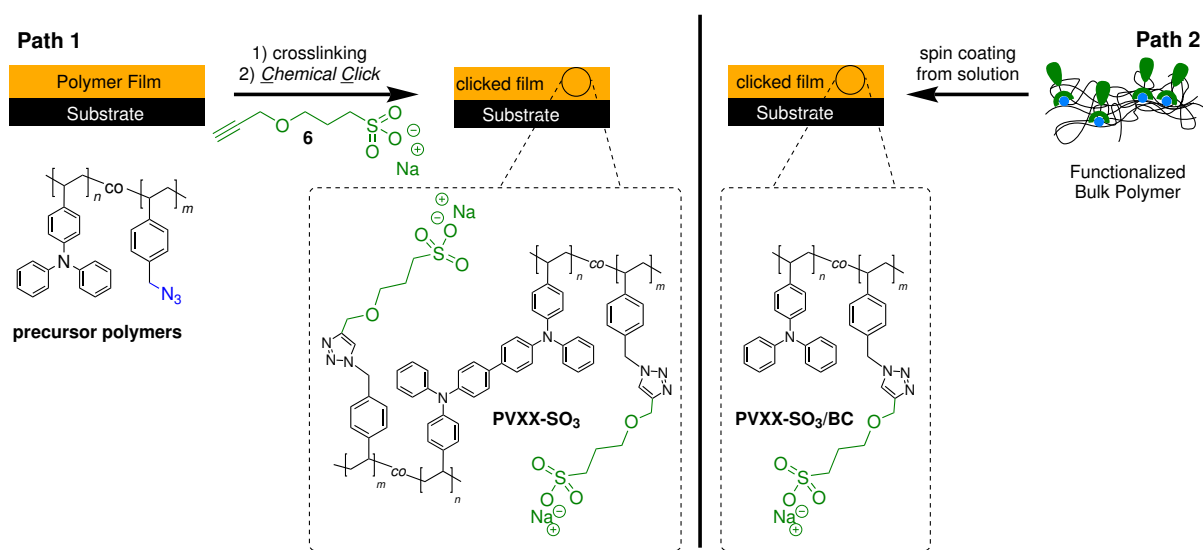


**Figure 3.26:** Water contact-angle comparisons of **PV73-A** (top) and **PV73-Fc** (bottom). **(a)** on gold electrode. **(b)** on interdigitated platinum electrode.

### 3.3 Sulfonate-functionalized Copolymers

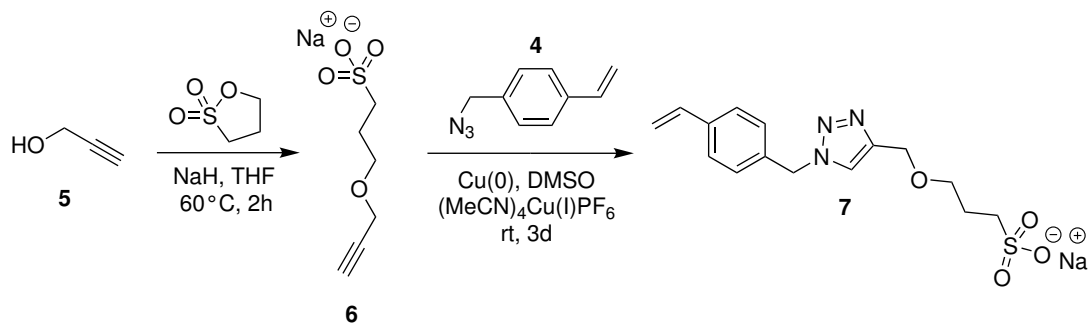


**Scheme 3.6:** Two approaches of obtaining polymer films with ionic sodium sulfonate groups. Path 1 starts from spin-coated **PVXX-A** polymer films which get crosslinked and clicked in film. Path 2 starts from already clicked bulk polymer from which solutions are produced to spin-coat thin films directly. No crosslinking is done in Path 2.

After successful confirmation of the effectiveness of the CC method for the introduction of ferrocene probes, the overall procedure of sample preparation was adopted for the introduction of ionic functionality. For this, first a model-reaction was employed in solution. Even though solubility after *clicking* ionic compounds should change dramatically, which would indicate a successful reaction, it's possible that only partial conversion occurs in the polymer. Identifying corresponding NMR-signals can enable one to make assessments about the conversion and provide another tool for characterization.

3-(Prop-2-ynyloxy)propane-1-sulfonate **6** was therefore readily prepared by nucleophilic ring opening of 1,3-propane sultone with propargyl alcohol **5** in dry THF (Scheme 3.7). The resulting sulfonate **6** was then reacted under inert atmosphere with Azidomethylstyrene **4** in DMSO with a reactant concentration of  $0.04 \text{ mmol mL}^{-1}$  and 5 mol-% of the copper(I) catalyst. Reaction conditions were based on earlier work.<sup>[127]</sup> After removal of the reaction solvent and washing of the obtained solid with chloroform the product was characterized by proton NMR spectroscopy.

Figure 3.27 gives the resulting  $^1\text{H-NMR}$  spectrum (top) in  $\text{DMSO-}d_6$  as well as both reaction partners' spectra for reference. The most crucial signals to look for are the ones corresponding to the  $\text{OCH}_2$  group neighbouring the alkyne unit in compound **6** (labelled



**Scheme 3.7:** Model reaction for the *Click* reaction of 4-(azidomethyl)styrene **4** with 3-(Prop-2-ynyloxy)propane-1-sulfonate **6** after synthesis of the latter.

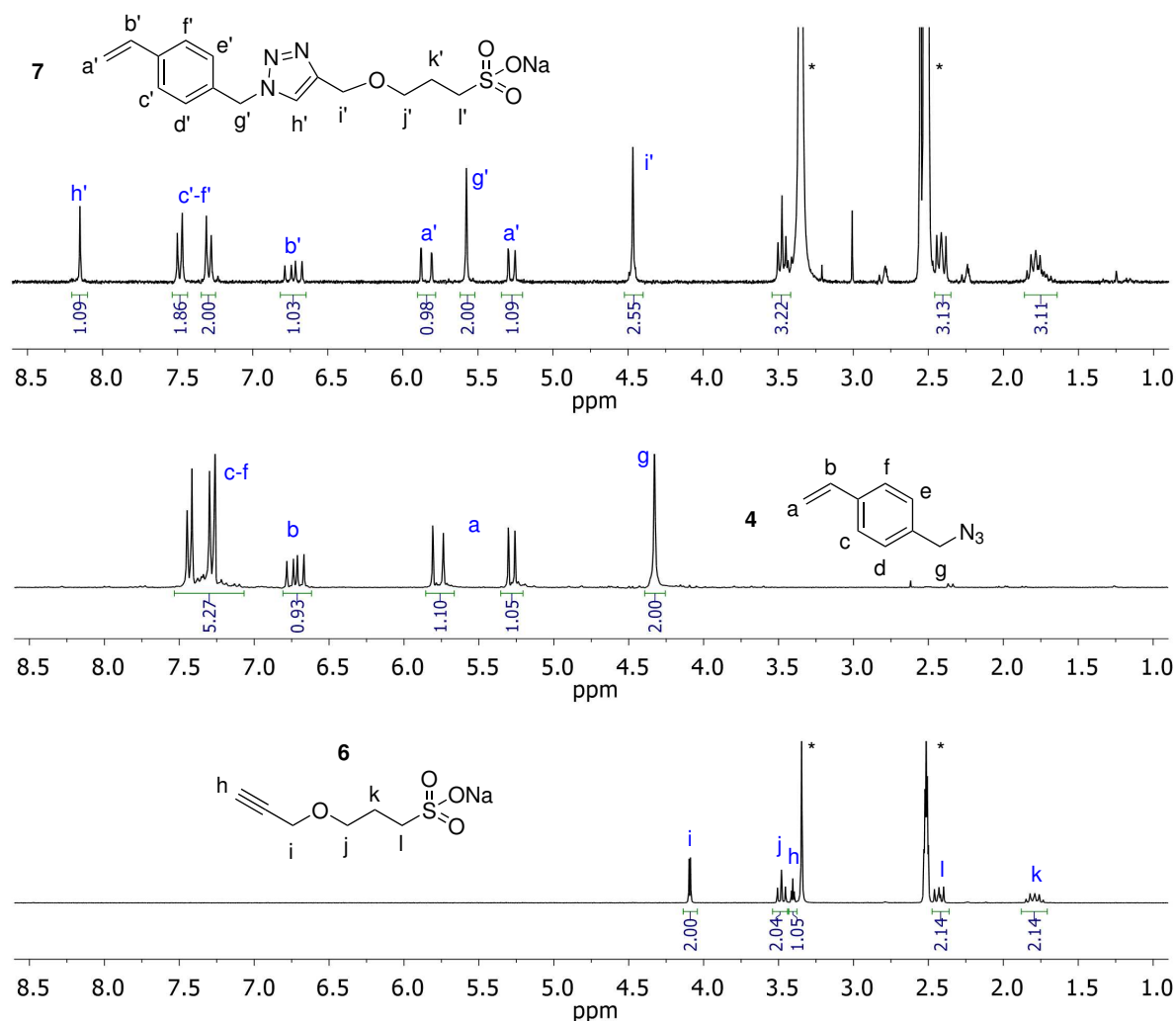


**Figure 3.27:** <sup>1</sup>H-NMR spectra of **6** (bottom) in DMSO-*d*<sub>6</sub> and **4** (middle) in CDCl<sub>3</sub> and spectrum of compound **7** in DMSO-*d*<sub>6</sub> as a result of the *Click* model reaction.

i) which is found as a doublet at 4.09 ppm and the  $\text{NCH}_2$  group in compound **4** (labelled g) which is found at 4.33 ppm in the corresponding spectrum. Be aware, though, that the spectrum of AMS **4** was measured in  $\text{CDCl}_3$ , as opposed to  $\text{DMSO}-d_6$  for the other two. After CC conversion, both groups' environment changed and so did their chemical shifts. In the top spectrum of Figure 3.27 the  $\text{NCH}_2$  group is now neighbored by two aromatic groups (benzene ring and 1,2,3-triazole, signal g') which caused the singlet to shift from 4.33 ppm to 5.58 ppm. Doublet i from the bottom spectrum became singlet i' in the top spectrum and shifted to 4.47 ppm. Assignments of these shifted alkyl signals were done with the help of literature data on a similar structure.<sup>[140]</sup> No residual peaks from the original signals can be found in the top spectrum although any remaining alkyne sulfonate **6** should be in the product mixture, due to the nature of the workup. Starting materials **4** and **6** were employed in a 1:1 ratio with the actual weigh-ins amounting to 0.955 mol of the azide and 0.946 mol of the alkyne, equating to 99% of the azide. Meanwhile, reaction yield was above 100% which is thought to be caused by residual solvents (most likely DMSO). Overall, with these results it was assumed that these reagents undergo a quantitative or near-quantitative conversion in this catalytic system.

### 3.3.1 Polymer Analogous Conversion of Copolymer Films

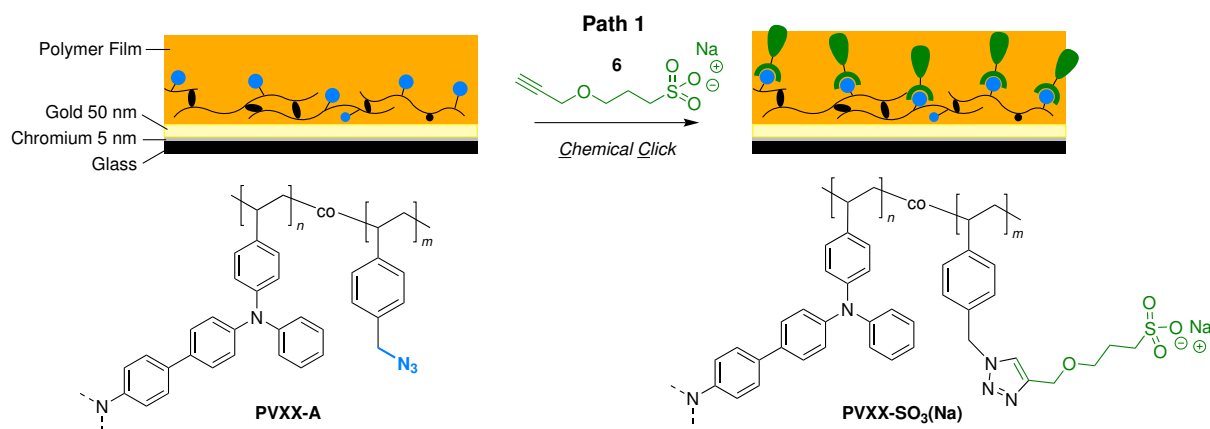


**Figure 3.28:** Schematic depiction of the chemical *click* of alkyne sulfonate **6** into thin polymer films *via* **Path 1**. Conditions: DMSO,  $(\text{MeCN})_4\text{Cu(I)PF}_6$ , alkyne **6**, copper(0) powder.

Subsequently, with this alkyne-carrying sulfonate **6**, polymer analogous conversion in films was attempted. Sample preparation and functionalization was kept the same as earlier, which included crosslinking the deposited films electrochemically before CuAAC. Samples were prepared from 5 M toluene solutions on gold and IDE substrates with two samples each using **PV73-A** due to it having the highest amount of functionalizable

groups. Interdigitated electrodes are not suited for any method of reaction evaluation available to us, which was the reason for having a set of gold electrodes for cross-reference. Likewise, conversion with ethynyl ferrocene on both electrode types in addition to alkyne sulfonate **6** provided another point of reference and a way to narrow down issues with the reaction should conversion with **6** not go as planned. For the sake of completeness, Figure 3.29 gives their corresponding crosslinking CV data. Hereby both interdigitated parts of the IDEs were connected to the same working electrode so as to being treated as one. Crosslinking proceeded without issues for both gold and IDE substrates.

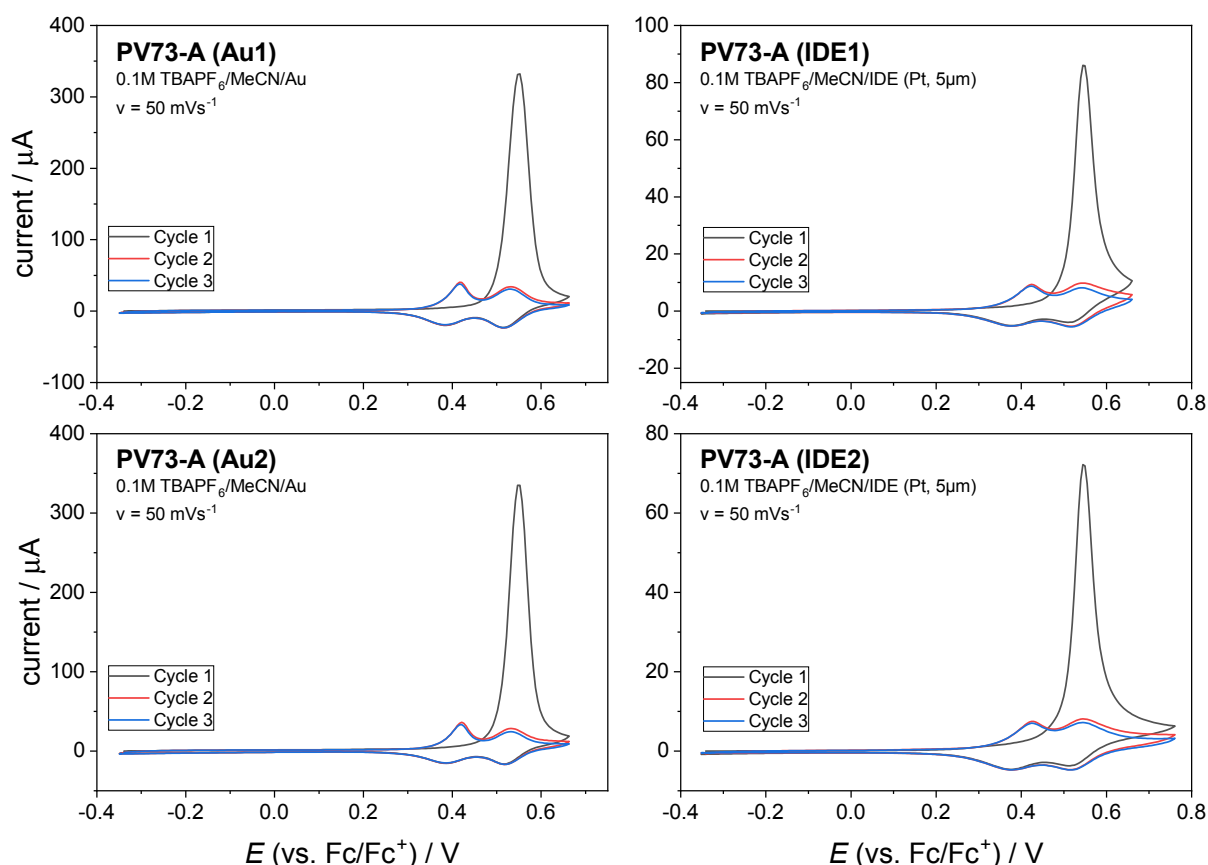


**Figure 3.29:** Electrochemical crosslinking of 4 samples for CC conversion, with 2 samples each for conversions on gold and interdigitated platinum electrodes to introduce ferrocene and sodium sulfonate groups on each type of substrate.

As before, reaction success was probed by PM-IRRAS before and after CC. Spectra were first recorded after crosslinking and later after CV characterisation subsequent to *click* conversion. As was mentioned, IRRAS could only be performed on gold substrates. Despite many efforts, surface size and structure of IDEs made it impossible to obtain any useable spectra. However, absorbance spectra of gold electrodes are given in Figure 3.30.

Conversion with ethynyl ferrocene shows similar results as in previous experiments, with a considerable but incomplete functionalization of the polymer film. Interestingly, reaction with the alkyne sulfonate yielded a near-full conversion. A small residual signal of unreacted azide can be seen from the IRRAS spectrum but it is notably smaller than the one from the ethynyl ferrocene conversion. The aliphatic chain of **6** should provide more flexibility than the coordinative make-up of ethynyl ferrocene which could enable it to penetrate the polymer film more effectively. Also, no precipitate can be observed in these reactions when using the alkyne sulfonate, contrary to reaction with E-Fc as has been discussed earlier (see chapter 3.2.2). As this precipitate can be rather strong there might be a side reaction occurring in these conversions, however, explanations for its nature remain speculative at this point.

One curiosity in the spectrum of **PV73-SO<sub>3</sub>-Gold** is the broad band extending from 1600  $\text{cm}^{-1}$  to 1700  $\text{cm}^{-1}$ , overlapping the C=C stretching band at 1593  $\text{cm}^{-1}$ . Band assignment was not possible because molecular structures that typically can be found in this region cannot occur in the present samples. However, looking at the structure of this band similarities to unassigned bands in earlier spectra in Figure 3.20 (chapter 3.2.2) can be seen, albeit the difference being the wavenumber at which the signal occurs. Due to this similar structure and the implausible band region it is assumed that those bands are somewhat random artifacts stemming from the baseline correction of the raw spectra.

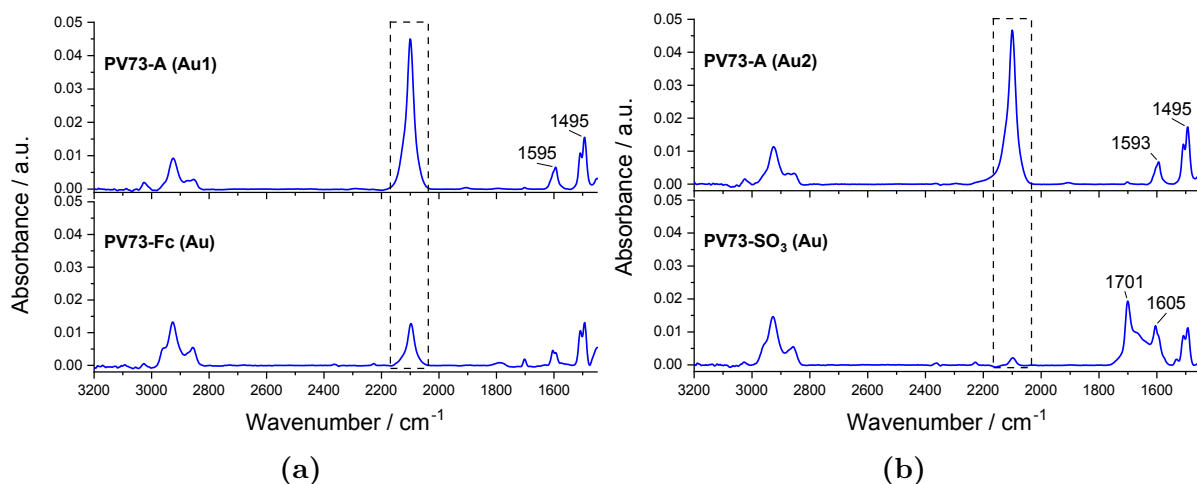


**Figure 3.30:** Comparative PM-IRRAS absorbance spectra of gold substrates before and after *click* functionalization (CC) of crosslinked **PV73-A** films with Fc (a) or sodium sulfonate (b). Decrease in band intensity of the highlighted azide band represents reaction conversion.

In any case, characterisation *via* IRRAS provided evidence for successful functionalisations, with the introduction of sulfonate groups proceeding well with high conversion. As

IDEs could not be measured here it has to be assumed conversion on these proceeded comparably to the gold samples. One way to verify this is comparison of water contact angles which is described in the next chapter.

Further characterisation was performed on this set of samples by means of water contact angle measurements to allow for statements about the reaction not only on the gold substrates used but on the IDEs as well. Comparisons were drawn between the unreacted (but cross-linked) samples and the same samples after their respective *click* conversion. Results are shown in Figure 3.26 on page 65 for the conversion with ethynyl ferrocene and in Figure 3.31 for the introduction of sulfonate groups. Both were performed on gold substrates as well as on interdigitated platinum electrodes (IDEs). The latter were prepared for the future characterisation by Impedance Spectroscopy. On each gold substrate at least three measurements were performed to get an average value. On IDE substrates, due to their smaller size, only two spots could be measured reliably.

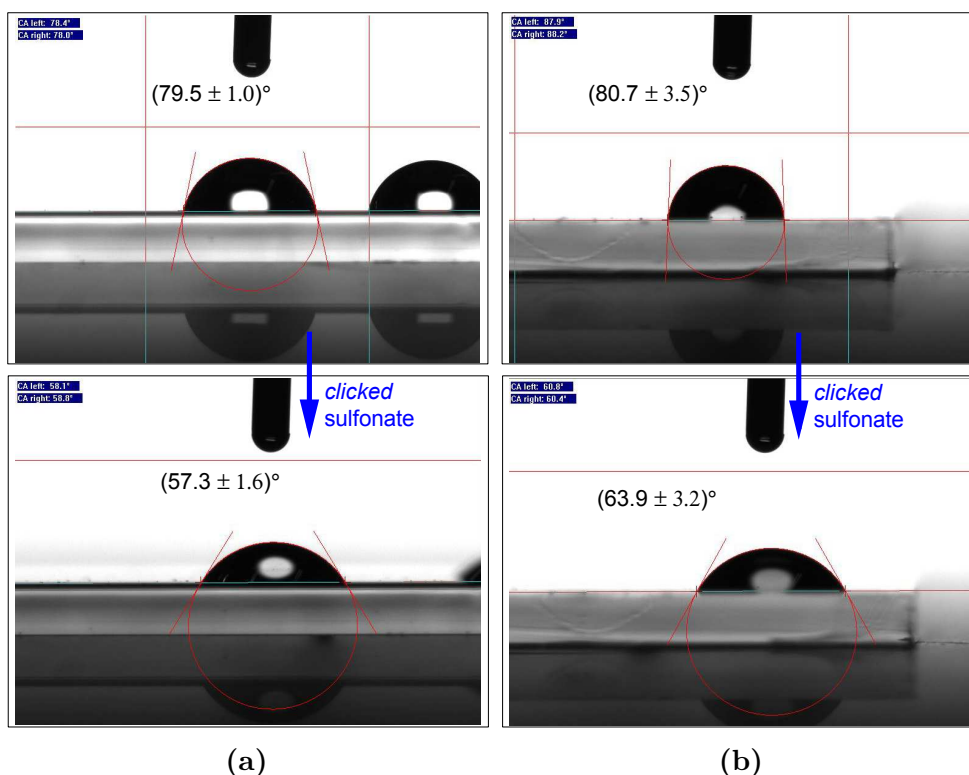


**Figure 3.31:** Water contact-angle comparisons of **PV73-A** (top) and **PV73-SO<sub>3</sub>** (bottom). **(a)** on gold electrode. **(b)** on interdigitated platinum electrode.

All four measurements of the unreacted samples show similar water contact angles within the margins of error. Values on the interdigitated electrons show a higher fluctuation which can be owed to the smaller surface area that's available for measuring and the

rougher surface caused by its interdigitated arms. Even within the bigger error margins of the IDEs, a clear increase in contact angle can be seen after attachment of ferrocene units from  $\approx 80^\circ$  to about  $130^\circ$  (gold) and  $131^\circ$  (IDE) respectively. Thus, the introduction of ferrocene units strongly reduces the surface's polarity. The opposite is expected for the introduction of highly polar sulfonate groups and indeed, this was observed in the corresponding contact angle measurements in Figure 3.31. Again, from a value of about  $80^\circ$ , contact angles changed noticeably and dropped to around  $57^\circ$  on gold and  $64^\circ$  on the IDE, respectively.

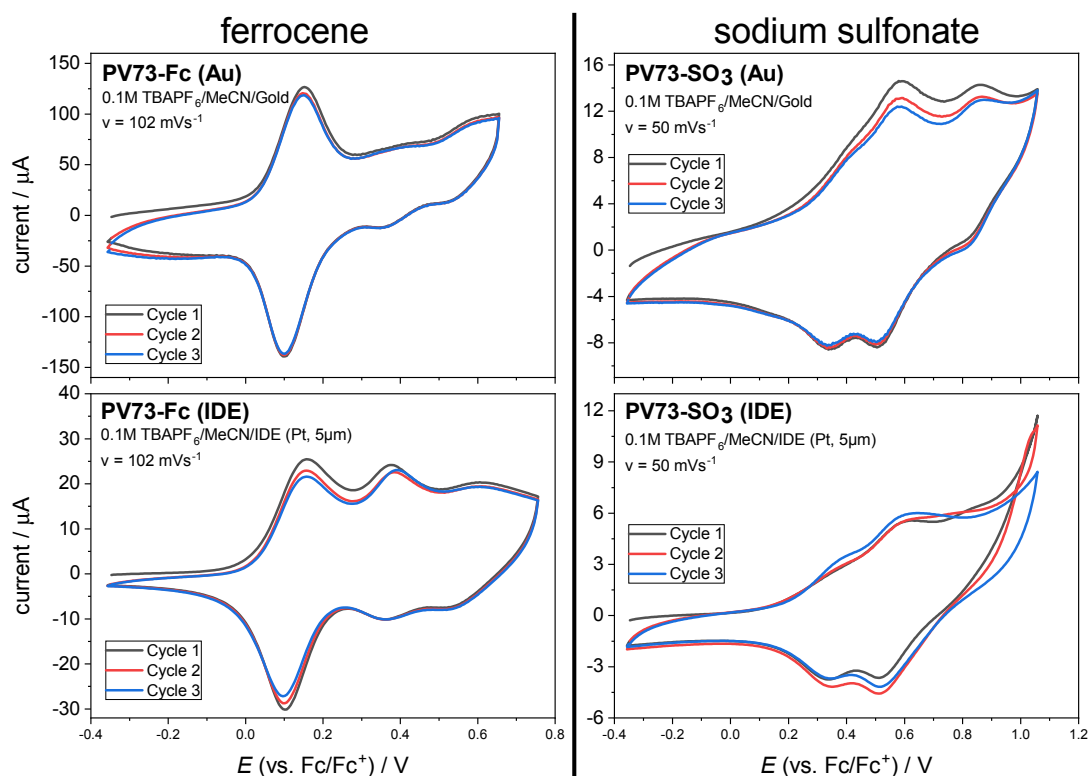


**Figure 3.32:** CVs of samples of **PV73-A** reacted with both, E-Fc and **6** by CC. Top row samples on gold. Bottom row samples on interdigitated platinum electrodes. **Left** Functionalized with ferrocene. **Right** Functionalized with sulfonate groups.

CVs of the reacted films are depicted in Figure 3.32. Conversions with ethynyl ferrocene was included here to provide a comparative reference. When comparing CV of the Fc-functionalized samples on gold and on an IDE there is a difference in current ratio between ferrocene and TPB signals. While on gold ferrocene's signal is more intense, as was observed with earlier samples, on IDE ferrocene and TPB signals show the same intensity. The difference does not seem to come down to electrode structure, as crosslinking voltammograms in Figure 3.29 looked highly similar in both types. This finding suggests

a lower click conversion with E-Fc in the IDE sample compared to the one on gold.

In the case of ionic functionalisation a new redox process can be observed in the CV as well, albeit strongly overlapping the polymer's TPB waves. The backward/reduction half-cycle even suggests the existence of two new redox processes in overlap with TPB's, due to the high reduction current of both peaks between 0.3 V and 0.6 V. The same experiment on IDE is less well-defined, nonetheless in this case intensity ratios between functionalized groups and TPB appear consistent with the sample on gold so that an equal conversion is assumed.

Taking into account all means of characterisation performed on the *clicked* films, one can safely assume CC to be a reliable process for the functionalization of **PV73-A**. Mixed redox systems have successfully been created with the introduction of ferrocene units in a range of different co-monomer ratios. While the introduction of sulfonate groups cannot be evaluated as nicely by electrochemistry as the introduction of ferrocene units, water contact angle measurements ultimately suggest its presence in the polymer, albeit indirectly. Subsequently, the next step was to characterize the samples' polyelectrolyte properties and decouple ionic and electronic conductivities, as will be discussed in the next chapter.

### Investigation of Polyelectrolyte Behaviour and Humidity Dependence

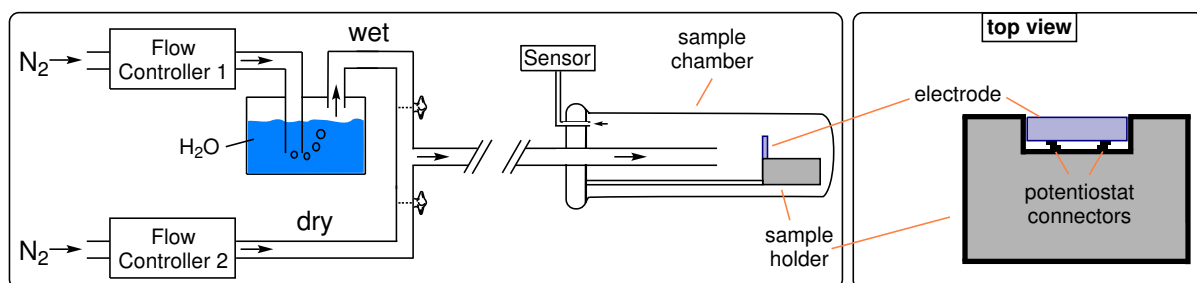


**Figure 3.33:** Schematic depiction of the experimental setup for water partial pressure dependent impedance spectroscopy, with polymer films deposited on interdigitated platinum electrodes.

To investigate humidity dependence of conductivity and decoupling ionic and electronic conductivities, samples were characterized by impedance spectroscopy. Before discussing characterization of the samples above, first two earlier samples made from **PV-CR76** will be presented, which were prepared for impedance spectroscopy according to procedures described earlier herein. They were deposited on interdigitated platinum electrodes (spin coating: 2000 rpm, 0 acc for 180 s) to be measured in an impedance setup. All IDEs

used featured a 5  $\mu\text{m}$  spacing between single electrode lines. These early **PV-CR76-SO<sub>3</sub>** films were created prior to the **PVXX-SO<sub>3</sub>** ones discussed above and had not yet been crosslinked prior to CC but were otherwise prepared in an identical manner.

After initial measurement at ambient conditions for evaluating the sample is showing a response, substrates have been equilibrated at 0.9 mbar water partial pressure over night to produce a fixed starting point for all samples before commencing characterisation. Subsequently, to assess humidity dependent behaviour, water partial pressure was changed step-wise, allowing the film to adjust to the new conditions for 2 h in between measurements. Figure 3.34 (b) shows the plot resulting from evaluation of the individual spectra obtained from these measurements. Figure 3.35 shows individual spectra exemplarily.

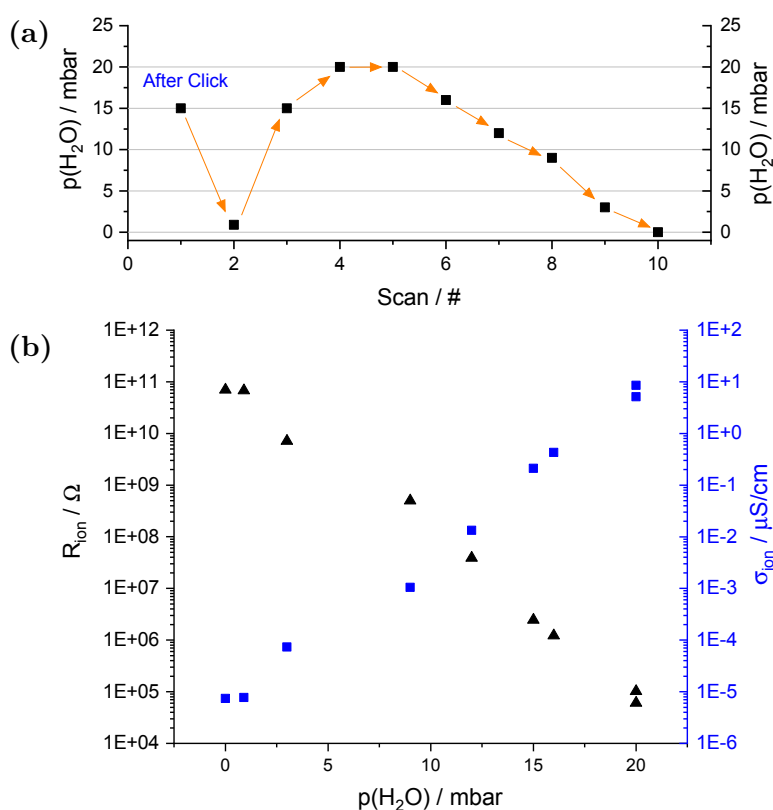


**Figure 3.34:** First water-partial-pressure-dependent Impedance Spectroscopy of a non-crosslinked sample of **PV-CR76-SO<sub>3</sub>** prepared on an interdigitated electrode (IDE) *via* CC. (a) Procedure applied for changing water partial pressure  $p_{H_2O}$ . Time given to equilibrate to each new  $p_{H_2O}$  was  $\geq 2$  h. (b) Ionic resistance plotted against water partial pressure  $p_{H_2O}$ . (c) Ionic conductivities per  $p_{H_2O}$  calculated from the obtained ionic resistance values.

From Figure 3.34 (b) a direct and inverted correlation between the applied water partial pressure  $p_{H_2O}$  and the resulting ionic resistance can be seen spanning over 7 orders of

magnitude, whereas electronic resistance is too high to be determined. With known channel length and channel width of the IDEs used, a corresponding ionic conductivity could be calculated following equation 3.5<sup>[101,141]</sup>, affording a maximum of  $8.6 \mu\text{S cm}^{-1}$  at 20 mbar  $p_{\text{H}_2\text{O}}$ . For this calculation, a film thickness of  $(49.8 \pm 1.0)$  nm was used, as determined *via* AFM on ITO.

$$\sigma = \frac{l}{Rwd} \quad (3.5)$$

with  $\sigma$ : conductivity,  $l$ : IDE channel length (here  $5 \mu\text{m}$ ),  $R$ : impedance at given frequency,  $w$ : IDE channel width (here  $1.917 \text{ m}$ ), and  $d$ : film thickness (here  $50 \text{ nm}$ ).

These first results were promising but measuring of the second IDE (Sample 2) already questioned the validity of those results. Figure 3.35 shows a comparison of the initial measurement of both samples as well as their spectra at 20 mbar  $p_{\text{H}_2\text{O}}$ . Spectra of Sample 2 are mostly non-characterisable due to their high impedance in the realm of  $\text{M}\Omega$  to even  $\text{G}\Omega$  even at high water partial pressure. The contrast to spectra of Sample 1 is stark when paying attention to the respective scales of impedance, which in turn is responsible for the difference in spectrum quality. Rough semi-circles can be determined for Sample 2 with hints of either *Warburg* elements or a large second semi-circle but impedance values are 3 orders of magnitude higher than in Sample 1. Since both samples were prepared in the identical way both results have to be questioned and the experiment was repeated.

The sample prepared in the previous chapter was then measured (**PV73-SO<sub>3</sub>/CC**) after thorough characterisation confirmed a successful functionalisation as was described there. Like with the early samples above, this one first underwent an initial measurement to evaluate its responsiveness. The corresponding spectrum is given in Figure 3.36. Even in untouched and ambient conditions, impedance lies in the region of  $\text{M}\Omega$  to  $\text{G}\Omega$  for this sample. Measured values fluctuate greatly due to the high resistance within the system and no indications of half-circles can be found. In other words, the sample does not show any measurable conductivity, electronic or ionic. This was rather unexpected, seeing the conclusive confirmation of ions being introduced into the system in the previous chapters. This result suggests the promising first sample was an exception, either because residual salts from the CuAAC reaction were still present and caused the notable ionic conductivity or because the lack of crosslinking provided a better template for functionalisation (as opposed to the crosslinked **PV73-SO<sub>3</sub>/CC** sample). On the other hand, even with crosslinking in place efficient conversions have been shown and presence of ionic groups has been confirmed in the samples. Impedance spectra, however, suggest there is no effective

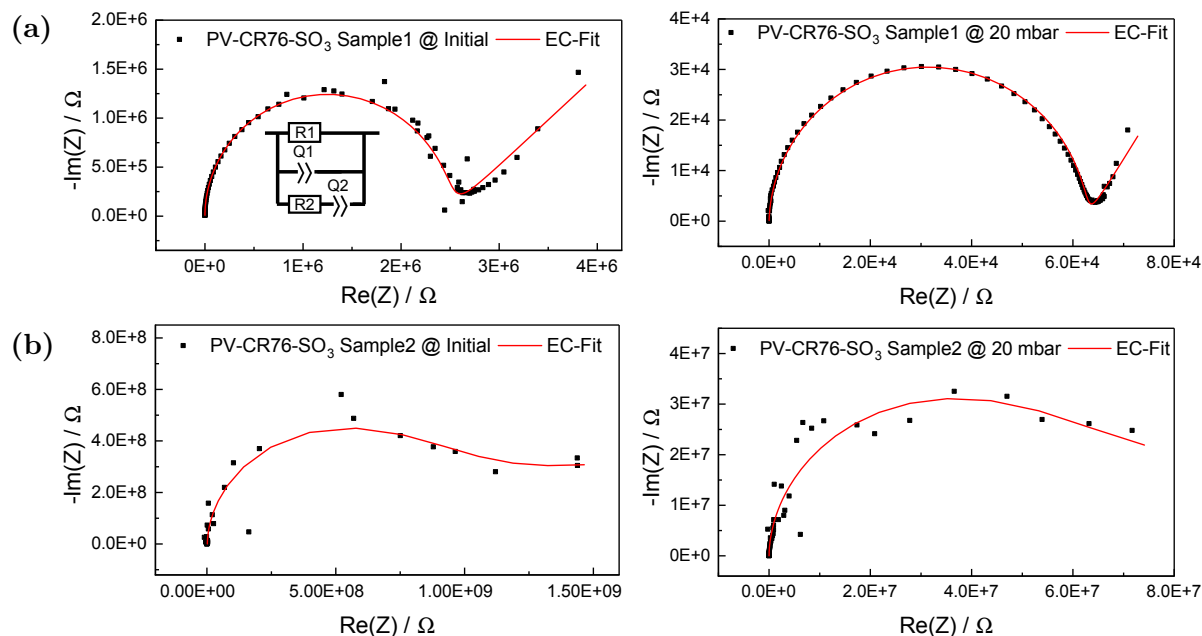


**Figure 3.35:** Comparison of impedance spectra of two non-crosslinked samples of **PV-CR76-SO<sub>3</sub>** prepared by CC. (a) Sample 1 has been characterised by varying water partial pressure in Figure 3.34. (b) Sample 2 shows extremely high impedance even at 20 mbar water partial pressure, further characterisation was thus not feasible. Displayed equivalent circuit used for all fits.

ionic pathway in the system (compare Scheme 1.15<sup>[13]</sup>).

This poses the question how the confirmed conversions and the lack of ionic pathways or mobilities go together. Remembering the fact that in all experiments small amounts of azide remained to varying degrees one assumption to be made is that *click* functionalization simply does not reach far enough into the polymer film to reach the electrode surface, despite the films only being 30 nm thin. This would mean that there is no connection of the ionic paths in the polymer to the electrode to give an answer to the frequency stimulation during impedance spectroscopy. As TPA groups are non-conducting in their undoped state as well,<sup>[3]</sup> no response is given. A way around this issue would be to functionalize the polymers before films are produced, meaning the *clicking* is performed in solution of the bulk material. The possible issues with this approach (termed Bulk Click BC) have been discussed earlier (see chapter 2). Nevertheless, the approach was pursued and started off with the BC functionalization of **PV73-A**.

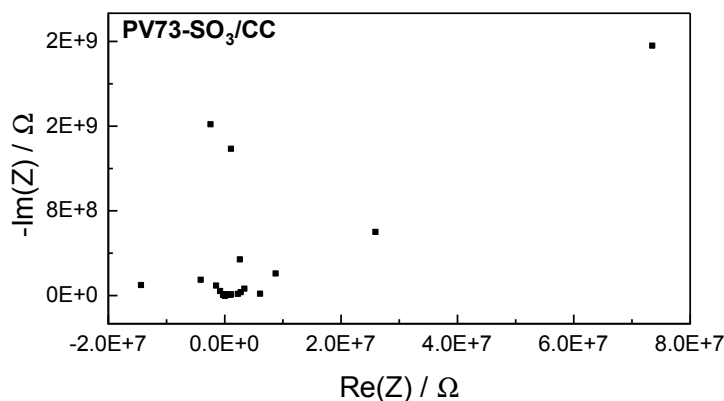
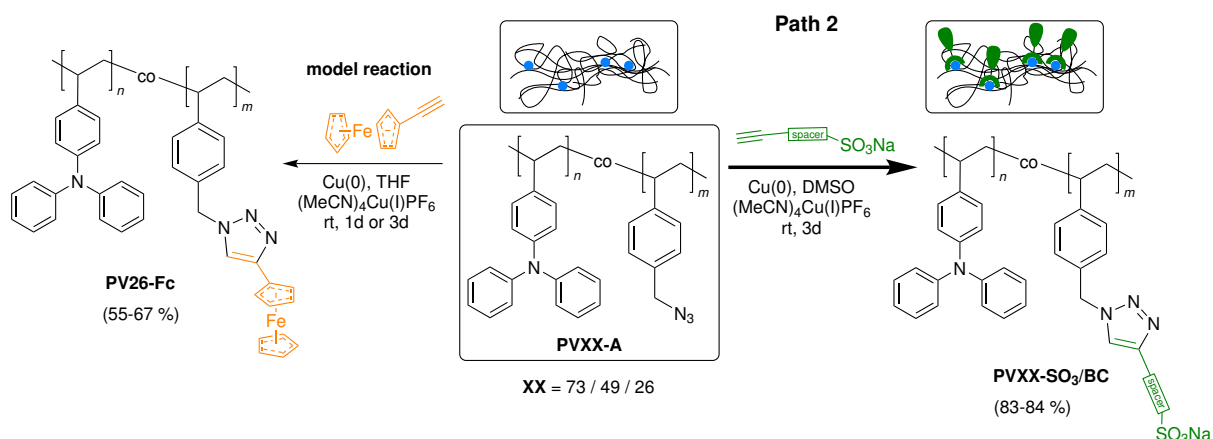


**Figure 3.36:** Nyquist plot of initial impedance measurement of crosslinked **PV73-SO<sub>3</sub>/CC**. Impedance values are large and no resistance could be determined.

### 3.3.2 Polymer Analogous Conversion of Dissolved Copolymers (BC)



**Scheme 3.8:** Reaction scheme for the bulk click functionalisation (BC) of the precursor polymers in solution. Clicking with E-Fc acts as a model reaction for the ionic functionalization.

A major advantage of the BC approach as described in chapter 2 is the fact that the functionalized polymer is obtained in bulk form and so can be characterised more easily and more thoroughly by additional techniques. Since the reaction is performed in a standard flask equipped with a stirrer and accordingly there's more movement involved it was deemed possible to shorten the reaction time from 3 days to an overnight reaction, which would give the method yet another advantage over functionalisation in film. Since I couldn't be sure about the precise repercussions the introduction of sulfonate groups into the polymer would have with regards to solubility and processability, ethynyl ferrocene was again used first to evaluate the reaction conditions, as with its nonpolar character it

wouldn't influence the polymer's solubility negatively.

These test reactions were performed with **PV26-A**, simply due to the amount of substance that was available of each of the three polymers. Workup was the same as for the original copolymers (PVXX) and reaction evaluation was done by IR (ATR) spectroscopy. DMSO was replaced by THF as reaction solvent for better polymer solubility. Figure 3.37 shows the comparing spectra before and after the overnight reaction. It's clearly visible that not all  $N_3$  groups have been converted and since the reaction is not done in film accessibility of those groups can not be the issue. Accordingly, the reaction was repeated and this time kept stirring for 3 days. The resulting IR spectrum is shown in Figure 3.37 (bottom) and no azide band can be found any more. Keeping to the original 3 days reaction time remains important with this catalytic system even when done in stirred solution.

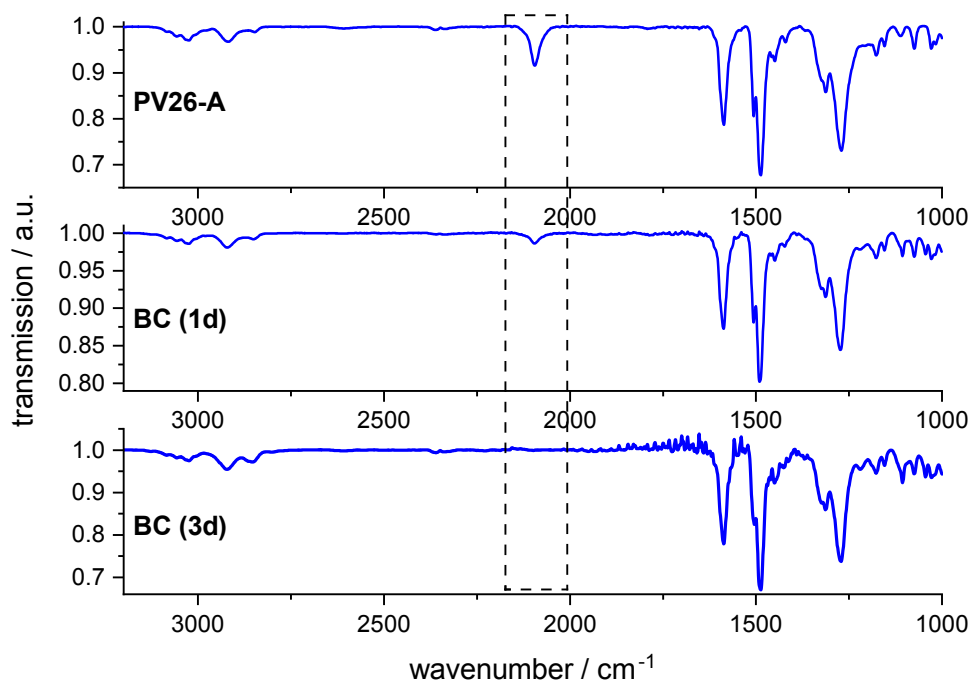


**Figure 3.37:** IR (ATR) transmission spectra of **PV26-A** (top) being converted with ethynyl ferrocene by BC for 1 day (center) and for 3 days (bottom). Azide band region is marked.

Subsequently, **PVXX-A** polymers were reacted under these conditions with the alkyne sulfonate **6**. As THF turned out to be unable to dissolve the ionic alkyne, DMSO was used again as the reaction solvent, although the polymers' solubility in it is mediocre. Due to the ionic groups changing the polymers' physical properties the work-up routine had to be altered as their solubility behaviour had changed dramatically. This in itself was a first

promising result pointing towards a successful functionalization, only the scope of which was not yet known. A number of solvents was tested for solubility, both for attempts for dissolving the polymer and to find a suitable solvent to precipitate it in, as methanol's polar character might make it a bad choice for that. Table 3.5 gathers the results of those tests.

**Table 3.5:** Solubility of **BC**-prepared polymers in various solvents.

Solvent	DMSO	CHCl <sub>3</sub>	MeOH	MeCN	Et <sub>2</sub> O	THF	H <sub>2</sub> O	THF/H <sub>2</sub> O
<b>Soluble</b>								
<b>PV26-SO<sub>3</sub>/BC</b>	No	No	No	No	No	No	No	(Yes)
<b>PV49-SO<sub>3</sub>/BC</b>	(Yes)	No	No	No	No	No	No	Yes
<b>PV73-SO<sub>3</sub>/BC</b>	(Yes)	No	No	No	No	No	No	Yes

In the case of **PV26-SO<sub>3</sub>/BC**, no viable solvent or solvent mixture could be found as the low share of ionic groups didn't make the polymer polar enough to dissolve in polar solvents, however made it polar enough to not dissolve in non-polar ones, either. Some solubility in THF/H<sub>2</sub>O (1:1) was found but too little for precipitation or the preparation of solutions for the production of films. This meant that this polymer could not be properly purified, nor used further. The other two polymers, however, could. Interestingly, neither water nor THF alone is able to dissolve them, a mixture of both, on the other hand, is. Accordingly, for the preparations of polymer solutions to cast films in the future it was decided to use 1:1 mixtures of THF and water. DMSO would provide another possibility but would prove to be notably harder to remove from the cast films afterwards, if not outright practically impossible. Furthermore, once the polymers were purified and dried, solubility in DMSO turned out to be too low for practical use.

Workup of the polymers was performed accordingly while it turned out that acetonitrile worked very well as a precipitation solvent. Thus, **PV73-SO<sub>3</sub>/BC** and **PV49-SO<sub>3</sub>/BC** were dissolved in THF/Water and precipitated in MeCN, affording fine polymer powders with a green or yellow tint, respectively. **PV26-SO<sub>3</sub>/BC** was washed with methanol in an attempt to purify it enough for basic characterization. Subsequently, ATR-IR characterisation of all powders was done, the spectra of which are provided in Figure 3.38. Azide band region is marked and as with the ferrocene BC conversion before, any traces of azide are completely gone in all three spectra. The reaction thus proceeded perfectly and 150 mg (**PV26-SO<sub>3</sub>/BC**), 180 mg (**PV49-SO<sub>3</sub>/BC**) and 230 mg (**PV73-SO<sub>3</sub>/BC**) of polymer were obtained, which translates to 61 %, 83 % and 84 % yield by mass, respectively.

From the spectra, a relationship between sulfonated parts of the polymers and triphenylamine-bearing parts can be assessed, e.g. one can look at the C=C band at 1490 cm<sup>-1</sup> and compare it to one of the S=O bands at 1190 cm<sup>-1</sup>/1045 cm<sup>-1</sup>. The stacked depiction

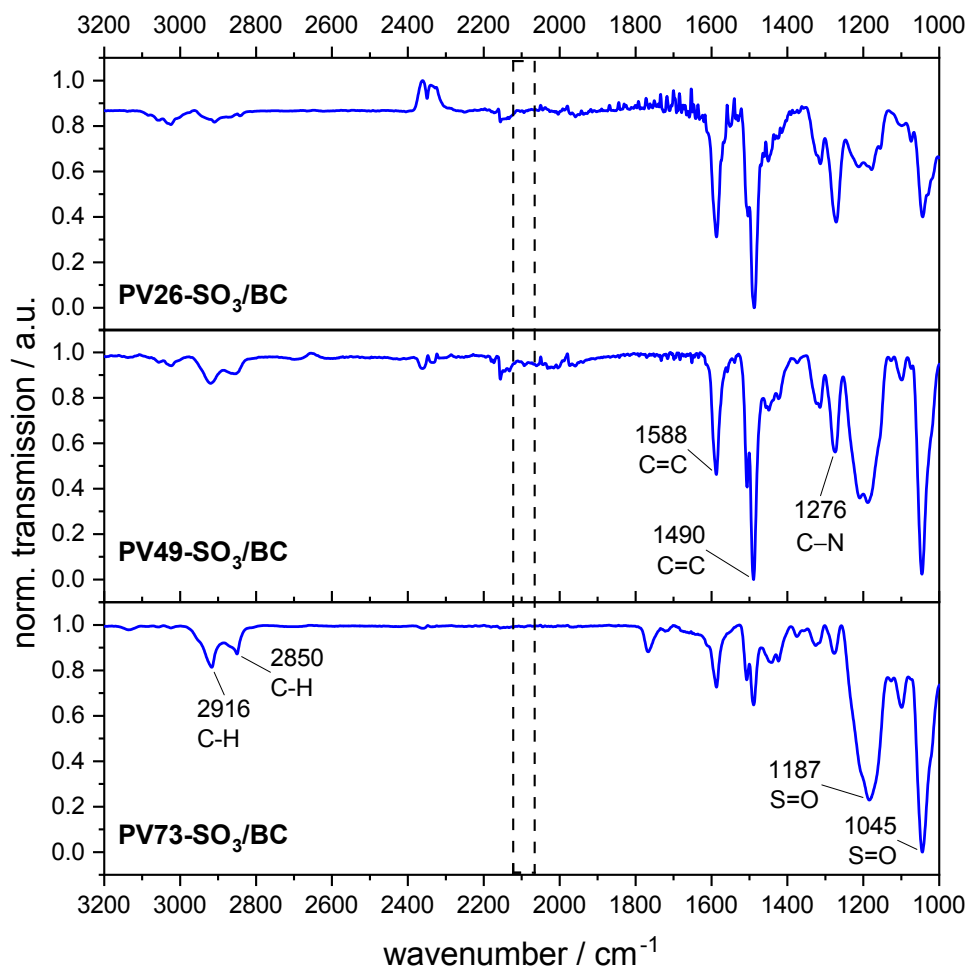


**Figure 3.38:** IR (ATR) transmission spectrum of **PV26-SO<sub>3</sub>**, **PV49-SO<sub>3</sub>** and **PV73-SO<sub>3</sub>** synthesized by BC from respective **PVXX-A** template polymers. Region where azide bands would be visible is marked.

shows nicely, how the ratio changes with an increasing amount of functionalized groups, as the number of C=C double bonds in the polymer decreases with decreasing TPA content.

TGA, displayed in Figure 3.39, showed a major step in each polymer with onset temperatures between 337 °C and 358 °C which are assigned to polymer backbone degradation. Compared with the respective **PVXX-A** precursors where this step lied above 380 °C this is a small reduction in overall stability. Another difference to the precursors lies in the number of steps that can be determined. Whereas the azide copolymer each showed one extra step at shortly over 200 °C degrees, conforming to azide degradation, these clicked polymers show between one and three steps, total. For **PV26-SO<sub>3</sub>/BC** one step can be found, for **PV73-SO<sub>3</sub>/BC** it's two steps and in **PV49-SO<sub>3</sub>/BC** three steps can be seen. However, for the 26 % polymer this could simply be due to the lower number of clicked groups being less pronounced in the overall spectrum as a hint of a second step at about

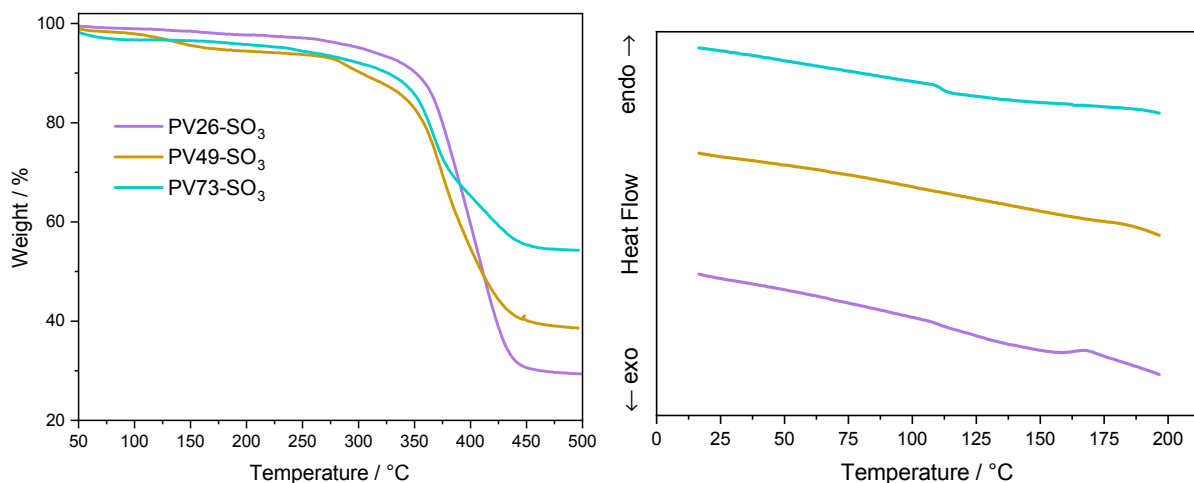


**Figure 3.39:** TGA (left) and DSC (right) spectra of **PVXX-SO<sub>3</sub>/BC** copolymers. TGA: 30 °C to 500 °C at 5 °C/min. DSC: 2nd heat curve at 10 °C/min, sorted by name.

100 °C can be observed and even a third one at the 260 °C range when zooming in closely. Nonetheless, only in the 49% copolymer are all three steps well-defined. **PV49-SO<sub>3</sub>/BC** and **PV73-SO<sub>3</sub>/BC** both show a second step overlapping the main steps at 273 °C and 278 °C, respectively, and are interpreted as side-chain degradation. Onset temperature for PV49-SO<sub>3</sub>'s third step lies at 107 °C. Considering that PV26-SO<sub>3</sub>'s low-intensity second step is close to 100 °C, as well as taking into consideration the polymers' ionic nature it is reasonable to assume that those steps relate to moisture trapped in the polymer escaping. All onset temperatures are summarized in Table 3.6.

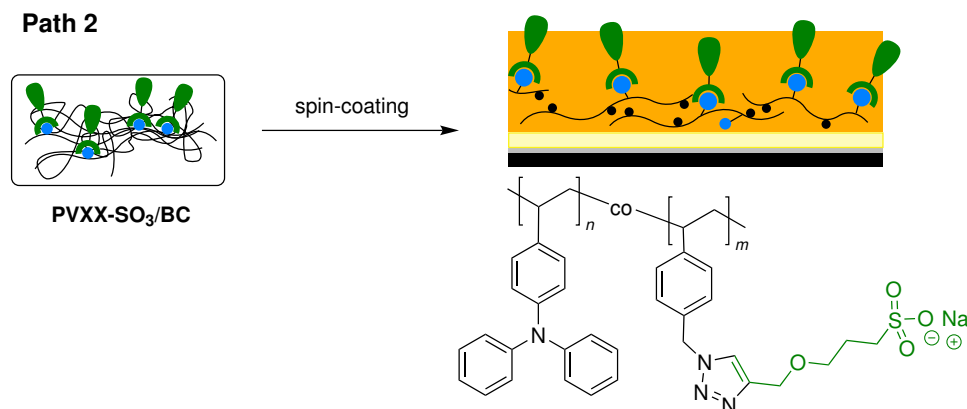
**Table 3.6:** Onset temperatures found in corresponding TGA spectra.  $T_g$  taken from DSC spectra. Numbers in parentheses are ill-defined in the spectra and thus not secured.

Polymer	$T_{Ons,1}$ / °C	$T_{Ons,2}$ / °C	$T_{Ons,3}$ / °C	$T_g$ / °C
PV26-SO <sub>3</sub> /BC	(100)	(26X)	358	163
PV49-SO <sub>3</sub> /BC	107	273	354	–
PV73-SO <sub>3</sub> /BC	–	278	337	112

DSC characterization of those polymers gave  $T_g$  values of 112 °C in **PV73-SO<sub>3</sub>/BC** and 163 °C in **PV26-SO<sub>3</sub>/BC** which is a notable difference to their respective precursors, both in numbers as well as in the difference between polymers. **PVXX-A** polymers'  $T_g$ s lied closer together in the range of 107 °C to 128 °C. For **PV49-SO<sub>3</sub>/BC**, however, no distinct  $T_g$  can be observed from the heat curve. Zooming in closely reveals a step in heat flow at about 172 °C which could be considered a  $T_g$  but a more sensitive instrument will

be necessary to confirm this.

## Impedance Spectroscopy and Water Uptake



**Scheme 3.9:** Schematic depiction of production of thin polyelectrolyte films as part of **Path 2** after the polymers have been functionalized in solution *via* BC. No crosslinking is performed in these films.

To probe the obtained bulk polymers (with the exception of **PV26-SO<sub>3</sub>/BC**), 5 mg mL<sup>-1</sup> solutions in equal mixtures of THF and water were prepared and spincoated onto interdigitated electrodes for use in impedance spectroscopy. Contrary to samples prepared *via* CC, these films were not crosslinked prior to impedance spectroscopy, as is depicted in Scheme 3.9. Channel length of employed electrodes was 5 μm unless stated otherwise. Measurements were performed at different water partial pressures starting from low water content after an initial measurement at ambient conditions. Figure 3.40 and Figure 3.41 provide exemplary impedance spectra at different water partial pressures ranging from low to high. The equivalent circuit model used to fit the obtained data and extract  $R_{ion}$  values is shown in the inserts. In most spectra the low frequency (high impedance) range is cut off, since due to  $R_{el}$  being so large the respective semi-circles would dwarf the ones shown here.

Figure 3.42 provides the employed humidity program and the ionic resistance values obtained from the corresponding impedance spectra. Overall, a clear and significant correlation of  $p_{H_2O}$  and ionic resistance  $R_{ion}$  can be observed. As discussed earlier, a similar dependency had been found in **PV73-SO<sub>3</sub>/CC** (clicked in film) but could not be reproduced by subsequent samples. Here, the values given are based on two separate samples and show good agreement at most water partial pressures. For **PV73-SO<sub>3</sub>/BC** depicted in Figure 3.42(a), starting from low air water content change in ionic resistance decreased rapidly over several orders of magnitude up to a  $p_{H_2O}$  that can be considered

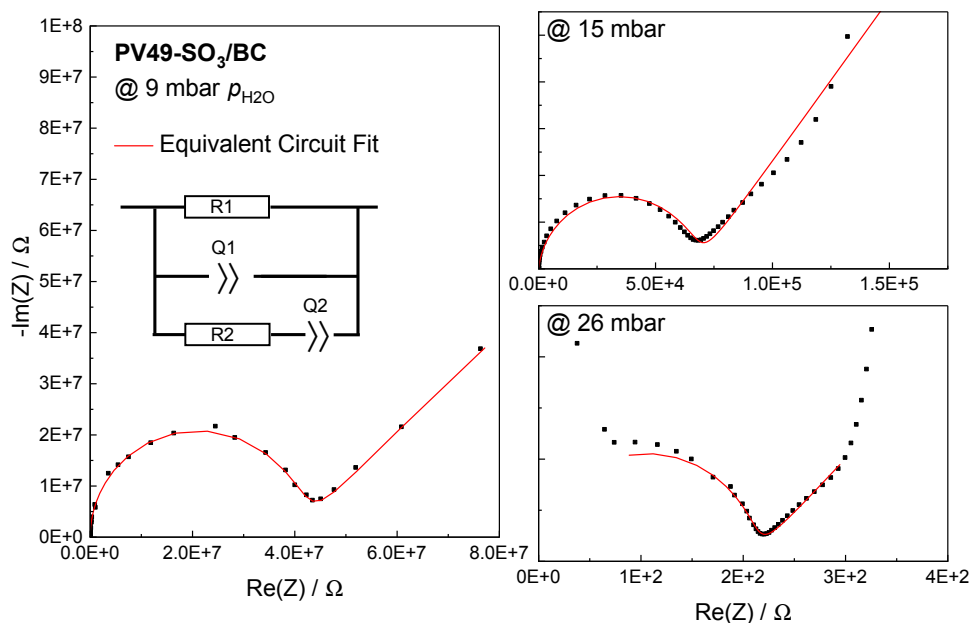


**Figure 3.40:** Exemplary impedance spectra of PV49-SO<sub>3</sub>/BC deposited as films on IDEs at different water partial pressures. Note the different orders of magnitude.

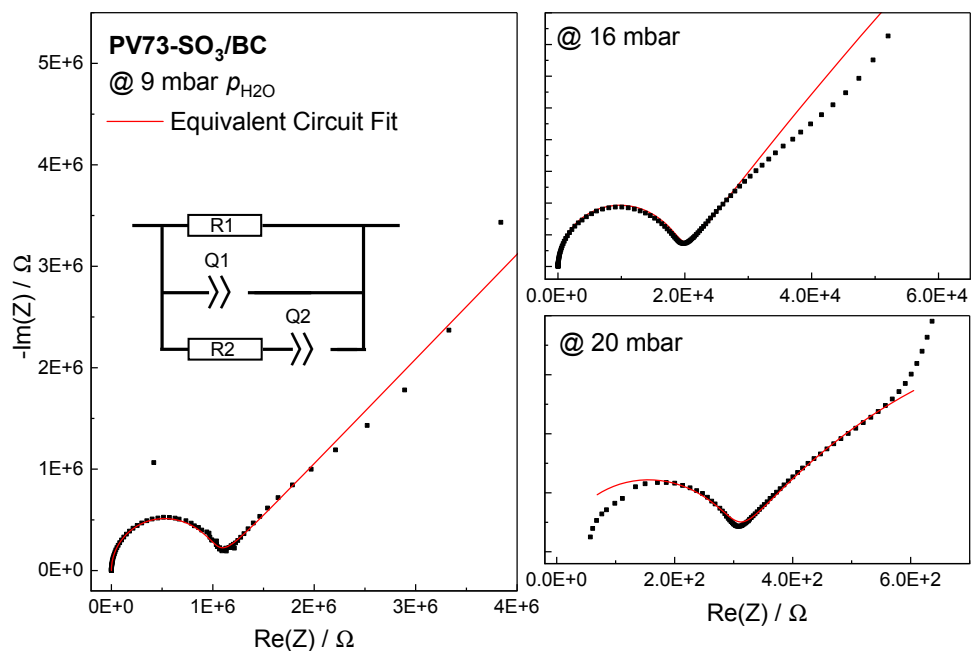


**Figure 3.41:** Exemplary impedance spectra of PV73-SO<sub>3</sub>/BC at different water partial pressures. Note the different orders of magnitude.

close to ambient conditions (roughly 15 mbar). In low  $p_{H_2O}$  atmosphere, resistance consistently lied in the gigaohm region. At this scale, exact values cannot be extracted from the obtained spectra because the high impedance is testing the limits of the spectrometer.

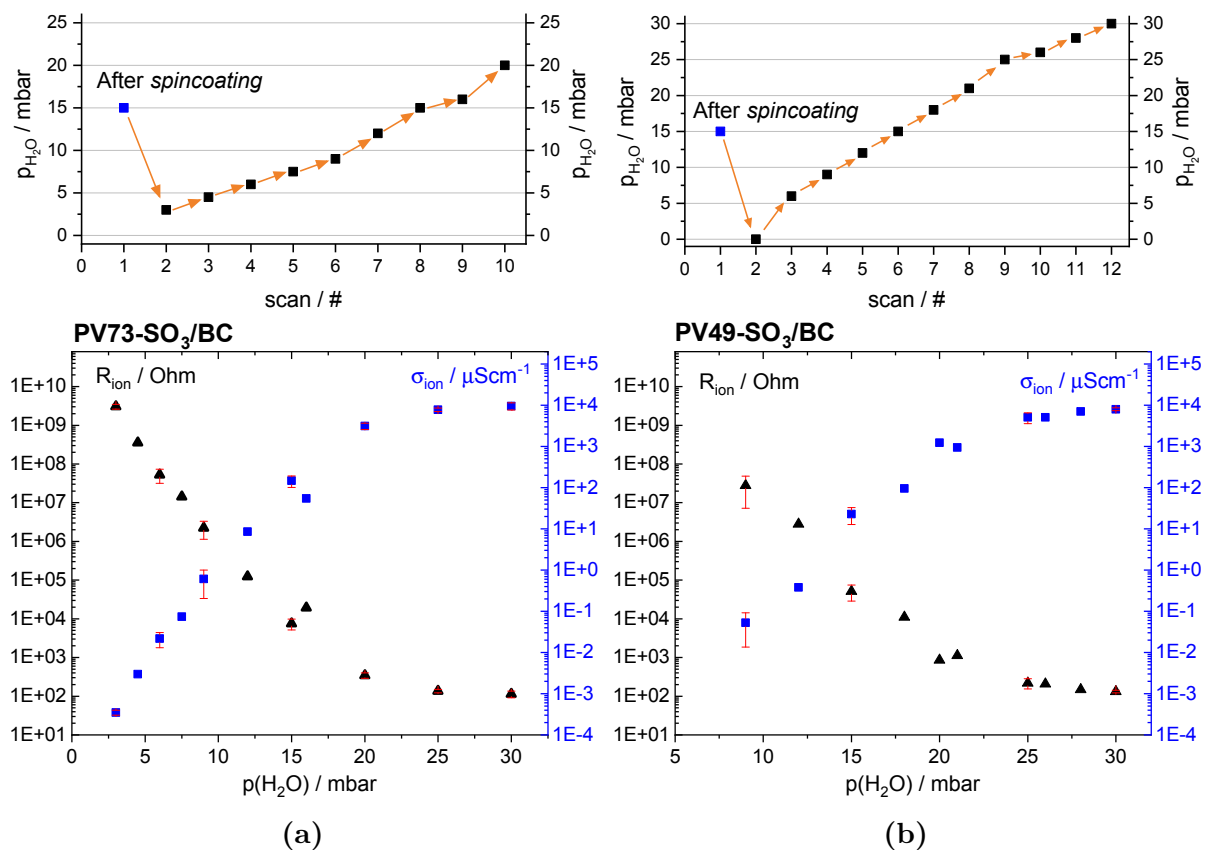


**Figure 3.42:** Water partial pressure dependent impedance spectroscopy of (a) **PV73-SO<sub>3</sub>/BC** and (b) **PV49-SO<sub>3</sub>/BC** prepared on interdigitated electrodes (IDE). (Top) Procedures applied for changing water partial pressure ( $p_{H_2O}$ ). Time given to equilibrate to each new  $p_{H_2O}$  was  $\geq 90$  min. (Bottom) Ionic resistance (black) and ionic conductivities (blue) plotted against  $p_{H_2O}$ . Ionic conductivities are calculated from the obtained ionic resistance values.

At 0 mbar, interpretations are outright impossible because no characteristic spectrum can be obtained, hence this water partial pressure could not be included in the given graphs. Going from 3 mbar to 15 mbar however, obtained resistance values decrease from the gigaohm scale to kilohm numbers, covering a range of 4 orders of magnitude. Higher water partial pressures of up to 30 mbar show a slower decrease and seem to plateau in the region of low hundreds of ohm, with 7530  $\Omega$  at 15 mbar and a minimum of 129  $\Omega$  at 30 mbar for this polymer. With lower ionic content in **PV49-SO<sub>3</sub>/BC** a very similar picture is observed, displayed in Figure 3.42(b). At 30 mbar a minimum resistance of

132  $\Omega$  was measured, virtually identical with **PV73-SO<sub>3</sub>/BC**. However, when moving to lower water partial pressures, resistance increases more strongly and at 15 mbar an  $R_{ion}$  of 51 500  $\Omega$  is already measured. Since interdigitated electrodes are ill-suited for film thickness determination *via* scratching because of their architecture and susceptibility to damage, films have been prepared analogously on undoped silicon substrates using the same polymer solutions and spincoating conditions. Thickness was then measured using atomic force microscopy and amounted to  $(28 \pm 4)$  nm for both polymers. Using this value and electrode dimensions given by the manufacturer, ionic conductivities in Figure 3.42 have been calculated. In **PV73-SO<sub>3</sub>/BC** a maximal ionic conductivity of 9542  $\mu\text{S cm}^{-1}$  was achieved at 30 mbar water partial pressure. With **PV49-SO<sub>3</sub>/BC**, 8000  $\mu\text{S cm}^{-1}$  were reached at this same humidity. Incidentally, this value appears to depict the plateau of achievable ionic conductivity in this experiment, as was the case for ionic resistance. When considering 15 mbar  $p_{H_2O}$  as close to ambient conditions, the polymers can still reach values of 23  $\mu\text{S cm}^{-1}$  (**PV49-SO<sub>3</sub>/BC**) and 147  $\mu\text{S cm}^{-1}$  (**PV73-SO<sub>3</sub>/BC**) in ambient atmosphere. From Figure 3.42(a) it can be observed, though, that a considerable deviation from these values is possible at this humidity level, with 16 mbar lying notably lower in conductivity.

With impedance spectroscopy showing a considerable humidity dependent ionic share in conductivity, characterising the polymers' behaviour in wet environment became of interest. This can be quantified by quartz crystal micro balance experiments, where change in polymer film weight at different water partial pressures can be determined. This then allows to calculate the water uptake of the film relative to its own mass. Measurements were run at different target relative humidities ranging from 0 % to 97 % while the quartz crystal substrate's vibrational frequency was recorded. Each new step in the relative humidity ladder was given at least 90 min to equilibrate except for the last which was held for twice that time. Figure 3.43 presents the resulting spectra where both ladder curves, rel. humidity (RH) and quartz crystal weight increase, calculated from measured vibrational frequencies, are given. A plateau can be observed at each new step in both curves which confirms that an equilibration time of 90 min is sufficient. As the mass of the polymer film increases with increasing water uptake from the ever more humid atmosphere, its frequency decreases accordingly. Unexpected behaviour can be observed during the last increase of humidity in Figure 3.43 (bottom, **PV73-SO<sub>3</sub>/BC**), as  $\Delta m_{crystal}$  seems to increase in a two-step process. The nature of this occurrence is not entirely clear but I hypothesize that either some internal reordering in the polymer film occurs at high water partial pressures that ultimately gives way to previously unoccupied water "traps", thus allowing for a smaller second increase in water uptake or, though unlikely under the employed conditions, that micro condensation is occurring on the polymer film, thus

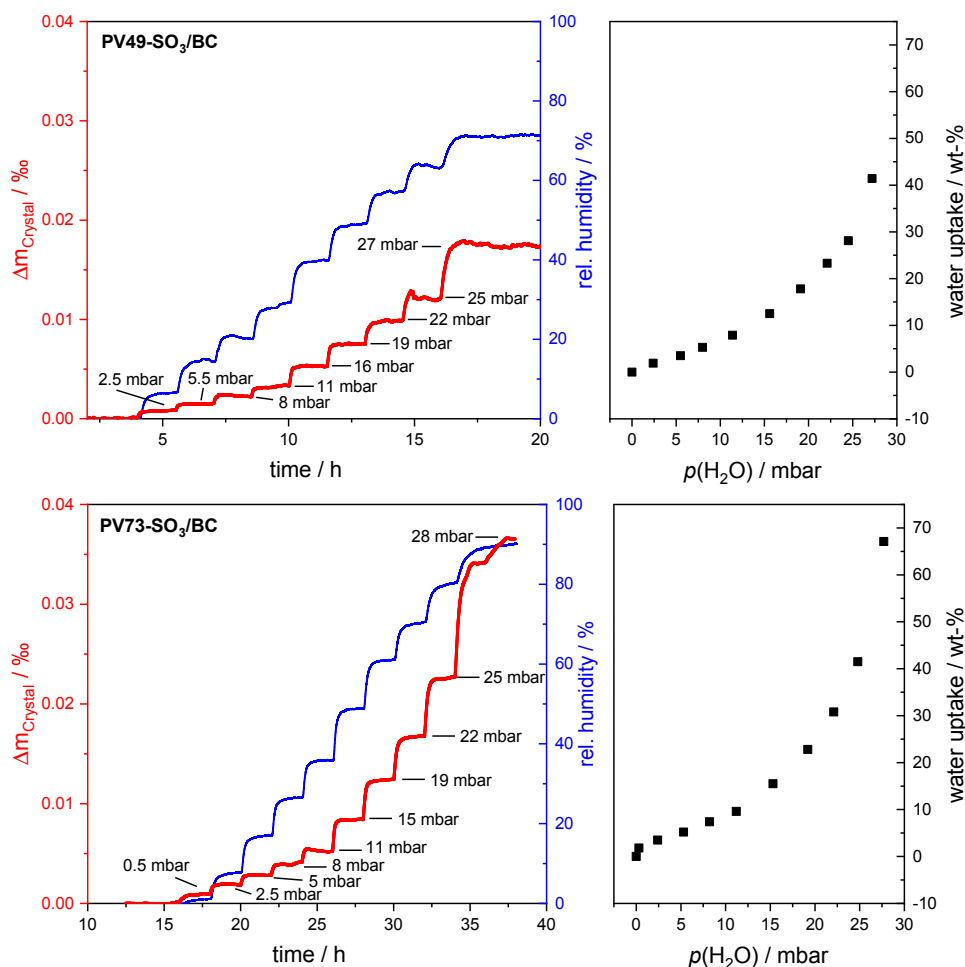


**Figure 3.43:** (Left) Quartz crystal microbalance determination of vibrational frequencies of **PV49-SO<sub>3</sub>/BC** and **PV73-SO<sub>3</sub>/BC** at different relative humidity values with calculated mass increase of the crystal. (Right) Proportional water uptake in weight percent with regards to polymer mass at increasing water partial pressure. Time given to equilibrate to each new RH between measurements was  $\geq 90$  min.

increasing its weight and decreasing its vibrational frequency. This effect was not observed in the measurement of **PV49-SO<sub>3</sub>/BC**, which would contradict this last explanation. It is also possible that the film simply does not swell homogeneously. It can be seen from Figure 3.43 (top) that RH has its plateau at lower values in this measurement, however, the maximum  $p_{\text{H}_2\text{O}}$  was similar. This deviation is due to summer temperatures in the laboratory at the time of measurement which influenced the data recorded by the humidity sensor positioned outside the temperature controlled oven. Nevertheless, temperature on the inside where the sample is placed was lower, according to the oven's sensor, thus this should not be a relevant factor. A notable difference can be seen in the relative mass increase of the quartz crystals, where in the case of **PV73-SO<sub>3</sub>/BC** increase topped of

at 0.037 ‰ of the crystal’s mass while **PV49-SO<sub>3</sub>/BC** only reached 0.018 ‰.

Water uptake in weight-% can be calculated from the obtained data *via* the formula

$$wt\text{-}\%(\text{H}_2\text{O}) = \frac{f_{dry} - f_{wet}}{f_{empty} - f_{dry}} \cdot 100 \quad (3.6)$$

with  $f_{empty}$ : vibrational frequency of the empty quartz crystal,  $f_{dry}$ : vibrational frequency of the polymer film in dry atmosphere and  $f_{wet}$ : frequency in wet atmosphere.

Figure 3.43(right) visualises the evolution of wt-%(H<sub>2</sub>O) with increasing water partial pressure in the experimental setup. As with the ionic resistance and conductivity, change in the lower humidity region is slow and only starts to pick up around half-way through the experiment in both polymers. Overall, the water uptake curves increase exponentially with increasing water partial pressure and reach a maximum of 67 wt-% at 28 mbar (90 ‰ RH) for **PV73-SO<sub>3</sub>/BC** and a maximum of 41 wt-% at 27 mbar (71 ‰ RH) for **PV49-SO<sub>3</sub>/BC**. Here,  $p_{\text{H}_2\text{O}}$  have been calculated from respective RH values using the temperature recorded by the humidity sensor during the experiment. In the case of **PV73-SO<sub>3</sub>/BC**, one step below the maximum RH was at 80 ‰ which corresponded to 24.8 mbar  $p_{\text{H}_2\text{O}}$  and provides a notably lower water uptake of 41.5 wt-%, underlining the fact that the polymer is able to take up a decent amount of water, relative to its own weight, but high water partial pressures close to a saturated atmosphere are required. Unsurprisingly, the polymer with less ionic groups is able to take up less water with its maximum of 41 wt-%. In fact, when putting both polymer’s share of ionic groups in relation (0.49/0.73) which gives a ratio of 0.67, maximum water uptake isn’t far off with a ratio of 0.58. Nonetheless, this also shows that **PV73-SO<sub>3</sub>/BC** outperforms **PV49-SO<sub>3</sub>/BC** with regards to water uptake per functional group. But if water uptake isn’t of quantitative interest in the sense of maximum values but is thought to be employed rather systematically, both experiments, QCM and impedance spectroscopy, characterise both copolymers with a consistent profile concerning responds to stimulus by water in the surrounding atmosphere, which can prove to be viable in corresponding applications, especially at ambient conditions and in more humid settings.

### 3.4 Summary

In this chapter, free radical polymerization of VTPA and CMS monomers was presented, based on reaction conditions from literature<sup>[131,132]</sup> and modified to give reliable results with different monomer feed ratios. Polymerizations afforded copolymers **PV26**, **PV49**

and **PV73**, wherein the numbers represent the share of functionalizable (CMS) groups in the respective polymers. Nucleophilic substitution of chlorine with azide in the polymer side-chains gave **PVXX-A** copolymers, ready to be converted in CuAAC *Click* reactions. Successful and complete substitution was confirmed by  $^1\text{H-NMR}$  and PM-IRRAS measurements. Thermogravimetry found the polymers to be stable up to about  $210\text{ }^\circ\text{C}$  where azide groups start to decompose.

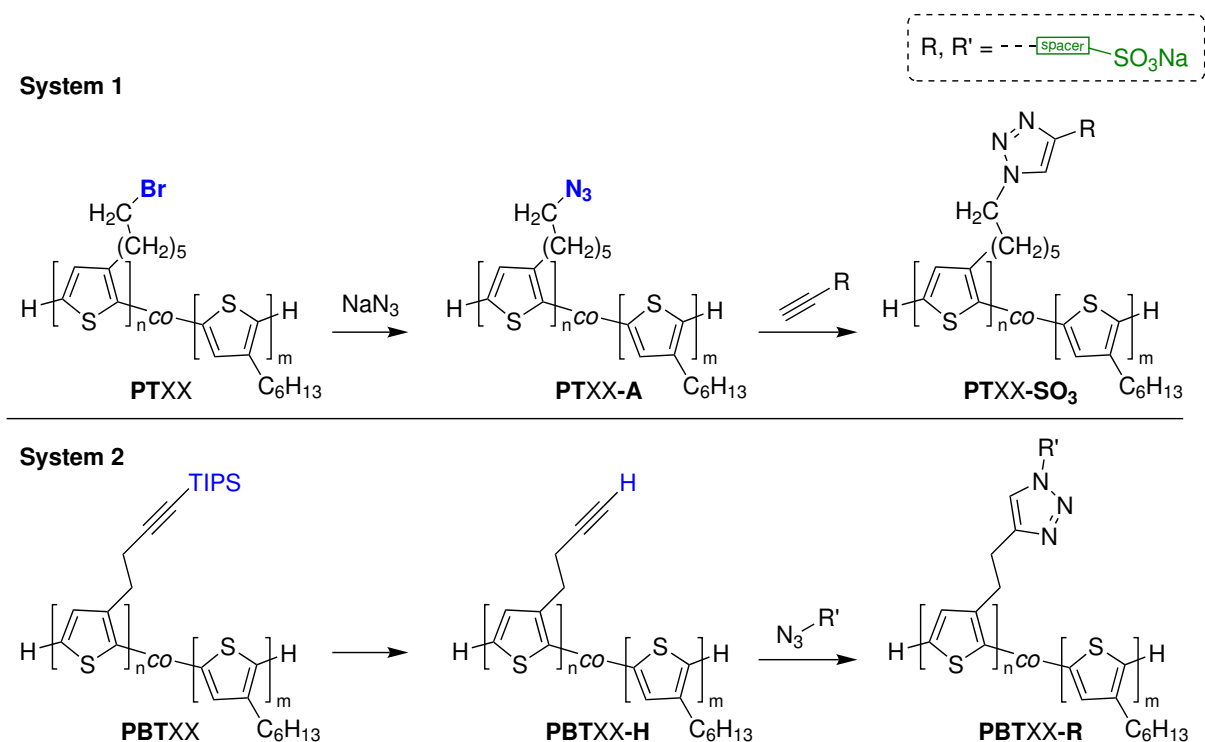
From the prepared polymers, thin films were cast by spin-coating. Electrochemical, oxidative cross-coupling of the polymers' TPA groups into TPB molecules stabilized the films against dissolution, crucial for click chemistry *via* CC procedure where the films are to be submerged in solvent for several days. Furthermore, crosslinking provides the films with stable redox switching. Cyclic voltammetry, including half-wave potentials were compared to similar, non-functional PVTPA:PS copolymers from earlier works and a change in CV structure with higher styrene (derivative) content was observed in a similar manner, attributed to the insulating character of polystyrene and thus impeded electrolyte ion diffusion.

Efficacy of EC vs CC procedure was assessed with the decision falling on CC for subsequent functionalizations. A model reaction with alkyne sulfonate **6** confirmed the validity of the CC/BC catalytic system and served to identify characteristic chemical shifts in  $^1\text{H-NMR}$  for later BC conversions. Further evaluation of the CC method was done by converting crosslinked **PVXX-A** films with Ethynylferrocene. PM-IRRAS characterization revealed that all polymers are converted, however, in all cases small amounts of unreacted azide groups remained in the polymers, suggesting that not all functional groups inside the polymer films are accessible during reaction, possibly a consequence of crosslinking. CV measurements of the converted **PVXX-Fc** films confirmed the covalent introduction of the redox-active ferrocene units *via* a comparison of voltammogram shapes of loose and immobilized ferrocene. Scan rate dependent cyclic voltammetry showed a linear relationship between peak currents  $i_p$  and scan rate  $\nu$ , further confirming the covalent binding in all polymers.

Accordingly, conversion was repeated with the ionic alkyne sulfonate **6**, both *via* CC and BC procedure. In the case of CC and even at high water partial pressures  $p_{\text{H}_2\text{O}}$ , impedance spectroscopy did not show ionic conduction, although successful introduction of ionic groups could be reasonably assumed. It seems that with this method, no effective ionic pathways were formed in the polymer. Ionic functionalization of **PVXX-A** polymers in solution *via* the BC method, however, proceeded quantitatively with regards to azide groups. Here, **PV26-SO<sub>3</sub>/BC** turned out to be insoluble in any solvent system tested and thus was not characterized except with IRRAS. For **PV49-SO<sub>3</sub>/BC** and **PV73-SO<sub>3</sub>/BC**, films cast from THF/H<sub>2</sub>O solutions showed ionic contributions in impedance

spectroscopy. **PV73-SO<sub>3</sub>/BC** gave a maximum ionic conductivity of 9542  $\mu\text{S cm}^{-1}$  at 30 mbar  $p_{\text{H}_2\text{O}}$  and humidity dependent water uptake determined by QCM gave a maximum uptake of 67 wt-% at 90 % RH/28 mbar. In comparison to that, **PV49-SO<sub>3</sub>/BC** with its lower ionic content showed a very similar maximum  $R_{ion}$  with 8000  $\mu\text{S cm}^{-1}$  at 30 mbar  $p_{\text{H}_2\text{O}}$ , although this value decreases much more quickly with lower water partial pressure. Also, its highest water uptake turned out lower than could be expected from comparing the number of ionic groups between polymers, with 41 wt-% at 71 % RH/27 mbar.

# 4 Thiophene-based Conjugated Polyelectrolytes



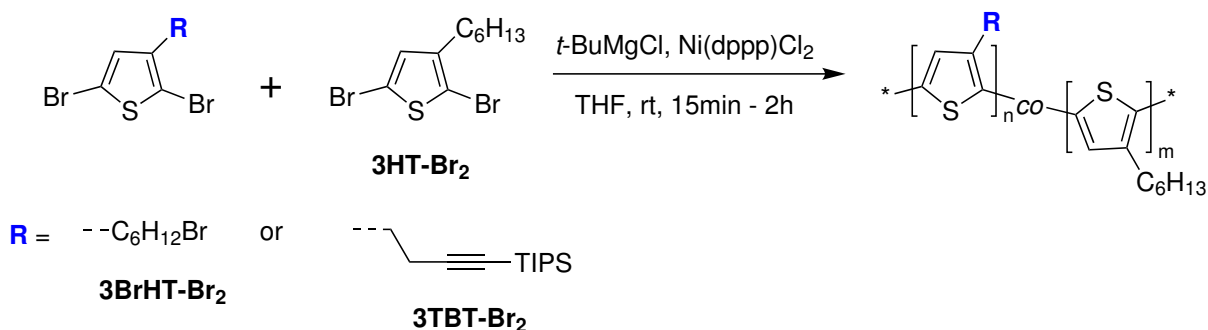
**Scheme 4.1:** Thiophene-based copolymer systems and their schematic functionalisation. **XX** can vary and states the molecular share of functionalizable monomers in the synthesized systems.

Two thiophene-based copolymer systems were created in the scope of this work based on three different monomers (see Scheme 4.2), offering inverted side-chain functionalities with respect to each other for use in CuAAC reactions.

Copolymer-system 1 (**PTXX**) is based on 3-Hexylthiophene (3HT) and 3-Bromohexylthiophene (3BrT) and is functionalized by azide groups. System 2 (**PBTXX**) offers alkyne-functionalities as part of its butynyl side-chains, stemming from its monomer 4-(thiophen-3-yl)-but-1-ynyl-triisopropylsilane (3TBT). Both systems and a schematic representation of their modification are depicted in Scheme 4.1. With different side-chain functionalities come different approaches for the introduction of ionic groups into the polymers. **PTXX** will be converted to the respective azide (**PTXX-A**) before CuAAC reaction with the sulfonate **6**, analogous to the conversion of TPA-based polymers before. Conversion of **PBTXX** requires the synthesis of a new reagent combining sulfonate- and

azide-functionalities into one molecule, as well as deprotection of the alkyne-group prior to CuAAC. Monomer- and polymer-synthesis of **PTXX** and **PBTXX** as well as subsequent functionalisations will be discussed in the following chapters.

## 4.1 Preparation of Polymers

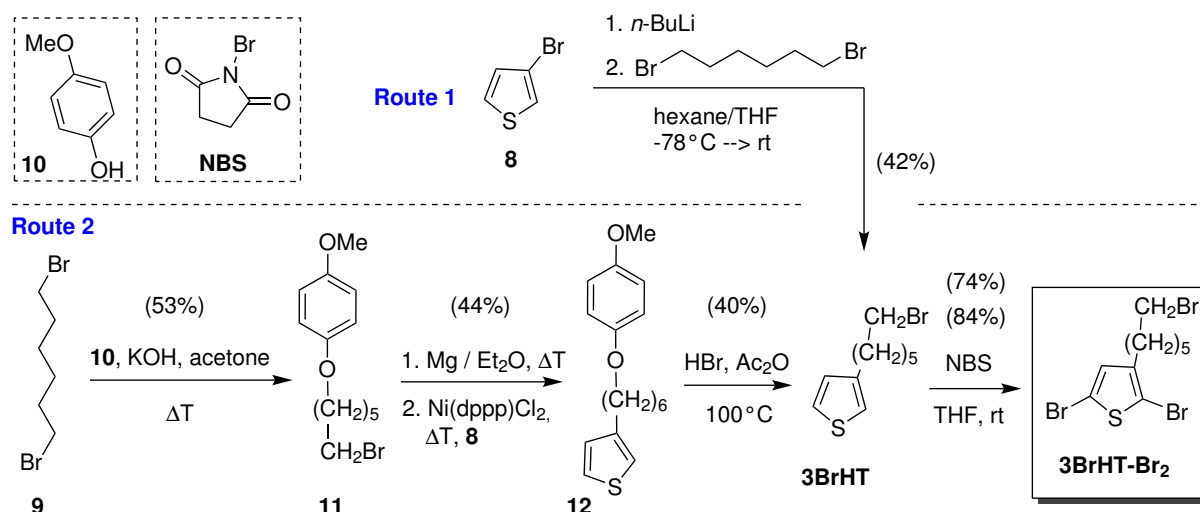


**Scheme 4.2:** Copolymerization schematic for GRIM-polymerizations. Structures of the three monomers are shown.

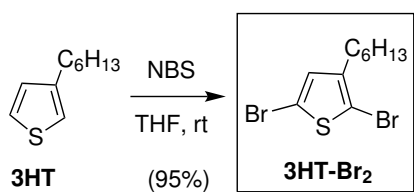
Polythiophenes in this work have been synthesized by *Grignard Metathesis Polymerization* (GRIM), often also referred to as *Kumada Catalyst Transfer Polymerization* (KCTP), employing Ni-based catalysis. Although this method of polymerization is well-known in literature and has already been successfully applied in this group multiple times, in our experience drawbacks concerning the quality of obtained polymers remained present to varying degrees, manifesting as either low-molecular tailing or unintended high-molecular peaks in size exclusion chromatograms. For this reason, synthesis of monomer **3BrHT-Br<sub>2</sub>** (see Scheme 4.3) was done in two different approaches and the subsequent polymerization reactions have been repeated a number of times with the intention of identifying and correcting factors negatively influencing the course of polymerization. The issues at hand as well as the different approaches will be discussed now.

### 4.1.1 Synthesis of 3HT-based monomers

Both monomers, **3HT-Br<sub>2</sub>** and **3BrHT-Br<sub>2</sub>** are brominated in the 2- and 5-position for use in the GRIM polymerization. In both cases this bromination can readily be achieved by reaction with excess of N-Bromosuccinimide (NBS) in THF. For **3HT-Br<sub>2</sub>**, commercially available 3-Hexylthiophene (3HT) can be used as a starting material and the yield is usually high or even close to quantitative.



**Scheme 4.3:** Reaction scheme for the synthesis of co-monomer **3BrHT-Br<sub>2</sub>** by two different routes.



**Scheme 4.4:** Reaction scheme for the synthesis of co-monomer **3HT-Br<sub>2</sub>**.

In case of the other co-monomer **3BrHT-Br<sub>2</sub>**, the precursor first has to be synthesized, which here was done in two ways. Both are shown in Scheme 4.3. Route 1, represented by the black reaction arrow, is a 2-step synthesis starting from 3-Bromothiophene **8** and 1,6-Dibromohexane **9**. Route 2 is a 4-step synthesis using the same starting compounds but modifying **9** first.

## 2-step synthesis

In the first step, **8** is being converted to the lithium analog *via* lithium-halogen-exchange before being reacted with 1,6-Dibromohexane **9** in equimolar fashion. Often the obtained crude product is now only worked up rudimentary before proceeding with the second step, the bromination. Because difficulties with the work-up after the second step were known, the goal was to try and improve the purification procedure after this first step before continuing with the second one. This included revisiting eluent mixtures for column chromatography as well as distillation methods. It showed that even multiple attempts with column chromatography gave little to no improvements. Instead, purification by

*Kugelrohr*-distillation appeared to be more effective, with the desired product distilling at 15 mbar/160 °C. NMR spectra displaying this situation are given in Figure 4.1. All efforts combined yielded about 42% of what was considered "pre-purified" **3BrHT**, ready to be converted further with NBS. This bromination follows the same procedure for both target molecules, **3HT-Br<sub>2</sub>** and **3BrHT-Br<sub>2</sub>**. In general, this second reaction is straight-forward but losses occur during the work-up process, especially in this 2-step synthesis due to difficult-to-remove impurities. This causes the work-up to be longer which might explain the difference in yield between route 1 and route 2. Despite many efforts in this work-up, signs of impurity can still be seen in Figure 4.1 which proved persistent against all purification attempts.

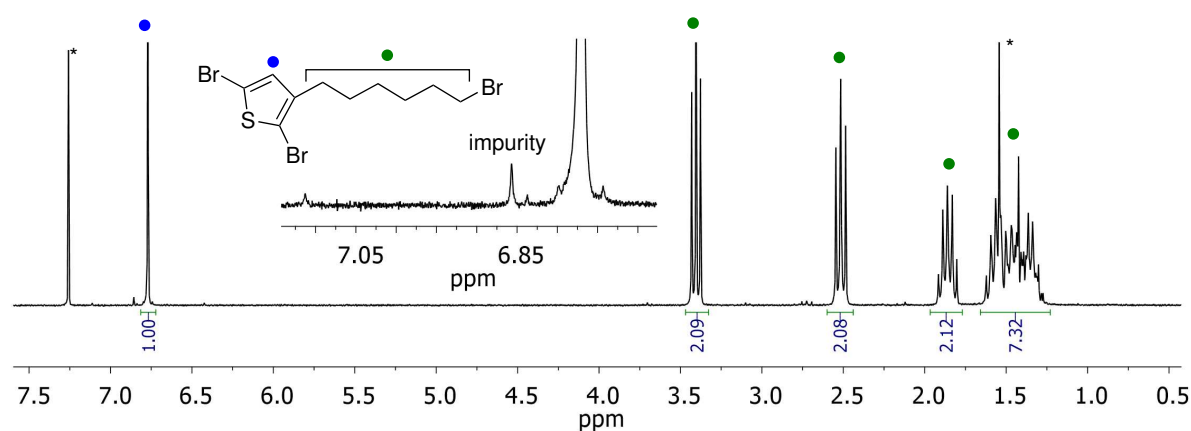


**Figure 4.1:** <sup>1</sup>H-NMR spectrum of purified **3BrHT-Br<sub>2</sub>** obtained from route 1.

All in all, this route 1 is short, but complicated by a difficult and tedious workup procedure with mediocre yields. Furthermore, double-substitution of Dibromohexane in the first step is not out of the question, as well as another side reaction known as *halogen-shuffling* which leads to the starting compound **8** being lithiated in the wrong position and was reported to occur by the *Thelakkat* group. Both are thought to potentially be the reason for these unknown signals which proved to be very persistent against various attempts of purification and which might be the cause of imperfections observed in the resulting polymers as will be shown later.

#### 4-step synthesis

For this reason, route 2, represented by the blue reaction arrows in Scheme 4.3, was also applied for the synthesis of **3BrHT-Br<sub>2</sub>**. This pathway is a 4-step synthesis adapted from literature<sup>[142,143]</sup> and while yields for 3 out of the 4 steps proved to be mediocre as

well, starting materials are affordable, workup-procedures mostly trouble-free and both aforementioned side-reactions cannot occur within this route. The monomer obtained by this synthesis should thus be of higher purity compared to route 1, giving way to higher-quality polymers which could ultimately be worth the extra effort.

This synthesis was done by first comparing different literature procedures for the same conversions with smaller-scale test reactions before repeating the complete route on a bigger scale with the conditions deemed most suitable. This was done by *Nils Hübener* within the scope of a research internship and details are discussed in the following.

Three procedures were considered for the first step, which is the mono-substitution of **9** with the protecting group **10**. Those could be found in literature from *Thelakkat et al.*<sup>[143]</sup> as well as *Abashev et al.*<sup>[144]</sup> and *Lin et al.*<sup>[145]</sup> among others. The respective conditions and comments can be found in Table 4.1, showing differences in the base used as well as solvent and reaction time. Since the procedure of the *Thelakkat* group demands inert conditions because of the use of hygroscopic sodium methoxide and a relatively low yield of 42 % was given, only the other two procedures were employed in test reactions as those can be done in ambient atmosphere and yields of 65 % and 78 % were given, respectively. Figure 4.2 shows the NMR spectra of the resulting crude products. Appearance of aromatic signals clearly shows a successful conversion, as does the new aliphatic signal at 3.77 ppm. Integrals of those signals fit well in both cases as is to be expected whereas the integral of the CH<sub>2</sub>-signal at 3.42 ppm deviates both times from what would be a full conversion, representing excess of unreacted **9**. Calculations from the aromatic signal and the CH<sub>2</sub>Br signal give a 73 % share of the target molecule in the crude product following the conditions of *Abashev et al.* and 48 % target compound **11** in the crude product following *Lin et al.* Taking into account crude yields of both, these amount to a calculated overall yield of 68 % following *Abashev et al.* and only 45 % following *Lin et al.*, although it has to be mentioned that the reaction time had to be shortened for the latter due to a lack of time which is of course expected to have an influence on this matter. However, within the direct comparison and with limited reaction time the stronger base KOH had a clear edge over *Lin*'s use of K<sub>2</sub>CO<sub>3</sub> and was thus used with an increased reaction time for the main synthesis. Here, an isolated yield of 53 % was achieved and the corresponding NMR of **11** is given in Figure 4.3.

The next step is the introduction of thiophene into the unprotected side of the Hexyl-chain by means of organomagnesium chemistry to yield **12**, following conditions by *Thelakkat et al.*<sup>[143]</sup> No test reaction was employed prior to the main synthesis. **11** was converted to the respective *Grignard* reagent over the course of 5.5 h before being treated

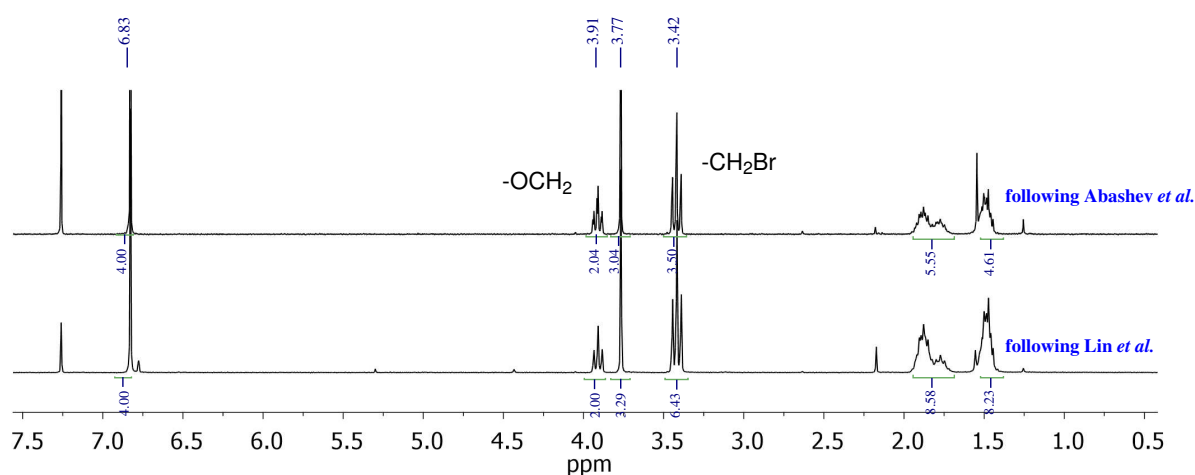


**Figure 4.2:** Crude product  $^1\text{H-NMR}$  spectra of test reactions for **11** following conditions by *Abashev et al.* and *Lin et al.*.<sup>[144,145]</sup>

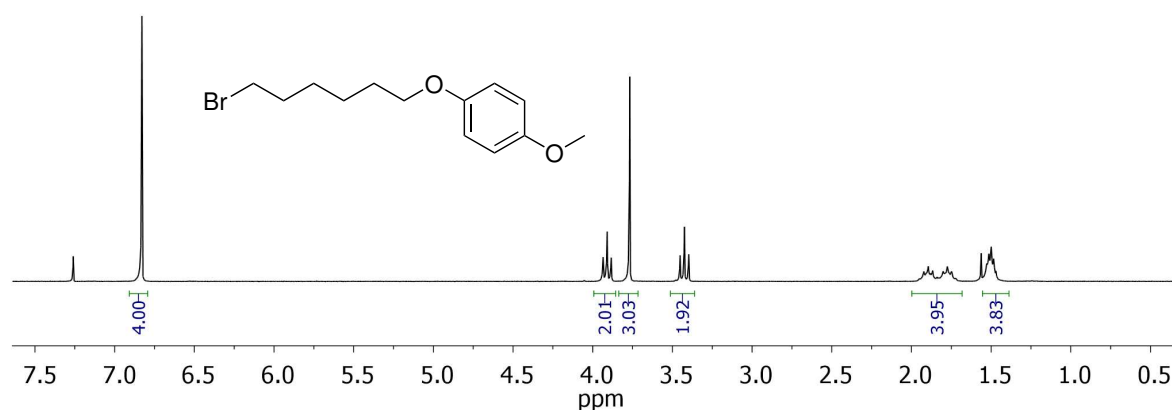


**Figure 4.3:**  $^1\text{H-NMR}$  spectra of purified **11** synthesized following conditions by *Abashev et al.*.

**Table 4.1:** Comparison of reaction conditions and yields given in literature for the protection of 1-6-Dibromohexane to obtain compound **11**.<sup>[143–146]</sup>

Group	Base	Solvent	time / h	yield given / %
Thelakkat <i>et al.</i>	NaOMe	EtOH	2	42
Abashev <i>et al.</i>	KOH	Acetone	1	65
Lin <i>et al.</i>	K <sub>2</sub> CO <sub>3</sub>	Acetone	48	78

with 3-Bromothiophene **8** under Ni-catalysis over night. Compared to literature, reaction times were shortened in this case as well, possibly explaining the comparably lower isolated yield of 44 % (lit. 60 %).  $^1\text{H-NMR}$  spectrum of purified **12** is given in Figure 4.4 and successful conversion can be seen by the emergence of new aromatic signals stemming from the thiophene ring as well as by the shift of the neighbouring  $\text{CH}_2$ -signal from 3.42 ppm to 2.64 ppm as a result of the substitution of bromine by the thiophene.

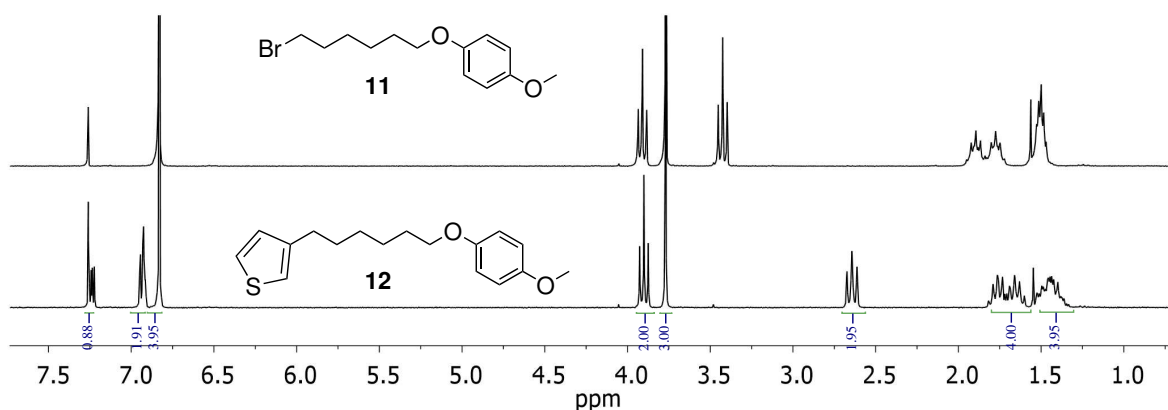


**Figure 4.4:**  $^1\text{H-NMR}$  spectra of the conversion of **11** to **12**. Successful introduction of the thiophene ring can be seen from new aromatic signals and an effective "shift" of the signal at 3.42 ppm to 2.64 ppm.

Third step is the removal of the 4-Methoxyphenolate group from the now-side-chain to reintroduce a bromine functionality, again following literature procedure but with changes in the workup due to unsatisfying results with the prescribed method. The reaction is performed in acetic anhydride with concentrated  $\text{HBr}$  for 21 h, yielding 40 % of **3BrHT** after column chromatography and *Kugelrohr*-distillation at  $120^\circ\text{C}$  under high vacuum. The disappearance of the Methoxyphenolate signals in  $^1\text{H-NMR}$  spectroscopy (Figure 4.5, center) indicates the exchange. Furthermore, the aliphatic peak of the neighbouring  $\text{CH}_2$ -group is being shifted from 3.77 ppm in **12** to 3.41 ppm in **3BrHT**.

Subsequent bromination to **3BrHT-Br<sub>2</sub>** is performed in the dark with N-Bromosuccinimide in slight excess in a mixture of THF and acetic acid for 20 h, in accordance with literature. After neutralisation with sodium hydrocarbonate and basic liquid-liquid-extraction, pure **3BrHT-Br<sub>2</sub>** was obtained by means of *Kugelrohr*-distillation at  $120^\circ\text{C}$  under high vacuum in 84 % yield. Furthermore, once the monomer starts showing signs of degradation over time, column chromatography in cyclohexane ( $R_f = 0.73$ ) can be used to purify it again.  $^1\text{H-NMR}$  spectroscopy (Figure 4.5) illustrates this by showing the successful conversion and

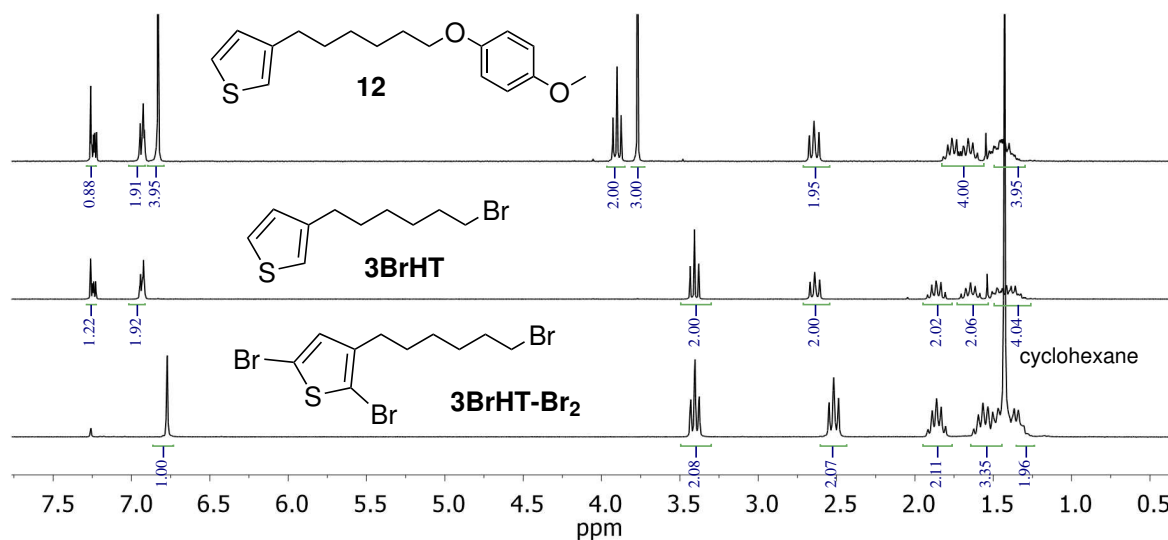


**Figure 4.5:** <sup>1</sup>H-NMR spectra of subsequent conversions of **12** to **3BrHT** and **3BrHT-Br<sub>2</sub>**.

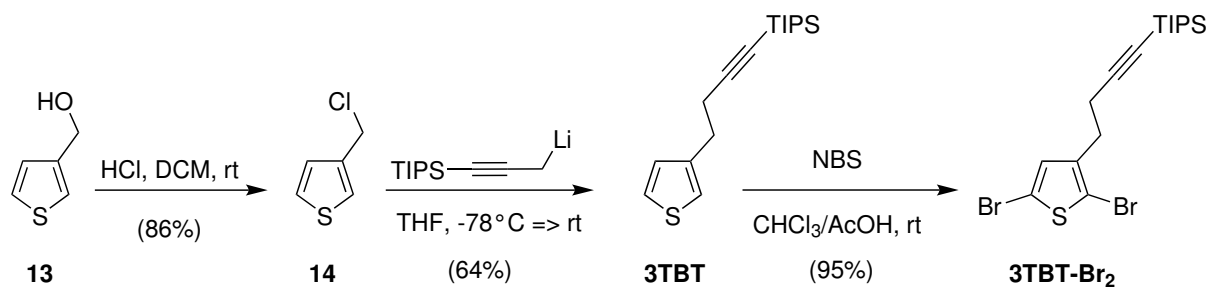
a highly pure monomer at the end of this 4-step synthesis, except for residual cyclohexane.

Likewise, bromination of **3HT** to **3HT-Br<sub>2</sub>** proceeded with a nearly quantitative isolated yield of 95 % as well, as can be seen from Scheme 4.4, providing 24 g of pure monomer.

Comparing both synthetic routes to **3BrHT-Br<sub>2</sub>**, the 2-step procedure clearly has the edge over the 4-step synthesis when it comes to overall yield, with 31 % for the former and about 8 % for the latter, also due to the yields of route 2 being notably lower than the ones given in the respective literature. The advantages of route 2 lie in easier synthetic procedures and less problematic workups all round with a highly pure monomer at the end of it. If this higher purity of **3BrHT-Br<sub>2</sub>** compared to route 1 is of any effect in the polymerization later on remains to be seen at this point and will be discussed in a later chapter.

#### 4.1.2 Synthesis of Butynyl-substituted thiophene monomer (3TBT)

Copolymer **PBTXX** is polymerized from **3HT** and (4-(thiophen-3-yl)-but-1-ynyl)-triisopropylsilane (**3TBT**) *via* GRIM polymerization in the same manner as **PTXX**. Thus, **3TBT-Br<sub>2</sub>** has to be synthesized. The synthetic route is a literature-known 3-step process starting from 3-Methanalthiophene **13** and is depicted in Scheme 4.5. Preparation of both monomers was done by *Nils von Seggern* within the scope of a research internship and in part by *Philipp Sliskovic*.



**Scheme 4.5:** Synthetic route for synthesis of **3TBT-Br<sub>2</sub>** starting from (3-Methanol)thiophene **13** following literature protocol.<sup>[2]</sup>

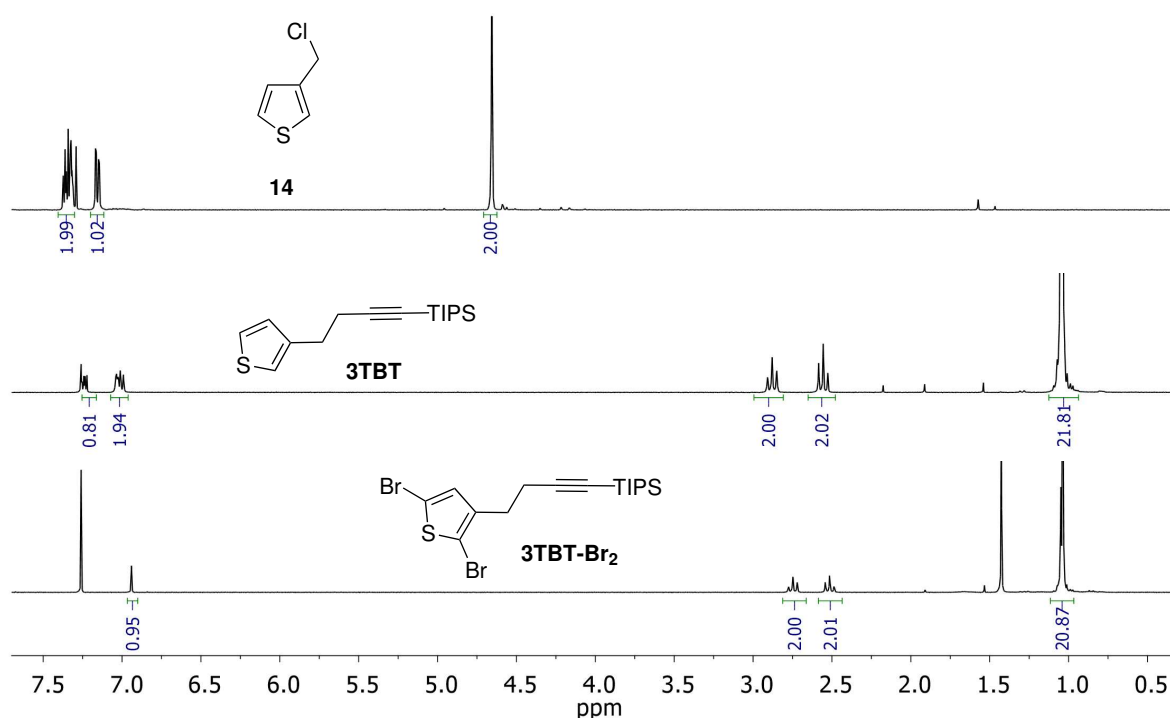
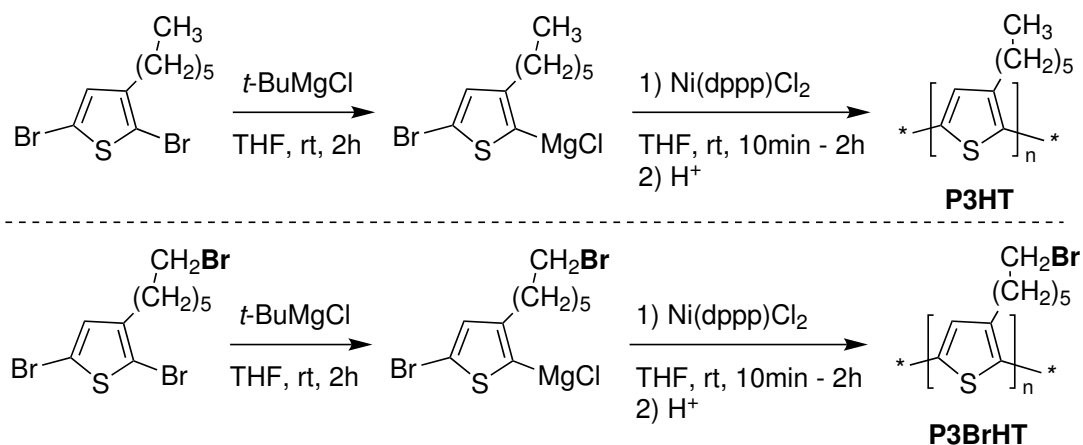


**Figure 4.6:** <sup>1</sup>H-NMR spectra of synthetic route to **3TBT-Br<sub>2</sub>**.

The first step sees the nucleophilic substitution of the hydroxy group of **13** by chlorine with an excess of concentrated hydrochloric acid in dichloromethane. The replacement proceeded with an isolated yield of **14** of 86 % after basic liquid-liquid extraction and was followed by the introduction of the triisopropylsilane (TIPS)-protected butyne side-chain. This was achieved by lithiating 1-(Triisopropylsilyl)-1-propyne with *n*-Butyllithium in THF and adding **14** to the solution, yielding 64 % of **3TBT** after column chromatography. Bromination was then performed under the same conditions as previous monomers in this discussion and gave 18 g (95 %) of **3TBT-Br<sub>2</sub>**.

### 4.1.3 Polymer Synthesis



**Scheme 4.6:** Reaction scheme for the discussed test homo polymerisations with the monomer being either **3BrHT-Br<sub>2</sub>** (bromine in side-chain) or **3HT-Br<sub>2</sub>**. First step is the Grignard metathesis of the monomer, followed by initiating chain growth by catalyst addition and subsequent reaction quenching.

Polymerization of **3HT-Br<sub>2</sub>** and their derivatives to polythiophenes *via* GRIM is an established method for the preparation of such polymers and has been employed in this group before. However, as mentioned earlier in this chapter, controlling the quality of obtained polymers proved difficult when applying high standards to their conformity in SEC. Specifically, this means that either low-molecular weight tailing or additional high-molecular weight fractions ('shoulders') could often be observed. While the former can often be reduced or removed by *Soxhlet* extraction, the latter essentially turned out to be inseparable from the rest of the polymer. On top of that, rarely did we have a polythiophene batch synthesized *via* GRIM that didn't show these high-molecular signals in varying intensity. Hypotheses have been made regarding the reasons for this and unexplained and, to a degree, non-removable impurities in the employed monomers were one possible explanation. An approach to solving these was discussed in a previous section, leading to the synthesis of a highly pure **3BrHT-Br<sub>2</sub>** monomer.

Other explanations of course were mistakes or shortcomings during the polymerization procedure itself and test-polymerizations have been done in an attempt to identify and correct these and shall be presented next. Additionally, these experiments provided an opportunity to attain experience and routine in performing GRIM polymerisations for the intended copolymer systems and probe reaction condition influences with regards to the shape of the respective molecular weight distributions, a polymer property that tends to be under-reported and reduced to mere dispersity values in literature. Furthermore

as described in the previous sections, synthesis of the monomers is time consuming and yield of GRIM polymerisations with regards to weight percentage is generally low so that production of reasonably sized polymer batches doesn't provide a large room for errors. Thus, evaluation of reaction conditions beforehand *via* these test reactions is crucial and allowed for minor optimizations in the way synthesis is performed.

Parts of the work to be discussed has been done by *Boshra Kachmar* as part of a research internship. First small-scale polymerisations of **P3BrHT** have been performed by me with **3BrHT-Br<sub>2</sub>** monomer, synthesized by the earlier route 1 (see Scheme 4.3). The reaction scheme for these test-polymerisations is given in Scheme 4.6.

Crucial parameters for the result of this synthesis are the reaction time given for the Grignard metathesis to produce the active monomer species, the polymerisation time after addition of the nickel catalyst and the method of reaction quenching after this given time. Following established procedure from literature and our group in terms of reaction times, 2 h was given for the active Grignard species to form, followed by 15 min of polymerisation time after catalyst addition. Different approaches for reaction quenching exist and literature<sup>[48]</sup> suggests that this step is decisive for the quality of the molecular weight distribution of the polymer. Quick addition of 5 M aqueous HCl is reported to provide best results and a shoulder-less GPC curve. In this work, no distinct difference was observable between quenching with 5 M HCl and quenching with methanol containing drops of hydrochloric acid. Unfortunately this meant that in both cases a high-molecular shoulder was observable as can be seen in Figure 4.7 (a). Also, applicable polymerisation times are dependant on the monomer system used in these polymerisations. This dependency has been reproduced within the scope of these test reactions. For single-monomer conversions as in this case a prolongation of the time-frame is counter-productive as is also evident from Figure 4.7. Here in red, in elugrams after polymerisation for 1 h no high-molecular shoulder can be seen, however the chain-length distribution can be described as multimodal, which is arguably worse in terms of polymer quality and reproducibility than a minor high-molecular fraction, which is observed when the reaction is stopped after the usual 15 min.

Similar observations were made by *Boshra Kachmar* when performing polymerisations of **P3HT**. Chain growth times of 10 min, 15 min and 2 h resulted in a low-quality polymer after 2 h, whereas the two shorter reactions afforded acceptable results. Specifically, in terms of low-molecular tailing and high-molecular shoulders both timings differed only slightly and in a way that could as well be attributable to human inconsistency between experiments. GPC spectra can be seen in Figure 4.7 (b). Since in these mentioned sets of polymerisations different batches of monomers were used (3BrHT-Br<sub>2</sub> and 3HT-Br<sub>2</sub>,

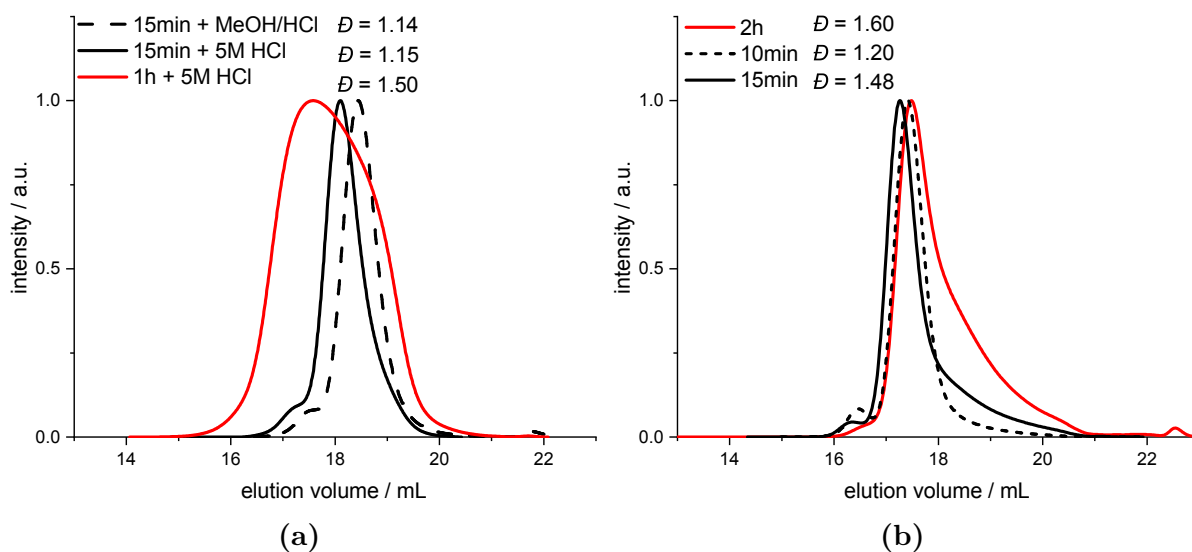
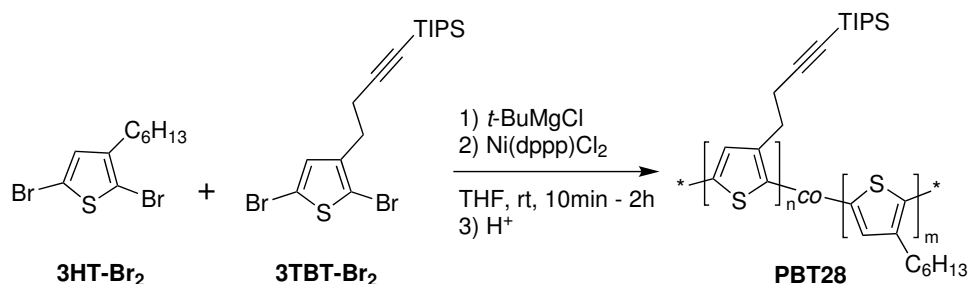


**Figure 4.7:** (a) Elugrams of GRIM polymerisations of **3BrHT-Br<sub>2</sub>** and comparison between polymerisation times and quenching methods. (b) Elugrams of GRIM polymerisations of **3HT-Br<sub>2</sub>** with different polymerisation times. Eluent: THF

respectively), the observed imperfections in the molecular weight distributions don't appear to be the result of monomer impurities. Also, both monomers are highly similar and only differ in a single bromine substitution at the side-chain. Accordingly, variations in reaction conditions had comparable influences on the resulting polymers.

When moving from homo- to copolymerizations however, the co-monomer can have a profound effect on the course of reaction. This is illustrated in Figure 4.8 where elugrams of different co-polymerisations are given. Figure 4.8 (b) presents the molecular weight distribution after co-polymerising the very similar monomers **3BrHT-Br<sub>2</sub>** and **3HT-Br<sub>2</sub>** for 1 h, resulting in the virtually identical situation to the prolonged homo-polymerisation of the respective compounds (see Figure 4.7). On the other hand, copolymerization of **3HT-Br<sub>2</sub>** with **3TBT-Br<sub>2</sub>** to afford **PBT28** as shown in Scheme 4.7 presents the inverse correlation between polymerisation time and polymer uniformity and elugrams are given in Figure 4.8 (a). After only 10 min of chain growth a multimodal product is obtained whereas after 2 h a great reduction of the high-molecular shoulder can be observed. Monomer feed ratio was 32:68 **3HT-Br<sub>2</sub>** to **3TBT-Br<sub>2</sub>** which resulted in a co-monomer ratio in the copolymer of 28:72 as determined from the corresponding <sup>1</sup>H-NMR spectrum depicted in Figure 4.9, thus this polymer was termed **PBT28**. Co-monomer ratio can be calculated from the respective aromatic protons of each repeating unit as marked in the spectrum. Additional signals can be found stemming from the solvent residual peak of deuterated chloroform as well as from solvent residues from *Soxhlet* extraction. Relative yield in this

case was 31 % which is in the expected range of GRIM polymerisations.



**Scheme 4.7:** Reaction scheme for the co-polymerisation of **3HT-Br<sub>2</sub>** and **3TBT-Br<sub>2</sub>** to afford **PBTXX**.

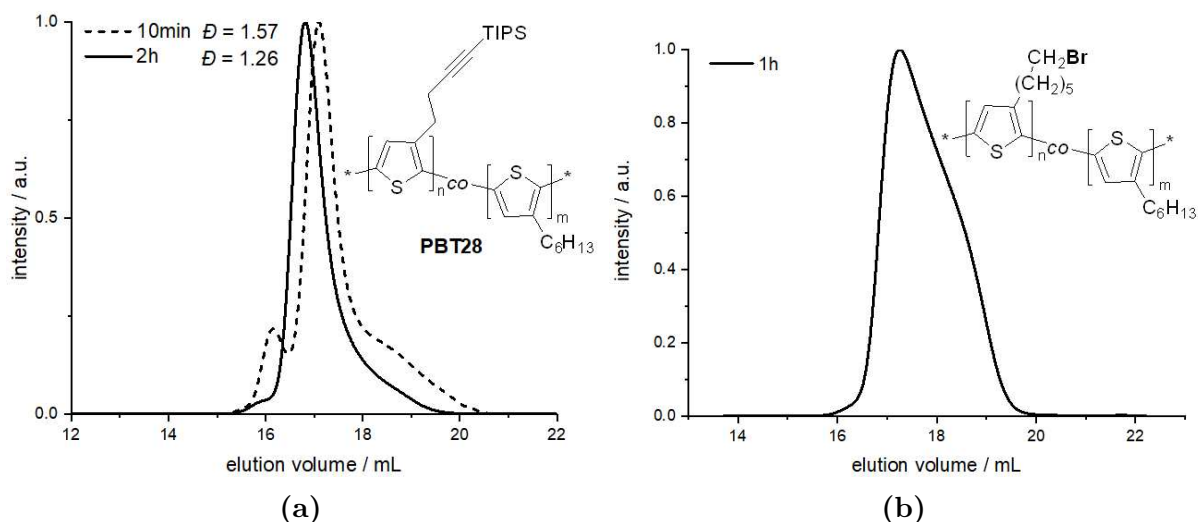


**Figure 4.8:** (a) Elugrams of co-polymerisations of **3HT-Br<sub>2</sub>** and **3TBT-Br<sub>2</sub>** with different polymerisation times. (b) Elugram of co-polymerisation of **3BrHT-Br<sub>2</sub>** and **3HT-Br<sub>2</sub>**. Here, the result resembles that of the corresponding homo-polymerisations. Eluent: THF

On a side-note, the low-molecular tailing is less of a concern because in our experience it is usually the result of minor mistakes in reaction execution and can in most cases be reduced or removed by *Soxhlet* extraction.

Overall, when it comes to homo-polymerisations with either **3HT-Br<sub>2</sub>** or **3BrHT-Br<sub>2</sub>**, test reactions confirmed the already established reaction conditions and provided the opportunity to become experienced in their execution. High-molecular shoulders could be eliminated in the aforementioned instances but at the cost of worse overall polymer quality. For this reason it was decided to stick with the established reaction conditions while moving the reaction setup from regular inert glassware to performing polymerisations

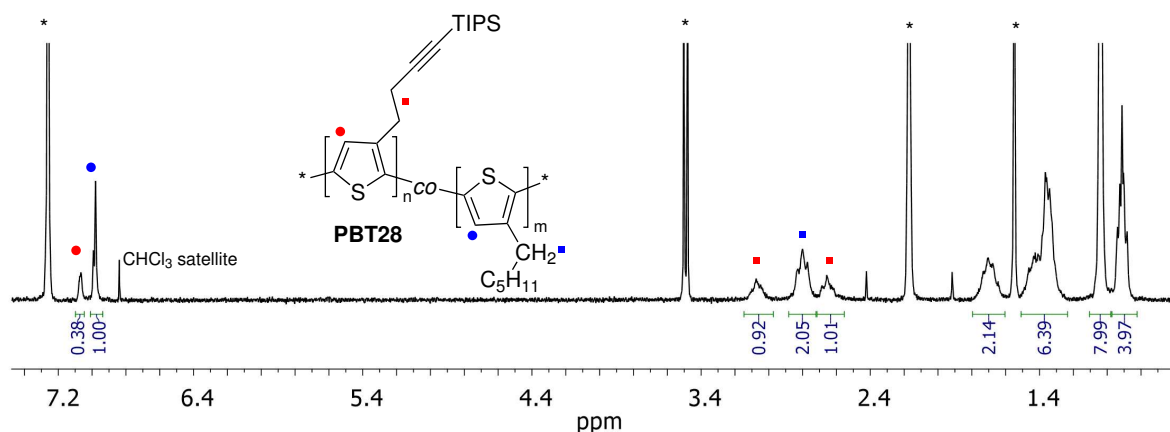


**Figure 4.9:** <sup>1</sup>H-NMR of **PBT28** copolymer in CDCl<sub>3</sub>.

inside a glovebox, which proved to facilitate the reproducibility of these reactions and allows for inert storage of solvent and catalyst. At this point, accepting a minor flaw in the molecular weight distribution of the polymers obtained this way was deemed preferable to a broader and less defined distribution by making major changes to reaction conditions.

### Main polymer 1 (PBT system)

Accordingly, another batch of **PBTXX** copolymer, meant for further functionalisation (as was laid out earlier) was synthesized. Resulting SEC spectrum is given in Figure 4.10 (b). 2 g of total monomer with a feed ratio of 70:30 3HT-Br<sub>2</sub> to 3TBT-Br<sub>2</sub> afforded 665 mg of copolymer which corresponds to a yield of 33%. From SEC the number average molecular weight was determined to be around 14 000 g mol<sup>-1</sup> with a dispersity of 1.40. The shape of the molecular weight distribution is overall very uniform with only minimal low-molecular tailing and a slight high molecular weight shoulder. The name given to this batch of PBTXX was determined to be **PBT24**, again based on the share of functionalizable groups assigned by the co-monomer ratio found in <sup>1</sup>H-NMR spectroscopy. The <sup>1</sup>H-NMR spectrum along with attenuated total reflectance infrared transmission is given in Figure 4.10. As marked inside the spectrum, co-monomer ratio can be calculated from the integral ratio of respective aromatic signals of the repeating units. The 3HT repeating unit is represented at 6.98 ppm and 3TBT groups stand at 7.07 ppm. As such, integral values correlate to a co-monomer ratio of 76:24 3HT to 3TBT.

Apart from residual water, likely from inside the deuterated solvent, no impurities of noteworthy intensity are found in the NMR spectrum.

Characterisation by infrared spectroscopy of bulk substance is depicted in Figure 4.10

(a). Stretching and bending vibrations of alkyl C-H bonds show strong infrared absorption between  $2850\text{ cm}^{-1}$  and  $2930\text{ cm}^{-1}$  (stretching), at  $1459\text{ cm}^{-1}$  and in the  $800\text{ cm}^{-1}$  region (bending). At  $1379\text{ cm}^{-1}$  medium intensity absorption can be observed which likely correlates to methyl groups of the TIPS protecting group in the 3TBT repeating units.  $\text{C}\equiv\text{C}$  stretching of the alkyne groups produce an absorption at  $2171\text{ cm}^{-1}$ . Aromatic C-H stretching gives a weak signal at  $3059\text{ cm}^{-1}$ .

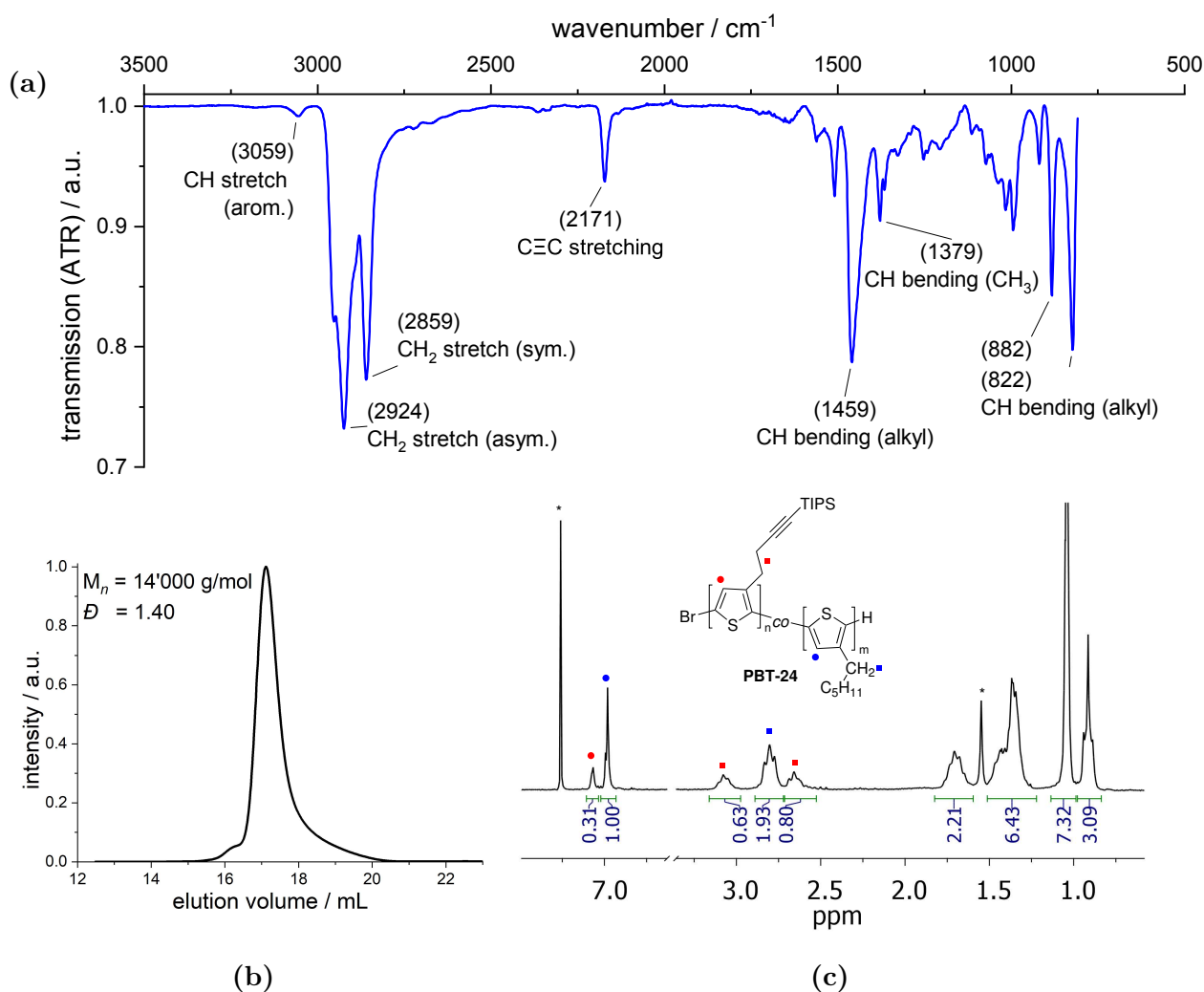


**Figure 4.10:** Characterisation of **PBT24** copolymer. (a) Infrared transmission spectrum of measured in attenuated total reflectance. (b) SEC chromatogram, Eluent: THF. (c)  $^1\text{H-NMR}$  spectrum in  $\text{CDCl}_3$ .

### Main polymer 2 (PT system)

For the other copolymer, **PTXX**, a new batch suited for further functionalisation was synthesized as well. Even though both monomers showed shoulders in all of the performed homo-polymerisations, it was decided to use the monomer 3BrHT- $\text{Br}_2$  obtained from route

2 (3BrHT-Br<sub>2</sub>-Route2) as it showed slightly higher purity compared to that of route 1. Figure 4.11 (a) shows the SEC curve of a first polymerisation of 3BrHT-Br<sub>2</sub>-Route2. While there is noticeable low-molecular tailing to be seen its origin can be attributed to imperfect addition of the catalyst in this specific instance. Other than that, however, no shoulder can be seen and the overall distribution is largely homogenous. Figure 4.11 (b) displays the successful attempt at the copolymerisation of 3BrHT-Br<sub>2</sub>-Route2 with 3HT-Br<sub>2</sub> which finally provided a high-quality and narrow molecular weight distribution with only minor tailing and a miniscule shoulder. It is noteworthy that although earlier polymerisations with different monomers did not hint at the monomer being a central cause of irregularities, here both syntheses using 3BrHT-Br<sub>2</sub>-Route2 eventually provided virtually shoulder-less molecular weight distributions.

The copolymer was synthesized from a monomer feed containing a total of 854 mg of co-monomers with a feed ratio of 74:26 3BrHT-Br<sub>2</sub>-Route2 to 3HT-Br<sub>2</sub>. This afforded 251 mg of polymer corresponding to a yield of 29%.

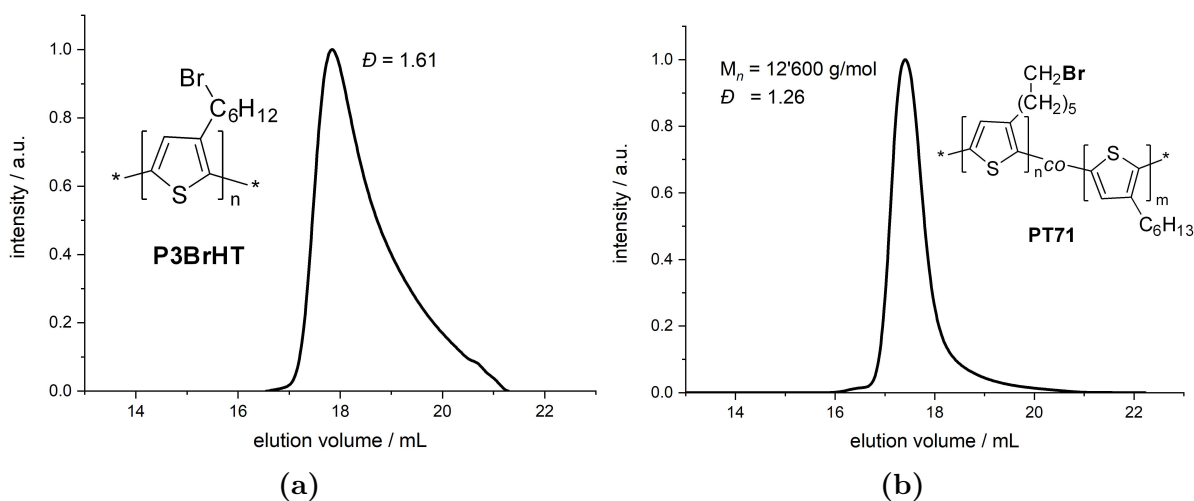


**Figure 4.11:** (a) SEC of homo-polymerisation of 3BrHT-Br<sub>2</sub>-Route2. (b) SEC of co-polymerisation of 3BrHT-Br<sub>2</sub>-Route2 and 3HT-Br<sub>2</sub>.

Calculation of the co-monomer ratio in the polymer can't be done by comparison of the aromatic proton signals because, as can be seen from Figure 4.12, both monomer units contribute to the same aromatic signal at 6.98 ppm. The ratio was instead determined by normalizing integration with regards to the methyl group in the 3HT repeating unit (marked red). Corresponding to this normalized integral would then be 1H in the aromatic region, providing a theoretical split of the 6.98 ppm signal into 1:2.49 3HT to 3BrHT repeating units. This equates to a co-monomer ratio of about 29:71 or a 71% share of functionalizable bromine units, close to the provided monomer feed. The copolymer was thus named **PT71**.

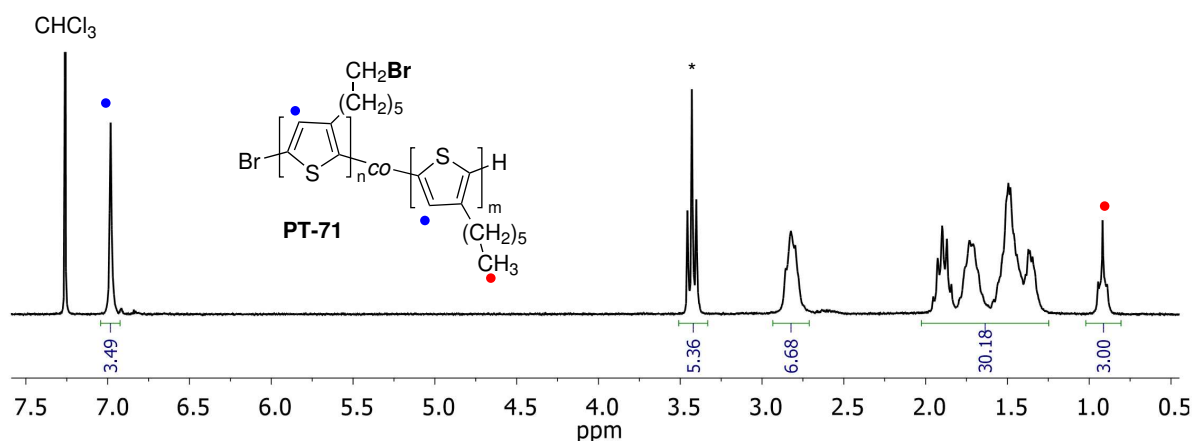


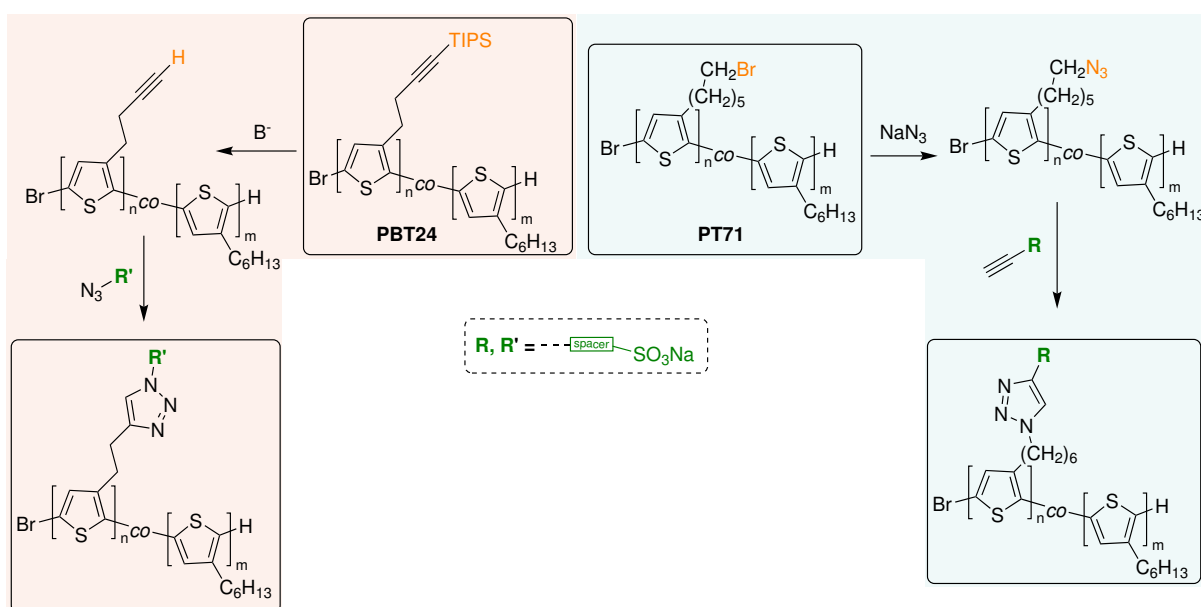
**Figure 4.12:**  $^1\text{H-NMR}$  of **PT71** copolymer

Another thing to address in this NMR spectrum is the triplet signal at 3.43 ppm which can also be found in the spectrum of pristine 3BrHT-Br<sub>2</sub>-Route2 (Figure 4.5) and corresponds to the CH<sub>2</sub>-group next to bromine in the side-chain. It is not, however, unreacted monomer that could have been left in the polymer after purification, since no other monomer signals can be found in the spectrum. It can only be speculated about the nature of this impurity other than that it seems likely to be a terminally brominated alkyl chain. Judging by the mechanism of this reaction (see chapter 1.2.1) no such compound should be created and such signal hasn't been observed in this intensity in other experiments before. However, the sharpness of the signal suggests it is a low-molecular component and not part of the polymer itself, so that further conversions of the copolymer were proceeded with, without further purification attempts, as workup procedures after the next syntheses might be more successful in removing the impurity, especially with changed solubility properties when ionic groups are introduced. These further conversions will be discussed in the next section.

Ultimately, revisiting of monomer and polymer synthesis procedures afforded highly pure 3BrHT-Br<sub>2</sub> monomer, which in turn was used with 3HT-Br<sub>2</sub> to produce the high quality copolymer **PT71** with narrow molecular weight distribution in GRIM-typical yield. For the other copolymer system, 3HT-Br<sub>2</sub> and 3TBT-Br<sub>2</sub> were copolymerized to afford **PBT24** in equally high quality.

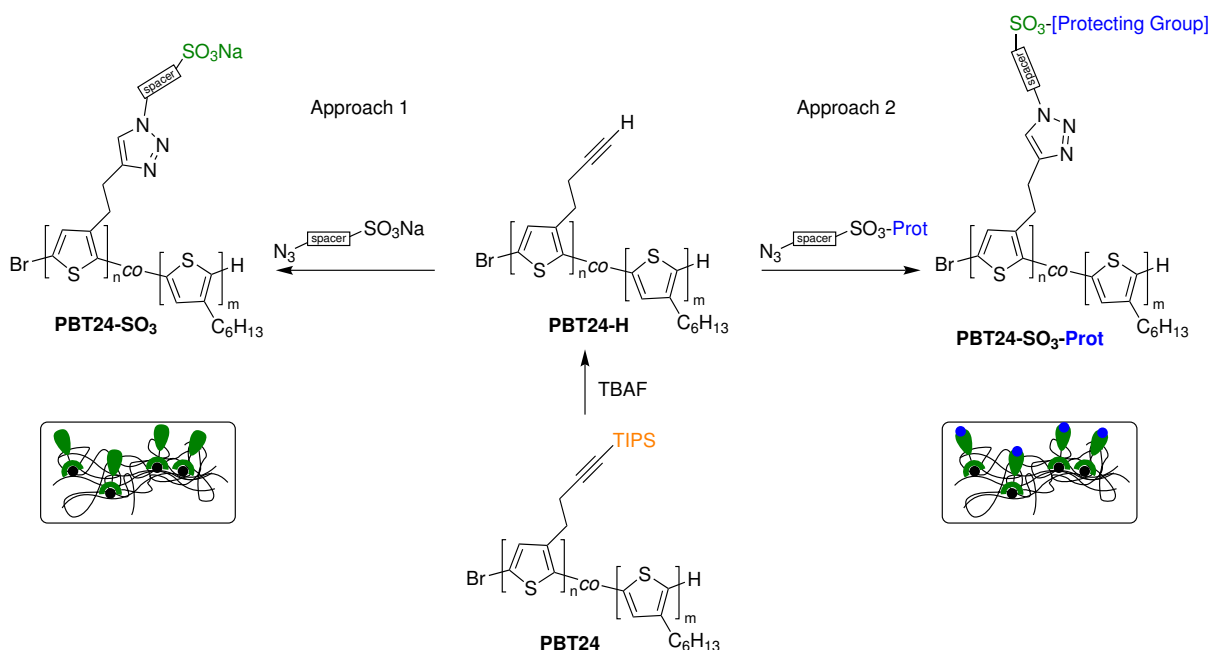
## 4.2 Polymer Functionalization with sodium sulfonate moieties

Copolymers **PBT24** ( $14\,000\text{ g mol}^{-1}$ ,  $D\ 1.40$ ) and **PT71** ( $12\,600\text{ g mol}^{-1}$ ,  $D\ 1.26$ ) discussed in the previous section are to be functionalized in polymer analogous reactions to introduce ionic functionalities. This introduction will ultimately be achieved by CuAAC. As described in the beginning of this chapter, both offer opposite functionalities with regards to use in this *Click* chemistry. This is exemplified in Scheme 4.8 which also depicts the two different pathways to ion-functionalisation. The Approaches to and preparation of these functionalized copolymers will be discussed next, starting with the synthesis of required reagents for functionalization of **PBT24**.



**Scheme 4.8:** Schematic illustration of polymer analogous functionalisation of copolymers **PBT24** and **PT71**.

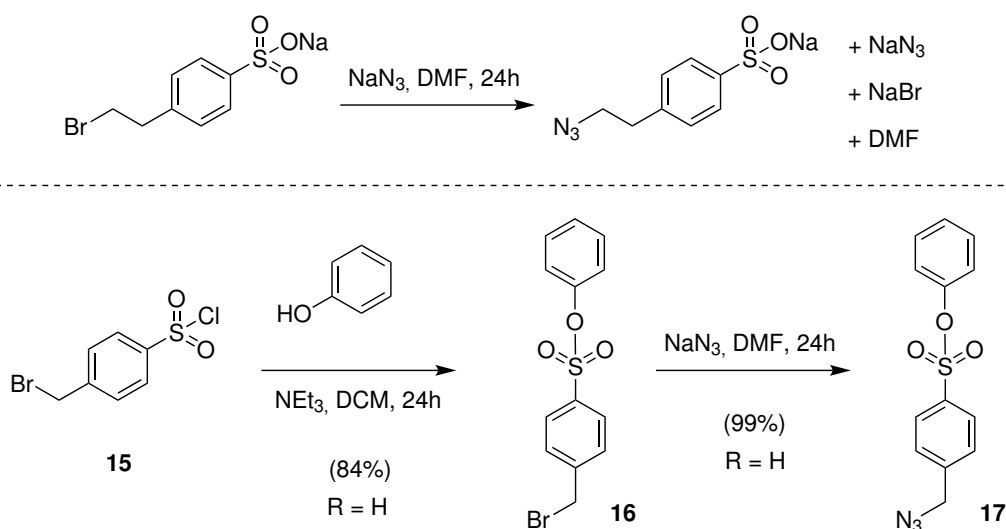
## 4.2.1 Synthesis of Protected and Azide-Bearing Sulfonate (-SO<sub>3</sub>-Prot)



**Scheme 4.9:** Schematic illustration of two possible approaches to CuAAC conversion in solution of copolymer **PBT24** to introduce ionic groups. Approach 1: direct introduction of ionic moieties. Approach 2: introduction of protected ionic groups to avoid solubility issues.

Functionalisation of the obtained copolymers was intended to be performed in solution *via* CuAAC, as to enable one to use a wider variety of characterisation methods. However, even in a bulk material, the introduction of ionic groups can complicate the matter as has been discussed before (see chapter 3.3.2). For this reason, the ionic group introduced shall be a protected one. Another reason for employing a protecting group is the structure of the clicking agent needed for conversion of **PBT-H** (see Scheme 4.9). Here, azide and ionic functionality need to be combined in one molecule which is not commonly found in literature and can be non-trivial to achieve, although the most straight-forward method for the synthesis of this kind of compound is by nucleophilic substitution of a halide, similar to the replacements done in copolymers **PV26**, **PV49** and **PV73**. Without protection of the ionic group beforehand, though, purification of the obtained product is virtually impossible, as starting material, side-products, reagents and the target molecule all share the same or highly similar solubility and polarity properties. The only option in this case is to proceed with the crude reaction mixture, for which there are examples in literature but which has been disregarded as an option here, for the presence of excess sodium azide

alone. Furthermore, as can be anticipated from earlier ionic conversions, the resulting polyelectrolyte will exhibit highly polar properties as well. A "late" purification, so to speak, would thus still be highly difficult, if possible at all. An illustration of this can be found in Scheme 4.10 along with the reaction scheme for the synthesis of the protected sulfonate.



**Scheme 4.10:** **Top** Illustration of the direct azidation of the sulfonate, yielding the target molecule, non-removable excess material ( $\text{NaN}_3$ DMF) and side-product ( $\text{NaBr}$ ). **Bottom** Protecting group approach, starting from commercially available **15**, yielding purified **17** in good yield after a two-step synthesis.

Accordingly, synthesis is done in two steps, starting from commercially available **15** and can be performed with either phenol or pentafluorophenol acting as protecting groups. Reaction conditions for the first step were taken from literature<sup>[147]</sup> and were probed by *Boshra Kachmar* during a research internship. Pentafluorophenol should be more easily removed in future deprotection steps as a result of the electron-withdrawing fluorine atoms but could not be coupled here in a first attempt. After slight modification of the literature conditions and replacement of pentafluorophenol by phenol, protection proceeded well and an isolated yield of 84% was achieved (see Scheme 4.10). Thus pentafluorophenol was not probed again, although with the tweaked conditions it might work just as well.

By using phenol instead of pentafluorophenol one is able to judge a successful reaction from the given  $^1\text{H-NMR}$  spectra (Figure 4.13), although the occurrence of a second aliphatic signal at 4.49 ppm in the otherwise clean spectrum was unexpected, given that the signal

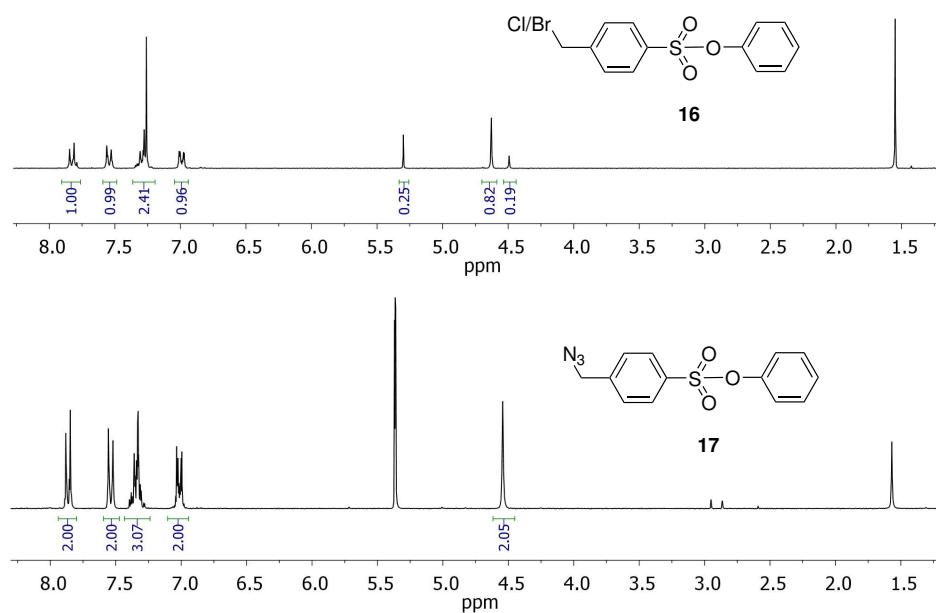


**Figure 4.13:**  $^1\text{H-NMR}$  spectrum of the halide-azide-exchange reaction from **16** to **17**. Signals at 4.63 ppm and 4.49 ppm correspond to the bromine and chlorine derivatives of the target molecule.

at 4.63 ppm corresponds to the benzylic  $\text{CH}_2$ -group and should not be affected by the reaction. Mass spectrometry was performed on the sample and indeed two compounds could be identified as is shown in Figure 4.14, with the second one simply being the chlorine-analogue of **16**. The chlorine released by substitution with phenol is seemingly enough to partially undergo a substitution reaction itself with the bromine, the latter being the better leaving group of the two. But since both, chlorine and bromine can be readily replaced with azide groups, this fact can be ignored and the compound be further reacted as is.

Thus, subsequent halide-azide-exchange was performed in the same fashion as before in this work, which worked flawlessly, giving a quantitative yield of pure **17**. NMR spectra of the different compounds are given in Figure 4.13.

Before attaching the synthesized protected sulfonate **17** to copolymer **PBT24-H**, efficiency of the subsequent deprotection reaction was first examined *via* model reaction on the monomeric compound. This was done to ensure the deprotection itself proceeds well and optimized conditions can be developed beforehand, should this not be the case. However, standard conditions found in literature<sup>[147]</sup> for phenols as protecting groups could not be applied here, when keeping in mind that the same reaction is to be done in a polymer analogous fashion later, as they usually revolve around butanol or other alcohols

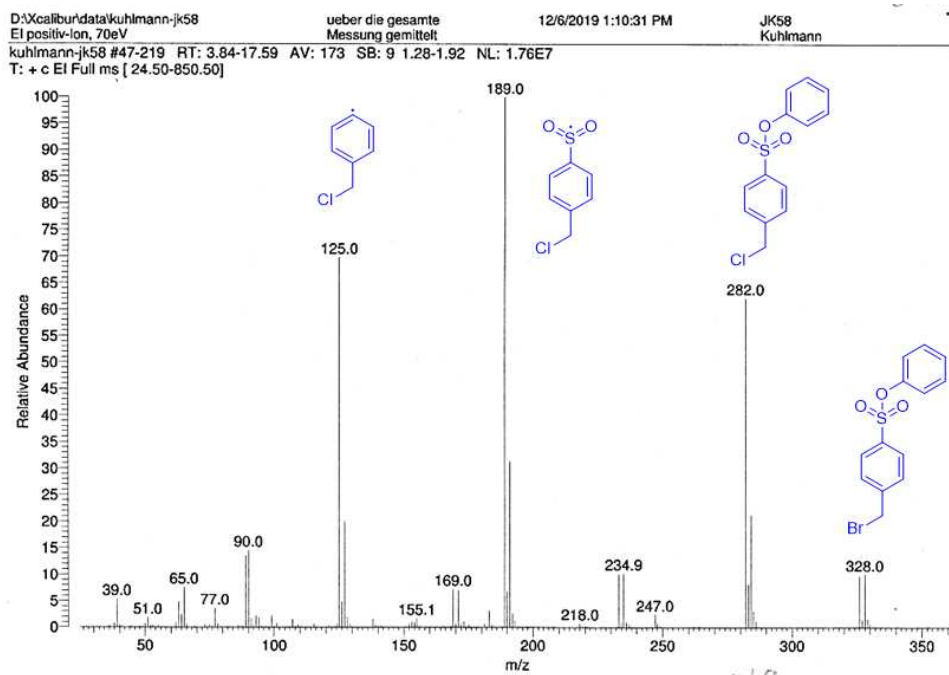


**Figure 4.14:** MS-spectrum of **16** showing the occurrence of the chlorine-analogue.

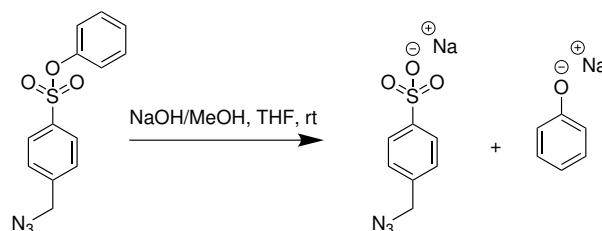


**Figure 4.15:** Model reaction for the deprotection of the protected sulfonate group after CuAAC.

as solvents which are not suitable for dissolving polymers.

Thus, based on similar conversions found in polymer literature<sup>[148]</sup> THF was used as a primary solvent and the base, here sodium hydroxide, was added as a solution in Methanol, while trying to keep volume of the latter as low as possible. Another challenge in the evaluation of the reaction is the fact that no direct assertion of the grade of conversion can be done from the crude product, as the mixture of cleavage products will not be distinguishable from the non-cleaved starting material in NMR-spectroscopy, nor was there any other suitable characterisation method available for this intention. Thus, reaction success was evaluated indirectly by separating the notably less polar starting compound from the rest of the reaction mixture by means of *silica gel* filtration with generous amounts of dichloromethane to ensure no unreacted **17** was missed.

After this process, only 2 mg of compound could be retrieved this way and  $^1\text{H-NMR}$  spectroscopy showed no traces of the starting material. Thus, it can be assumed the deprotection reaction proceeded quantitatively with the chosen conditions and as such are suitable for conversion of bulk polymers.

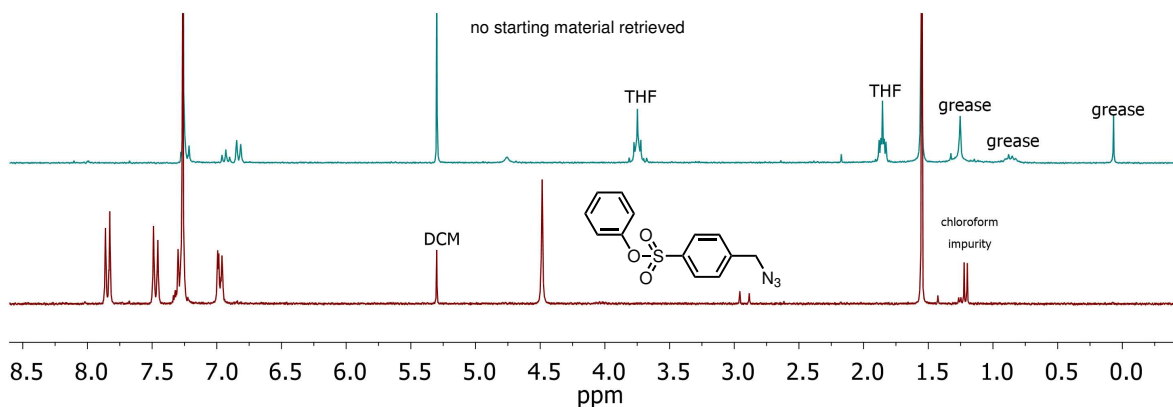
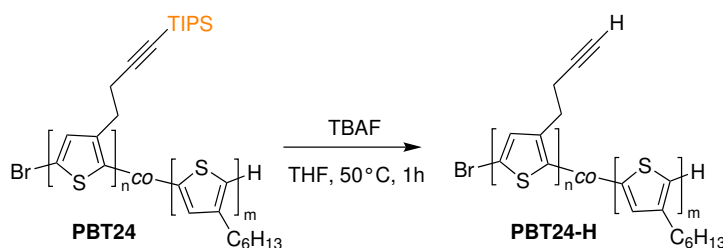


**Figure 4.16:**  $^1\text{H-NMR}$  spectra of protected sulfonate (bottom) and of retrieved residual compound which was recovered after deprotection and filtration over silica (top). Top spectrum shows that no starting material was retrieved.

## 4.2.2 Polymer Analogous Reactions of Alkyne-bearing PBT24



**Scheme 4.11:** Deprotection of butynyl units in **PBT24** with excess of tetra-*n*-butylammonium fluoride (TBAF).

Copolymer **PBT24** was prepared for subsequent functionalization by deprotection of its TIPS-protected butynyl units with a 5-fold excess of tetra-*n*-butylammonium fluoride (TBAF) as is depicted in Scheme 4.11. The reaction was performed in THF at 50 °C for 1 h before being diluted with chloroform and extracted with water. After drying of the organic phase over  $\text{Mg}_2\text{SO}_4$   $^1\text{H-NMR}$  spectroscopy still showed major signals of the

TIPS protecting group. However, in IR spectroscopy a  $\text{C}\equiv\text{C}-\text{H}$  vibrational band could be observed. Thus, the polymer was dissolved in  $\text{CHCl}_3$  at  $50^\circ\text{C}$  and precipitated in methanol. Subsequent filtering, removal of solvent and NMR spectroscopy resulted in the spectrum shown in Figure 4.17.

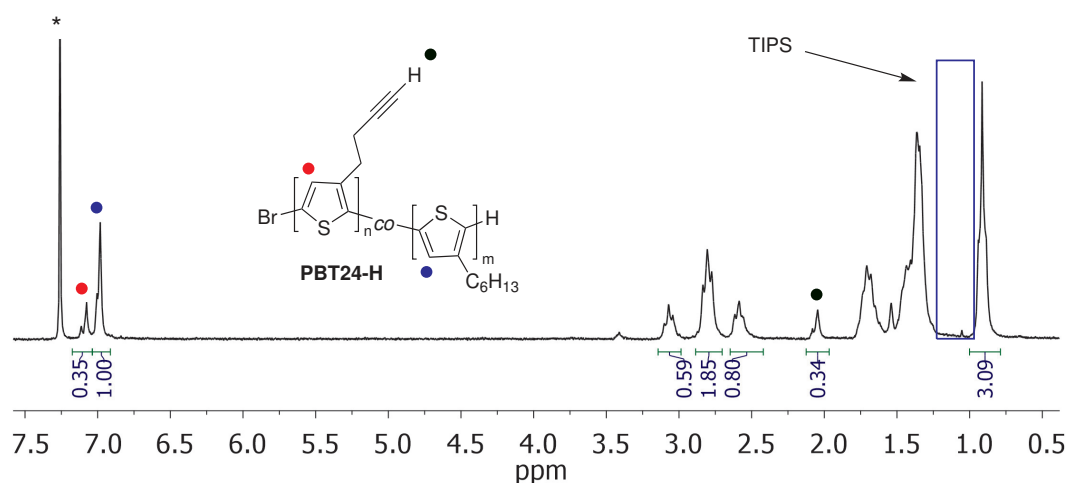


**Figure 4.17:**  $^1\text{H}$ -NMR spectrum of **PBT24-H** after precipitation in methanol from hot  $\text{CHCl}_3$ . No TIPS signal remains.

The area between about 1.0 ppm and 1.25 ppm shows no residual TIPS signal (for comparison see Figure 4.10), thus the deprotection was completed successfully. Integral values fit the expected numbers and a new signal at 2.04 ppm emerged, indicative of the  $\text{C}-\text{H}$  bond belonging to the now unprotected butynyl groups.

Accordingly some changes can be observed in the IR transmission spectrum (Figure 4.18). The  $\text{C}\equiv\text{C}$  bond stretching band shifted from about  $2170\text{ cm}^{-1}$  to now  $2117\text{ cm}^{-1}$  due to the alkyne units turning from secondary into terminal groups. A corresponding  $\text{C}\equiv\text{C}-\text{H}$  stretching band can now be observed at  $3312\text{ cm}^{-1}$ . Other  $\text{C}-\text{H}$  stretching and bending bands remain unchanged.

257 mg of **PBT24** afforded 170 mg deprotected **PBT24-H** in a yield of 66 wt-%. Losses mostly consist of reduced molecular weight from the removal of TIPS protecting groups and material loss during liquid-liquid extraction. Applying a 24% share of 3TBT repeating units in the polymer as was determined by NMR spectroscopy, removal of the protecting groups translates to a reduction in molecular weight of about 13% overall, leaving 21% in mass lost during workup.

Since terminal alkyne groups are highly reactive **PBT24-H** was further converted shortly after in CuAAC with the protected sulfonate azide **17** (Scheme 4.12). Solvent used was again THF and the reaction was kept running inside the glovebox for the usual 3

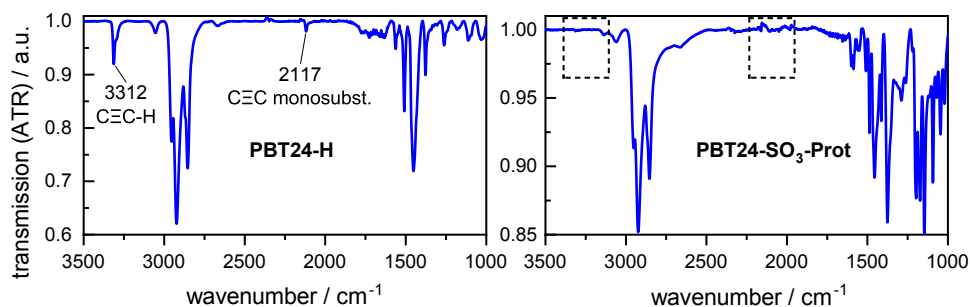
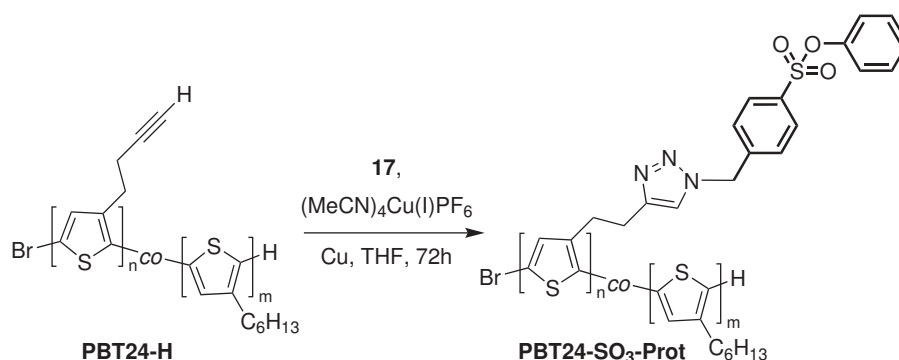


**Figure 4.18:** (Left) IR (ATR) transmission spectrum of **PBT24-H**. Unprotected butynyl groups result in corresponding  $\text{C}\equiv\text{C}(-\text{H})$  stretching bands. (Right) Transmission spectrum of **PBT24-SO<sub>3</sub>-Prot**. Alkyne signals disappeared.

days. Because of the still relatively non-polar nature of azide **17** methanol was expected to be a suitable solvent for precipitation of the obtained copolymer **PBT24-SO<sub>3</sub>-Prot**, but neither precipitation from THF, nor from chloroform worked to any useable degree. Instead, precipitation from chloroform in acetonitrile proved to be better suited. 170 mg of **PBT24-H** are expected to afford 198 mg of **PBT24-SO<sub>3</sub>-Prot** at 100 % conversion when applying a share of functionalizable repeating units of 24 %. The actual amount obtained was 212 mg and as such above the theoretical 100 %. However, <sup>1</sup>H-NMR spectroscopy (Figure 4.19) does not reveal solvent or reactant residues besides water and chloroform. These two could attribute to the higher mass as could a deviation in the polymer's comonomer ratio from the calculated 24 % which is a reasonable assumption within a few percentage points.



**Scheme 4.12:** Reaction scheme for the CuAAC of **PBT24-H** with protected sulfonate azide **17**.

Looking at the NMR spectrum the aromatic region became more complex due to the phenyl rings in the protected sulfonate as well as the now overlapping residual chloroform

signal. Direct comparison of the co-monomer ratio to earlier measurements isn't possible now, although of course it isn't expected to change outside a small margin or error. However, a new signal appeared at 5.56 ppm indicative of the CH<sub>2</sub>-group next to nitrogen in the newly attached part of the side-chain as marked green in Figure 4.19 while at 2.04 ppm no remains of the terminal alkyne protons can be found. On the other side of the triazole units that have been formed by CuAAC both CH<sub>2</sub>-group's surrounding became more similar due to the change from alkyne (sp) to triazole (sp<sup>2</sup>) next to one of them. Accordingly in the spectrum both groups merged into one signal, marked in red. 3HT's thiophene-neighbouring CH<sub>2</sub> peak (blue) remains unchanged. When normalizing integral values relative to the 3HT unit's methyl groups at 0.91 ppm, the co-monomer ratio can be calculated *via* the blue and green signals. In this case a calculated share of clicked units of 25.5 % is obtained.

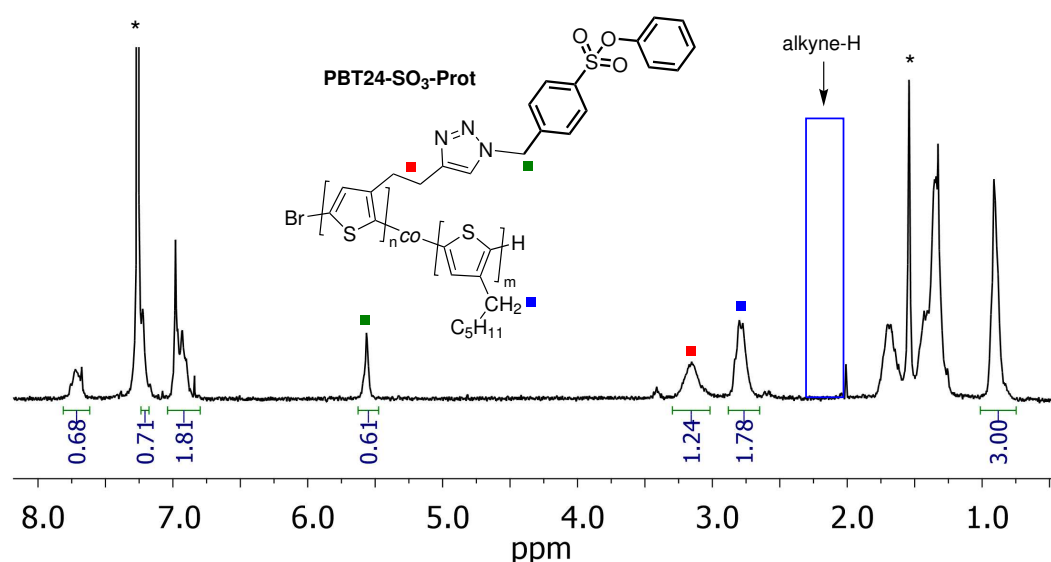


**Figure 4.19:** <sup>1</sup>H-NMR spectrum of CuAAC functionalized PBT24-SO<sub>3</sub>-Prot.

Further characterization was done *via* thermal methods in TGA and DSC, displayed in Figure 4.20. Two overlapping steps can be seen in TGA with onset temperatures at 353 °C and 450 °C. This effect has also been observed in literature for pristine P3HT and in a similar temperature range, where in nitrogen atmosphere a single decomposition stage is observed but two are seen in air.<sup>[149,150]</sup> In DSC, indication of a possible  $T_g$  can be seen below 50 °C which is a common temperature range for polythiophenes and their derivatives, although they are difficult to characterize *via* DSC.<sup>[151–153]</sup> Here, the  $T_g$  is not clearly defined either and will require confirmation by a more sensitive instrument but could be interpreted to be at about 41 °C.

After this characterization, it was proceeded with conversion of the polymer. The

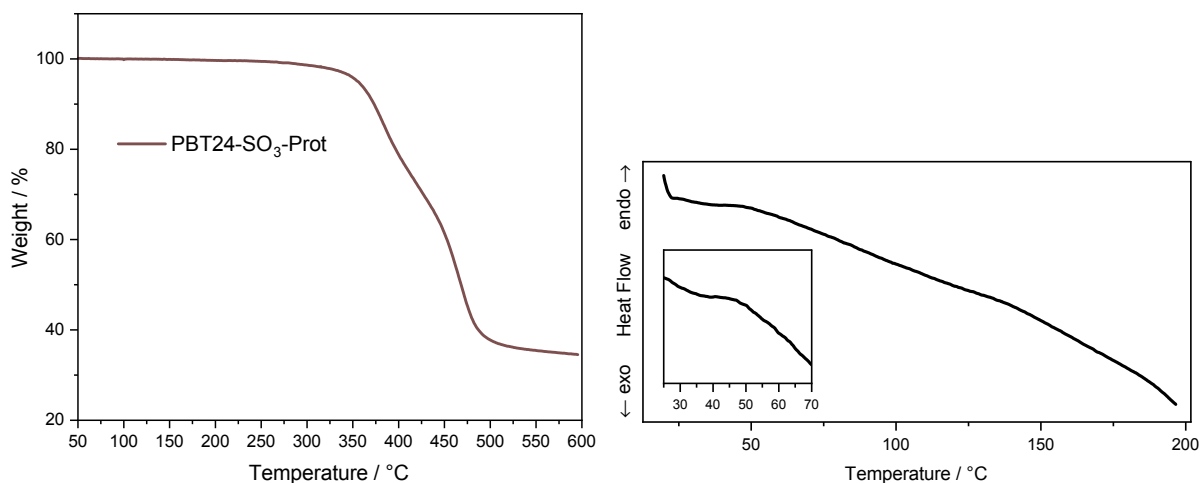


**Figure 4.20:** TGA (left) and DSC (right) spectra of **PBT24-SO<sub>3</sub>-Prot**. TGA: 30 °C to 600 °C at 5 °C/min. DSC: 2nd heat curve at 10 °C/min. Measuring onset dip can be seen at low temperature. Insert shows possible  $T_g$ .

last step in the functionalisation is the removal of the protecting phenyl group from the sulfonate units. This can be performed in solution of the bulk polymer or in thin films of **PBT24-SO<sub>3</sub>-Prot**. Since troubles with solubility were foreseen when attempting this deprotection in the bulk polymer, caused by the relatively low amount of ionic groups of about 25 %, it was proceeded with fabrication of thin films. The schematic representation of this step is depicted in Figure 4.21.

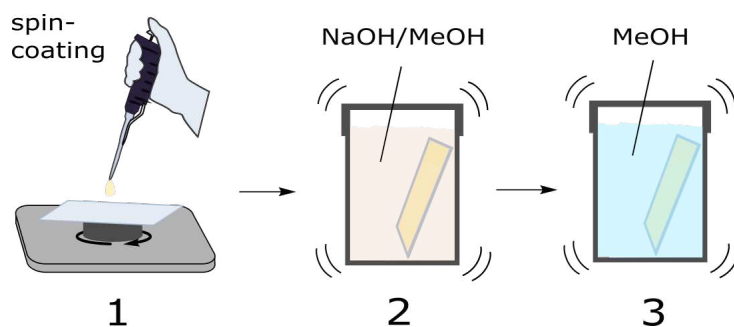


**Figure 4.21:** Procedure for preparation of thin films and deprotection of **PBT24-SO<sub>3</sub>-Prot** to obtain films of **PBT24-SO<sub>3</sub>**. (1) Preparation of thin films *via* spin-coating from 5 g L<sup>-1</sup> solutions in chloroform. (2) Deprotection of sulfonate units by gentle shaking in alkaline methanol solution for 24+ h. (3) Washing of films by gentle shaking in pristine methanol for 30 min.

First, films of **PBT24-SO<sub>3</sub>-Prot** were spin-coated from 5 g L<sup>-1</sup> solutions in chloroform on cleaned glass substrates. The substrates were then placed in glass vials filled with 20 mg mL<sup>-1</sup> solutions of sodium hydroxide in methanol and shaken gently for 24 h and

48 h respectively. Afterwards samples were rinsed with methanol to remove excess NaOH. While NaOH's solubility in water is higher than in methanol which would thus be a more efficient solvent to remove excess salts, using water turned out to delaminate the polymer films from the glass substrates. Instead, after initial rinsing with methanol samples were placed in new vials filled with clean methanol and shaken for another 30 min before further experiments.

Success of the deprotection of these polymer films was confirmed by water contact angle measurements. Figure 4.22 (a) and (b) show representative images of the values obtained before and after the reaction. The top pictures represent the situation before deprotection and bottom picture afterwards. A clear reduction in contact angle from about  $104^\circ$  in both cases to  $87.5^\circ$  and  $83.9^\circ$ , respectively can be observed, owing to the increased polarity of the polymer films. However, the film measured in (a) was washed in water and thus partially delaminated as discussed. It is possible its higher contact angle after washing is due to water being more efficient in removing excess salts from the polymer, but given the damaged nature of the film this is only speculation and since water proved ill-suited for the cleaning step, methanol was used for the next sample.

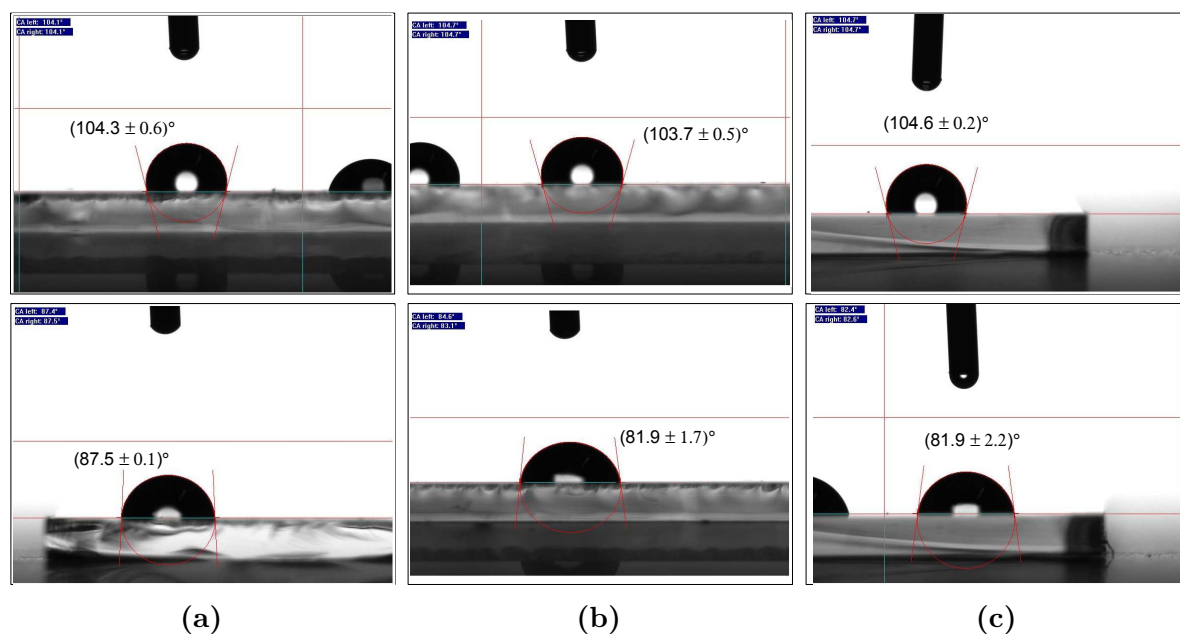


**Figure 4.22:** Water contact angle measurements of **PBT24-SO<sub>3</sub>-Prot** (top) and **PBT24-SO<sub>3</sub>** (bottom) on (a) glass substrate, film cleansed with water. (b) glass substrate, film cleansed with MeOH. (c) IDE, film cleansed with MeOH.

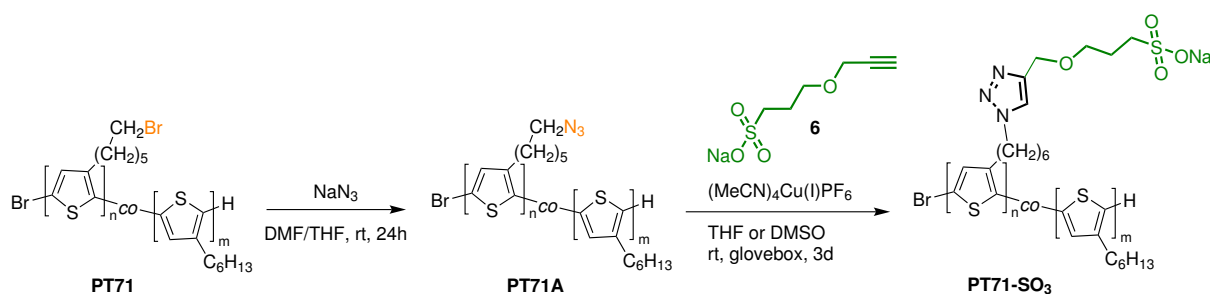
This next sample was prepared accordingly, but on interdigitated platinum electrodes for characterisation of the resulting **PBT24-SO<sub>3</sub>** in impedance spectroscopy. The time given

for deprotection was 24 h. Water contact angle before and after are shown in Figure 4.22 (c) and closely resemble those of the samples on glass.

In preparation for polymer characterisation, film thickness of samples obtained under the employed conditions was determined by AFM. For this, prepared films were scratched with needles. Because of the sensitivity of glass towards scratches and the unsuitable geometry of IDEs, films were prepared on silicon wafers instead and their film thickness measured, giving values of  $(27.5 \pm 1.0)$  nm.

Due to the nature of both the polymer and its protecting group, no quantitative analysis of the deprotection step in film can be performed with the analytical methods available to us. However, the test reaction done beforehand showed the protective group to be removed readily by NaOH. Furthermore, the low thickness of created polymer films and the relatively small size of sodium hydroxide, methanol and the protecting phenyl groups give good reasons to expect a good penetration of the films and thus the reaction to proceed with high conversion.

### 4.2.3 Polymer Analogous Reactions of Bromine-bearing PT71



**Scheme 4.13:** Reaction scheme for the polymer analogous halide-azide exchange reaction of **PT71** followed by introduction of ionic groups *via* CuAAC (BC).

Following procedures of earlier conversions, 194 mg of **PT71** was reacted with sodium azide to replace its side-chain bromine atoms with azide groups. In contrast to the **PVXX** polymers (3.1.3) this polythiophene copolymer showed insufficient solubility in DMF. Since NaN<sub>3</sub> is practically insoluble in any ether, however, a 2:3 solvent mixture of DMF and THF was employed and the polymer dissolved by carefully heating below the boiling point of THF until a clear solution was obtained. Addition of NaN<sub>3</sub> was only done after letting the solution cool down to room temperature and the reaction continued as in previously discussed reactions. After washing of the crude reaction mixture with water and

removal of solvents 169 mg of **PT71A** were obtained with some losses occurring during the liquid-liquid extraction process and a reduced molecular weight due to the heavier bromine atoms being replaced by lighter azide  $N_3$  units.

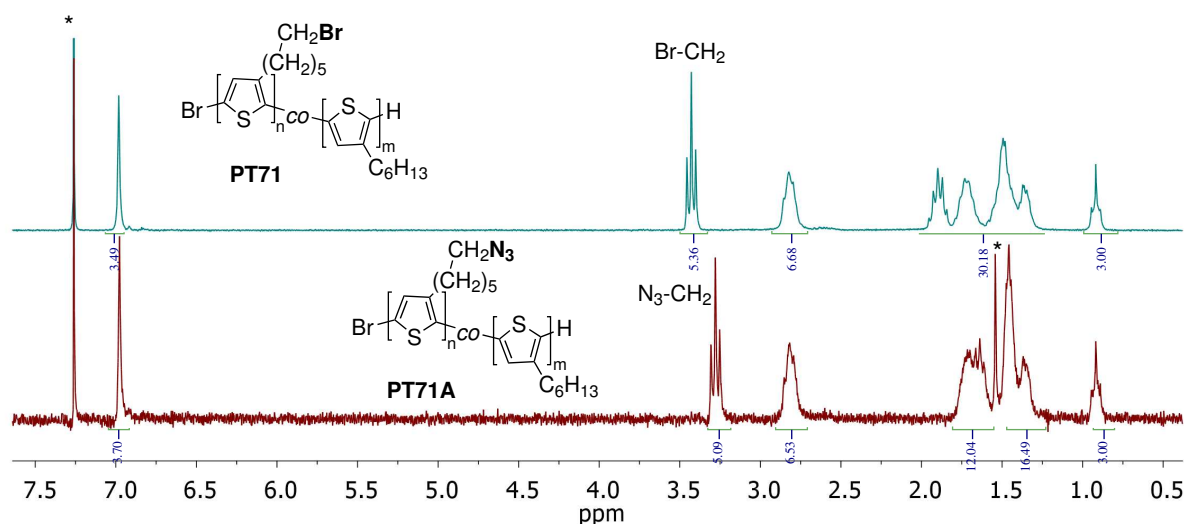


**Figure 4.23:**  $^1\text{H-NMR}$  spectra of **PT71** and **PT71A** showing comparison before and after polymer analogue halide-azide exchange.

Figure 4.23 compares the obtained NMR spectrum of **PT71A** with the same spectrum before conversion. Both spectra look almost identical except for **PT71**'s signal at 3.43 ppm, which disappeared completely and was replaced by a peak at 3.28 ppm instead, reflecting the change in side-chain end-groups. As no residual signal at 3.43 ppm can be found, a complete conversion is assumed. Other than that a minor change in peak structure can be observed with the signals at 1.90 ppm and 1.72 ppm in **PT71**, as they merge into one multiplet at about 1.68 ppm.

Final step in the polymer analogous functionalisation of **PT71** is the copper catalyzed alkyne-azide cycloaddition *Click* reaction to incorporate sulfonate **6** into the side-chains as depicted in Scheme 4.13. Due to the high amount of functionalizable units in the copolymer it was deemed feasible to convert the polymer *via* the bulk solution method (BC) and use the advantages this approach brings, because the high share of ionic groups after successful conversion is expected to alter the polymer's solubility enough to become soluble in polar solvents. Thus, **PT71A** was reacted in a solution of **6**, copper and catalyst  $(\text{MeCN})_4\text{Cu(I)PF}_6$  in THF for 3 days under inert atmosphere in a glovebox. Afterwards the solvent was removed and the crude product's solubility was probed in different solvents and solvent mixtures. Tested was water, THF, DMSO, methanol and a 1:1 mixture of  $\text{H}_2\text{O}$  and THF but none of these proofed suitable for dissolving the obtained copolymer, even

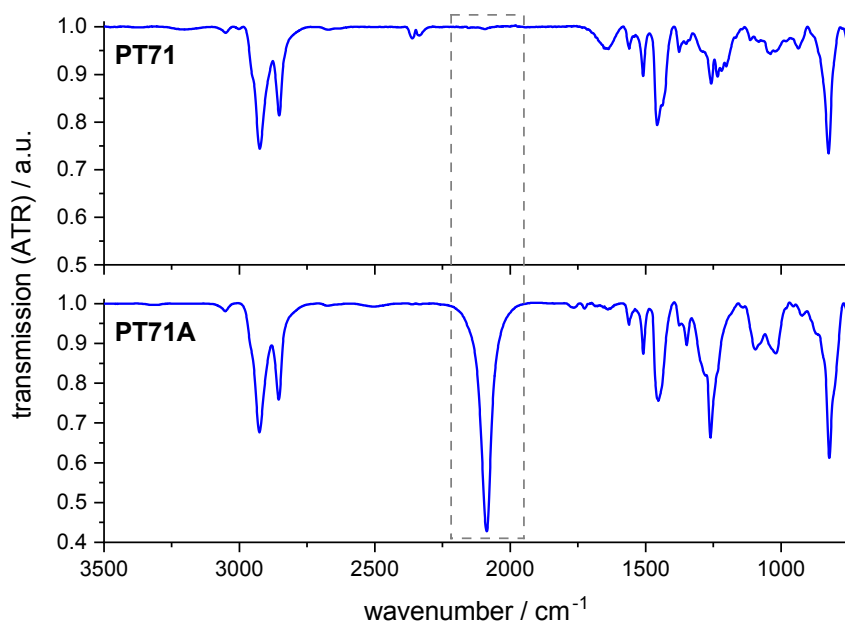


**Figure 4.24:** ATR-IR transmission spectra of **PT71** (top) and **PT71A** (bottom). N=N=N-stretching band is framed by the dashed line.

after prolonged waiting periods of several days or heating of the dispersions. In any of the tested solvents solubility stayed low. This was surprising as the high number of ionic groups that should be present in the polymer should provide a good enough solubility in at least one of these systems. Thus, the crude product was measured in infrared spectroscopy without prior workup to look for remaining azide groups.

Indeed, as can be seen in Figure 4.25 not all N<sub>3</sub> units were reacted during CuAAC. Both, methyl C–H bending band at 1450 cm<sup>-1</sup> and alkyl C–H stretching bands at 2850 cm<sup>-1</sup> are used as reference bands for the intensity of the azide N=N=N-stretching band at 2090 cm<sup>-1</sup>. As marked by the red lines in all three spectra, relative intensity of the alkyl and methyl bands remain consistent throughout and a reduction in azide band intensity with regards to this red line can be observed after the first CuAAC conversion. From signal intensity comparisons it can be calculated that about 40 % of azide groups were converted, leading to an estimated content of ionic repeating units in the copolymer of 28 %. This low number explains the solubility issues with the obtained polymer.

The crude product was filtrated, dried and converted again under the same conditions except for the solvent. It was hypothesized that in this copolymer system, THF isn't polar enough to dissolve the polymer once parts of it become functionalized, thus hindering the reaction. As DMSO is more polar and more effective at dissolving ionic polymers it was used instead. After 3 days, the solution was filtered once again, dried and the substance analysed in IR. As is clear in the bottom spectrum in Figure 4.25 this second CuAAC

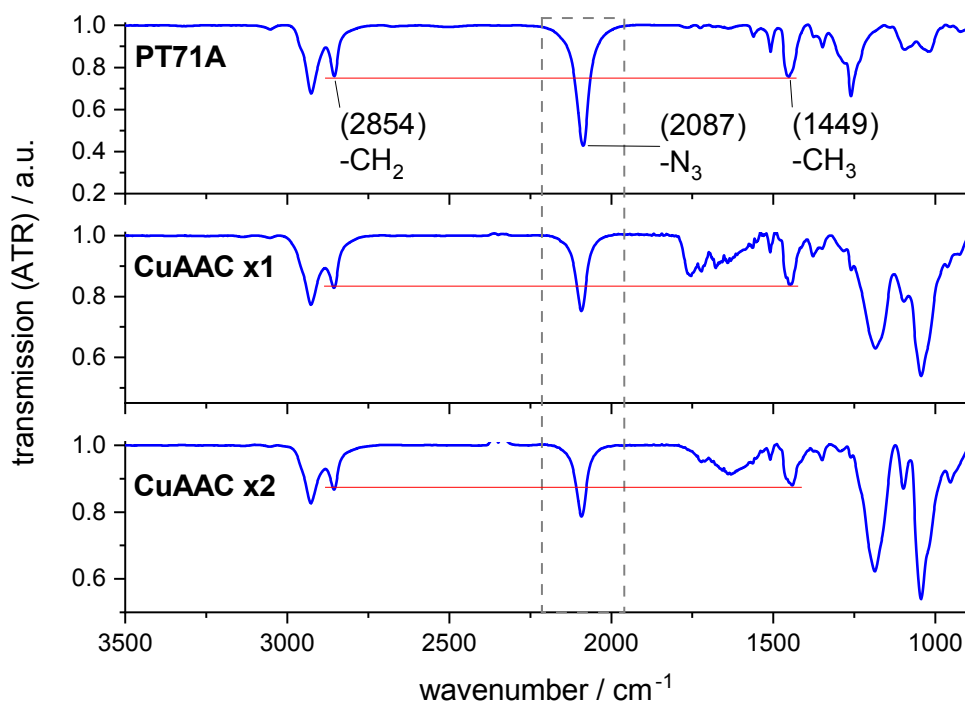


**Figure 4.25:** ATR-IR transmission spectra of **PT71-A** (top) and results of subsequent repeated conversion *via* CuAAC in solution. Red lines serve as reference points with respect to  $1449\text{ cm}^{-1}$  band.

had no effect on the number of converted azide units. Seeing that other similar reactions posed no such difficulties one has to look at the specific situation in this copolymer. The functionalizable side-chains are comparably long already when put side-to-side with the different PVXX copolymers of chapter 3.3.2. On top of this comes the relatively big size of sulfonate **6**, creating long and bulky side chains as is apparent in Scheme 4.13. Even though we have no direct way of confirming this, it is easy to imagine that this is leading to a sterically complicated situation in the polymer, making it more and more difficult for the big anion **6** to reach the polymer's azide groups along with the copper catalyst. On the other hand, twisting of individual thiophene units could alleviate this steric hindrance albeit at the cost of conjugation length, ultimately allowing for higher rate of functionalisation. If and why this apparently doesn't happen could potentially be answered by computational chemistry in future works.

### 4.3 Characterization

Since **PT71-SO<sub>3</sub>** only afforded partial functionalisation of its azide units which lead to solubility issues, no samples could be produced for further characterisation. Hence, only

**PBT24-SO<sub>3</sub>** could be characterised and shall be discussed in the following sections.

### 4.3.1 Impedance Spectroscopy of PBT24-SO<sub>3</sub>

After preparation and functionalisation of the respective sample in chapter 4.2.2, **PBT24-SO<sub>3</sub>** was characterised on an interdigitated platinum electrode in impedance spectroscopy. The experimental setup is depicted in Figure 4.26. Measurements were taken at a controlled temperature of 25 °C unless stated otherwise and different water vapour partial pressures inside the enclosed sample holder were accomplished by controlled flows of dry N<sub>2</sub> and wet N<sub>2</sub> that's been blown through a reservoir of water. By precisely adjusting both nitrogen streams *via* flow controllers the desired water partial pressures  $p_{H_2O}$  were set. Before each new  $p_{H_2O}$  the sample was allowed to equilibrate to the new atmosphere for about 90 min.

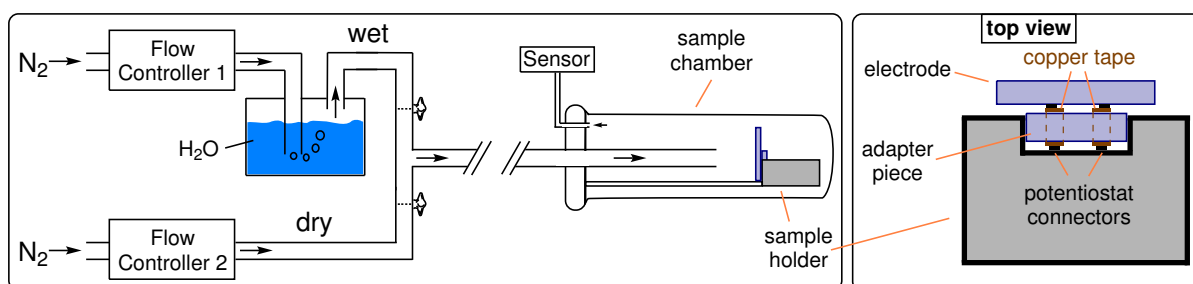


**Figure 4.26:** Schematic depiction of the experimental setup for water partial pressure dependent impedance spectroscopy and placement of the contact adapter piece.

Compared to earlier impedance measurements, IDEs used here were of greater physical dimensions (while providing the same channel length of 5  $\mu\text{m}$ ), thus an adapter piece made with copper tape was used to provide electrical contact with the sample holder. The situation is depicted in Figure 4.26. The overall experimental setup and both a side view and a top view of the sample holder are provided to visualize the electrode and adapter placement. A small gap designed for older IDEs with smaller substrate dimensions contains the potentiostat connectors which are inaccessible for these larger IDE substrates. The adapter piece fits inside the gap and relays the electronic contact from one side to the other *via* copper tape wrapping around the back. The electrode is positioned on the other side so that its contact arms touch the adapter. A side-effect of this setup was an increased internal resistance of the sample holder of 12-18  $\Omega$  (compared to up to 4  $\Omega$  before). Seeing that relevant regions in the impedance experiments with ion conducting (co)polymers lie in the hundreds in the best case and usually far higher than that, this

wasn't an issue for the most part. In some cases, however, very high frequency scans that resulted in very low impedance values could start to give somewhat scattered data points when measuring at frequencies approaching the limit of what the potentiostat was able to provide. This was not observed in earlier experiments without an adapter but it has to be noted that the potentiostat was showing signs of wear and tear over time with increasing issues at the highest frequencies. Thus it cannot be concluded for sure that scattered data in high-frequency regions were because of the use of this adapter and not due to ageing hardware. That being said, all data remained fully treatable as relevant features of the spectra kept their interpretability in all cases, even with somewhat scattered data points in some situations.

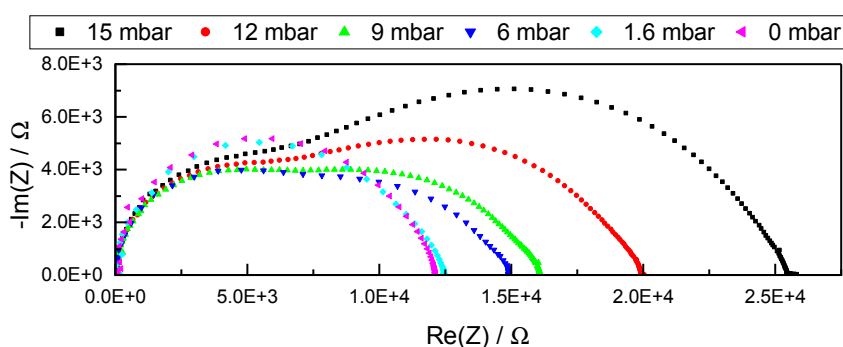


**Figure 4.27:** Impedance spectroscopy at different water partial pressures  $p_{H_2O}$  as a representation of the evolution of spectra shape and dimensions. Higher  $p_{H_2O}$  increased impedance by several orders of magnitude and thus aren't included for practical reasons.

Figure 4.27 shows the spectra measured in the  $p_{H_2O}$  range of 0 mbar to 15 mbar to demonstrate the evolution of shape and dimensions of the obtained data with increasing water vapour content. Measurements at higher water partial pressures resulted in a much stronger increase in impedance values and are thus not included in this depiction as their scale would dwarf the other spectra. A change from single semi-circle to two overlapping semi-circles can be observed in this comparison with the low-frequency part shifting to higher impedance values with increasing water vapour content. In parallel, the high-frequency semi-circle, once appeared, shifts to lower impedance values while decreasing in size. This illustrates increasing electronic resistance with growing water partial pressure while ionic resistance decreases, which might be due to higher ion mobilities in the increasingly wet environment.

This is further illustrated in Figure 4.29, which gives three representative impedance graphs at distinguished points in the experiment along with their respective equivalent circuit fits (EC-Fits). The data provided represents low, medium and high water partial pressures from (a) to (c). The equivalent circuit used for calculation of fitting curves and

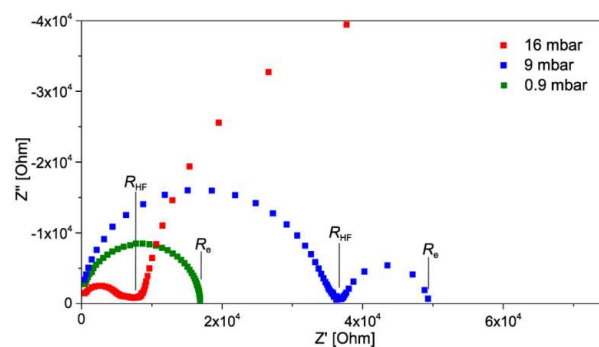


**Figure 4.28:** AC impedance spectra from literature at different  $p_{H_2O}$  with indicated electronic resistance  $R_{el}$  as obtained from DC experiments. Adapted with permission from reference<sup>[13]</sup>. Copyright © 2020 American Chemical Society.

extraction of resistance values is given in Figure 4.29 (a) and was employed for all spectra. Here, **R1** and **R2** are resistor elements while **Q** or **CPE** represents constant phase elements. In a simple model, a resistor in series with **Q** represents the low frequency response of an ionic conductor in between ion-blocking but electronically conducting electrodes, as is the case with the IDEs used here.<sup>[103]</sup> For mixed electronic/ionic conductors the behaviour can be described with the equivalent circuit shown, where with a decent fit R1 provides  $R_{el}$  and R2 gives  $R_{ion}$ . Alternatively, both resistances could be calculated from the impedance spectra by reading out the x-axis intercepts (also compare Figure 4.28). In this case, the low frequency intercept is  $R_{el}$  and  $R_{ion}$  can be calculated from the high frequency intercept  $R_{hf}$  via  $R_{hf} = (R_{el}R_{ion})/(R_{el} + R_{ion})$ .<sup>[13,103,154]</sup>

Looking at the spectra given, at 0 mbar a single semi-circle could be observed which can be assumed to exclusively represent  $R_{el}$  of the aromatic polythiophene backbone, as ionic conductivity is hindered in dry atmosphere. Indeed, the EC fit gives an electronic resistance of 12.14 k $\Omega$  and a value of  $R_{ion}$  in the  $10^{-12}$   $\Omega$  region which equates to no contribution, since in the context of equivalent circuit fitting this states that the R2 element is not needed to calculate the fit. DC galvanostatic polarisation experiments were performed additionally in which a constant current is applied and the system's resulting potential is measured. From this, statements can be made about the influence of ionic processes and the electronic resistance can be read from the curves' plateau. Corresponding plots are given in Figure 4.29 as well, next to their partnering impedance spectra. At 0 mbar the plateau gives an electronic resistance of 12.08 k $\Omega$  in good agreement with the value extracted from impedance. A slight initial bending can be seen after current is applied in the beginning but is not found again when the system is allowed to relaxate, thus no clear polarisation effect and as such no ionic contribution is witnessed.

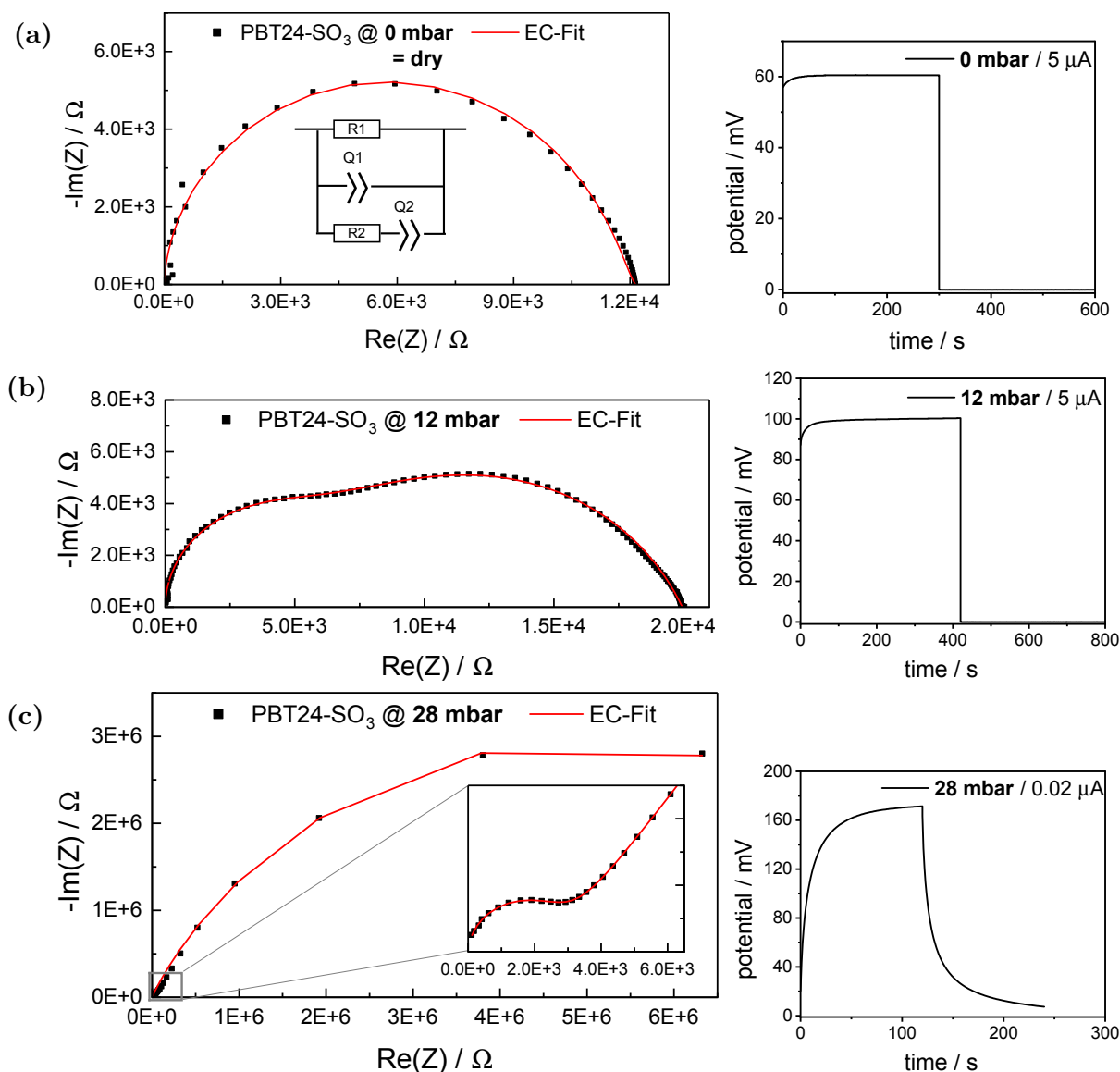


**Figure 4.29:** Left Exemplary impedance spectroscopy data of PBT24-SO<sub>3</sub> measured at different water partial pressures and their equivalent circuit (EC) fits. (a) at 0 mbar and depiction of the EC used for these fits. (b) at 12 mbar (c) at 28 mbar. Right Corresponding galvanostatic polarisation.

Moving on to medium humidity impedance does show signs of two semi-circles and an EC fit provides  $R_{el}$  of 20.0 k $\Omega$  and  $R_{ion}$  of 10.5 k $\Omega$ . However, the ionic part is still not reflected in the polarisation experiment (see Figure 4.29 (b)). Although the initial bending in the DC curve seems slightly more pronounced no polarisation is observed in the relaxation process. Only in higher water vapour content of above 21 mbar is it that we begin to clearly see both, two distinct semi-circles, reminiscent of two conduction processes and polarisation in the DC experiment. Both together are indications of ionic

processes influencing the polymer's overall conductivity. In Figure 4.29 (c) the situation at 28 mbar is provided and at this high water partial pressure electronic conductivity is severely impaired such that the low-frequency semi-circle could only be measured partially due to the high resistance. In comparison, the high-frequency semi-circle is dwarfed and only seen by strongly zooming into the plot. Since the dimensions are so vastly different (three orders of magnitude), fitting was only possible with highest accuracy by doing two separate fits for both regions while accepting somewhat less accurate values for the other semi-circle. This resulted in  $R_{ion}$  of 2.93 k $\Omega$  and  $R_{el}$  of 11 M $\Omega$  at 28 mbar  $p_{H_2O}$ .

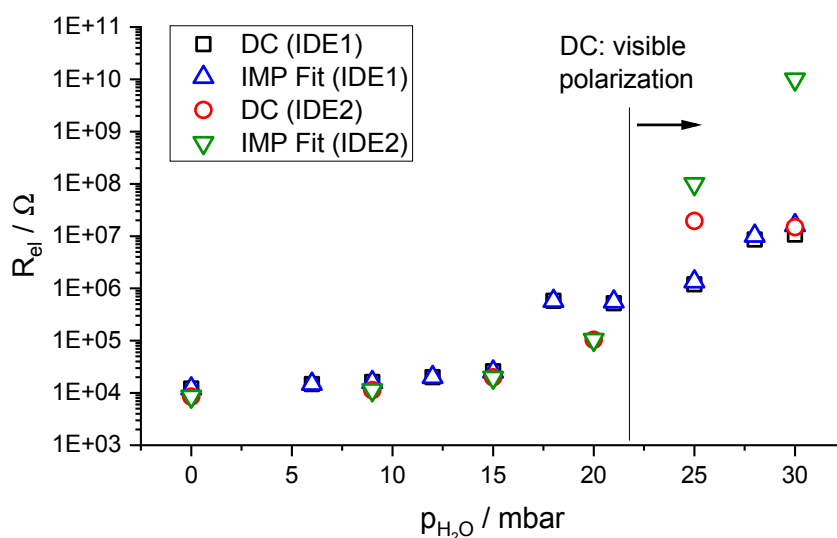


**Figure 4.30:** Comparison of electronic resistance values  $R_{el}$  as determined from AC impedance and DC polarisation experiments on two samples.

Another sample of **PBT24-SO<sub>3</sub>** was prepared analogously and values of  $R_{el}$  obtained from these measurements were cross-checked in both, AC impedance and DC polarisation experiments. Figure 4.30 displays a plot of the electronic resistances gathered that way. Due to the many orders of magnitude that are covered in these experiments a logarithmic y-scale was chosen to be able to display the results. This of course makes differences between experiments appear smaller than they are, however values are consistent across experiments up until 21 mbar  $p_{H_2O}$  and for the most part all the way to 30 mbar. Larger deviations are observed mainly for  $R_{el}$  extracted from impedance at highest water partial pressures with IDE2 for which there are explanations. Firstly, EC fitting was less accurate for the low-frequency range in these measurements because compared to earlier experiments a smaller part of the semi-circle was measured. The reason for this is that measuring of low frequencies takes exponentially longer the lower is measured. Seeing that electronic resistances in high  $p_{H_2O}$  were consistently in the range of mega ohm and higher there

is limited additional information to be gathered from long measurements as resistances of this order ultimately convert to miniscule electronic conductivity of the thin films. Secondly, accuracy of the experimental setup decreases at very large impedance values. Thus, with the limited time available for measurements at the setup it was concluded to cut the time spent for low-frequency experiments, resulting in the higher deviation of these two data points from the others. However, values obtained from the corresponding DC measurements (red circles) mostly fit the trend of the other datasets well, with an exception at 25 mbar.

Also depicted in Figure 4.30 is the point after which polarisation was observed in DC measurements. Consistently, no such ionic contribution was observed up to and including 21 mbar  $p_{H_2O}$ , despite low-frequency semi-circles being visible in impedance at lower humidities. At 25 mbar however, ionic contribution was very clear in both samples. As such, the limit at which this contribution starts to be observed lies somewhere between 21 and 25 mbar.

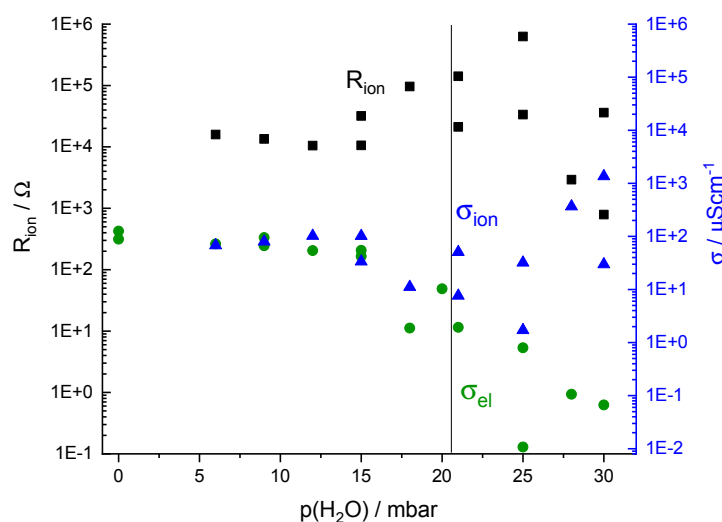


**Figure 4.31:** Ionic resistance and ionic conductivity as determined from impedance spectroscopy of thin films of **PBT24-SO<sub>3</sub>**. Electronic conductivity values are included in green as determined from impedance.

At 0 mbar water partial pressure no ionic conductivity was observed while  $\sigma_{el}$  of these undoped films amounted to up to  $126 \mu\text{S cm}^{-1}$ . Highest ionic conductivity achieved at 30 mbar  $p_{H_2O}$  was  $1361 \mu\text{S cm}^{-1}$   $\sigma_{ion}$  while electronic conductivity  $\sigma_{el}$  dropped to  $0.07 \mu\text{S cm}^{-1}$ . These results are depicted in Figure 4.31. However, as can be seen in this figure, evolution of resistance and conductivity values across experiments showed considerable fluctuation, mostly in the case of ionic values. Between 15 mbar and 25 mbar  $R_{ion}$  and as such  $\sigma_{ion}$  even trends opposite to the expected direction. The reasons for

this are unclear but might be connected to the contradicting results from impedance and DC polarisation concerning the presence of ionic influence. It could be considered that high-frequency semi-circles in this  $p_{H_2O}$  range are not actually representative of ionic resistance but belong to a third process which overlaps (and thus hides) the actual ionic part. However, further evaluation of the data obtained from fitting did not give any conclusive answer to this. If both semi-circles were to be considered electronic processes, plotting of the ionic resistance/conductivity would only start beyond the vertical line in Figure 4.31 while the electronic part would remain as is, since in the high humidity region of 25 mbar and higher, values return to the expected trend. Further interpretation of this situation was done after QCM measurements.

### 4.3.2 Water Uptake of PBT24-SO<sub>3</sub> by QCM

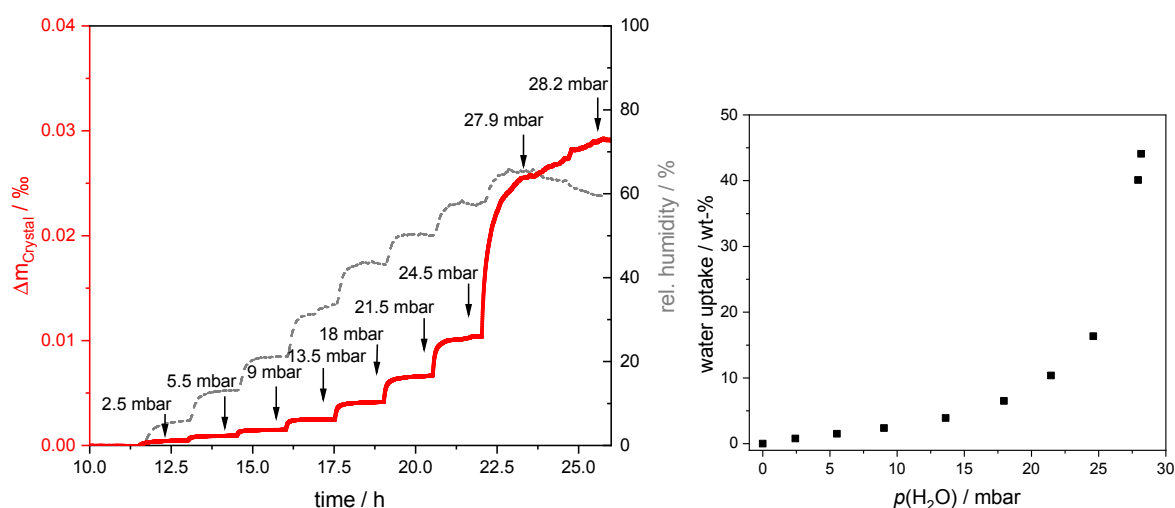


**Figure 4.32:** **Left** Relative weight increase of the polymer coated quartz crystal in increasingly humid atmosphere. Development of RH is given by the grey dashed line. **Right** Relative water uptake with regards to polymer mass depending on water partial pressure.

Figure 4.32 shows the evolution of relative weight increase of a quartz crystal coated with PBT24-SO<sub>3</sub> in an increasingly wet atmosphere. It can be seen nicely how the polymer film takes up water stepwise with each new increase in relative humidity. The higher RH, the more water is taken up with a maximum uptake of 44 wt-% at about 28 mbar water partial pressure (60 % RH). Summer temperatures in the laboratory caused the maximum RH to lie in this region with the setup used. Interestingly, water uptake increases notably just about the 25 mbar mark which is the point after which more conclusive results were obtained for ionic contributions in the preceding impedance and DC experiments. A

possible interpretation could be that it is only at 25 mbar and above where enough water is present in the polymer film to form effective ion channels. Before this, the long and sterically large side-chains in this polymer could inhibit rearrangements necessary for allowing channels to form. However, more research is needed to make definitive conclusions to these results.

## 4.4 Summary

In this chapter, synthesis of two conjugated precursor polymer systems and functionalisation *via* CuAAC was achieved. Both copolymer systems, **PT** and **PBT**, are based on a polythiophene backbone with 3-hexylthiophene as co-monomer. With regards to CuAAC, **PT** offers halogen/azide functionality while **PBT** contains alkyne groups. Monomers have been prepared as described in literature<sup>[2,146]</sup>, while synthesis of monomer **3BrHT** was re-evaluated with a comparison of a 2-step synthesis<sup>[1]</sup> with a 4-step synthesis compiled from literature resources.<sup>[142,144,146]</sup> Here, the longer synthesis resulted in a lower overall yield but in a slightly cleaner monomer built from inexpensive starting materials.

Copolymers **PBT24** (24 % of TIPS-protected alkyne side-chains) and **PT71** (71 % brominated side-chains) were polymerized following established conditions except for minor deviations and bromine in **PT71** was substituted by azide in analogy to chapter 3.1.3. The polymer was then *clicked* with alkyne sulfonate **6** in solution. Contrary to CuAAC reactions before, only about 40 % of the polymer's azide groups were converted here, as determined by qualitative ATR-IR. Subjecting the reacted polymer to another round of CuAAC didn't increase the number of converted azide. It is possible that the long side-chains and the relatively large alkyne are too sterically demanding to allow for a higher degree of functionalization in this polymer. Furthermore, the partial conversion lead to unfavourable solubility properties, thus it was not possible to create solution-processed films from it for further characterization.

For conversion of **PBT24** a suitable azide sulfonate was first synthesized from commercially available 4-Bromomethyl-benzenesulfonyl chloride **15** and protected with phenol to afford **17**. A reliable deprotection procedure was ensured *via* model reactions. Prior to CuAAC, **PBT24** was deprotected following literature conditions.<sup>[2]</sup> Subsequent clicking of the protected azide sulfonate **17** onto the polymer was then confirmed by PM-IRRAS and <sup>1</sup>H-NMR spectroscopy and proceeded quantitatively to give **PBT24-SO<sub>3</sub>-Prot**. Due to the polymer's low share of functional groups, deprotection of the sulfonate units was expected to introduce unfavourable solubility properties. Thus this step was not performed in solution but within thin films created from **PBT24-SO<sub>3</sub>-Prot** solutions in chloroform, both on glass substrates and on interdigitated platinum electrodes. Evaluation of the

consequent deprotection was done by water contact angle measurements and on both substrates a notable and comparable decrease in contact angle after deprotection of the ionic groups was observed.

Subsequently, characterization by humidity dependent impedance spectroscopy presented both, electronic and ionic contributions to the polymer's overall conductivity, albeit its  $R_{el}$  was high in this undoped state. However, clear ionic contributions were only observed at water partial pressures above 21 mbar, reaching a maximum value for  $\sigma_{ion}$  of  $1360 \mu\text{S cm}^{-1}$  at 30 mbar  $p_{H_2O}$ . In humidity dependent QCM, at the maximally reached 28 mbar  $p_{H_2O}$  the polymer showed a relative water uptake of 44 wt-%, comparable with that of unconjugated polymer **PV49-SO<sub>3</sub>/BC** but with a considerably lower maximal ionic conductivity.

# 5 Conclusion and Outlook

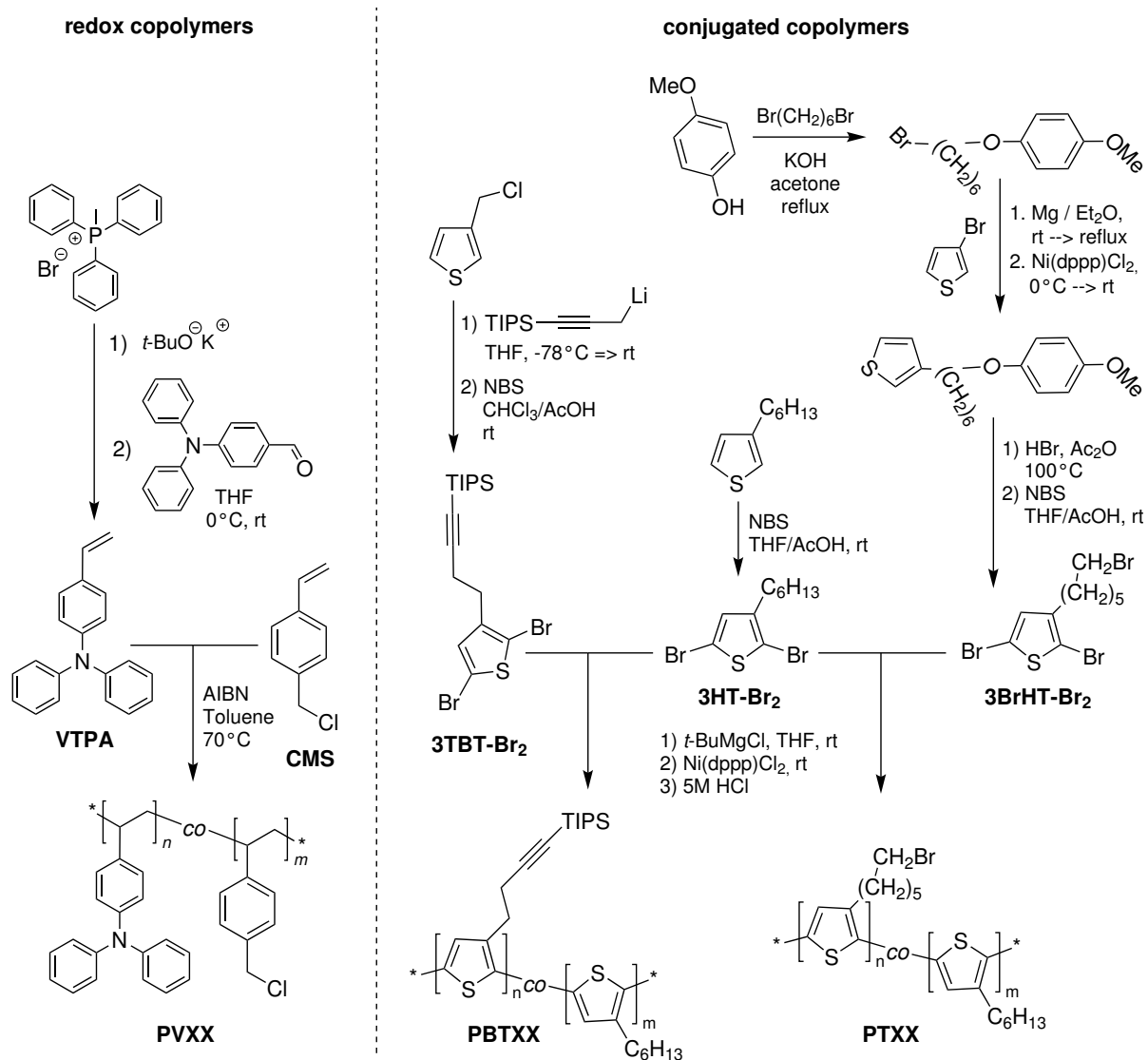
The work presented in this dissertation picked up on side-chain functionalization topics from earlier works. These included synthesis of modified poly(alkylthiophene)s to obtain conducting polymers enhanced with additional functionality as well as redox polymers based on triphenylamine (TPA) or carbazole side-groups which can provide electronic conductivities of  $10^{-3} \text{ S cm}^{-1}$  in doped homopolymers,<sup>[4]</sup> stable redox-switching and the ability to stabilize the film and its morphology by (electro)chemical crosslinking. Thus, the approaches in this thesis included conjugated regio-regular poly(3-alkyl)thiophenes with modifiable side-chain end groups and (non-conjugated) polyvinyl redox polymers based on TPA side groups and functionalizable styrene derivative co-monomers. Statistical copolymers have been created accordingly to obtain highly versatile copolymer template systems and redox-active and ionic functionality was connected covalently. Evaluation of covalent functionalization *via Click* chemistry and determination of humidity dependent properties was performed.

## Task 1 - Preparation of versatile copolymer systems for polymer analogous functionalization

Synthetic routes to the different copolymer systems are given in Scheme 5.1. The copolymers obtained here are referred to as *base copolymers* as they need to be converted polymer analogously before being suitable for CuAAC functionalizations. Due to its redox and crosslinking capabilities (Scheme 5.2) the **PVXX** system was chosen as the main target of interest, as different co-monomer ratios not only allow for tuning of the influence from functional groups but for adjustments to morphology and polymer network size obtained from TPA crosslinking, as well. Polymerization conditions were based on literature<sup>[131,155]</sup> and earlier experiments and were further optimized to give reliable results with all monomer feed ratios. 3 copolymers with different VTPA/CMS ratios were synthesized and gave molecular weight averages  $\overline{M}_n$  of  $6000 \text{ g mol}^{-1}$  to  $11\,500 \text{ g mol}^{-1}$  with dispersities  $D$  between 2.01 and 2.41.

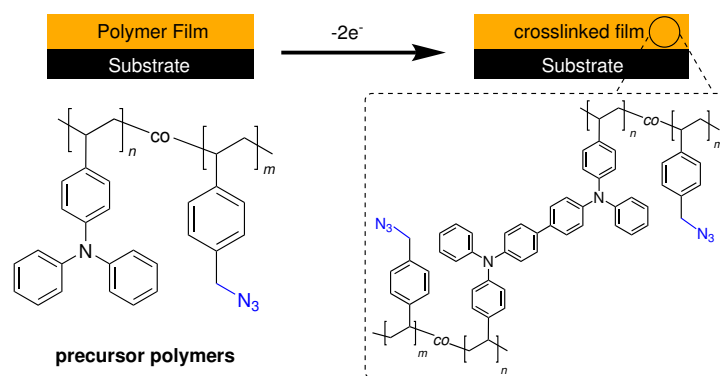
Conjugated copolymer systems **PBTXX** and **PTXX** were synthesized in one ratio each after polymerization conditions were revisited to probe for potential improvements to overall polymer quality. For **PBTXX** existing conditions<sup>[2,128]</sup> were eventually kept largely the same from monomer synthesis to polymerization. For **PTXX**, minor non-removable impurities in the **3BrHT-Br<sub>2</sub>** monomer from a shorter 2-step synthesis were deemed to contribute to shoulders in SEC. They could be avoided by switching to a longer 4-step

synthesis from inexpensive starting materials as depicted, affording highly pure monomer. Subsequent polymerization was again based on existing conditions<sup>[1,146,156]</sup> with small adjustments for reliable results in a controlled reaction environment.



**Scheme 5.1:** Synthetic routes to base copolymers of the systems prepared in this dissertation, offering redox and crosslinking functionality (**PVXX**) or conjugated backbones (**PBTXX** and **PTXX**). All polymers can be copolymerized with varying monomer feed ratios.

The resulting main batch of polymer used for further experiments consisted 2:1 of functionalizable **3BrHT-Br<sub>2</sub>** and co-monomer **3HT-Br<sub>2</sub>**. The reverse ratio was given in the final **PBTXX** copolymer. Resulting molecular weight averages amounted to  $\bar{M}_n$  of  $12\,600\text{ g mol}^{-1}$  with dispersities  $D$  of 1.26 for **PT71** (with 71% **3BrHT-Br<sub>2</sub>**) and  $\bar{M}_n$  of  $14\,000\text{ g mol}^{-1}$  with dispersities  $D$  of 1.40 for **PBT24** (with 24% **3TBT-Br<sub>2</sub>**).

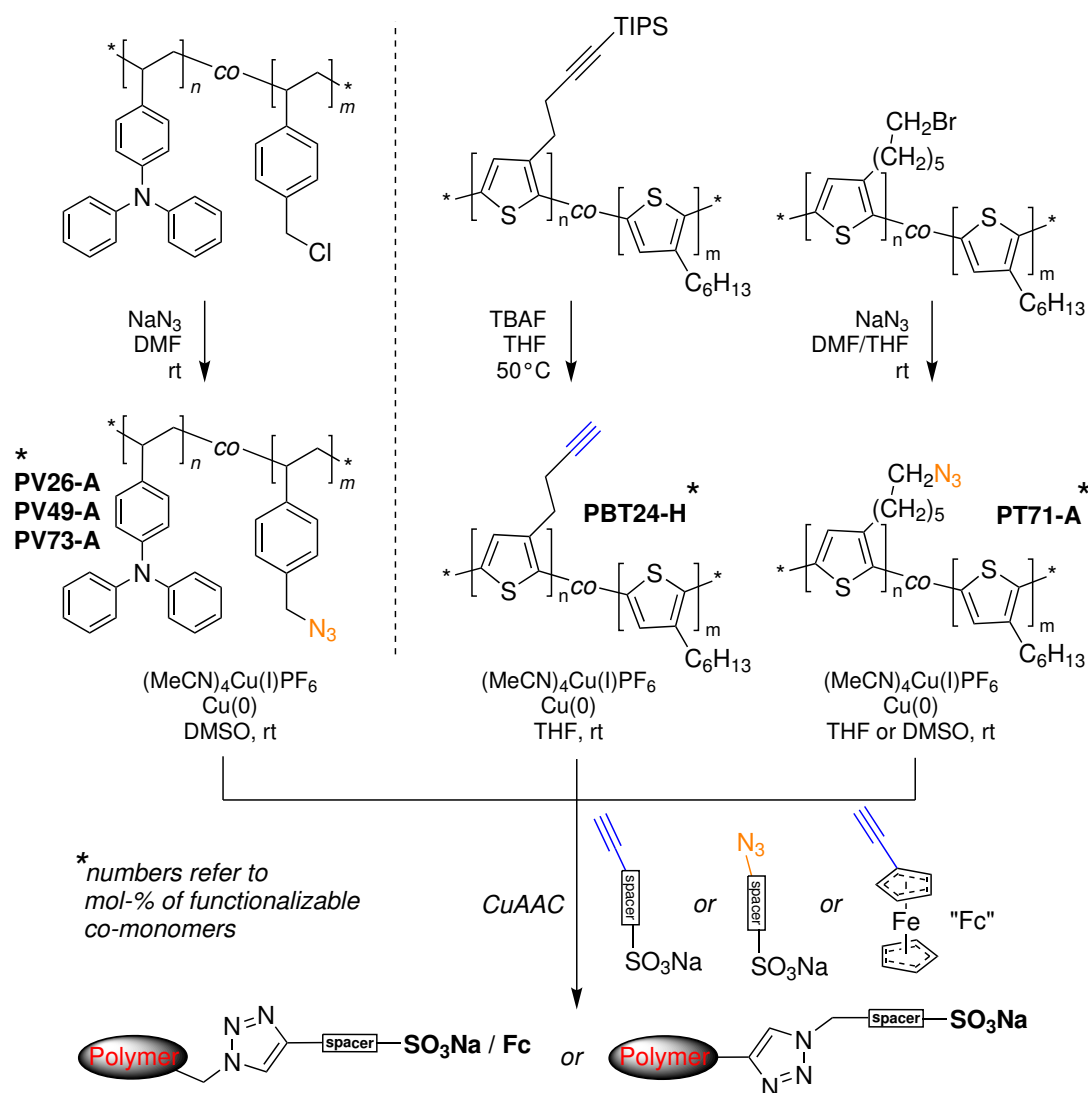


**Scheme 5.2:** Depiction of crosslinking in **PVXX** polymer films intended for subsequent CuAAC.

## Task 2 - Introduction of ionic moieties *via* Click Chemistry

Scheme 5.3 gives the co-monomer ratios of the main polymerization batches obtained from polymer analogous conversions of the base copolymers. These polymers are referred to as *polymer precursors* because they serve as versatile platforms for click functionalizations. The numbers depict molar shares of functional (coloured) repeating units as determined from  $^1\text{H-NMR}$  spectroscopy. From halide-bearing copolymers **PV26**, **PV49**, **PV73** and **PT71**, azide-functionalized polymers (...-A) were attained by nucleophilic substitution at room temperature, giving stable copolymers that can be stored in ambient conditions for future conversion. Losses from this procedure largely originate of workup efforts to remove the reaction solvent from the product polymer. In the case of **PBT24**, the butyne side-chain was deprotected only prior to click chemistry due to the limited stability of terminal alkynes, resulting in polymer **PBT24-H**.

First experiments towards CuAAC reactions were done on **PVXX-A** polymers and the azidomethylstyrene (AMS) monomer. Model reactions were used to assess the catalytic system which had been used before on different systems<sup>[127]</sup> and to identify characteristic signal shifts in IR and NMR spectroscopy. Furthermore, different methods of performing CuAAC were approached; electrochemically in films (**EC**), chemically in films (**CC**) and chemically in solutions of bulk polymers (**BC**). Between both in-film methods, CC was chosen as the preferred one due to somewhat more reliable results and the fact that CC and BC share the same catalytic system, thus a higher degree of comparability is given. This was deemed important, due to limited viable methods of assessing these CuAAC conversions in thin films. Prior to reactions in films, TPA-containing polymers were electrochemically crosslinked (Scheme 5.2) to stabilize the polymer films against



**Scheme 5.3:** Synthetic route from base polymers to polymer precursors with subsequent copper catalyzed *Click* chemistry (CuAAC) to introduce new functionalities. Template polymers have been prepared in various co-monomer ratios as depicted.

dissolution in the reaction solvent.

In Figure 5.1 (a) and (b) PM-IRRAS spectra of CC CuAAC conversions with functional groups ferrocene (Fc) and sulfonate (SO<sub>3</sub>) are given and compared with ATR-IR spectra of BC conversions of the same polymer, (c) and (d). Both methods were found to give high degrees of conversion with some advantage to sulfonate functionalization over ferrocene. However, truly quantitative modifications were in both cases only achieved in solution *via* BC. In addition to IRRAS spectroscopy, water contact angle (CTA) and electrochemical characterization was done on **PV73-A** and **PV73-Fc/CC** films, including scan rate dependent cyclic voltammetry. Presence of Fc in the polymer films was confirmed from

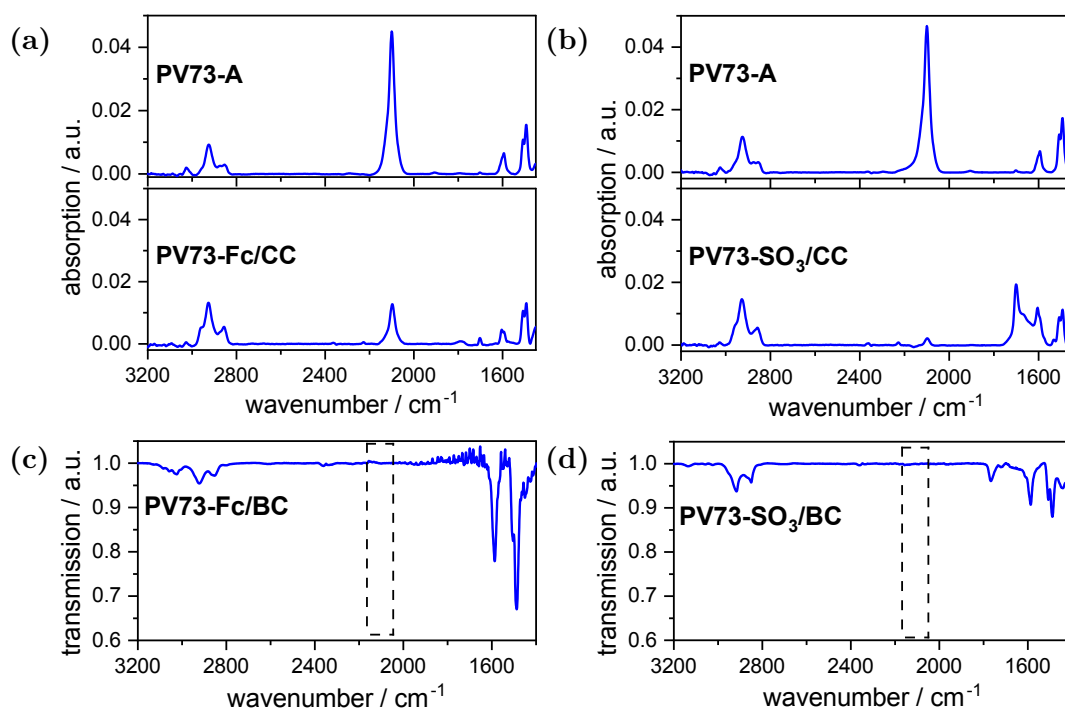
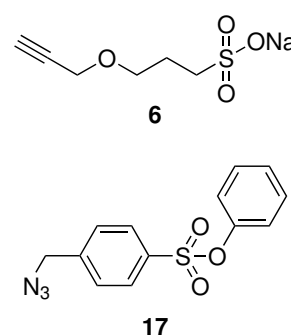


**Figure 5.1:** Comparison of CuAAC functionalization in film (CC) and in solution (BC) with ferrocene and sulfonate moieties by infrared spectroscopy characterization. (a) PM-IRRAS spectra of **PV73-A** films on gold functionalized with ethynylferrocene *via* CC. (b) PM-IRRAS spectra of **PV73-A** films on gold functionalized with ionic alkyne sulfonate **6** (see page 136) *via* CC. (c) ATR-IR spectrum of bulk **PV73-A** after functionalization with ethynylferrocene *via* BC. (d) ATR-IR spectrum of bulk **PV73-A** functionalized with ionic alkyne sulfonate **6** *via* BC.

CVs while scan rate and ferrocene peak current values were found to follow a linear relationship that is expected for adsorbed/covalently bound species, as opposed to a square root dependency that is observed for loose/freely diffusing compounds.<sup>[157–159]</sup> Thus, despite some unreacted azide groups that remained after CC, successful CuAAC with ferrocene was confirmed and analogously performed reactions for the introduction of ionic sulfonate groups were confirmed by comparative IRRAS and CTA measurements. Surprisingly, humidity dependent AC impedance spectroscopy with sulfonate-functionalized films (**PV73-SO<sub>3</sub>/CC**) did not give reproducible confirmation of ionic influences to the polymer's overall conductivity. Figure 5.2 (a) gives the polymer's response at ambient conditions which equates to a medium humidity level. Due to its TPB's non-conductive nature in the undoped state, effectively only ionic responses would be interpretable in AC impedance, however, no clear response was observed. Looking at Figure 5.2 (b) as a comparison, films from pre-clicked **PV73-SO<sub>3</sub>/BC** give a clearly visible semi-circle,

representative of ionic contributions to its resistance  $R_{ion}$ . The steep increase in impedance at lower frequencies/higher real part impedance stems from the incomparably larger electronic resistance due to its aliphatic backbone and undoped TPA's low electronic conductivity  $\sigma_{el}$ . Since the BC polymer was not crosslinked, the presence of a more restrained interconnected polymer network in the CC polymer is a possible explanation for this difference. However, CC clicking without prior crosslinking poses issues with film stability which would complicate a direct future comparison of crosslinked and non-crosslinked films but new information might be retrieved by morphological studies *via* AFM or (cross-sectional) SEM.

As a result of this CC/BC difference, introduction of ionic moieties in all **PVXX-A** polymers was done by BC, instead of CC. In case of the 26 % copolymer, change in physical properties accompanying this conversion lead to unfavourable solubility so that film preparation wasn't feasible. Both other polymers, however, were spin-cast and characterized in AC impedance as summarized in Figure 5.2 (c) and (d). Dependence on water partial pressure  $p_{H_2O}$  is clearly visible and the undoped polymer films reached ionic conductivities of up to  $8000 \mu\text{S cm}^{-1}$  (**PV49-SO<sub>3</sub>/BC**) and  $9500 \mu\text{S cm}^{-1}$  (**PV73-SO<sub>3</sub>/BC**) at 30 mbar.



A difference can be found in how quickly this conductivity deteriorates with decreasing  $p_{H_2O}$  in the environment, e.g. at 15 mbar, which can be considered close to ambient conditions, **PV73-SO<sub>3</sub>/BC** still reached  $147 \mu\text{S cm}^{-1}$   $\sigma_{ion}$  while **PV49-SO<sub>3</sub>/BC** dropped to  $23 \mu\text{S cm}^{-1}$  at that same level, reminiscent of **PV73-SO<sub>3</sub>/BC**'s larger ionic network. These values are accompanied by different levels of relative water uptake into the polymer films as was determined by humidity dependent quartz crystal micro balance characterization (summarized in Figure 5.2 (e) and (f)). Here, at the highest reached humidity setting of 28 mbar  $p_{H_2O}$ , **PV73-SO<sub>3</sub>/BC** showed a wt-%( $H_2O$ ) of 67 % while **PV49-SO<sub>3</sub>/BC** topped off at 41 %. Relating these numbers to the ionic shares in each polymer, not only are **PV73-SO<sub>3</sub>/BC**'s raw numbers higher, the water uptake per ionic group slightly surpasses that of **PV49-SO<sub>3</sub>/BC**, as well. Nevertheless, both systems gave promising results with predictable ionic resistance and water uptake behaviour across the whole humidity spectrum, with both polymers reaching conductivity levels comparable to polystyrene sulfonate (PSS)<sup>[104]</sup> while offering additional functionalities *via* their TPA units, namely network formation by crosslinking, redox activity and stable redox switching as well as electronic conduction when doped.<sup>[4]</sup> Future work could assess effects of chemical doping on the polymers' overall conductivity characteristic, where common dopants such as 7,7,8,8-tetracyano-2,3,5,6-tetrafluoroquinodimethane (F4TCNQ) or  $\text{FeCl}_3$  are not only

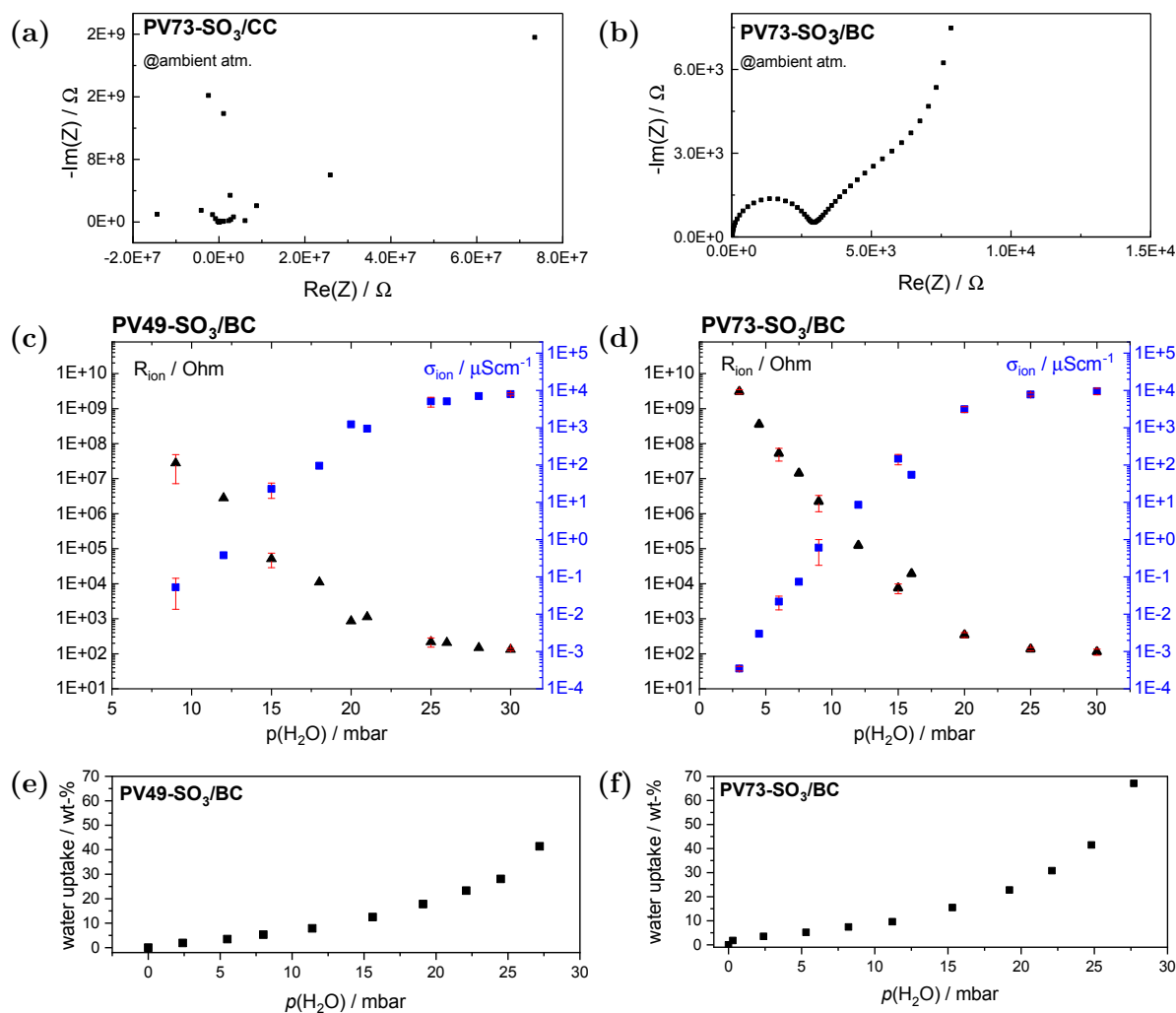


**Figure 5.2:** (a)/(b) Determination of AC impedance of **PV73-SO<sub>3</sub>** obtained from **PV73-A** by CC (in film) vs BC (in bulk solution) in ambient atmosphere. (c)/(d) Results of humidity dependent AC impedance characterization of **PV49-SO<sub>3</sub>** and **PV73-SO<sub>3</sub>** obtained from BC. Ionic resistance and conductivity is displayed at different water partial pressures  $p_{\text{H}_2\text{O}}$ . (e)/(f) Results of humidity dependent quartz crystal micro balance characterization of **PV49-SO<sub>3</sub>** and **PV73-SO<sub>3</sub>** obtained from BC. Relative water uptake of polymer films at different water partial pressures is given.

expected to boost the electronic conduction but the ionic one as well, due to the introduction of additional charges. Furthermore, the influence of crosslinking to the overall system can be examined, alongside explorations into modified redox characteristics by employing substituted VTPA monomers instead of pristine ones.<sup>[3]</sup>

Moving on to the conjugated polymer systems, two approaches were explored by using the two polymers. The now established BC CuAAC method was attempted for **PT71-A** to introduce the same alkyne sulfonate as in the **PVXX-A** copolymers with the goal of

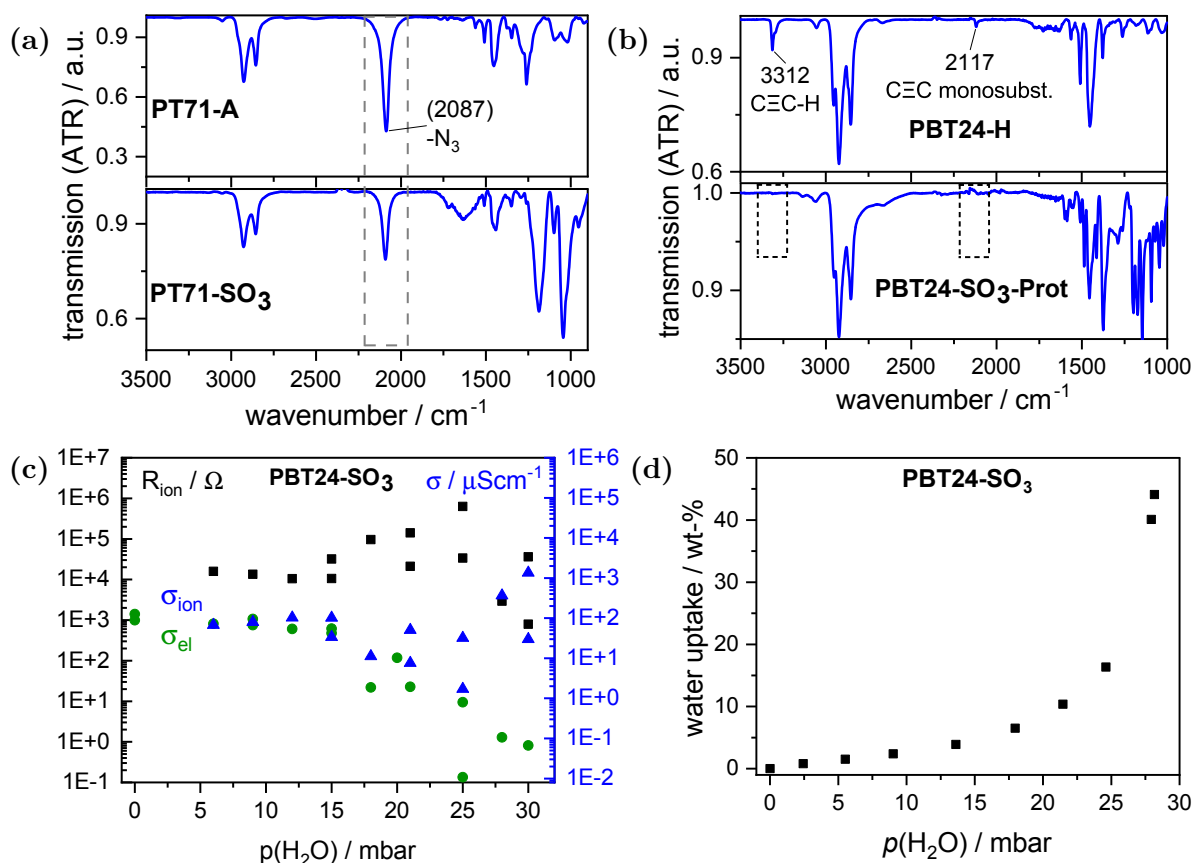


**Figure 5.3:** (a)/(b) ATR-IR spectra of polythiophene-based template polymers **PT71-A** and **PBT24-H** after BC functionalization with sulfonate moieties. Notice reductions in band intensities of characteristic azide and alkyne bands, as marked respectively. (c) Results of humidity dependent AC impedance characterization of **PBT24-SO<sub>3</sub>** obtained from deprotection of **PBT24-SO<sub>3</sub>-Prot** films. Ionic resistance alongside ionic and electronic conductivity is displayed at different water partial pressures  $p_{H_2O}$ . (d) Results of humidity dependent quartz crystal micro balance characterization of **PBT24-SO<sub>3</sub>** films. Relative water uptake of polymer films at different water partial pressures is given.

casting films from the fully functionalized polymer powder. However, conversion only proceeded partially in this system, as can be seen in Figure 5.3 (a). The bottom spectrum displays the situation after two consecutive BC reactions in THF and DMSO, respectively. No further reduction in azide band intensity could be achieved and this partial ionic functionalization lead to solubility properties which didn't allow for thorough workup, nor the creation of polymer solutions to cast films from. When considering the molecular structure of **PT71-A** it is likely that the length of the alkyl side chains leads to steric hindrance when alkyne sulfonate **6**, which is rather spacious in itself, is introduced. Thus,

future attempts should either move to a sulfonate with shorter spacer length, use monomers with shorter alkyl side chains, or both. On the other hand, from the IRRAS spectrum a conversion of about 40 % of azides can be estimated, thus a respective copolymer with less functional groups should be fully functionalizable, although the solubility issues would need to be addressed, potentially in the same way as for **PBT24-H**.

In **PBT24-H** another approach was taken which allowed for a lower share of functional groups, despite the preceding negative results. Here, BC was undertaken with the protected azido sulfonate **17** (page 136). Hereby, polarity of the polymer didn't change during CuAAC and the product could be fully characterized and processed. Figure 5.3 (b) gives the corresponding ATR-IR spectra showcasing a full conversion by disappearance of all alkyne signals to give **PBT24-SO<sub>3</sub>-Prot**. From this polymer, films were cast and deprotection was first assessed by model reactions with compound **17** and preliminary polymer film deprotections on glass substrates which served to identify changes in CTA upon removal of the protecting group. Subsequently, films were cast on interdigitated electrodes and deprotected accordingly to give **PBT24-SO<sub>3</sub>** before being characterized by humidity dependent AC impedance and QCM measurements. Figure 5.3 (c) and (d) summarize the results.  $\sigma_{ion}$  and  $\sigma_{el}$  overall show characteristics expected from increasing surrounding water content, which is an increase in ionic and a decrease in electronic conduction. However, in the medium humidity region, AC impedance and DC polarisation experiments showed conflicting features which seem to point towards an onset of ionic contributions at ambient humidity levels, only to then disappear before ultimately reappearing at high humidity levels, causing a bend in the graph before the expected behaviour is observed, as can be seen from the figure. Further assessments of this polymer system will be necessary to answer what is happening in the film but it seems likely that a third process (e.g. grain boundary/interface effects) is taking part in shaping the impedance response. This further research may also include comparisons with higher shares of functional groups. Seeing that this polymer system has inherent electronic conduction due to its conjugated polythiophene backbone, an additional overlying electronic mechanism seems plausible. This conjugated backbone gives the copolymer undoped electronic conductivity in the dry state of about  $100 \mu\text{S cm}^{-1}$ , which reduces to  $0.07 \mu\text{S cm}^{-1}$  at 30 mbar  $p_{H_2O}$ . Ionic conductivity reaches a maximum of  $1360 \mu\text{S cm}^{-1}$ , although with a notable deviation between measurements. This is accompanied by a maximal relative water uptake of 44 wt-% which is comparable to that of **PV49-SO<sub>3</sub>/BC** despite the lower number of ionic groups. On the other hand, ionic conduction is low and rather unreliable, so more work is needed to compare **PBTXX** systems with higher ionic shares to both, **PBT24-SO<sub>3</sub>** and the **PVXX-SO<sub>3</sub>/BC** copolymers.

# 6 Experimental Part

## 6.1 Analytical Methods and Devices

### Nuclear Magnetic Resonance (NMR)

$^1\text{H}$ - and  $^{13}\text{C}$ -NMR spectroscopy was carried out at room temperature with a *Bruker Avance DPX 250* spectrometer at 250 MHz and 63 MHz, respectively. Spectra were calibrated with their respective solvent residual signal.<sup>[160]</sup>

### Size-Exclusion-Chromatography (SEC)

SEC measurements were conducted at an *Agilent 1260 Infinity* system at room temperature with a solvent flow rate of  $1\text{ mL min}^{-1}$  and THF as the eluent. The column cascade stationary phase consisted of a *SDV 5  $\mu\text{m}$*  precolumn (5 cm) and two mixed-bed *SDV linear 5  $\mu\text{m}$*  main columns (30 cm) from *Polymer Standards Service (PSS)*. Detection occurred using UV ( $\lambda = 275\text{ nm}$ ) or refractive index (RI) detectors. Calibration was done using narrowly distributed polystyrene standards from *PSS* for all measurements.

### Differential Scanning Calorimetry (DSC)

Measurements were done on a *PerkinElmer DSC 4000* system with a heating rate of  $10\text{ K/min}$  and a cooling rate of  $5\text{ K/min}$  and 3 cycles of heating and cooling each run.

### Thermogravimetric Analysis (TGA)

Thermogravimetric analysis was carried out at a *TGA 4000* Thermogravimetric Analyzer from *Perkin Elmer*. Characterization was performed with a heating rate of  $5\text{ K min}^{-1}$ . Prior to each measurement, the ceramic pan meant to hold sample material was heated to incandescence using a Bunsen burner to remove any unwanted residues.

### Mass Spectrometry (MS)

Mass spectrometry was measured at the *Institute of Organic Chemistry* at the *University of Stuttgart* using Electrospray Ionization (ESI), Electron Impact Ionization (EI) or Chemical Ionization (CI) in positive or negative mode on a *micrOTOF-Q* spectrometer from *Bruker Daltonics* or on a *Finnigan MAT 95* spectrometer from *Fisher Scientific*.

## Atomic Force Microscopy (AFM)

AFM was used to determine film thickness of spin-coated polymer films by scratching said films and measuring the scratches on a *Bruker Dimension Icon* device. Image processing was done with the *Bruker Nanoscope Analysis* software. Scratches were made with either wooden toothpicks (for glass and gold substrates) or with metal syringe tips (on silicon substrates).

Multiple scratches were measured at different positions on the substrate for each sample and the resulting thickness values are given as averaged numbers.

## UV-VIS Spectroscopy

UV-VIS spectroscopy was carried out in solution in the absorption range from 200 nm to 900 nm using a *Lambda 35* spectrometer from *PerkinElmer*.

## Infrared Spectroscopy

Attenuated Total Reflectance (ATR) and Grazing Incidence experiments were measured at an *IFS 66/S* spectrometer from *Bruker*. Different sample modules were employed, depending on the method. ATR scans were performed with a diamond ATR unit ("*Golden Gate*"), grazing incidence was done using a *VeeMAXTM II Variable Angle Specular Reflectance* unit from *Pike Technologies*.

Polarization Modulation Infrared Reflection Absorption Spectroscopy (PM-IRRAS) of thin films was carried out with a *Vertex70v* spectrometer from *Bruker* in the research group of Prof. Dr. Frank Gießelmann at the *Institute of Physical Chemistry* of the *University of Stuttgart*. Unless otherwise stated, the controller was set to focus measurements on  $2100\text{ cm}^{-1}$ . Baselines of the recorded spectra were flattened in manual mode for improved precision and the data processed within the software *OPUS v7.5* as described in the accompanying manual.

## Water Contact Angle Measurements (CA)

Water contact angle was determined using a *Water Contact Angle System OCA 20* from *DataPhysics Instruments GmbH*. Drops of  $1\text{ }\mu\text{L}$  volume were brought onto polymer film substrates and the angle calculated with the help of a recorded freeze frame of the drop's profile using an elliptic fit.

Samples on interdigitated electrodes were measured with two drops only, because of the small physical dimensions of the electrode area. Gold and glass substrates were measured with at least four drops each.

## Cyclic Voltammetry (CV)

Cyclic Voltammetry of thin polymer films was measured at room temperature in a three-electrode setup with platinum electrodes as counter-electrodes, polymer-coated substrates (ITO- or gold-coated glass slides) as working electrodes and a AgCl-coated silver wire inside the electrolyte solution as a pseudo-reference. The electrolyte solution consisted of 0.1 M  $\text{NBu}_4\text{PF}_6$  in acetonitrile unless otherwise noted in an argon atmosphere. At the end of experiments, ferrocene was added to the solution and measured against an empty working electrode. All data, unless described differently is reported against the half-wave potential of the ferrocene/ferrocenium ( $\text{Fc}/\text{Fc}^+$ ) redox pair.

## Spectroelectrochemistry

*In-situ* spectroelectrochemistry was carried out inside custom built quartz glass cells with the same electrode setup as in cyclic voltammetry with a platinum wire as the counter electrode. Polymer films were spin-coated on ITO coated glass slides bought from *Präzisions Glas & Optik GmbH* ( $\leq 20\Omega/\text{sq}$ ). The covered substrate was employed as the working electrode and placed inside the spectrometer's light beam. At each potential step of the CV cycle transmission spectra were recorded automatically.

## Relative Humidity Control

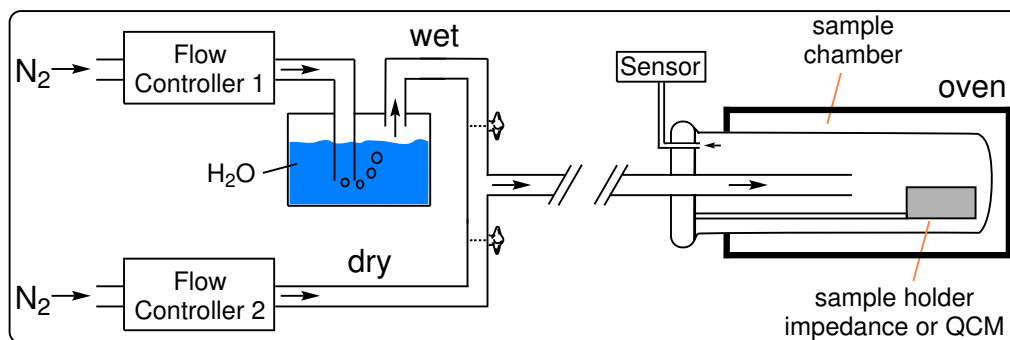


**Figure 6.1:** Experimental Setup for humidity and temperature controlled AC impedance, DC polarisation and QCM measurements.

AC impedance and QCM measurements were performed at different relative humidity values. The setup for humidity control is shown in Figure 6.1. A total gas flow of 40 sccm/min ( $\sim 40$  mL/min) was provided by two flow controllers wherein one stream of  $\text{N}_2$  gas is guided through a water reservoir and recombined with dry nitrogen afterwards. Division of total gas flow between the dry and wet nitrogen was calculated for different

water partial pressure values ranging from 0 mbar to 30 mbar  $p_{H_2O}$  for a setup temperature of 25 °C. Air flow inside the setup was measured at an exit with a *Rotronic Hygro Clip 2* relative humidity sensor after passing the sample holder. As the actual RH in the system is temperature dependent, an encasing oven was used to keep the sample chamber at  $(25 \pm 1)$  °C and the external humidity sensor measured the temperature of gas flow leaving the system. Additionally, internal temperature of the sample holder was documented with another sensor and read out prior to each measurement.

## AC Impedance and DC Polarisation

DC experiments were run by applying a constant current  $I$  for times between 30 s and 10 min, after which time the current was disabled and the samples allowed to relaxate while monitoring the resulting potential, according to Ohm's law, during the whole process. Applied currents were chosen at such a scale that resulting potentials remained below 200 mV at all times in order to avoid internal damages to the polymer films. Respective current values were assessed from preceding AC impedance experiments.

In samples with no ionic charge carriers, changes in applied current result in an immediate and sharp step in potential to reach a steady state. However, when moving ions are involved with ion-blocking electrodes (like Pt), the electric potential response is delayed by ions moving to the electrode to become blocked at the interface (see stoichiometric/Hebb-Wagner polarization).<sup>[161,162]</sup> Final potential values are only reached once an equilibrium is found, which is reflected in the resulting spectrum by curved, exponential responses to changes in applied current. In some cases where measuring time was too short to reach a true plateau (e.g. because of schedule restrictions) the experimental data was extrapolated with a logistic growth function with

$$f(t) = B + \frac{(A - B)}{(1 + (t/t_0)^p)} \quad (6.1)$$

For  $\lim_{t \rightarrow \infty}$  the fraction approaches 0 and the plateau  $B$  is found.

AC impedance describes a method in which a system is subjected to either alternating current or alternating potential with different frequencies and the system's resulting answer is recorded. Both, electrochemical systems and solid state materials can be measured this way, while polymer films like in this work belong into the latter category. The technique has become a primary tool for the characterisation of fuel cells<sup>[163]</sup>, batteries<sup>[164]</sup>, photovoltaics<sup>[165]</sup> and mixed electronic/ionic conductors<sup>[103]</sup>, and can be used in the latter case to separately extract ionic and electronic partial conductivity values  $\sigma_{ion}$  and  $\sigma_{el}$ , which it has been used for in the present work. This was carried out in a two-

electrode configuration by usage of interdigitated platinum electrodes and connecting both electrode arms to an *IM 6 Electrochemical Workstation* from ZAHNER MESSSYSTEME.

An alternating potential  $V(t)$  with sinusoidal character can be described with its amplitude  $V_0$  and its alternation frequency  $\omega$  as

$$V(t) = V_0 \sin(\omega t) \quad (6.2)$$

wherein  $\omega$  is the *angular frequency* described as  $2\pi f$ .

Introducing a sinusoidal potential  $V(t)$  will result in a sinusoidal current  $I(t)$  of the same frequency but lagging behind the potential in time, described by a phase shift  $\phi$  as

$$I(t) = I_0 \sin(\omega t + \phi) \quad (6.3)$$

Figure 6.2 visualizes this relationship. Considering Ohm's law with  $U = R \cdot I$  with the resistance  $R$ , one can replace  $R$  with the impedance  $Z$ , which is the complex resistance of a system and can be considered to exhibit resistor, capacitor and inductor characteristics. This gives

$$Z(t) = \frac{V(t)}{I(t)} \quad (6.4)$$

All three terms can also be expressed in their complex forms as

$$V(t) = V_0 e^{i\omega t} \quad I(t) = I_0 e^{i(\omega t + \phi)} \quad Z(t) = Z_0 e^{-i\phi} \quad (6.5)$$

The potential-impulse current-response relationship can be displayed on the time scale as in Figure 6.2 or on the (angular) frequency scale, where the x-axis is the real part of the impedance and the imaginary part of  $Z$  lies on the y-axis (see Figure 6.3). This latter version is known as a *Nyquist* plot and is often used to display impedance data. It is important to note that  $\omega$  increases towards  $x = 0$  and decreases with increasing  $x$ . Another way is to plot  $Z'$  ( $\text{Re}(Z)$ ) and  $Z''$  ( $\text{Im}(Z)$ ) on the y-axis against the frequency  $f$  on the x-axis, called *Bode* plot.

As mentioned, impedance embodies different characteristics. For  $\phi = 0^\circ$  it presents a resistance with no imaginary part and no frequency dependence. At  $\phi = 90^\circ$  it is purely imaginary and presents a capacitance which varies inversely with frequency.  $\phi = -90^\circ$  corresponds to ideal inductance with proportional dependence on frequency.<sup>[157,165]</sup> These characteristics mean that the impedance of a system at any frequency can be described by real life basic circuit elements (called equivalent circuits) with varying influence. To extract

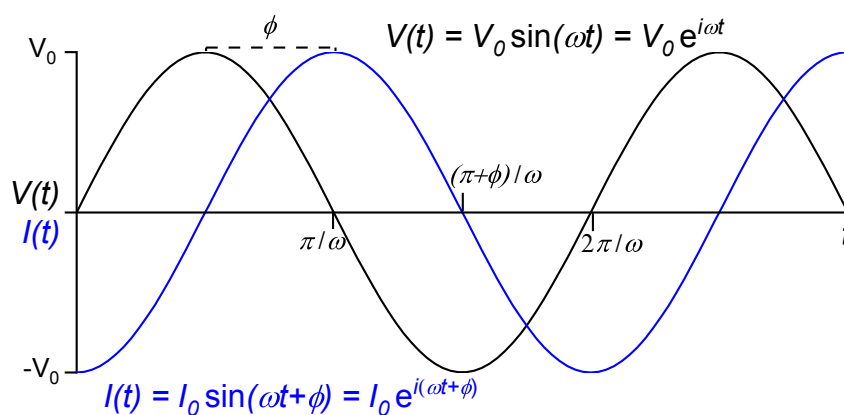


**Figure 6.2:** Alternating potential with amplitude  $V_0$  and resulting alternating current  $I(t)$  with phase shift  $\phi$  as functions of time.

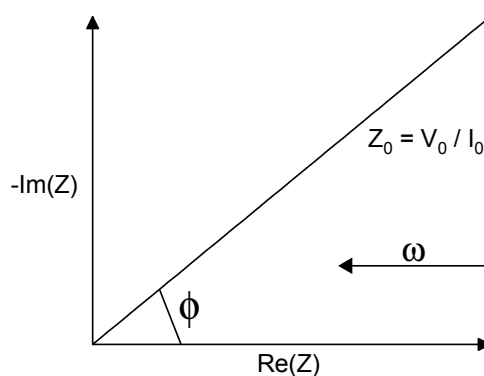


**Figure 6.3:** Depiction of impedance  $Z$  in the frequency realm, divided into real part  $\text{Re}(Z)$  ( $Z'$ ) and imaginary part  $\text{Im}(Z)$  ( $Z''$ ).

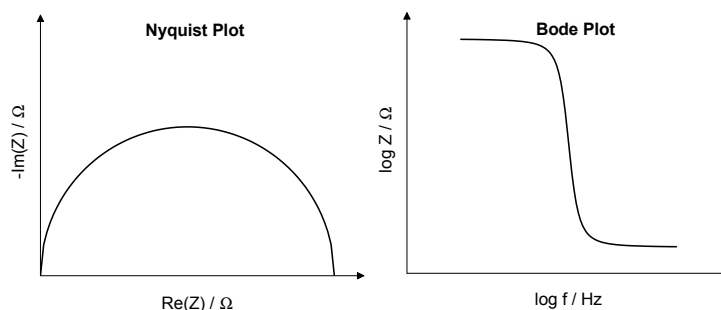


**Figure 6.4:** Schematic depictions of Nyquist and Bode plots of impedance data.

data from frequency dependent impedance measurements this fact is used by constructing equivalent circuit (EqC) models that aim to describe the electrical behaviour of the measured system accurately with as few components as possible. These models are used to calculate fits for the measured data, which then allow to determine e.g. ionic and electronic resistance values separately. Ideal circuit elements like resistors (R), capacitors (C) and inductors (L), but also non-ideal elements like Warburg elements (W) and constant phase elements (Q or CPE) are employed. Resistors resist current flow, capacitors accumulate charge carriers and inductors resist changes to current flow *via* electromagnetic force. Warburg elements, describing Warburg impedance  $Z_W$  deal with linear diffusion of charge carriers which is found in *Nyquist* plots as a linear increase at a  $45^\circ$  angle.<sup>[154]</sup> Constant phase elements, however, are special cases as they essentially provide a generalized version of the other elements. Their impedance can be described as

$$Z_Q = \frac{1}{J(i\omega)^n} \quad (6.6)$$

where  $J$  takes on a different physical meaning, depending on the dispersion parameter  $n$ . For  $n = 1$  the CPE reduces to an ideal capacitor, for  $n = 0.5$  it represents a Warburg element and for  $n = 0$  it becomes a resistor.<sup>[165,166]</sup> Although arbitrary, this makes it a flexible element to include into an equivalent circuit model. In this work, the model used most (unless specifically noted) is depicted in Figure 6.5, which is an EqC used in literature for mixed conductivity systems.<sup>[13,103,154]</sup> Since platinum electrodes were used in impedance experiments in this work, which are only transmissible for electrons but not ions, inclusion of a Warburg element to describe ion diffusion to the non-transmissive electrode would be possible, however, accurate fits were achieved without it and distinct Warburg impedance was rarely observed in the measured spectra.

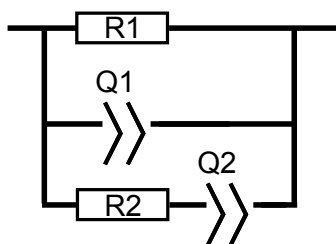


**Figure 6.5:** Equivalent Circuit Model used for fits in this work unless noted otherwise.

Interpretation of obtained resistance values has to be done on a case-to-case basis but in the case of two semi-circles in the *Nyquist* plot it can usually be assumed that for ion-blocking electrodes the low-frequency semi-circle gives  $R_{el}$  and  $R_{ion}$  dominates the high-frequency region.  $R_{ion}$  can be calculated from the diameter of the high-frequency

semi-circle  $R_{hf}$  via  $R_{hf} = (R_{el} \cdot R_{ion}) / (R_{el} + R_{ion})$  or determined from the EC fit, where  $R1$  corresponds to  $R_{el}$  and  $R2$  to  $R_{ion}$ .<sup>[103]</sup> Calculation of corresponding conductivities can then be performed by

$$\sigma = \frac{s}{R \cdot b \cdot d} \quad (6.7)$$

where  $\sigma$  is the ionic or electronic conductivity and  $s$  the distance between electrodes, which equates to the channel length in an interdigitated electrode (IDE).  $b$  and  $d$  make up the cross-sectional area and are the electrode length (channel width in an IDE) and the film thickness, respectively.<sup>[141]</sup>

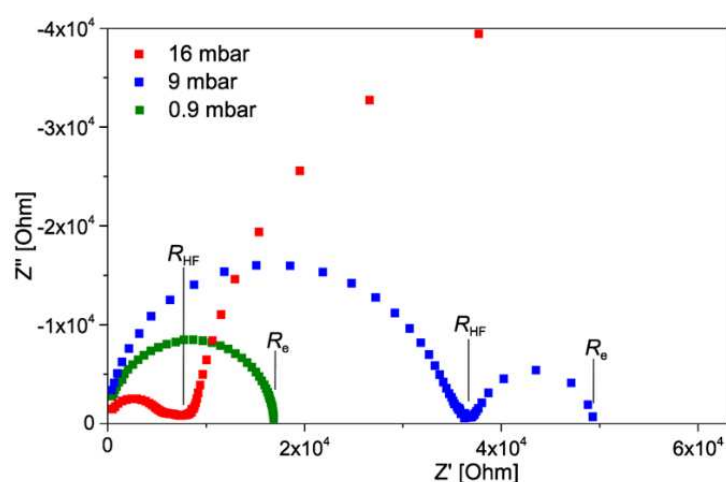


**Figure 6.6:** Exemplary impedance spectra displaying x-axis intercepts/minima for determination of  $R_{el}$  and  $R_{hf}$ . Adapted with permission from reference<sup>[13]</sup>. Copyright © 2020 American Chemical Society.

Samples were prepared by spin-coating polymer films on the respective IDE. After connection to the experimental setup, a first initial impedance measurement was performed to check for a material answer before subjecting the samples to a dry  $N_2$  stream over night. This was done to provide a universal starting point for all experiments. Subsequently, AC impedance was carried out with an excitation voltage amplitude of  $V_0 = 50$  mV in the frequency range of  $f = 100$  mHz–8 MHz. Nyquist plots were fitted with the freely available *EIS Spectrum Analyzer* developed by the *Research Institute for Physical-Chemical Problems* of the Belarusian State University. Between each new water partial pressure setting the samples were allowed 90 min to equilibrate to the new atmosphere. After a series of measurements from low to high  $p_{H_2O}$ , a number of additional steps from high to low  $p_{H_2O}$  were measured to assure reversibility. Additionally, most polymers were measured in two separate samples and experiments.

## Quartz Crystal Microbalance (QCM)

Water uptake of ionic polymers was determined *via* QCM. The initial step for each sample was the measurement of the clean quartz crystal substrate to obtain the empty frequency  $f_{empty}$ . Afterwards, crystals were removed from the sensor and thin polymer films were spin-cast on them. Edges of the crystal were cleansed from polymer to provide undisturbed contact and the substrate reinserted into the sensor. The experiment was run with a front load single sensor and a STM-2 controller from INFICON. As in impedance, samples were subjected overnight to a dry flow of nitrogen, before the experiment was started and run across several different water partial pressures using the same experimental setup as described above. Throughout the humidity program the substrate's resonance frequency was recorded. The more water is taken up by the polymer, the heavier the film and the lower its measured frequency, since changes in mass and changes in frequency are linked by a constant factor of the quartz substrate through the *Sauerbrey* equation.<sup>[167]</sup> To be able to calculate relative water uptake in wt-%, applicability on the *Sauerbrey* equation has to be ensured. Its limitations have been investigated and were determined to lie in a maximum thickness of the added layer of 300 kÅ in the case of aluminium deposition and a maximum increase in frequency between uncoated and coated quartz crystal of 15%. These are under the assumption of rigid polymer films throughout the experiment so that addition of mass because of polymer films has the same effect as adding the same mass *via* a thicker crystal.<sup>[168–171]</sup> Furthermore, for hydrated polyelectrolyte films, applicability of the *Sauerbrey* equation was found to be given for water uptakes under 100 wt-% by Vogt *et al.*, a limit which has not been crossed in this work. Film thickness of the polymers used here were also far below even 100 nm, so below even 1 kÅ and resonance frequency of bare and coated crystals only differed by  $\sim 0.01\%$  at most, so overall it was assumed the *Sauerbrey* equation is valid and can be applied here.

Under the mentioned assumptions, changes in frequency  $f$  can be equated to changes in crystal thickness  $h$  which are, again, analogous to coating with a rigid polymer film, so that

$$\frac{\Delta f}{f_{empty}} = -\frac{\Delta h}{h_{empty}} \propto -\frac{\Delta m_{crystal}}{m_{crystal}} = -\frac{m_{film}}{m_{crystal}} \quad (6.8)$$

from which it follows that  $\Delta f_{film} \propto \Delta m_{film}$ . Thus, relative water uptake was calculated from a relative decrease in frequency between the dry polymer films and films under water partial pressures  $p_{H_2O}$  *via*

$$\frac{\Delta f_{uptake}}{\Delta f_{film}} \cdot 100 = \frac{f_{dry} - f_{wet}}{f_{empty} - f_{dry}} \cdot 100 \text{ [wt-\%]} \quad (6.9)$$

with  $f_{dry}$  as the frequency at 0 mbar water partial pressure,  $f_{wet}$  as the frequency at different  $p_{H_2O}$  above 0 mbar and  $f_{empty}$  as the frequency of the respective pristine quartz crystal substrate.

## 6.2 Drying of organic solvents

### Dichloromethane (DCM), Hexane

Dichloromethane (p.a.) or *n*-Hexane was passed through a column of activated alumina and collected in a *Schlenk* flask equipped with freshly activated 4 Å molecular sieve. The solvent was then kept standing under argon at least overnight before use.

### Dimethylformamide (DMF)

DMF was bought in dry grade, taken from the sealed container equipped with a septum and transferred to a dried *Schlenk* flask equipped with freshly activated 4 Å molecular sieve. The solvent was then kept standing under argon at least overnight before use.

### Tetrahydrofuran (THF)

Dry THF was taken from an automated solvent purification system (SPS). For use in polymerization reactions it was further dried by storing it over freshly activated 4 Å molecular sieve for at least one day before use.

## 6.3 Polymer film preparation

Thin polymer films were produced by spin-coating of  $5 \text{ g L}^{-1}$  polymer solutions from chloroform, toluene or a 50/50 mixture of THF and  $\text{H}_2\text{O}$ , depending on the polymer. Substrates used included ITO coated glass slides, gold coated (30 nm or 50 nm) glass slides with a chromium adhesive layer (3 nm or 5 nm), interdigitated platinum electrodes, non-coated glass slides and silicon wafers. Prior to spin-coating, substrates were cleaned with ultrasound while submerged in water, 2-propanole and acetone for 15 min each, in this order. Additionally, ITO substrates were afterwards treated with  $\text{O}_2$  plasma for 10 min.

Spincoating was done with 10  $\mu\text{L}$  to 40  $\mu\text{L}$  solution, depending on substrate size. The spinning program was chosen depending on solvent. From chloroform and toluene, coating was done inside a glovebox with a two-step program consisting of

- 1) 2000 rpm, 0 acc for 180 s
- 2) 6000 rpm, 0 acc for 30 s

Spincoating from THF/H<sub>2</sub>O was done in a regular fumehood and the program used was

- 1) 3000 rpm, 10 acc for 180 s
- 2) 4000 rpm, 60 acc for 60 s

## 6.4 Click Chemistry

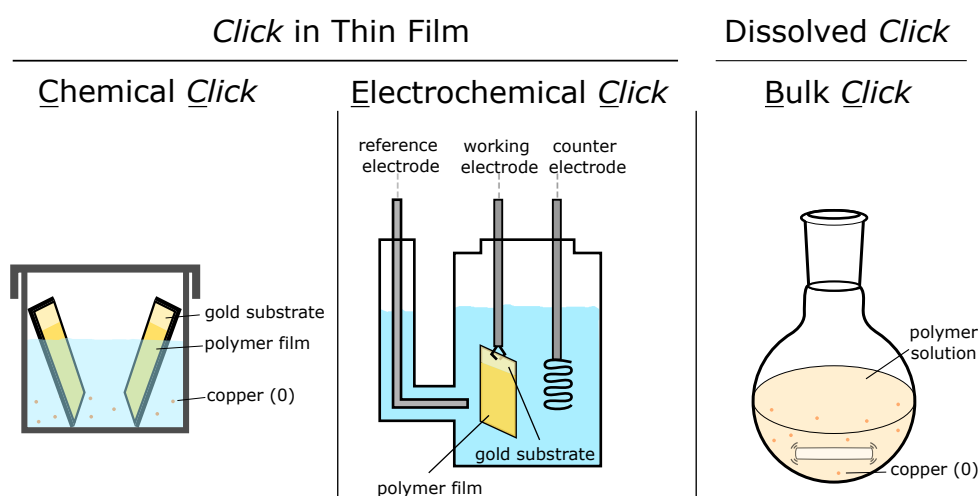


**Figure 6.7:** Experimental setups for the different CuAAC procedures. **Left** CC, solution consists of DMSO, (MeCN)<sub>4</sub>Cu(I)PF<sub>6</sub>, **6** and copper(0). **Center** EC, solution consists of DMF and Cu(II)SO<sub>4</sub>, -0.5 V applied for 30 min. **Right** BC, solution consist of DMSO, (MeCN)<sub>4</sub>Cu(I)PF<sub>6</sub>, **6**, copper(0) and organic azide.

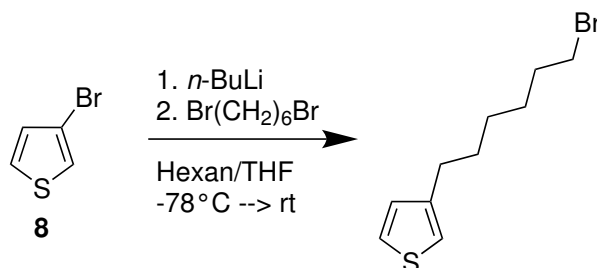
Experimental setups are visualized in Figure 6.7. For the electrochemical conversion (EC), spin-coated samples were put into electro-chemical cells containing DMF solutions of the sulfonate **6** and Cu(II)SO<sub>4</sub>. A negative potential of -0.5 V (vs. Ag/AgCl) was applied for 30 min and more, following the procedure developed by Jonglack Kim.

The *Chemical Click* (CC) procedure was performed in glass vials inside a glovebox, where a reaction mixture of elemental copper, sulfonate **6** or **17** and the catalyst tetrakis(acetonitrile)-copper(I) hexafluorophosphate in DMSO was added to the polymer films. The vials were kept standing inside the glovebox for 3 days.

In the case of *Bulk Click* (BC), no films were produced, as bulk polymer and the reagents copper(0), sulfonate **6** and the catalyst (MeCN)<sub>4</sub>Cu(I)PF<sub>6</sub> were put into a flask or vial and dry DMSO was added inside a glovebox. The mixture was then stirred for 3 days.

## 6.5 Synthesis of Monomers and Reactants

### 6.5.1 1-Step synthesis of 3-(6-Bromohexyl)thiophene

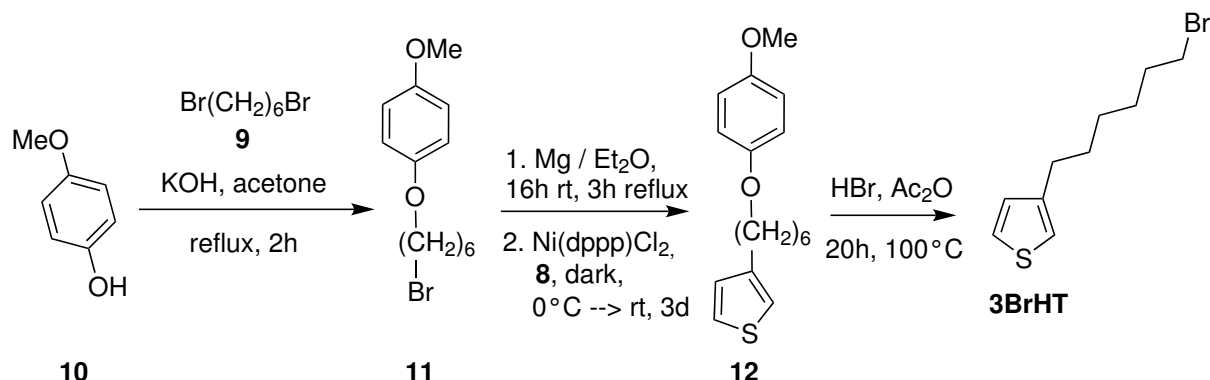


In inert atmosphere 3-Bromothiophene **8** (11.98 g, 6.89 mL, 73.5 mmol) was added to dry *n*-hexane (170 mL) and cooled down to  $-78\text{ }^{\circ}\text{C}$ . *n*-Butyllithium (1.6 M in hexane, 43.6 mL, 69.8 mmol, 0,95 eq) was added dropwise within 30 min after which the solution was kept stirring for another 45 min. Subsequently THF (17 mL) was added slowly before stirring for another 70 min during which a white precipitate formed. The solution was then removed *via* cannula, leaving behind the precipitate to which new *n*-hexane (120 mL) and THF (12 mL) were added. 1,6-Dibromohexane (113.1 mL, 735 mmol, 10 eq) was added quickly at  $-78\text{ }^{\circ}\text{C}$  before letting the reaction mixture warm up to room temperature and stir for another 90 min. Finally, the reaction was quenched by addition of a saturated aqueous solution of NaHCO<sub>3</sub> and diluted with diethylether. The phases were separated, the organic phase washed with water and brine, then dried over MgSO<sub>4</sub>. The solvent was removed *in vacuo*.

The crude product was purified by fractional distillation (bp.  $110\text{ }^{\circ}\text{C}/15\text{ mbar}$ ), which afforded 10.8 g of product in 50% purity and a residual distillation feed still containing notable amounts of the target compound as determined by TLC. Both were thus purified further by *Kugelrohr* distillation which afforded 3-(6-Bromohexyl)-thiophene **3BrHT** in 83% purity (determined by NMR) as a yellow oil (9.21 g, 42%).

<sup>1</sup>H-NMR (250 MHz, CDCl<sub>3</sub>):  $\delta$  (ppm) = 7.27–7.21 (m, 1H), 6.96–6.89 (m, 2H), 3.46–3.36 (m, 2H), 3.82 (s, 3H), 2.64 (dd,  $J = 7.78\text{ Hz}, 7.33\text{ Hz}$ , 2H), 1.94–1.78 (m, 2H), 1.72–1.56 (m, 2H), 1.56–1.28 (m, 4H).

## 6.5.2 3-Step synthesis of 3-(6-Bromohexyl)thiophene



**Step 1** To a solution of 4-methoxyphenol **10** (7.50 g, 60.4 mmol) in acetone (150 mL) 1,6-dibromohexane **9** (29.47 g, 18.31 mL, 120.8 mmol, 2 eq) was added dropwise and the mixture subsequently heated under reflux for 2 h. After cooling to room temperature the solution was diluted with water (60 mL) and dichloromethane (50 mL) and undissolved precipitate was filtered off. Phases were separated and the organic phase extracted with water (3 x 20 mL), dried over  $\text{MgSO}_4$  and the solvents removed *in vacuo*. The crude product was distilled (bp.  $45^\circ\text{C}/1.7 \times 10^{-3}$  mbar) and subsequently recrystallized from ethanol, yielding 9.3 g **11** (32.3 mmol, 53 %) as a colorless oil.

$^1\text{H-NMR}$  (250 MHz,  $\text{CDCl}_3$ ):  $\delta$  (ppm) = 6,83 (s, 2H), 3.91 (t,  $J = 6.39$  Hz, 2H), 3.77 (s, 3H), 3.42 (t,  $J = 6.78$  Hz, 2H), 1.97–1.70 (m, 4H), 1.48–1.53 (m, 4H).

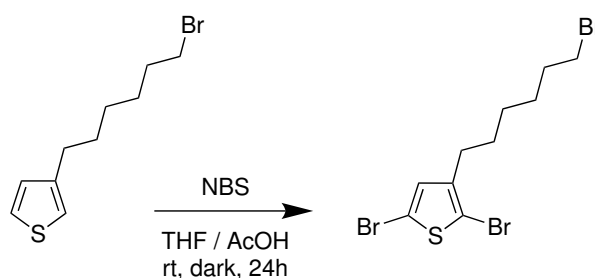
**Step 2** Under inert atmosphere, to a suspension of magnesium (727.2 mg, 29.9 mmol) and dry diethyl ether (2.5 mL) was added 1/5 of a solution of **11** (8591 mg, 29.9 mmol) in dry  $\text{Et}_2\text{O}$  (70 mL) to start the reaction. The rest of the solution was carefully added dropwise and the mixture stirred subsequently for 5.5 h under reflux. In a second flask, again in inert atmosphere,  $\text{Ni(dppp)Cl}_2$  (22.2 mg, 0.1 mmol, 0.33 mol-%) and 3-bromothiophene **8** (2.7 mL, 28.4 mmol) were prepared and kept cooled at  $0^\circ\text{C}$ . The Grignard solution from the first flask was then slowly transferred into this second flask while keeping the temperature steady. After addition, the reaction mixture was slowly heated to reflux and allowed to react for 16 h in the dark. After this the reaction was stopped by adding hydrochloric acid (6 mL, 1 M) and water (35 mL). Phases were separated and the organic phase extracted with  $\text{Et}_2\text{O}$  (3 x 20 mL), then dried over  $\text{MgSO}_4$  and the solvent removed *in vacuo*. The crude product was then distilled (bp.  $100^\circ\text{C}/2.2 \times 10^{-3}$  mbar), yielding 3.8 g of **12** (13.09 mmol, 44 %) as a colorless, crystalline solid.

<sup>1</sup>H-NMR (250 MHz, CDCl<sub>3</sub>):  $\delta$  (ppm) = 7.27–7.21 (m, 1H), 6.97–6.90 (m, 2H), 6.83 (s, 4H), 3.90 (t,  $J$  = 6.48 Hz, 2H), 3.82 (s, 3H), 2.64 (dd,  $J$  = 7.90 Hz, 7.34 Hz, 2H), 1.83–1.32 (m, 8H).

**Step 3** To compound **12** (3.55 g, 12.2 mmol) under inert atmosphere was added slowly a prepared solution of hydrobromic acid (8.26 mL, 8.9 M, 73.4 mmol) and acetic anhydride (11.80 mL, 122.3 mmol). The solution was then stirred for 21 h at 100 °C before water (10 mL) was added, phases separated and the organic phase extracted with Et<sub>2</sub>O (3 x 10 mL). The combined organic phases were washed with saturated, aqueous NaHCO<sub>3</sub> solution until occurrence of gas bubbles seized. Subsequently, the organic phase was separated again and dried over MgSO<sub>4</sub>. To remove solid residues, the yellow oil was dissolved in cyclohexane (50 mL) and filtered, then the solvent was removed *in vacuo*. Further purification was done *via* flash column chromatography (silica, ethyl acetate/cyclohexane 10:1) and subsequent *Kugelrohr* distillation (bp. 100 °C/1 × 10<sup>-3</sup> mbar). The product **3BrHT** (1.21 g, 40 %) was obtained as a colorless oil.

<sup>1</sup>H-NMR (250 MHz, CDCl<sub>3</sub>):  $\delta$  (ppm) = 7.27–7.22 (m, 1H), 6.96–6.91 (m, 2H), 3.41 (t,  $J$  = 6.81 Hz, 2H), 2.64 (dd,  $J$  = 7.77 Hz, 7.40 Hz, 2H), 1.93–1.80 (m, 2H), 1.72–1.57 (m, 2H), 1.52–1.29 (m, 4H).

### 6.5.3 2,5-Dibromo-3-(6-bromohexyl)thiophene



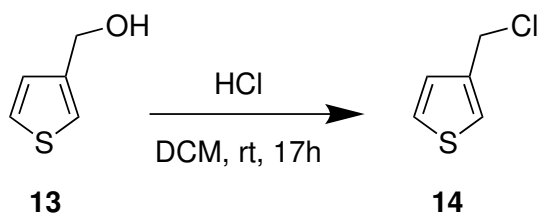
3-(6-Bromohexyl)thiophene **3BrHT**, which had been prepared by different synthetic approaches with varying purities (see above) was dissolved in a 1/1 mixture of THF and acetic acid, affording a 0.25 M solution. N-Bromosuccinimide (2.5 eq) was added and the reaction mixture stirred in the dark for 24 h. The reaction was stopped by careful addition of saturated aqueous NaHCO<sub>3</sub>-solution until gas development seized. The mixture was diluted with Diethylether, phases were separated and the organic phase washed with NaHCO<sub>3</sub> and brine, then dried over MgSO<sub>4</sub> and the solvent removed *in vacuo*. Further workup varied depending on previous synthetic routes.

The crude product resulting from conversion of the reaction mixture from section 6.5.1 (1-step synthesis) was freed from excess dibromohexane *in vacuo* at 80 °C prior to further workup by *Kugelrohr*-distillation (bp. 150 °C / 0.1 mbar), then followed by column chromatography (cyclohexane,  $R_f$ : 0.62). 2,5-Dibromo-3-(6-bromohexyl)thiophene **3BrHT-Br<sub>2</sub>** (6.67 g, 16.47 mmol, 53 %) was obtained as a colorless liquid.

The crude product resulting from conversion of the reaction mixture from section 6.5.2 (3-step synthesis) was purified by *Kugelrohr*-distillation (bp. 140 °C /  $2 \times 10^{-3}$  mbar). 2,5-Dibromo-3-(6-bromohexyl)thiophene **3BrHT-Br<sub>2</sub>** (1.67 g, 4.12 mmol, 84 %) was obtained as a colorless liquid.

<sup>1</sup>H-NMR (250 MHz, CDCl<sub>3</sub>):  $\delta$  (ppm) = 6.77 (s, 1H), 3.41 (t,  $J = 6.77$  Hz, 2H), 2.52 (t,  $J = 7.50$  Hz, 2H), 1.94–1.78 (m, 2H), 1.65–1.25 (m, 6H).

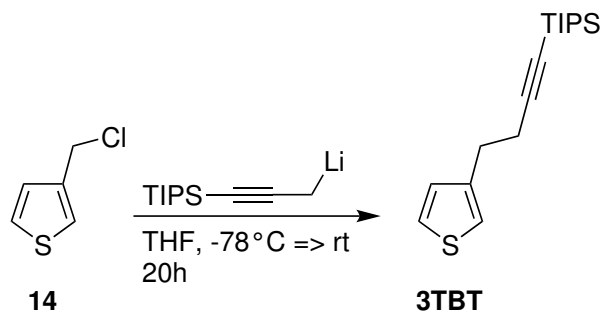
#### 6.5.4 3-Chloromethylthiophene



To a solution of 3-Thiophenemethanol **13** (11.4 mL, 120.85 mmol) in dichloromethane (304 mL), conc. HCl (37 %, 300 mL, 3.58 mmol, 29.6 eq) was added and the reaction mixture stirred for 17 h at room temperature. Phases were separated and the aqueous phase extracted with CH<sub>2</sub>Cl<sub>2</sub> (2 x 200 mL). The combined organic phases were washed with sat. aqueous NaHCO<sub>3</sub>-solution (2 x 200 mL) and water (200 mL), dried over MgSO<sub>4</sub> and the solvent removed *in vacuo*. 3-Chloromethylthiophene **14** (13.82 g, 104.2 mmol, 86 %) was obtained as a light-brown liquid.

<sup>1</sup>H-NMR (250 MHz, CDCl<sub>3</sub>):  $\delta$  (ppm) = 7.34–7.28 (m, 2H), 7.13 (dd,  $J = 5.0$  Hz, 2.5 Hz, 1H), 4.63 (s, 2H).

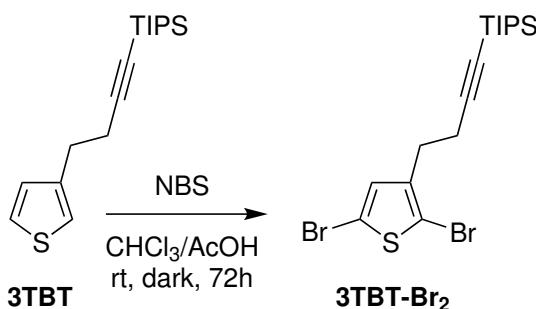
### 6.5.5 Triisopropyl-(4-thiophenyl-1-butynyl) silane



Under inert atmosphere, 1-(Triisopropylsilyl) 1-propyne (20.5 g, 104.2 mmol, 25 mL, 1 eq) in dry THF (500 mL) was subjected dropwise to *n*-Butyllithium (2.5 M in hexane, 44 mL, 110 mmol, 1.06 eq) at  $-78^{\circ}\text{C}$ . After addition, the mixture was stirred for 2 h before **14** (13.8 g, 104.2 mmol, 1 eq) was added slowly. The mixture was allowed to warm up to room temperature and stirred for 20 h subsequently. Reaction was stopped by addition of water, phases separated and the aqueous phase extracted with  $\text{Et}_2\text{O}$  (3 x 200 mL). Combined organic phases were washed with water (300 mL) and saturated NaCl-solution (350 mL), dried over  $\text{MgSO}_4$  and the solvent removed *in vacuo*. The crude product was further purified by column chromatography (silica, DCM:cyclohexane 5:95 v:v,  $R_f = 0.60$ ). **3TBT** (19.43 g, 66.56 mmol, 64 %) was obtained as a colorless oil.

$^1\text{H-NMR}$  (250 MHz,  $\text{CDCl}_3$ ):  $\delta$  (ppm) = 7.24 (dd,  $J = 4.8$  Hz, 3.0 Hz, 1H), 7.04–6.99 (m, 2H), 2.91 (t,  $J = 7.3$  Hz, 2H), 2.59 (t,  $J = 7.3$  Hz, 2H), 1.10–0.96 (m, 21H).

### 6.5.6 4-(2,5-dibromothiophenyl)-1-butynyl triisopropylsilane

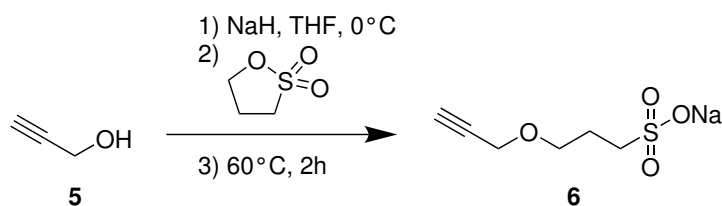


N-Bromosuccinimide (NBS, 17 g, 95.5 mmol) was added to a solution of **3TBT** (14 g, 0.048 mmol) in acetic acid/chloroform (1:1, 200 mL) and stirred for 3 h in the dark. After this time, more NBS (12 g, 67.4 mmol) was added and the mixture stirred further for 72 h.

The reaction was stopped by addition of water (150 mL) and phases were separated. The aqueous phase was extracted with chloroform (2 x 30 mL), the combined organic phases washed with H<sub>2</sub>O and saturated aqueous NaHCO<sub>3</sub>-solution, dried over MgSO<sub>4</sub> and the solvent removed *in vacuo*. The orange colored crude product was further purified by column chromatography (silica gel, petrol ether, high boiling,  $R_f = 0.54$ ). **3TBT-Br<sub>2</sub>** (17.03 g, 95 %) was obtained as a light-yellow liquid.

<sup>1</sup>H-NMR (250 MHz, CDCl<sub>3</sub>):  $\delta$  (ppm) = 6.94 (s, 1H), 2.75 (t,  $J = 7.02$  Hz, 2H), 2.52 (t,  $J = 6.82$  Hz, 2H), 1.08–1.00 (m, 21H).

### 6.5.7 3-(Prop-2-ynyloxy)propane-1-sulfonate

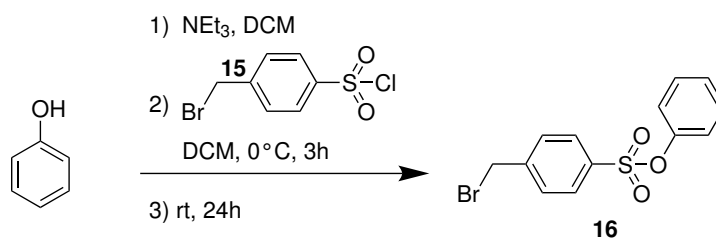


Sodium hydride (0.4 g, 16.67 mmol) in DMF (12 mL) was cooled to 0 °C before Propargyl alcohol (0.93 g, 0.96 mL, 16.67 mmol) in DMF (12 mL) was added dropwise within 10 min. Afterwards, 1,3-propane sultone (2.04 g, 1.47 mL, 16.67 mmol) in DMF (12 mL) was added dropwise within 10 min and the mixture kept stirring in the cold for another 10 min. Subsequently it was heated to 60 °C and stirred for 2 h before heat was turned off and the solvent volume reduced *in vacuo*. The crude product was precipitated from cold diethylether (200 mL), filtered and dissolved again in methanol (25 mL). After precipitating again from cold diethylether (300 mL) it was filtered, washed with Et<sub>2</sub>O, dried *in vacuo* and stored under inert atmosphere. The product (3.03 g) was obtained as an off-white solid in 91 % yield.

<sup>1</sup>H-NMR (250 MHz, CD<sub>2</sub>Cl<sub>2</sub>):  $\delta$  (ppm) = 7.90–7.83 (m, 2H), 7.58–7.50 (m, 2H), 7.40–7.27 (m, 3H), 7.06–6.96 (m, 2H), 4.54 (s, 2H).

IR (ATR):  $\tilde{\nu}$ [cm<sup>-1</sup>] = 2106 (N<sub>3</sub>), 1376 (S=O).

### 6.5.8 Phenyl 4-(bromomethyl)benzene sulfonate

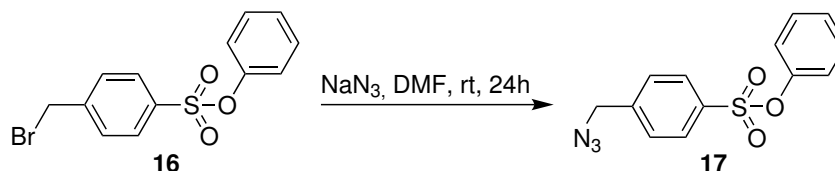


Under inert atmosphere, phenol (366.7 mg, 0.34 mL, 3.90 mmol) and triethylamine (409.2 mg, 0.65 mL, 4.04 mmol) were dissolved in dry dichloromethane (3.2 mL) and cooled to  $0^\circ\text{C}$ . A solution of 4-(Bromomethyl)benzenesulfonyl chloride **15** (1000 mg, 3.22 mmol) in dry DCM (10 mL) was added slowly and the reaction mixture stirred at  $0^\circ\text{C}$  for 3 h before being allowed to warm up to room temperature and stir for another 72 h. Afterwards, the mixture was washed with water (3 x 15 mL), dried over  $\text{MgSO}_4$  and the solvent removed *in vacuo*. The target molecule **16** was obtained with 84 % yield (881 mg). It has to be noted that  $^1\text{H-NMR}$  spectroscopy and mass spectrometry revealed that a considerable amount of bromine atoms had been substituted by chlorine during the course of reaction. However, for the subsequent conversion this had no relevance, thus the product was considered clean.

$^1\text{H-NMR}$  (250 MHz,  $\text{CDCl}_3$ ):  $\delta$  (ppm) = 7.87–7.77 (m, 2H), 7.59–7.50 (m, 2H), 7.36–7.24 (m, 3H), 7.04–6.94 (m, 2H), 4.63 (s, 2H,  $\text{CH}_2\text{Cl}$ ), 4.49 (s, 2H,  $\text{CH}_2\text{Br}$ ).

**MS** ( $\text{EI}^+$ ): calculated for  $\text{M}^+$ :  $m/z$  = 327.96 (bromomethyl), 282.01 (chloromethyl). Found:  $m/z$  = 328.0 (bromomethyl),  $m/z$  = 282.0 (chloromethyl).

### 6.5.9 Phenyl 4-(azidomethyl)benzene sulfonate



Phenyl 4-(bromomethyl)benzene sulfonate **16** (881 mg, 2.69 mmol) was dissolved in dry DMF (8.8 mL) and sodium azide (875 mg, 13.46 mmol, 5 eq) was added in one portion. The mixture was stirred for 24 h at room temperature before being diluted with dichloromethane and washed with 50 % brine (6 x 15 mL) and  $\text{H}_2\text{O}$  (15 mL). The combined organic phases were dried over  $\text{MgSO}_4$  and the solvent removed *in vacuo*. Phenyl 4-(azidomethyl)benzene

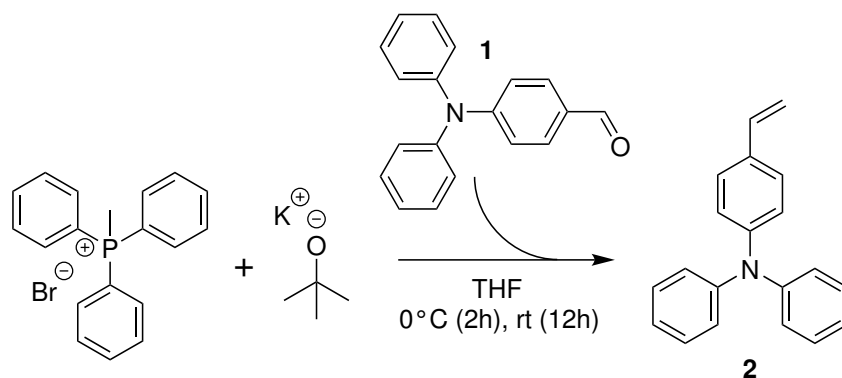
sulfonate **17** was obtained in 99 % yield (727.3 mg).

<sup>1</sup>H-NMR (250 MHz, CD<sub>2</sub>Cl<sub>2</sub>): δ (ppm) = 7.90–7.83 (m, 2H), 7.58–7.50 (m, 2H), 7.40–7.27 (m, 3H), 7.06–6.96 (m, 2H), 4.54 (s, 2H).

<sup>13</sup>C-NMR (63 MHz, CDCl<sub>3</sub>): δ (ppm) = 149.58, 142.32, 135.14, 129.82, 129.15, 128.53, 127.39, 122.44, 53.91.

IR (ATR):  $\tilde{\nu}$ [cm<sup>-1</sup>] = 2106 (N<sub>3</sub>), 1376 (S=O).

### 6.5.10 N,N-Diphenyl-2-vinylaniline (VTPA)

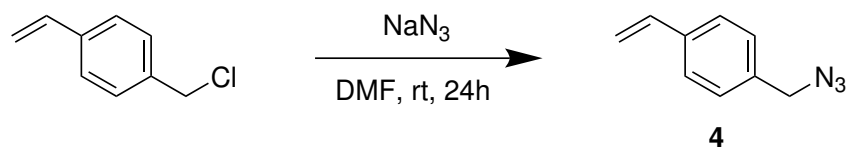


Synthesized by *Philipp Sliskovic*. Wittig-olefination of 4-(Diphenylamino)benzaldehyde **1** was achieved by first dissolving Methyl-triphenylphosphoniumbromide (8 g, 22.3 mmol) in dry THF (50 mL) and cooling the solution to 0 °C. Potassium *tert*-butoxide (2.5 g, 22.3 mmol) was added while stirring. Next, a solution of aldehyde **1** (5 g, 18.3 mmol) in dry THF (30 mL) was carefully added dropwise. The reaction mixture was stirred at 0 °C for 2 h and at room temperature for another 12 h. Reaction was then stopped by addition of methanol to the mixture. Subsequently, the crude product was dried over MgSO<sub>4</sub> and solvents removed *in vacuo* before being purified further by column chromatography (silica, cyclohexane:DCM, 10:1, v:v, *R<sub>f</sub>*: 0.66). VTPA **2** was obtained in 88 % yield (4.38 g).

<sup>1</sup>H-NMR (250 MHz, CD<sub>2</sub>Cl<sub>2</sub>): δ (ppm) = 7.40–7.23 (m, 6H), 7.20–7.01 (m, 8H), 6.72 (dd, *J* = 17.6 Hz, 10.9 Hz, 1H) 5.69 (dd, *J* = 17.6 Hz, 0.9 Hz, 1H), 5.21 (dd, *J* = 10.9 Hz, 0.9 Hz, 1H).

## 6.6 Model Reactions

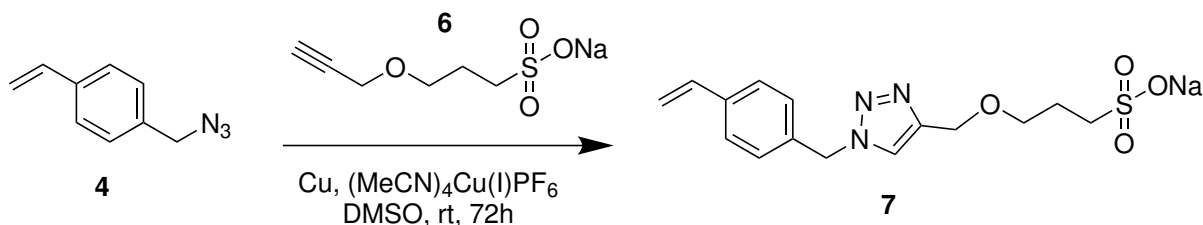
### 6.6.1 4-(Azidomethyl)styrene



4-(Chloromethyl)styrene **6** (0.92 mL, 6.25 mmol) was dissolved in dimethylformamide (DMF, 15 mL) in inert atmosphere and  $\text{NaN}_3$  (857 mg, 13.1 mmol, 2 eq) was added in one portion. The reaction mixture was stirred overnight, diluted with ethylacetate and the phases separated. The organic phase was washed with 50 % brine, dried over  $\text{MgSO}_4$  and the solvent removed *in vacuo*. 4-(Azidomethyl)styrene **7** (630 mg, 3.96 mmol, 63 %) was obtained as a yellow liquid.

$^1\text{H-NMR}$  (300 MHz,  $\text{CDCl}_3$ ):  $\delta$  (ppm) = 7.50–7.20 (m, 4H), 6.72 (dd,  $J = 17.6$  Hz, 10.9 Hz, 1H), 5.77 (d,  $J = 17.6$  Hz, 1H), 5.28 (d,  $J = 10.9$  Hz, 1H), 4.33 (s, 2H).

### 6.6.2 CuAAC Model Reaction

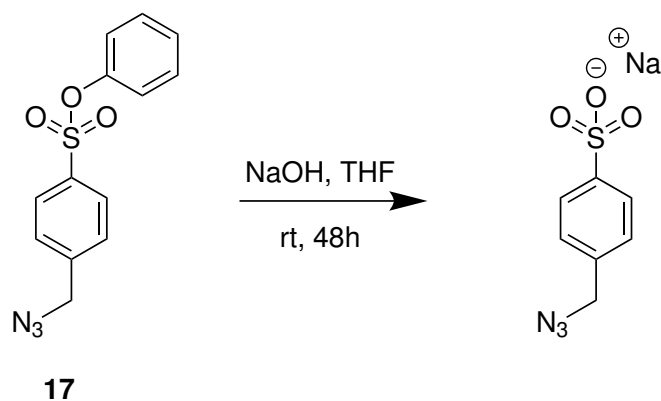


4-Azidomethylstyrene **4** (152.1 mg, 0.96 mmol), Sodium 3-(prop-2-ynoxy)propane-1-sulfonate **6** (189.3 mg, 0.95 mmol), copper powder (61.3 mg, 0.97 mmol) and the catalyst Tetrakis(acetonitrile)copper(I) hexafluorophosphate (17.3 mg, 0.05 mmol) were weighted out into a *Schlenk* flask and DMSO (dry, 23.5 mL) was added under inert atmosphere. Argon was bubbled through the suspension for 30 min before the mixture was stirred at room temperature for 72 h. The solvent was removed *in vacuo* and chloroform added to the residue. The insoluble part was filtered off, dried *in vacuo* and characterised by NMR-spectroscopy. The product was obtained as a dark-yellow solid.

$^1\text{H-NMR}$  (300 MHz,  $\text{DMSO-d}_6$ ):  $\delta$  (ppm) = 8.15 (s, 1H), 7.55–7.25 (m, 4H), 6.73 (dd,  $J = 17.6$  Hz, 10.9 Hz, 1H), 5.85 (d,  $J = 17.6$  Hz, 1H), 5.58 (s, 2H), 5.28 (d,  $J = 10.9$  Hz,

1H), 4.47 (s, 2H), 3.46 (br, 3H), 2.42 (br, 2H), 1.78 (br, 2H).

### 6.6.3 Sulfonate Deprotection



Phenyl-4-(azidomethyl)benzene sulfonate **17** (92 mg, 0.35 mmol) was dissolved in THF (4 mL) and a 100 g L<sup>-1</sup> solution of NaOH in methanol (1 mL) was added dropwise, causing a yellow tint of the solution immediately. The solution was kept stirring at room temperature for 2 days, during which it became murky and changed colour to orange-red. The solvent was removed *in vacuo* and the reaction success determined indirectly *via silica plug* filtration with dichloromethane. 2 mg of compound were obtained after thorough washing of the *plug* with CH<sub>2</sub>Cl<sub>2</sub> and <sup>1</sup>H-NMR spectroscopy gave no indications of any starting material in this compound. Therefore, it was concluded that all of the starting material was successfully converted and thus stuck on the *silica gel*.

## 6.7 Polythiophenes

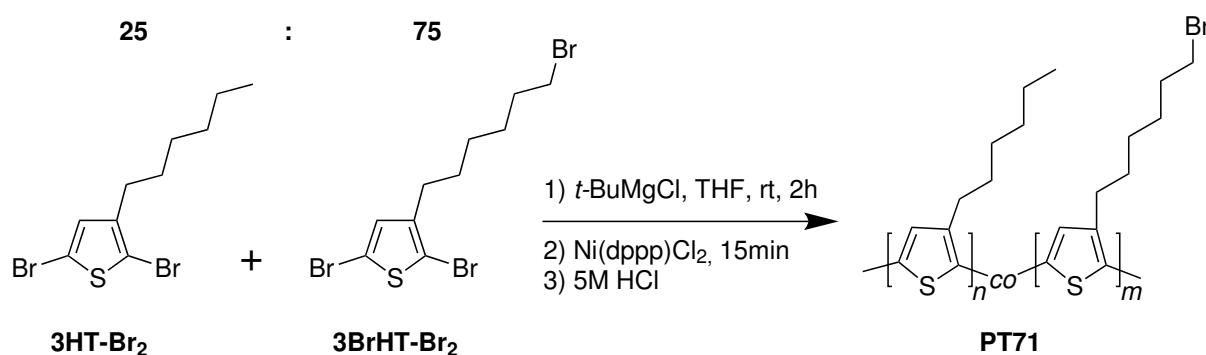
Based on polymerization conditions which had been used before,<sup>[1,2]</sup> efforts were made to improve the quality of obtained polymers by altering those conditions. This was done looking at molecular weight averages, but more importantly at the dispersity *D* and features found in the size exclusion chromatograms of synthesized polymers (see section 4.1.3). In this process, yields were not deemed a deciding factor, thus are not given. The general procedure for those polymerizations was as follows:

2,5-Dibromo-3-(6-bromohexyl)thiophene **5** was dissolved in dry THF under inert atmosphere, affording x-y M solutions. *t*-Butylmagnesium chloride (0.95 to 1 eq) was added dropwise and the solution stirred for 2 h. After dilution with dry THF to afford x-y M solutions, dichloro(1,3-bis(diphenylphosphino)propane)nickel (Ni(dppp)Cl<sub>2</sub>) was added in

one portion under rigorous stirring and the polymerization was allowed to proceed for 10 min to 120 min. The reaction was stopped by addition of Methanol or 5 M aqueous HCl and subsequently precipitated from Methanol. After collection of the precipitate and characterization by SEC, *Soxhlet*-extraction was done where deemed beneficial.

Results of these variation can be found in the discussion chapter of this work. In the following, detailed procedures shall be given for the polymerizations from which the resulting polymers were then used for further conversions.

### 6.7.1 Poly[3-hexylthiophene-*co*-3-(6-bromohexyl)thiophene] (PT71)



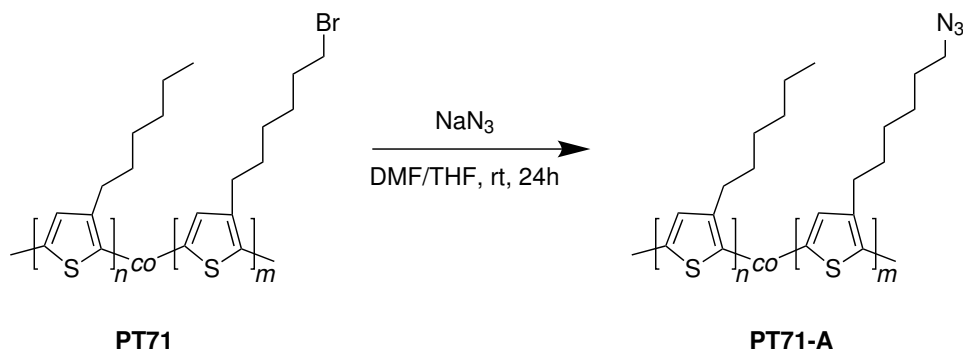
**3HT-Br<sub>2</sub>** (189.9 mg, 0.58 mmol, 1 eq) and **3BrHT-Br<sub>2</sub>** (664 mg, 1.73 mmol, 3 eq) were weighted out in a glass vial and transferred inside a glovebox. There, dry THF (4.5 mL) was added to dissolve the monomers. *t*-Butylmagnesium chloride (1 M in THF, 2.3 mL, 2.30 mmol, 1.0 eq) was added dropwise under stirring and the mixture allowed to stir at room temperature for 2 h. The solution was then diluted with THF (17 mL). Subsequently, under vigorous stirring, catalyst Ni(dppp)Cl<sub>2</sub> (12.5 mg, 0.023 mmol, 1 mol-%) dispersed in dry THF (1 mL) was added in one quick motion using a glass syringe. The polymerization was allowed to proceed for 15 min before the vial was quickly taken out of the glovebox and quenched with 5 M aqueous HCl and the polymer precipitated in cold methanol. After centrifugation and subsequent drying in a vacuum oven, **PT71** (251 mg) was obtained in a 29 % yield.

<sup>1</sup>H-NMR (250 MHz, CD<sub>2</sub>Cl<sub>2</sub>): δ (ppm) = 6.97 (s), 3.43 (t, *J* = 6.7 Hz), 2.82 (br), 1.89 (br), 1.72 (br), 1.42 (br), 1.36 (br), 0.92 (br).

IR (ATR):  $\tilde{\nu}$ [cm<sup>-1</sup>] = 3053 (C–H arom.), 2923 (C–H alkyl), 2854 (C–H alkyl), 1450 (C–C arom.), 821 (C–H arom.).

SEC (THF, PS standards):  $\overline{M}_n$  = 12 700 g mol<sup>-1</sup>,  $\overline{M}_w$  = 16 000 g mol<sup>-1</sup>, *D* = 1.26.

## 6.7.2 Poly[3-hexylthiophene-co-3-(6-azidohexyl)thiophene] (PT71-A)



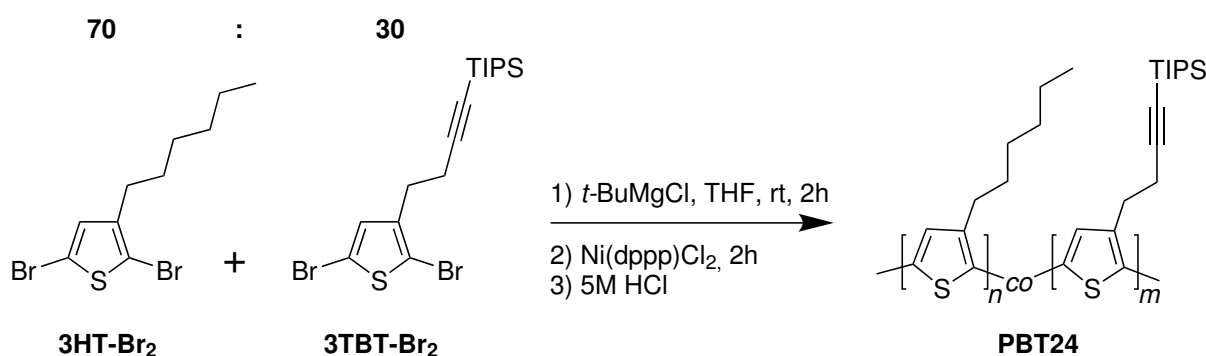
**PT71** (194 mg) was dissolved in a 2:3 mixture of dry DMF and dry THF (6 mL:9 mL) by carefully heating the dispersion in a Schlenk flask under inert atmosphere. After complete dissolution of the polymer the solution was allowed to cool to room temperature and sodium azide (558 mg) was added in one portion. The mixture was kept stirring for 22 h. Afterwards, chloroform (15 mL) was added and the organic phase washed repeatedly with water (7 x 15 mL) to remove any traces of sodium azide and DMF. The remaining organic phase was dried over  $\text{MgSO}_4$  and the solvent removed under reduced pressure. **PT71-A** (169 mg) was obtained in a 87 % yield.

**$^1\text{H-NMR}$**  (250 MHz,  $\text{CD}_2\text{Cl}_2$ ):  $\delta$  (ppm) = 6.97 (s), 3.28 (t,  $J = 6.8$  Hz), 2.82 (br), 1.68 (br), 1.46 (br), 1.37 (br), 0.92 (br).

**IR (ATR):**  $\tilde{\nu}[\text{cm}^{-1}] = 3053$  (C–H arom.), 2926 (C–H alkyl), 2855 (C–H alkyl), 2086 ( $\text{N}_3$ ), 1450 ((C–C arom.)), 821 (C–H arom.).

**SEC (THF, PS standards):**  $\overline{M}_n = 15\,000 \text{ g mol}^{-1}$ ,  $\overline{M}_w = 19\,500 \text{ g mol}^{-1}$ ,  $D = 1.30$ .

### 6.7.3 Poly[3-hexylthiophene-co-3-(4-triisopropylsilylbutyne)-thiophene] (PBT24)



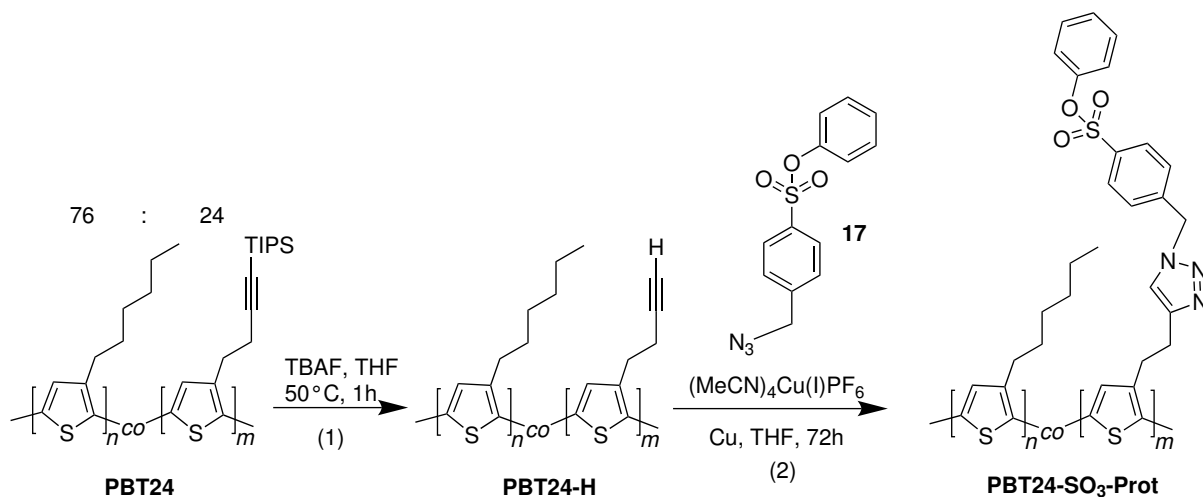
**3HT-Br<sub>2</sub>** (1312 mg, 4.03 mmol, 0.7 eq) and **3TBT-Br<sub>2</sub>** (700 mg, 1.73 mmol, 0.3 eq) were weighed out into a round flask and transferred inside a glovebox. There, dry THF (11.5 mL) was added to dissolve the monomers. *t*-Butylmagnesium chloride (1 M in THF, 5.75 mL, 5.75 mmol, 1.0 eq) was added dropwise under stirring and the mixture allowed to stir at room temperature for 2 h. The solution was then diluted with THF (45 mL). Subsequently, under vigorous stirring, catalyst Ni(dppp)Cl<sub>2</sub> (31.8 mg, 0.058 mmol, 1 mol-%) dispersed in dry THF (1 mL) was added in one quick motion using a glass syringe. The polymerization was allowed to proceed for 2 h before the flask was quickly taken out of the glovebox and quenched with 5 M aqueous HCl and the polymer precipitated in cold methanol. The crude polymer was filtered off, washed with methanol and transferred into a *Soxhlet* extraction filter. Extraction was done with methanol, acetone and chloroform in this order and the chloroform fraction collected for characterisation. 665 mg of **PBT24** were obtained, translating to a 33 % yield.

<sup>1</sup>H-NMR (250 MHz, CDCl<sub>3</sub>):  $\delta$  (ppm) = 7.07 (br), 6.98 (br), 3.07 (br), 2.81 (br), 2.66 (br), 1.71 (br), 1.37 (br), 1.04 (br), 0.91 (br).

IR (ATR):  $\tilde{\nu}$ [cm<sup>-1</sup>] = 3059 (C–H arom.), 2924 (C–H alkyl), 2859 (C–H alkyl), 2171 (C≡C disubst.), 1459 ((C–H alkyl)), 1379 (CH<sub>3</sub>) 822 (C–H).

SEC (THF, PS standards):  $\overline{M}_n$  = 14 000 g mol<sup>-1</sup>,  $\overline{M}_w$  = 19 700 g mol<sup>-1</sup>,  $D$  = 1.39.

### 6.7.4 Poly[3-hexylthiophene-*co*-3-(2-(3-(phenyl-benzyl-4-sulfonate)-triazole)ethyl)thiophene] (PBT24-SO<sub>3</sub>-Prot)



**PBT24** (257 mg, ca. 1.3 mmol/0.3 mmol alkyne) was dissolved in dry THF (50 mL) and Tetra-*n*-butylammonium fluoride (TBAF, 1 M in THF, 1.44 mL, 1.44 mmol, 5 eq) was added dropwise. The solution was heated to 50 °C and stirred for 1 h. After cooling to room temperature the solution was diluted with chloroform and water and extracted with chloroform (2 x). The organic phase was then washed with water (4 x), the solvent removed *in vacuo* and the obtained polymer dissolved again in chloroform at 50 °C. Precipitation in cold methanol and filtration of the polymer afforded **PBT24-H** (170 mg). Successful deprotection was confirmed by infrared spectroscopy.

**IR (ATR):**  $\tilde{\nu}$ [cm<sup>-1</sup>] = 3312 (C≡C-H), 2923 (C-H alkyl), 2857 (C-H alkyl), 2117 (C≡C monosubst.), 1452 ((C-H alkyl)), 1378 (CH<sub>3</sub>).

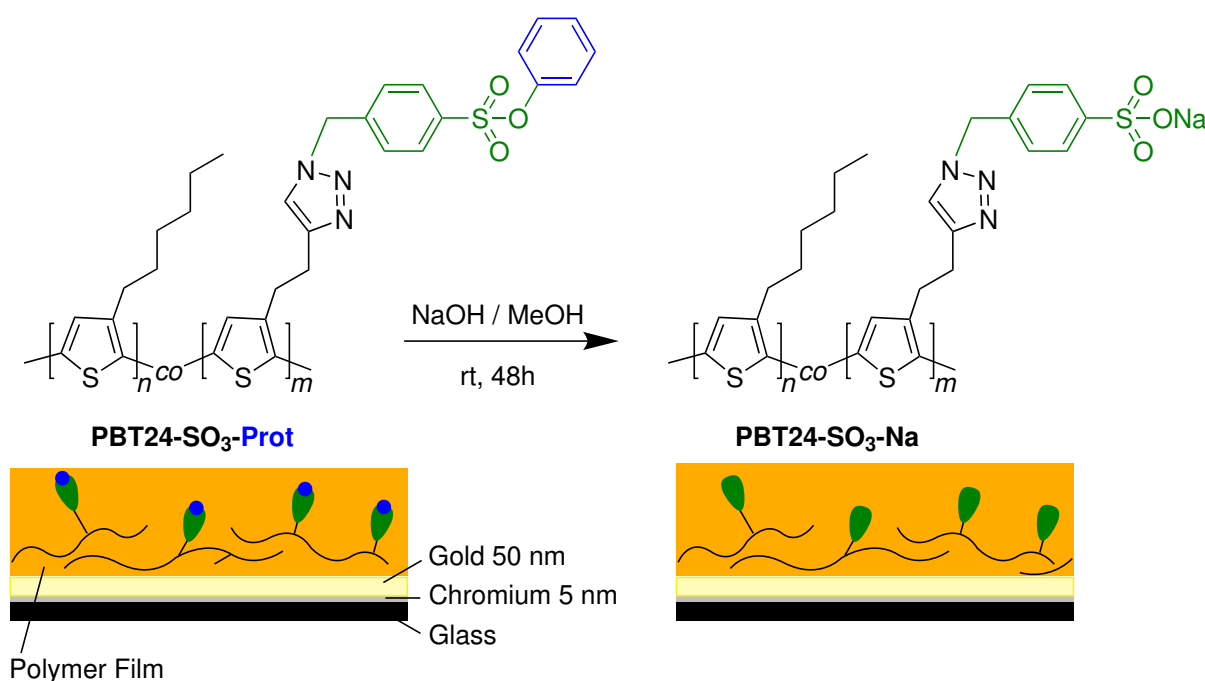
In the second step, **PBT24-H** (170 mg, ca. 0.88 mmol/0.21 mmol alkyne) and copper powder (12.68 mg, 0.2 mmol) were weighted out into a glass vial and transferred into a glovebox. The copper(I) catalyst (4.09 mg, 0.01 mmol, 5 mol-%) and the protected sulfonate azide **17** (79.5 mg, 0.27 mmol, 1.3 eq) were dissolved in dry THF (14 mL) and the solution added to the polymer. The mixture was then stirred for 72 h during which time it changed colours from dark purple to red. The solvent was removed *in vacuo* and the crude product subsequently dissolved in chloroform. Precipitation in acetonitrile and centrifugation of the precipitate afforded 212 mg of **PBT24-SO<sub>3</sub>-Prot**.

$^1\text{H-NMR}$  (250 MHz,  $\text{CDCl}_3$ ):  $\delta$  (ppm) = 7.72 (br), 7.22 (br), 6.98 (br), 6.93 (br), 5.56 (br), 3.15 (br), 2.78 (br), 1.70 (br), 1.33 (br), 0.91 (br).

**IR (ATR):**  $\tilde{\nu}[\text{cm}^{-1}]$  = 3063 (C–H arom.), 2924 (C–H alkyl), 2856 (C–H alkyl), 1458 ((C–H alkyl)), 1374 (S=O).

**SEC (THF, PS standards):**  $\overline{M}_n$  = 13 000  $\text{g mol}^{-1}$ ,  $\overline{M}_w$  = 20 000  $\text{g mol}^{-1}$ ,  $D$  = 1.54.

### 6.7.5 Poly[3-hexylthiophene-*co*-3-(2-(3-(sodium-benzyl-4-sulfonate)triazole)ethyl)thiophene] (Deprotection, PBT24-SO<sub>3</sub>Na)

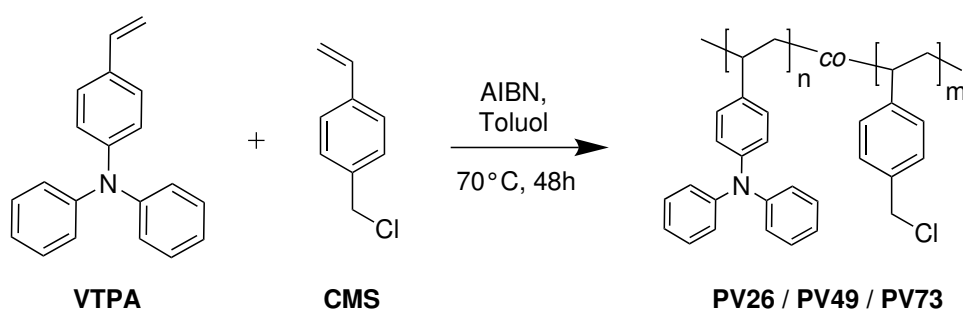


From  $5 \text{ g L}^{-1}$  solutions of **PBT24-SO<sub>3</sub>-Prot** in chloroform, thin films on glass substrates, interdigitated platinum electrodes and quartz crystal substrates were prepared *via* spin-coating. The films were then put in individual glass vials and submerged in  $20 \text{ g L}^{-1}$  solutions of NaOH in methanol. After continuous shaking for 24 h to 48 h on a lab shaker, substrates were transferred in new vials with pristine methanol and shaken for another 30 min. Afterwards, they were washed with methanol, blow-dried with argon gas and kept under reduced pressure for 30 min, before the successful deprotection was assessed *via* water contact angle measurements.

## 6.8 Redox Polymers

Redox polymers based on VTPA were synthesized in free radical copolymerization with chloromethylstyrene (CMS) in three different co-monomer ratios. For preparation and synthesis of these monomers, please refer to chapter 6.5. Azobisisobutyronitrile (AIBN) was freshly recrystallized from methanol prior to these polymerizations. Co-monomer feed ratios of VTPA:CMS were 25:75, 50:50 and 75:25. The general procedures shall be described below and weighted portions will be given in respective tables.

### 6.8.1 Poly[vinyl(triphenylamine)-*co*-(chloromethyl)styrene]



VTPA was dissolved in dry toluene in a *Schlenk* flask before CMS was added. AIBN was added and the mixture degassed *via* freeze-pump-thaw. Subsequently, it was heated to 70 °C and stirred for 48 h, after which time the crude polymer was precipitated in cold methanol. When needed, precipitation was repeated until a colourless polymer was obtained. The three main batches were synthesized by *Philipp Sliskovic*.

**Table 6.1:** Weighted portions and yields of copolymerizations

	<b>PV26</b>	<b>PV49</b>	<b>PV73</b>
VTPA	3.05 g/11.25 mmol	2.04 g/7.5 mmol	1.25 g/4.6 mmol
CMS	0.52 mL/3.75 mmol	1.06 mL/7.5 mmol	2.27 mL/13.8 mmol
AIBN	0.0246 g/0.15 mmol	0.0246 g/0.15 mmol	0.0246 g/0.15 mmol
Toluene	15 mL	15 mL	15 mL
Yield	2.78 g (77 %)	1.27 g (53 %)	2.07 g (62 %)

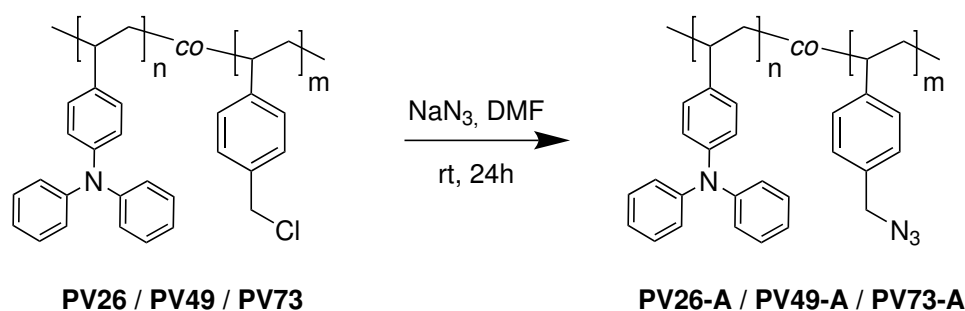
<sup>1</sup>H-NMR (250 MHz, CDCl<sub>3</sub>): **PV26**:  $\delta$  (ppm) = 7.02 (br), 6.95 (br), 6.57 (br), 4.38 (br), 1.97 (br), 1.51 (br), 1.18 (br), 1.04 (br). **PV49**:  $\delta$  (ppm) = 7.12 (br), 6.95 (br), 6.82 (br), 6.54 (br), 4.44 (br), 1.85 (br), 1.47 (br), 1.17 (br), 1.03 (br). **PV73**:  $\delta$  (ppm) = 7.18 (br), 6.98 (br), 6.78 (br), 6.50 (br), 4.47 (br), 1.69 (br), 1.41 (br), 1.13 (br), 0.92 (br).

**SEC (THF, PS standards): PV26:**  $\bar{M}_n = 6900 \text{ g mol}^{-1}$ ,  $D = 2.01$ . **PV49:**  $\bar{M}_n = 11\,500 \text{ g mol}^{-1}$ ,  $D = 2.15$ . **PV73:**  $\bar{M}_n = 6000 \text{ g mol}^{-1}$ ,  $D = 2.41$ .

**Table 6.2:** Weighted portions and yields after polymer analogous halide-azide exchange reactions

	<b>PV26-A</b>	<b>PV49-A</b>	<b>PV73-A</b>
Polymer	1998 mg	1050 mg	1510 mg
NaN <sub>3</sub>	726 mg/11.28 mmol	747 mg/11.67 mmol	1950 mg/30.25 mmol
DMF	14 mL	8 mL	20 mL
Yield	1.78 g (89 wt-%)	0.8 g (76 wt-%)	1.38 g (91 wt-%)

### 6.8.2 Poly[vinyl(triphenylamine)-*co*-(azidomethyl)styrene]



The halide-azide exchange reaction shall be described exemplarily for polymer **PV73**. Weighted portions for all reactions can be found in Table 6.2. Each polymer's share of CMS units, as determined from NMR, was used to assess an estimate of the amount of CMS groups in the polymer. Amounts of sodium azide were calculated based on these estimates.

**PV73** (1510 mg, estimated 6.05 mmol of CMS groups) was dissolved in dry DMF (20 mL). To the solution, sodium azide (1950 mg, 30.25 mmol, 5 eq) was added in one portion and the mixture allowed to stir under argon atmosphere for 24 h. The reaction mixture was then diluted with chloroform and the organic phase washed thoroughly with 50 % brine (3 x 40 mL) and water (3 x 40 mL) to remove most traces of sodium azide and DMF. After drying over MgSO<sub>4</sub> and removal of the solvent under reduced pressure the polymer was again dissolved in a generous volume of chloroform, heated to 50 °C and *n*-heptane was added to obtain a 2:1 solvent mixture of chloroform:*n*-heptane. The solvent mixture was then slowly removed under reduced pressure at 50 °C. Afterwards, the polymer was yet again dissolved in chloroform and precipitated from methanol to remove residual *n*-heptane. Only for **PV73** was this followed by filtration and *Soxhlet* extraction with cyclohexane. **PV73-A** (1.38 g, 91 wt-%) was obtained as an off-white solid.

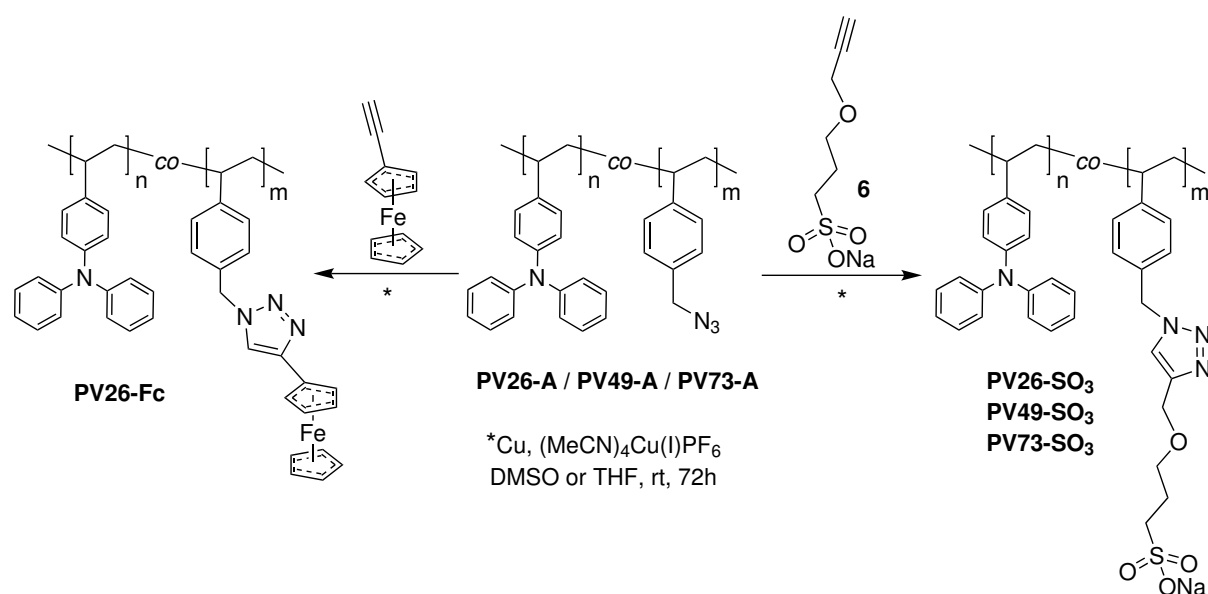
<sup>1</sup>H-NMR (250 MHz, CDCl<sub>3</sub>): **PV26-A**: δ (ppm) = 7.03 (br), 6.92 (br), 6.53 (br), 4.09

(br), 1.95 (br), 1.47 (br), 1.13 (br), 1.01 (br). **PV49-A**:  $\delta$  (ppm) = 7.12 (br), 6.93 (br), 6.78 (br) 6.50 (br), 4.12 (br), 1.82 (br), 1.44 (br), 1.14 (br), 1.01 (br). **PV73-A**:  $\delta$  (ppm) = 7.18 (br), 6.96 (br), 6.75 (br) 6.50 (br), 4.17 (br), 1.71 (br), 1.44 (br), 1.12 (br), 0.90 (br).

**SEC (THF, PS standards):** **PV26-A**  $\overline{M}_n = 5200 \text{ g mol}^{-1}$ ,  $D = 2.34$ . **PV49-A**  $\overline{M}_n = 12\,600 \text{ g mol}^{-1}$ ,  $D = 2.52$ . **PV73-A**  $\overline{M}_n = 9500 \text{ g mol}^{-1}$ ,  $D = 2.74$ .

**IR (ATR):** **PV26-A**  $\tilde{\nu}[\text{cm}^{-1}] = 2096 (\text{N}_3)$ . **PV49-A**  $\tilde{\nu}[\text{cm}^{-1}] = 2093 (\text{N}_3)$ . **PV73-A**  $\tilde{\nu}[\text{cm}^{-1}] = 2093 (\text{N}_3)$ .

### 6.8.3 Solution Clicking of Poly[vinyl(triphenylamine)-*co*-(azidomethyl)styrene]



The general procedure for clicking in solution shall be described in the following. Weighted portions are given in Table 6.3. Polymers **PV26-A**, **PV49-A** and **PV73-A** have been converted in solution with alkyne sulfonate **6**. Ethynyl ferrocene was clicked in solution to **PV26-A**. Reactions were performed in a glovebox with the respective bulk polymer and elemental copper powder weighed into a glass vial. A solution of the desired alkyne and the catalyst (MeCN)<sub>4</sub>Cu(I)PF<sub>6</sub> in DMSO or THF was added and the solution stirred for 3 days (see also chapter 6.4). Crude polymers were precipitated in methanol (ferrocene-functionalized) or acetonitrile (sulfonate-functionalized). Reaction success was assessed by disappearance of the characteristic azide bands of the precursor polymers (PVXX-A).

**Table 6.3:** Weighted portions and yields after CuAAC in solution. Alkyne for ferrocene introduction: ethynyl ferrocene. Alkyne for sulfonate introduction: alkyne sulfonate **6**.

	<b>PV26-Fc/BC</b>	<b>PV26-SO<sub>3</sub>/BC</b>	<b>PV49-SO<sub>3</sub>/BC</b>	<b>PV73-SO<sub>3</sub>/BC</b>
Polymer	147 mg	200 mg	150.5 mg	150 mg
Alkyne	43.5 mg/0.20 mmol	54.1 mg/0.27 mmol	82.6 mg/0.39 mmol	145 mg/0.73 mmol
Catalyst	3.4 mg/0.008 mmol	4.21 mg/0.011 mmol	6.09 mg/0.016 mmol	11.84 mg/0.03 mmol
Cu(0)	11.0 mg/0.17 mmol	15.5 mg/0.23 mmol	23.3 mg/0.33 mmol	38.6 mg/0.61 mmol
THF	4.2 mL	-	-	-
DMSO	-	8.7 mL	8.4 mL	15 mL
Yield	100 mg (68%)	150 mg (61%)	180 mg (83%)	230 mg (84%)

# Bibliography

- [1] R. Merkle, P. Gutbrod, P. Reinold, M. Katzmaier, R. Tkachov, J. Maier, S. Ludwigs, *Polymer (Guildf)*. **2017**, *132*, 216–226, DOI 10.1016/J.POLYMER.2017.10.064.
- [2] P. Reinold, K. Bruchlos, S. Ludwigs, *Polym. Chem.* **2017**, *8*, 7351–7359, DOI 10.1039/C7PY01688C.
- [3] P. Blanchard, C. Malacrida, C. Cabanetos, J. Roncali, S. Ludwigs, *Polym. Int.* **2019**, *68*, 589–606, DOI 10.1002/pi.5695.
- [4] C. Malacrida, Y. Lu, K. Dirnberger, S. Gámez-Valenzuela, M. C. Ruiz Delgado, S. Ludwigs, *J. Mater. Chem. C* **2020**, *8*, 15393–15405, DOI 10.1039/D0TC03090B.
- [5] L. Åkerlund, R. Emanuelsson, G. Hernández, F. Ruipérez, N. Casado, D. Brandell, M. Strømme, D. Mecerreyes, M. Sjödín, *ACS Appl. Energy Mater.* **2019**, *2*, 4486–4495, DOI 10.1021/acsaem.9b00735.
- [6] Y. Liang, Z. Tao, J. Chen, *Adv. Energy Mater.* **2012**, *2*, 742–769, DOI 10.1002/aenm.201100795.
- [7] Z. Song, H. Zhou, *Energy Environ. Sci.* **2013**, *6*, 2280, DOI 10.1039/c3ee40709h.
- [8] R. Gracia, D. Mecerreyes, *Polym. Chem.* **2013**, *4*, 2206–2214, DOI 10.1039/c3py21118e.
- [9] *Iontronics*, (Eds.: J. Leger, M. Berggren, S. Carter), CRC Press, **2016**, DOI 10.1201/b10277.
- [10] M. S. Freund, B. A. Deore, *Self-Doped Conducting Polymers*, Wiley, **2007**, pp. 1–326, DOI 10.1002/9780470061725.
- [11] J. Heinze, B. A. Frontana-Uribe, S. Ludwigs, *Chem. Rev.* **2010**, *110*, 4724–4771, DOI 10.1021/cr900226k.
- [12] C.-k. K. Mai, R. A. Schlitz, G. M. Su, D. Spitzer, X. Wang, S. L. Fronk, D. G. Cahill, M. L. Chabinyc, G. C. Bazan, *J. Am. Chem. Soc.* **2014**, *136*, 13478–13481, DOI 10.1021/ja504284r.
- [13] M. Wieland, C. Dingler, R. Merkle, J. Maier, S. Ludwigs, *ACS Appl. Mater. Interfaces* **2020**, *12*, 6742–6751, DOI 10.1021/acsaami.9b21181.
- [14] H. Ling, S. Liu, Z. Zheng, F. Yan, *Small Methods* **2018**, *2*, 1800070, DOI 10.1002/smt.d.201800070.
- [15] R. Xiong, A. M. Grant, R. Ma, S. Zhang, V. V. Tsukruk, **2018**, DOI 10.1016/j.mser.2018.01.002.

- 
- [16] T. Someya, Z. Bao, G. G. Malliaras, *Nature* **2016**, *540*, 379–385, DOI 10.1038/nature21004.
- [17] O. Yaghmazadeh, F. Cicoira, D. A. Bernards, S. Y. Yang, Y. Bonmassieux, G. G. Malliaras, *J. Polym. Sci. Part B Polym. Phys.* **2011**, *49*, 34–39, DOI 10.1002/polb.22129.
- [18] C. Liao, M. Zhang, M. Y. Yao, T. Hua, L. Li, F. Yan, *Adv. Mater.* **2015**, *27*, 7493–7527, DOI 10.1002/adma.201402625.
- [19] R. J. Mortimer, A. L. Dyer, J. R. Reynolds, *Displays* **2006**, *27*, 2–18, DOI 10.1016/j.displa.2005.03.003.
- [20] E. Smela, *MRS Bull.* **2008**, *33*, 197–204, DOI 10.1557/mrs2008.45.
- [21] Fraunhofer Institute for Solar Energy Systems ISE, Organic Solar Cells, <https://www.ise.fraunhofer.de/en/business-areas/photovoltaics/perovskite-and-organic-photovoltaics/organic-solar-cells-and-modules.html> (visited on 08/03/2021).
- [22] Y. Zang, F. Zhang, D. Huang, X. Gao, C.-a. Di, D. Zhu, *Nat. Commun.* **2015**, *6*, 6269, DOI 10.1038/ncomms7269.
- [23] M. Noda, N. Kobayashi, M. Katsuhara, A. Yumoto, S. Ushikura, R. Yasuda, N. Hirai, G. Yukawa, I. Yagi, K. Nomoto, T. Urabe, *J. Soc. Inf. Disp.* **2011**, *19*, 316, DOI 10.1889/JSID19.4.316.
- [24] H. Shirakawa, A. G. Macdiarmid, C. C. K., *Phys. Rev. Lett.* **1977**, *39*, 1098–1101.
- [25] C. K. Chiang, C. R. Fincher, Y. W. Park, A. J. Heeger, H. Shirakawa, E. J. Louis, S. C. Gau, A. G. MacDiarmid, *Phys. Rev. Lett.* **1977**, *39*, 1098–1101, DOI 10.1103/PhysRevLett.39.1098.
- [26] H. Shirakawa, E. J. Louis, A. G. MacDiarmid, C. K. Chiang, A. J. Heeger, *J. Chem. Soc. Chem. Commun.* **1977**, *6*, 578, DOI 10.1039/c39770000578.
- [27] J. Roncali, *Chem. Rev.* **1992**, *92*, 711–738, DOI 10.1021/Cr00012a009.
- [28] D. M. Ivory, G. G. Miller, J. M. Sowa, L. W. Shacklette, R. R. Chance, R. H. Baughman, *J. Chem. Phys.* **1979**, *71*, 1506–1507, DOI 10.1063/1.438420.
- [29] G. Tourillon, F. Garnier, *J. Electroanal. Chem. Interfacial Electrochem.* **1982**, *135*, 173–178, DOI 10.1016/0022-0728(82)90015-8.
- [30] A. J. Heeger, *Rev. Mod. Phys.* **2001**, *73*, 681–700, DOI <https://doi.org/10.1103/RevModPhys.73.681>.
- [31] R. S. Mulliken, *Science (80-. )*. **1967**, *157*, 13–24, DOI 10.1126/science.157.3784.13.
-

- [32] H. Shirakawa, T. Ito, S. Ikeda, *Die Makromol. Chemie* **1978**, *179*, 1565–1573, DOI 10.1002/macp.1978.021790615.
- [33] M. Rehahn, *Chemie unserer Zeit* **2003**, *37*, 18–30, DOI 10.1002/ciuz.200390000.
- [34] J. L. Bredas, G. B. Street, *Acc. Chem. Res.* **1985**, *18*, 309–315, DOI 10.1021/ar00118a005.
- [35] *P3HT Revisited – From Molecular Scale to Solar Cell Devices*, (Ed.: S. Ludwigs), Springer Berlin Heidelberg, Berlin, Heidelberg, **2014**, pp. 1–87, DOI 10.1007/978-3-662-45145-8.
- [36] Y.-J. Cheng, S.-H. Yang, C.-S. Hsu, *Chem. Rev. (Washington DC U. S.)* **2009**, *109*, 5868–5923, DOI 10.1021/cr900182s.
- [37] S. Allard, M. Forster, B. Souharce, H. Thiem, U. Scherf, *Angew. Chemie Int. Ed.* **2008**, *47*, 4070–4098, DOI 10.1002/anie.200701920.
- [38] H. Shi, C. Liu, Q. Jiang, J. Xu, *Adv. Electron. Mater.* **2015**, *1*, 1500017, DOI 10.1002/aelm.201500017.
- [39] J. Poater, J. Casanovas, M. Solà, C. Alemán, *J. Phys. Chem. A* **2010**, *114*, 1023–1028, DOI 10.1021/jp908764s.
- [40] R. M. S. Maior, K. Hinkelmann, H. Eckert, F. Wudl, *Macromolecules* **1990**, *23*, 1268–1279, DOI 10.1021/ma00207a008.
- [41] G. Koßmehl, G. Chatzitheodorou, *Die Makromol. Chemie Rapid Commun.* **1981**, *2*, 551–555, DOI 10.1002/marc.1981.030020903.
- [42] R. D. McCullough, R. D. Lowe, *J. Chem. Soc. Chem. Commun.* **1992**, *70*, DOI 10.1039/c39920000070.
- [43] R. D. McCullough, R. D. Lowe, M. Jayaraman, D. L. Anderson, *J. Org. Chem.* **1993**, *58*, 904–912, DOI 10.1021/jo00056a024.
- [44] T.-A. Chen, X. Wu, R. D. Rieke, *J. Am. Chem. Soc.* **1995**, *117*, 233–244, DOI 10.1021/ja00106a027.
- [45] R. S. Loewe, S. M. Khersonsky, R. D. McCullough, *Adv. Mater.* **1999**, *11*, 250–253, DOI 10.1002/(SICI)1521-4095(199903)11:3<250::AID-ADMA250>3.0.CO;2-J.
- [46] R. S. Loewe, P. C. Ewbank, J. Liu, L. Zhai, R. D. Mccullough, **2001**, DOI 10.1021/ma001677.
- [47] R. H. Lohwasser, M. Thelakkat, *Macromolecules* **2011**, *44*, 3388–3397, DOI 10.1021/ma200119s.

- 
- [48] R. Miyakoshi, A. Yokoyama, T. Yokozawa, *Macromol. Rapid Commun.* **2004**, *25*, 1663–1666, DOI 10.1002/marc.200400281.
- [49] R. Miyakoshi, A. Yokoyama, T. Yokozawa, *J. Am. Chem. Soc.* **2005**, *127*, 17542–17547, DOI 10.1021/ja0556880.
- [50] M. C. Iovu, E. E. Sheina, R. R. Gil, R. D. McCullough, *Macromolecules* **2005**, *38*, 8649–8656, DOI 10.1021/ma051122k.
- [51] M. P. Bhatt, H. D. Magurudeniya, P. Sista, E. E. Sheina, M. Jeffries-EL, B. G. Janesko, R. D. McCullough, M. C. Stefan, *J. Mater. Chem. A* **2013**, *1*, 12841, DOI 10.1039/c3ta13258g.
- [52] R. Miyakoshi, A. Yokoyama, T. Yokozawa, *J. Am. Chem. Soc.* **2005**, *127*, 17542–17547, DOI 10.1021/ja0556880.
- [53] Y. Geng, L. Huang, S. Wu, F. Wang, *Sci. China Chem.* **2010**, *53*, 1620–1633, DOI 10.1007/s11426-010-4048-2.
- [54] P. Reinold, K. Bruchlos, S. Ludwigs, *Polym. Chem.* **2017**, *8*, 7351–7359, DOI 10.1039/C7PY01688C.
- [55] E. Zhou, Z. Tan, Y. Yang, L. Huo, Y. Zou, C. Yang, Y. Li, *Macromolecules* **2007**, *40*, 1831–1837, DOI 10.1021/ma062633p.
- [56] P. L. Golas, K. Matyjaszewski, *Chem. Soc. Rev.* **2010**, *39*, 1338–1354, DOI 10.1039/B901978M.
- [57] B. Liu, W.-L. Yu, Y.-H. Lai, W. Huang, *Macromolecules* **2002**, *35*, 4975–4982, DOI 10.1021/ma010974r.
- [58] D. Fournier, R. Hoogenboom, U. S. Schubert, *Chem. Soc. Rev.* **2007**, *36*, 1369, DOI 10.1039/b700809k.
- [59] Y. Li, G. Vamvounis, J. Yu, S. Holdcroft, *Macromolecules* **2001**, *34*, 3130–3132, DOI 10.1021/ma010293w.
- [60] Y. Li, G. Vamvounis, S. Holdcroft, *Macromolecules* **2001**, *34*, 141–143, DOI 10.1021/ma001413n.
- [61] Y. Li, G. Vamvounis, S. Holdcroft, *Macromolecules* **2002**, *35*, 6900–6906, DOI 10.1021/ma020140o.
- [62] L. Zhai, R. L. Pilston, K. L. Zaiger, K. K. Stokes, R. D. McCullough, *Macromolecules* **2003**, *36*, 61–64, DOI 10.1021/ma0255884.
- [63] E. Zeglio, M. M. Schmidt, M. Thelakkat, R. Gabrielsson, N. Solin, O. Inganäs, *ChemistrySelect* **2016**, *1*, 4340–4344, DOI 10.1002/slct.201600920.
-

- [64] J. M. Lobež, T. L. Andrew, V. Bulović, T. M. Swager, *ACS Nano* **2012**, *6*, 3044–3056, DOI 10.1021/nn204589u.
- [65] Y. Shirota, *J. Mater. Chem.* **2000**, *10*, 1–25, DOI 10.1039/a908130e.
- [66] R. Rybakiewicz, M. Zagorska, A. Pron, *Chem. Pap.* **2017**, *71*, 243–268, DOI 10.1007/s11696-016-0097-0.
- [67] M.-Y. Chou, M.-k. Leung, Y. O. Su, C. L. Chiang, C.-C. Lin, J.-H. Liu, C.-K. Kuo, C.-Y. Mou, *Chem. Mater.* **2004**, *16*, 654–661, DOI 10.1021/cm034735p.
- [68] J. Wang, K. Liu, L. Ma, X. Zhan, *Chem. Rev.* **2016**, *116*, 14675–14725, DOI 10.1021/acs.chemrev.6b00432.
- [69] M. Thelakkat, *Macromol. Mater. Eng.* **2002**, *287*, 442, DOI 10.1002/1439-2054(20020701)287:7<442::AID-MAME442>3.0.CO;2-H.
- [70] J. Kwak, W. K. Bae, M. Zorn, H. Woo, H. Yoon, J. Lim, S. W. Kang, S. Weber, H.-J. Butt, R. Zentel, S. Lee, K. Char, C. Lee, *Adv. Mater.* **2009**, *21*, 5022–5026, DOI 10.1002/adma.200902072.
- [71] B. C. Wang, H. R. Liao, J. C. Chang, L. Chen, J. T. Yeh, *J. Lumin.* **2007**, *124*, 333–342, DOI 10.1016/j.jlumin.2005.11.016.
- [72] P. Cias, C. Slugovc, G. Gescheidt, *J. Phys. Chem. A* **2011**, *115*, 14519–14525, DOI 10.1021/jp207585j.
- [73] C. Su, F. Yang, L. Ji, L. Xu, C. Zhang, *J. Mater. Chem. A* **2014**, *2*, 20083–20088, DOI 10.1039/C4TA03413A.
- [74] H. Zhuang, Q. Zhou, Q. Zhang, H. Li, N. Li, Q. Xu, J. Lu, *J. Mater. Chem. C* **2015**, *3*, 416–422, DOI 10.1039/C4TC01844C.
- [75] T. Manifar, S. Rohani, *Can. J. Chem. Eng.* **2008**, *82*, 323–334, DOI 10.1002/cjce.5450820213.
- [76] J. P. Wolfe, S. Wagaw, S. L. Buchwald, *J. Am. Chem. Soc.* **1996**, *118*, 7215–7216, DOI 10.1021/ja9608306.
- [77] T. Hatakeyama, R. Imayoshi, Y. Yoshimoto, S. K. Ghorai, M. Jin, H. Takaya, K. Norisuye, Y. Sohrin, M. Nakamura, *J. Am. Chem. Soc.* **2012**, *134*, 20262–20265, DOI 10.1021/ja309845k.
- [78] P. Shen, G. Sang, J. Lu, B. Zhao, M. Wan, Y. Zou, Y. Li, S. Tan, *Macromolecules* **2008**, *41*, 5716–5722, DOI 10.1021/ma800847f.
- [79] E. J. W. Crossland, P. Cunha, S. Scroggins, S. Moratti, O. Yurchenko, U. Steiner, M. A. Hillmyer, S. Ludwigs, *ACS Nano* **2010**, *4*, 962–966, DOI 10.1021/nn901447a.

- 
- [80] O. Yurchenko, J. Heinze, S. Ludwigs, *ChemPhysChem* **2010**, *11*, 1637–1640, DOI 10.1002/cphc.201000131.
- [81] O. Yurchenko, D. Freytag, L. zur Borg, R. Zentel, J. Heinze, S. Ludwigs, *J. Phys. Chem. B* **2012**, *116*, 30–39, DOI 10.1021/jp208076z.
- [82] E. Stavrinidou, P. Leleux, H. Rajaona, D. Khodagholy, J. Rivnay, M. Lindau, S. Sanaur, G. G. Malliaras, *Adv. Mater.* **2013**, *25*, 4488–4493, DOI 10.1002/adma.201301240.
- [83] S. Inal, G. G. Malliaras, J. Rivnay, *Nat. Commun.* **2017**, *8*, 1–7, DOI 10.1038/s41467-017-01812-w.
- [84] P. Lin, F. Yan, J. Yu, H. L. W. Chan, M. Yang, *Adv. Mater.* **2010**, *22*, 3655–3660, DOI 10.1002/adma.201000971.
- [85] A. Malti, J. Edberg, H. Granberg, Z. U. Khan, J. W. Andreasen, X. Liu, D. Zhao, H. Zhang, Y. Yao, J. W. Brill, I. Engquist, M. Fahlman, L. Wågberg, X. Crispin, M. Berggren, *Adv. Sci.* **2016**, *3*, 1500305, DOI 10.1002/advs.201500305.
- [86] Q. Pei, G. Yu, C. Zhang, Y. Yang, A. J. Heeger, *Science (80-. )*. **1995**, *269*, 1086–1088, DOI 10.1126/science.269.5227.1086.
- [87] A. V. Volkov, K. Wijeratne, E. Mitraka, U. Ail, D. Zhao, K. Tybrandt, J. W. Andreasen, M. Berggren, X. Crispin, I. V. Zozoulenko, *Adv. Funct. Mater.* **2017**, *27*, 1700329, DOI 10.1002/adfm.201700329.
- [88] M. Modarresi, J. F. Franco-Gonzalez, I. Zozoulenko, *Phys. Chem. Chem. Phys.* **2019**, *21*, 6699–6711, DOI 10.1039/c8cp07141a.
- [89] K.-D. Kreuer, *Chem. Mater.* **2014**, *26*, 361–380, DOI 10.1021/cm402742u.
- [90] A. Kusoglu, A. Z. Weber, *Chem. Rev.* **2017**, *117*, 987–1104, DOI 10.1021/acs.chemrev.6b00159.
- [91] E. Zeglio, M. Vagin, C. Musumeci, F. N. Ajjan, R. Gabrielsson, X. T. Trinh, N. T. Son, A. Maziz, N. Solin, O. Inganäs, *Chem. Mater.* **2015**, *27*, 6385–6393, DOI 10.1021/acs.chemmater.5b02501.
- [92] S. H. Kim, J. G. Kim, *Bull. Korean Chem. Soc.* **2009**, *30*, 2283–2286, DOI 10.5012/bkcs.2009.30.10.2283.
- [93] H. Tomita, R. A. Register, *Macromolecules* **1993**, *26*, 2791–2795, DOI 10.1021/ma00063a024.
- [94] T. W. Baughman, C. D. Chan, K. I. Winey, K. B. Wagener, *Macromolecules* **2007**, *40*, 6564–6571, DOI 10.1021/ma070841r.
-

- [95] C. Cutler, M. Bouguettaya, J. Reynolds, *Adv. Mater.* **2002**, *14*, 684–688, DOI 10.1002/1521-4095(20020503)14:9<684::AID-ADMA684>3.0.CO;2-7.
- [96] A. D. Child, J. R. Reynolds, *Macromolecules* **1994**, *27*, 1975–1977, DOI 10.1021/ma00085a050.
- [97] R. Rulken, M. Schulze, G. Wegner, *Macromol. Rapid Commun.* **1994**, *15*, 669–676, DOI 10.1002/marc.1994.030150902.
- [98] H. Jiang, P. Taranekar, J. R. Reynolds, K. S. Schanze, *Angew. Chemie Int. Ed.* **2009**, *48*, 4300–4316, DOI 10.1002/anie.200805456.
- [99] J. Rivnay, S. Inal, B. A. Collins, M. Sessolo, E. Stavrinidou, X. Strakosas, C. Tassone, D. M. DeLongchamp, G. G. Malliaras, *Nat. Commun.* **2016**, *7*, 1–9, DOI 10.1038/ncomms11287.
- [100] S. D. Collins, O. V. Mikhnenko, T. L. Nguyen, Z. D. Rengert, G. C. Bazan, H. Y. Woo, T. Q. Nguyen, *Adv. Electron. Mater.* **2017**, *3*, DOI 10.1002/aelm.201700005.
- [101] H. Wang, U. Ail, R. Gabrielsson, M. Berggren, X. Crispin, *Adv. Energy Mater.* **2015**, *5*, 1500044, DOI 10.1002/aenm.201500044.
- [102] E. S. Muckley, C. B. Jacobs, K. Vidal, J. P. Mahalik, R. Kumar, B. G. Sumpter, I. N. Ivanov, *ACS Appl. Mater. Interfaces* **2017**, *9*, 15880–15886, DOI 10.1021/acsmi.7b03128.
- [103] R. A. Huggins, *Ionics (Kiel)*. **2002**, *8*, 300–313, DOI 10.1007/BF02376083.
- [104] H. Wang, D. Zhao, Z. U. Khan, S. Puzinas, M. P. Jonsson, M. Berggren, X. Crispin, *Adv. Electron. Mater.* **2017**, *3*, 1700013, DOI 10.1002/aelm.201700013.
- [105] H. C. Kolb, M. G. Finn, K. B. Sharpless, *Angew. Chemie Int. Ed.* **2001**, *40*, 2004–2021, DOI 10.1002/1521-3773(20010601)40:11<2004::AID-ANIE2004>3.0.CO;2-5.
- [106] M. Meldal, C. W. Tornøe, *Chem. Rev.* **2008**, *108*, 2952–3015, DOI 10.1021/cr0783479.
- [107] V. Castro, H. Rodríguez, F. Albericio, *ACS Comb. Sci.* **2016**, *18*, 1–14, DOI 10.1021/acscmbosci.5b00087.
- [108] R. Huisgen, *Angew. Chemie Int. Ed. English* **1963**, *2*, 565–598, DOI 10.1002/anie.196305651.
- [109] L. Liang, D. Astruc, *Coord. Chem. Rev.* **2011**, *255*, 2933–2945, DOI 10.1016/j.ccr.2011.06.028.
- [110] L. Zhang, X. Chen, P. Xue, H. H. Y. Sun, I. D. Williams, K. B. Sharpless, V. V. Fokin, G. Jia, *J. Am. Chem. Soc.* **2005**, *127*, 15998–15999, DOI 10.1021/ja054114s.

- [111] J. E. Hein, V. V. Fokin, *Chem. Soc. Rev.* **2010**, *39*, 1302, DOI 10.1039/b904091a.
- [112] J. LUTZ, Z. ZARAFSHANI, *Adv. Drug Deliv. Rev.* **2008**, *60*, 958–970, DOI 10.1016/j.addr.2008.02.004.
- [113] U. Mansfeld, C. Pietsch, R. Hoogenboom, C. R. Becer, U. S. Schubert, *Polym. Chem.* **2010**, *1*, 1560, DOI 10.1039/c0py00168f.
- [114] E. Haldón, M. C. Nicasio, P. J. Pérez, *Org. Biomol. Chem.* **2015**, *13*, 9528–9550, DOI 10.1039/C5OB01457C.
- [115] L. Zhu, C. J. Brassard, X. Zhang, P. M. Guha, R. J. Clark, *Chem. Rec.* **2016**, *16*, 1501–1517, DOI 10.1002/tcr.201600002.
- [116] B. T. Worrell, J. A. Malik, V. V. Fokin, *Science (80-. )*. **2013**, *340*, 457–460, DOI 10.1126/science.1229506.
- [117] C. Özen, N. Ş. Tüzün, *J. Mol. Catal. A Chem.* **2017**, *426*, 150–157, DOI 10.1016/j.molcata.2016.11.010.
- [118] J. E. Hein, V. V. Fokin, *Chem. Soc. Rev.* **2010**, *39*, 1302, DOI 10.1039/b904091a.
- [119] H.-B. Bu, G. Götz, E. Reinold, A. Vogt, R. Azumi, J. L. Segura, P. Bäuerle, *Chem. Commun.* **2012**, *48*, 2677, DOI 10.1039/c2cc17374c.
- [120] N. Shida, Y. Ishiguro, M. Atobe, T. Fuchigami, S. Inagi, *ACS Macro Lett.* **2012**, *1*, 656–659, DOI 10.1021/mz300210w.
- [121] J. U. Lind, C. Acikgöz, A. E. Daugaard, T. L. Andresen, S. Hvilsted, M. Textor, N. B. Larsen, *Langmuir* **2012**, *28*, 6502–6511, DOI 10.1021/la300503p.
- [122] M. Wieland, C. Malacrida, Q. Yu, C. Schlewitz, L. Scapinello, A. Penoni, S. Ludwigs, *Flex. Print. Electron.* **2020**, *5*, 014016, DOI 10.1088/2058-8585/ab76e0.
- [123] X.-Y. Wang, A. Kimyonok, M. Weck, *Chem. Commun.* **2006**, 3933, DOI 10.1039/b609382e.
- [124] G. Demirci, M. A. Tasdelen, *Eur. Polym. J.* **2015**, *66*, 282–289, DOI 10.1016/j.eurpolymj.2015.02.029.
- [125] J. U. Lind, T. S. Hansen, A. E. Daugaard, S. Hvilsted, T. L. Andresen, N. B. Larsen, *Macromolecules* **2011**, *44*, 495–501, DOI 10.1021/ma102149u.
- [126] H.-B. Bu, G. Götz, E. Reinold, A. Vogt, S. Schmid, R. Blanco, J. L. Segura, P. Bäuerle, *Chem. Commun.* **2008**, 1320, DOI 10.1039/b718077b.
- [127] M. Goll, A. Ruff, E. Muks, F. Goerigk, B. Omiecienski, I. Ruff, R. C. González-Cano, J. T. Lopez Navarrete, M. C. Ruiz Delgado, S. Ludwigs, *Beilstein J. Org. Chem.* **2015**, *11*, 335–347, DOI 10.3762/bjoc.11.39.

- [128] T. L. Benanti, A. Kalaydjian, D. Venkataraman, *Macromolecules* **2008**, *41*, 8312–8315, DOI 10.1021/ma801798p.
- [129] T. S. Hansen, A. E. Daugaard, S. Hvilsted, N. B. Larsen, *Adv. Mater.* **2009**, *21*, 4483–4486, DOI 10.1002/adma.200900980.
- [130] J. Kim, Master Thesis, University of Stuttgart, **2016**.
- [131] X.-Y. Wang, M. Weck, *Macromolecules* **2005**, *38*, 7219–7224, DOI 10.1021/ma050579r.
- [132] X.-Y. Wang, R. N. Prabhu, R. H. Schmehl, M. Weck, *Macromolecules* **2006**, *39*, 3140–3146, DOI 10.1021/ma060032s.
- [133] S. Koltzenburg, M. Maskos, O. Nuyken in *Polym. Chem.* Springer Berlin Heidelberg, Berlin, Heidelberg, **2017**, pp. 349–380, DOI 10.1007/978-3-662-49279-6\_13.
- [134] W.-F. Su in *Princ. Polym. Des. Synth.* Springer Berlin Heidelberg, Berlin, Heidelberg, **2013**, pp. 137–183, DOI 10.1007/978-3-642-38730-2\_7.
- [135] G. L'abbe, *Chem. Rev.* **1969**, *69*, 345–363, DOI 10.1021/cr60259a004.
- [136] J. Rieger, *J. Therm. Anal.* **1996**, *46*, 965–972, DOI 10.1007/BF01983614.
- [137] K. Bruchlos, PhD Thesis, University of Stuttgart, **2019**.
- [138] D. K. Gosser, *Synth. React. Inorg. Met. Chem.* **1994**, *24*, 1237–1238, DOI 10.1080/00945719408001398.
- [139] A. J. Bard, L. R. Faulkner, *Electrochemical Methods: Fundamentals and Applications*, 2nd Edition, Wiley, **2000**.
- [140] L. B. de Oliveira Freitas, P. Eisenberger, C. M. Crudden, *Organometallics* **2013**, *32*, 6635–6638, DOI 10.1021/om400743c.
- [141] T. Stöcker, A. Köhler, R. Moos, *J. Polym. Sci. Part B Polym. Phys.* **2012**, *50*, 976–983, DOI 10.1002/polb.23089.
- [142] P. Bäuerle, F. Würthner, S. Heid, *Angew. Chemie Int. Ed. English* **1990**, *29*, 419–420, DOI 10.1002/anie.199004191.
- [143] C. J. Mueller, T. Klein, E. Gann, C. R. McNeill, M. Thelakkat, *Macromolecules* **2016**, *49*, 3749–3760, DOI 10.1021/acs.macromol.5b02659.
- [144] D. G. Selivanova, O. A. Maiorova, E. V. Shklyueva, G. G. Abashev, *Russ. J. Org. Chem.* **2015**, *51*, 735–739, DOI 10.1134/S1070428015050267.
- [145] T.-B. Wei, J.-D. Ding, J.-F. Chen, B.-B. Han, X.-M. Jiang, H. Yao, Y.-M. Zhang, Q. Lin, *New J. Chem.* **2018**, *42*, 1271–1275, DOI 10.1039/C7NJ03937A.

- [146] J. C. Brendel, M. M. Schmidt, G. Hagen, R. Moos, M. Thelakkat, *Chem. Mater.* **2014**, *26*, 1992–1998, DOI 10.1021/cm500500t.
- [147] R. Rulkens, M. Schulze, G. Wegner, *Solutions* **1994**, *676*, 669–676.
- [148] K. Nilles, P. Theato, *Polym. Chem.* **2011**, *2*, 376–384, DOI 10.1039/c0py00261e.
- [149] R. Ramani, J. Srivastava, S. Alam, *Thermochim. Acta* **2010**, *499*, 34–39, DOI 10.1016/j.tca.2009.10.019.
- [150] A. Rodrigues, M. C. R. Castro, A. S. Farinha, M. Oliveira, J. P. Tomé, A. V. Machado, M. M. M. Raposo, L. Hilliou, G. Bernardo, *Polym. Test.* **2013**, *32*, 1192–1201, DOI 10.1016/j.polymertesting.2013.07.008.
- [151] Y. Zhao, G. Yuan, P. Roche, M. Leclerc, *Polymer (Guildf)*. **1995**, *36*, 2211–2214, DOI 10.1016/0032-3861(95)95298-F.
- [152] T. T. Ngo, D. N. Nguyen, V. T. Nguyen, *Adv. Nat. Sci. Nanosci. Nanotechnol.* **2012**, *3*, 045001, DOI 10.1088/2043-6262/3/4/045001.
- [153] D. Thanasamy, D. Jesuraj, S. K. Konda kannan, V. Avadhanam, *Polymer (Guildf)*. **2019**, *175*, 32–40, DOI 10.1016/j.polymer.2019.03.042.
- [154] D. Vladikova, *Proc. Int. Work. "Advanced Tech. Energy Sources Investig. Testing"* **2004**, 1–28.
- [155] X.-Y. Wang, A. Kimyonok, M. Weck, *Chem. Commun.* **2006**, 3933, DOI 10.1039/b609382e.
- [156] D. Bondarev, J. Zedník, I. Šloufová, A. Sharf, M. Procházka, J. Pflieger, J. Vohlídal, *J. Polym. Sci. Part A Polym. Chem.* **2010**, *48*, 3073–3081, DOI 10.1002/pola.24085.
- [157] A. J. B. L. R. Faulkner, *Electrochemical Methods: Fundamentals and Applications, 2nd Edition*, **2000**, pp. 1–864.
- [158] J. P. Collman, N. K. Devaraj, C. E. D. Chidsey, *Langmuir* **2004**, *20*, 1051–1053, DOI 10.1021/1a0362977.
- [159] Y. Sato, F. Mizutani, K. Shimazu, S. Ye, K. Uosaki, *J. Electroanal. Chem.* **1999**, *474*, 94–99, DOI 10.1016/S0022-0728(99)00305-8.
- [160] N. R. Babij, E. O. McCusker, G. T. Whiteker, B. Canturk, N. Choy, L. C. Creemer, C. V. D. Amicis, N. M. Hewlett, P. L. Johnson, J. A. Knobelsdorf, F. Li, B. A. Lorschach, B. M. Nugent, S. J. Ryan, M. R. Smith, Q. Yang, *Org. Process Res. Dev.* **2016**, *20*, 661–667, DOI 10.1021/acs.oprd.5b00417.
- [161] J.-S. Lee, J. Jamnik, J. Maier, *Monatshefte für Chemie - Chem. Mon.* **2009**, *140*, 1113–1119, DOI 10.1007/s00706-009-0130-x.

- [162] I. Riess, *Solid State Ionics* **1992**, *51*, 219–229, DOI 10.1016/0167-2738(92)90204-3.
- [163] X. YUAN, H. WANG, J. COLINSUN, J. ZHANG, *Int. J. Hydrogen Energy* **2007**, *32*, 4365–4380, DOI 10.1016/j.ijhydene.2007.05.036.
- [164] L. A. Middlemiss, A. J. Rennie, R. Sayers, A. R. West, *Energy Reports* **2020**, *6*, 232–241, DOI 10.1016/j.egyr.2020.03.029.
- [165] E. von Hauff, *J. Phys. Chem. C* **2019**, *123*, 11329–11346, DOI 10.1021/acs.jpcc.9b00892.
- [166] A. Lasia in *Mod. Asp. Electrochem. Vol. 32*, Kluwer Academic Publishers, Boston, **1999**, pp. 143–248, DOI 10.1007/0-306-46916-2\_2.
- [167] G. Sauerbrey, *Zeitschrift für Phys.* **1959**, *155*, 206–222, DOI 10.1007/BF01337937.
- [168] D. R. Denison, *J. Vac. Sci. Technol.* **1973**, *10*, 126–129, DOI 10.1116/1.1317921.
- [169] C.-S. Lu, O. Lewis, *J. Appl. Phys.* **1972**, *43*, 4385–4390, DOI 10.1063/1.1660931.
- [170] B. D. Vogt, E. K. Lin, W.-L. Wu, C. C. White, *J. Phys. Chem. B* **2004**, *108*, 12685–12690, DOI 10.1021/jp0481005.
- [171] I. M. Ismail, N. D. Gray, J. R. Owen, *J. Chem. Soc. Faraday Trans.* **1996**, *92*, 4115, DOI 10.1039/ft9969204115.